

Universiteit
Antwerpen

Faculteit Wetenschappen
Departement Fysica

**Emergent phenomena in superconductors and
superfluids with multicomponent quantum
condensates**

**Emergente fenomenen in supergeleiders en
superfluiden met multicomponent kwantum
condensaten**

Proefschrift voorgelegd tot het behalen van de graad van doctor in de
wetenschappen aan de Universiteit Antwerpen te verdedigen door

Natalia Orlova

Promotor
Prof. Dr. Milorad Milošević

Antwerpen

May 2016

Members of the Jury:

Chairman

Prof. Dr. Michiel Wouters, Universiteit Antwerpen, Belgium

Supervisor

Prof. Dr. Milorad Milošević, Universiteit Antwerpen, Belgium

Members

Prof. Dr. Sara Bals, Universiteit Antwerpen, Belgium,

Dr. Igor Cherednikov, Universiteit Antwerpen, Belgium,

Prof. Dr. Mauro M. Doria, Universidade Federal do Rio de Janeiro, Brazil,

Prof. Dr. David Neilson, University of Camerino, Italy,

Prof. Dr. Jacques Tempere, Universiteit Antwerpen, Belgium.

Contact Information

Natalia Orlova

G.U. 205

Groenenborgerlaan 171

2020 Antwerpen

Belgium

natalia.orlova@seznam.cz

Preface

This thesis focuses on multi-component quantum systems such as multi-band superconductors, superconductors in which multiband physics arises due to quantum confinement, and multi-component Bose-Einstein condensates (BECs). Such multicomponent systems are of high interest today, since they harbor plethora of nontrivial phenomena unattainable in their single-component counterparts. In case of multiband superconductors one can e.g. point out the highly-debated nonstandard vortex configurations recently observed in MgB_2 [1, 2], the BCS-BEC crossover revealed in experiments on, e.g., $\text{FeSe}_x\text{Te}_{1-x}$ [3, 4], theoretically predicted chiral superconducting states [5, 6], the hidden criticality [7], significant broadening of the type-I/type-II transitional domain [8], etc.

Still, the most convenient tool to study all the mentioned phenomena is a generalized Ginzburg-Landau (GL) theory for multiband superconductors. The generalization of the GL theory to the multiband case is still a highly debated issue. The theory represents a system of nonlinear GL-type equations, one for each band gap, coupled via the linear Josephson-type terms, and the corresponding multicomponent functional. The generalization of the GL theory appears intuitively justified, partially by a familiar structure of the obtained equations. However, it was reported [19, 20, 216] that the generalized GL theory contains a few shortcomings. Therefore, the objective of this thesis is *to revise the generalized Ginzburg-Landau theory for multi-band superconductors*.

Superconductors under quantum confinement attract a lot of research interest nowadays. It is mostly due to the quantum-size resonance effects in superconducting characteristics [21], i.e., oscillations of the critical temperature T_c , enhancement of the critical magnetic field H_c (thermodynamic, but

upper and lower), and the excitation gap. Until recently there was no suitable theory to calculate the complex magnetic response of such superconductors, and for example, investigate complex configurations of vortices taking into account the multiband physics. The standard Ginzburg-Landau theory is not applicable to superconductors under quantum confinement (nanofilms), since the thickness of such superconductors is much smaller than the bulk BCS coherence length. Therefore, the next objective of the thesis is *to derive a manageable multiband theory for nanofilms*.

On the other hand, the interest in multi-component BEC originates from the successful experimental realization of rotating BECs of two hyperfine spin states of atoms of the same kind [9, 10, 11, 12, 13, 14]. Afterwards, it was shown that already in a two-component Bose-Einstein condensate (BEC) case, rotating atomic gases host nontrivial vortex lattices [15, 16], vortex sheets [17], and skyrmions [18]. More components, and nontrivial coupling between them, are bound to lead to further rich physics. Therefore, another objective of the thesis is to study nontrivial coupling between the components of multi-component BECs and to which interesting vortex physics this can lead.

This thesis is therefore divided into two main parts, one part devoted to the derivation of manageable theories and study of multiband superconductors and nanofilms, and the other to the study of rotating multi-component Bose-Einstein condensates. The thesis is organized as follows.

Chapter 1 gives the historical overview of superconductivity, outlines theoretical aspects relevant for the further considerations in the thesis and presents the hallmark properties of multi-band superconductors. A brief introduction to superconductivity under quantum confinement is also provided, such as in nanofilms. Then Bose-Einstein condensation is reviewed giving a theoretical basis for further calculations and a computational method is described which is used in further calculations. The fundamental description of topological defects is given such as vortices and skyrmions which are studied in the thesis.

In **Chapter 2**, the Ginzburg-Landau formalism for multiband superconductors is derived from the generalized BCS Hamiltonian by applying the Green's function technique developed by Gor'kov. Two scenarios are examined here, when the solution for the critical temperature is non-degenerate and when it is degenerate. In accordance with the type of a solution, the Ginzburg-Landau theory is constructed. The particular case of a three-band superconductor is considered, and it is found that this system exhibits degenerated solutions for the critical temperature, which leads to a non-trivial phase difference between the bands, often called chiral solutions. The possibility of having the chiral states as the ground state, and their relevance to

recent materials, are discussed.

Chapter 3 presents derivation of the Ginzburg-Landau theory for superconductors under quantum confinement. First, the derivation starts with the construction of a suitable BCS Hamiltonian for nanofilms by integrating out the dependence of a coordinate in which the electronic motion is restricted and causes formation of discrete electron subbands. Afterwards, the same technique is applied similar to one used in the derivation of the Ginzburg-Landau theory for the multiband superconductors. Finally, the range of applicability of the derived formalism and the consequences on well established phenomena in thin films are discussed.

Chapter 4 concerns the study of a rotating harmonically trapped Rabi-coupled three-component Bose-Einstein condensate. It is shown that this system can host unconventional vortex lattices in its ground state, all of which have skyrmionic topology. The discovered lattices comprise square and zig-zag patterns, vortex dimers and chains, and doubly quantized vortices. In view of the Rabi energy suppression and the global phase frustration, parametric regions in the equilibrium phase diagram are identified where the three-component condensate starts to behave as a two-component condensate with only density-density interactions. The study focuses on intermediate Rabi coupling strengths, where the unique vortex physics is found which occurs neither in the two-component counterpart nor in the purely density-density-coupled three-component system.

In **Chapter 5**, a rotating harmonically trapped two-component Bose-Einstein condensate based on the mixture of atoms of two kinds with the atomic mass imbalance was studied in three distinctly different regimes. According to the common paradigm, giant vortices are not supported by a rotating harmonically trapped single component BEC. In the case of two-component BECs, giant multi-quantum vortices as ground-state solutions are discovered in all three regimes. In two of the regimes, skyrmionic solutions are found and corresponding pseudospin textures are plotted.

Finally, the results are summarized and outlook of the thesis is provided in **Chapter 6**.

Contents

Acknowledgement	iii
Preface	iv
1 Introduction	1
1.1 Historical overview of superconductivity	1
1.2 Ginzburg-Landau theory for single band superconductors . . .	5
1.2.1 Free energy expansion	5
1.2.2 Ginzburg-Landau equations	7
1.2.3 Two characteristic length scales in the GL theory . . .	9
1.3 The BCS theory	11
1.3.1 Emergence of an energy gap	13
1.3.2 The GL equation from the BCS theory	18
1.4 Multiband superconductors	23
1.4.1 The crystal structure of MgB ₂ and some of pnictides .	25
1.4.2 The Fermi surface of multiband superconductors . . .	26
1.4.3 The isotope effect measurements	27
1.4.4 Experimental evidence of multiple gaps	29
1.4.5 The pairing symmetry	31
1.5 Superconductors under quantum confinement	33
1.6 Multi-component Bose-Einstein condensation	36
1.6.1 Achievement of Bose-Einstein condensation	36
1.6.2 Experimental technique	38
1.6.3 Gross-Pitaevskii theory for a Bose-Einstein condensate	39
1.6.4 Multi-component Bose-Einstein condensates	43

1.6.5	Theory for multicomponent Bose-Einstein condensates	44
1.6.6	Dimensionless GP equations	45
1.6.7	Introduction of link-variables to the GP equations . .	47
1.6.8	Numerical simulation of the coupled GP equations . . .	50
1.7	Skyrmions in multi-component systems	52
1.7.1	Vortices	52
1.7.2	Skyrmions	55
1.8	Goals of the thesis	58
2	The chiral regime of three-band superconductors	61
2.1	Introduction	61
2.2	Derivation of the GL theory	64
2.2.1	Truncated gap equation	64
2.2.2	Reconstructed GL theory	66
2.3	Explicit form of the GL equations	68
2.3.1	Nondegenerate case	68
2.3.2	Degenerate case	70
2.4	Three-band system	71
2.4.1	Eigenvectors	71
2.4.2	Chiral state with phase frustration	73
2.5	Summary and conclusions	77
3	Nanofilms as multiband superconductors	79
3.1	Introduction	79
3.2	Multiband BCS Hamiltonian for nano-films	81
3.3	Gor'kov truncation for multiband superconductors	83
3.4	Reconstructed truncation and the GLtheory	86
3.5	Applicability domain of the GL theory for nanofilms	88
3.6	Summary and conclusions	89
4	Skyrmionic vortex lattices in three-component BECs	91
4.1	Introduction	91
4.2	Theoretical framework	94
4.3	Numerical results	95
4.3.1	Lattice phase diagrams	96
4.3.2	Rabi suppression in the three-component system	108
4.3.3	Domain walls in the relative phases	111
4.3.4	Vortex phases revisited	113
4.4	Summary and Conclusions	114

5	Multiquantum vortices in two-component BEC	117
5.1	Introduction	117
5.2	Model	119
5.3	Ground-state multiquantum vortices	120
5.4	Pseudospin textures	124
5.5	Summary and Conclusions	126
6	Summary and outlook	129
7	Samenvatting en vooruitzichten	133
	Bibliography	137

CHAPTER 1

Introduction

1.1 Historical overview of superconductivity

Superconductivity was discovered in 1911 by H. Kamerlingh Onnes in Leiden [22]. Using previously developed refrigeration technique to reach temperatures of a few Kelvin, Onnes expected that in ultra-clean metals the resistance gradually reduces to zero at ultralow temperatures, and performed experiments on mercury to prove that hypothesis. Instead, Kamerlingh Onnes observed that resistance of the sample abruptly dropped to zero at 4.2 K [Fig. 1.1(a)]. Later on, this phenomenon of perfect conductivity was termed superconductivity, and the temperature at which a sample became superconducting, was named critical temperature T_c . For many years the phenomenon remained unexplained, despite the further established characteristics, such as the perfect diamagnetism via the so-called Meissner effect [Fig. 1.1(b)] [23].

The first theories to explain the phenomenon of superconductivity were phenomenological and based on the Maxwell equations. One of those theories was proposed by brothers London in 1935 to describe the distribution of fields and currents [24]. Pippard subsequently developed the nonlocal generalization of the London theory in 1953 [25]. The disadvantage of these approaches was their inability to address the spatial distribution of the carriers of superconductivity, or to explain how nonlinear effects of fields could deplete the density of carriers to zero at the critical temperature. Known characteristics of superconducting materials suggested that superconductivity was a macroscopic manifestation of quantum effects occurring on a microscopic

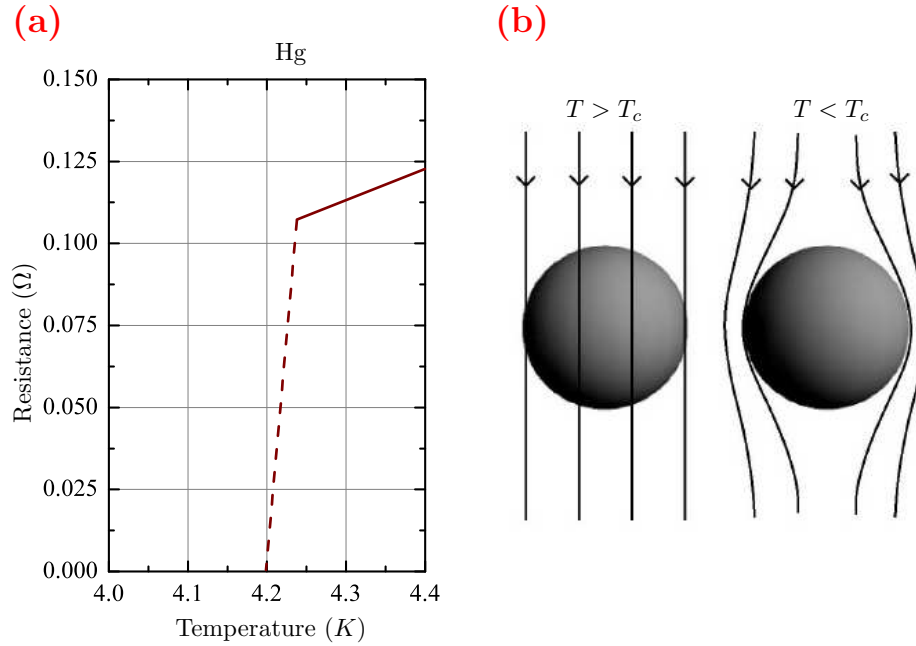


Figure 1.1: Hallmark characteristics of superconducting materials: (a) resistance (in this case of mercury) drops to zero at T_c (4.2 K); (b) expulsion of the magnetic field at $T < T_c$.

scale in a material, when it enters the superconducting regime. Therefore, developing of a new theory, which would take into account quantum effects and would help to address the issues which the London and Pippard theories could not, was crucially important. Encouraged by the success of the quantum mechanics in explanation of metallic behavior, many prominent theorists of the time, such as Bohr, Pauli, Heisenberg, Bloch, Landau, Frenkel, Brillouin and Kronig, started to apply quantum mechanical tools to explain superconductivity [26]. There were two main concepts developed. The first were the spontaneous current theories of Bloch, Landau and Frenkel based on the notion of a current-bearing equilibrium state (1929-1933) [26]. The second was the electron-lattice or electron-chain theory of Bohr and Kronig (1932-1933) [26]. The idea of the first theory was that in equilibrium the thermodynamically favored superconducting ground state, corresponding to a minimum of the free energy, bears a finite spontaneous current below the critical temperature, while at higher temperatures current-free equilibrium states have statistically greater probability [26]. In other words, it was the theory of a ground state with finite current. The second concept premised

that the interactions between electrons lead to appearance of a rigid lattice intermeshed with the ionic lattice [26]. Superconductivity results, in this theory, from the coherent quantum motion of a lattice of electrons. However, these two theories failed to fully agree with existing experiments.

Another phenomenological theory was proposed by Ginzburg and Landau in 1950 [27]. The Ginzburg-Landau (GL) theory was based on the expansion of a complex order parameter ψ , describing the superconducting state, in the proximity of the critical temperature, within Landau's general theory of second-order phase transitions. The advantage of the GL theory was in its elegant and convenient formulation, although it was a phenomenological theory. A major significance of the theory was its ability to describe the intermediate state of superconductors in which superconducting and normal domains coexist at the thermodynamic critical field [28, 29].

One of the crucial experiments that pointed towards the correct approach to understand superconductivity was the isotope effect [30, 31], showing that the transition temperature depends on the mass of the atoms of the superconducting material. Motivated by this discovery, theorists suggested that superconductivity should be related to lattice vibrations (phonons). As a result, an electron-phonon mediated interaction theory of superconductivity was proposed by Bardeen, Cooper, and Schrieffer in 1957, which was received with enthusiasm [32]. The BCS theory showed that even a weak attractive electron-phonon interaction induces an instability of the Fermi-sea ground state of the electron gas, favoring the formation of the bound pairs of electrons, occupying states with equal and opposite momentum and spin near the Fermi surface. The bound pairs were called Cooper-pairs. Being bosons, the Cooper-pairs can condense into same ground state, i. e. they form the superconducting condensate. Thus, this theory could explain the appearance of a gap in the energy spectrum of a superconductor, which was observed before the theory was proposed [33, 34, 35].

It should be emphasized that Gor'kov showed in 1959 that the GL theory can be derived from the BCS theory and, in fact, is a limiting form of the microscopic theory, valid near T_c , in which the order parameter is proportional to the gap parameter [36].

Between 1950 and 1980 many different superconducting intermetallic compounds were discovered. The highest superconducting transition temperature was observed in Nb_3Ge with $T_c = 23$ K. All these superconducting materials exhibited common features, such as the isotope effect, existence of the energy gap which followed the BCS behavior, the Cooper-pair creation stemming from the electron-phonon interaction, and pairing of s -wave symmetry. These superconductors were named conventional.

However, the discovery of copper oxide-based ceramic superconductors

with $T_c = 30$ K by Bednorz and Müller [37] in 1986 prompted a new era [38, 39, 40, 41, 42]. Later it was shown that T_c of the cuprates can exceed liquid nitrogen temperature. As a result, copper oxide-based ceramic superconductors were named high-temperature superconductors (HTS). The cuprate family offered not only new horizons in transition temperature but also a plenty of interesting phenomena like d -wave pairing symmetry [43, 44], pseudogap [45], charge stripes [46, 47], and exotic pairing mechanisms [48, 49, 50], so were named unconventional. Conventional wisdom suggests that these new horizons were enabled by the complexity of multielement compounds. It was evident that a search for new superconductors should be held in complex compounds.

Another breakthrough happened in 2001 with realization that magnesium diboride becomes superconducting at ≈ 39 K [51]. Although 39 K was much lower than 160 K, this finding revealed a possibility of relatively high critical temperature for an intermetallic and conventional superconductor and meant that MgB_2 can be cooled to an operational temperature by either liquid hydrogen or readily available, fairly inexpensive, closed-cycle refrigerators [51]. The initial interest in MgB_2 arose simply from its high T_c , however, further experiments and theoretical works showed that magnesium diboride offers a new ground for superconductivity originating from its multi-band and two-gap nature and hosting plethora of remarkable features different from intermetallic superconductors known before [51, 52, 53, 54, 55, 56, 57, 58, 59, 60, 61, 62].

Recently, a new family of superconducting materials was discovered containing iron arsenide layers [63, 64, 65, 66, 67]. The critical temperature of these superconductors varies from 26 up to 52 K. A great deal of information has been collected on these materials in a relatively short time, but, as for the copper oxide-based ceramic superconductors, there is still no clear agreement over the pairing mechanism. There are strong indications that magnetism may have an important role in these materials [68, 69]. It has been shown that the order parameter is not a simple s -wave state but is unconventional [68, 69, 70, 71] and changes sign between different parts of the Fermi surface [70, 71]. There is also strong evidence that iron-based superconductors are predominantly multi-band superconductors [72, 73, 74], which makes them relevant for this thesis.

Another example of multi-band superconductivity is found in superconductors under quantum confinement (superconducting nanofilms), which were shown to form the quantum-well states (QWSs) [76] due to limited motion of electrons in one of the dimensions. The initial interest for these materials arose due to the thickness-dependent quantum-size oscillations of the critical temperature and the energy gap [76, 77, 78, 79, 80, 81]. The subsequent stud-

ies revealed that in superconducting nanofilms the long-range superconducting order is frustrated due to proliferation of superconductive fluctuations when the film thickness is reduced, and the Berezinskii-Kosterlitz-Thouless physics [82, 83] governs the global phase coherence in the system [84].

This thesis concerns the theory of multiband superconductors. Before getting to that, we first recall the fundamental theories on superconductivity, presented in Sections 1.2 and 1.3. Subsequently, in Section 1.4 we review and compare essential characteristics of MgB₂ and iron-based superconductors, to prepare the grounds for our theoretical considerations of multiband superconductors.

1.2 Ginzburg-Landau theory for single band superconductors

The Ginzburg-Landau theory was the first formalism for superconductivity that took into account the quantum effects, and suggested that the superconductivity was a transition into an ordered state at the critical temperature T_c . The GL theory is based on the theory of second-order phase transitions developed by Landau [198]. Such transitions are always occurring with a discontinuous reduction of the symmetry, while the state of a system changes gradually. Moreover, the ordered state exhibits lower symmetry. The examples of the second-order transitions are: the ferromagnetic transition at the Curie point, the transition of helium into superfluid state, a number of order-disorder transitions in alloys, and superconductivity.

1.2.1 Free energy expansion

In order to describe the ordered state, one can introduce an order parameter $\psi(\mathbf{r})$ which is non-zero at $T < T_c$, and vanishes at $T \geq T_c$. Then the free energy density of the superconducting material can be expanded in powers of $|\psi|^2$ and $|\nabla\psi|^2$ in proximity of the critical temperature T_c as

$$F_s = F_n + \alpha|\psi|^2 + \frac{\beta}{2}|\psi|^4 + \frac{1}{2m^*} \left| \frac{\hbar}{i} \nabla\psi - \frac{e^*}{c} \mathbf{A}\psi \right|^2 + \frac{B^2}{8\pi}, \quad (1.1)$$

where F_n is the free energy density in the normal state, m^* is the mass of the carrier, e^* is the carrier charge, c is the speed of light, and α and β are phenomenological expansion coefficients, the meaning of which will be given later; \mathbf{B} is magnetic field at a given point of the superconductor, with corresponding vector potential \mathbf{A} . It should be noted that Eq. (1.1) was

proposed under assumption that $|\psi|^2$ and $|\nabla\psi|^2$ are small near the critical temperature, which imposes a restriction on the expansion to be valid in proximity of the critical temperature T_c .

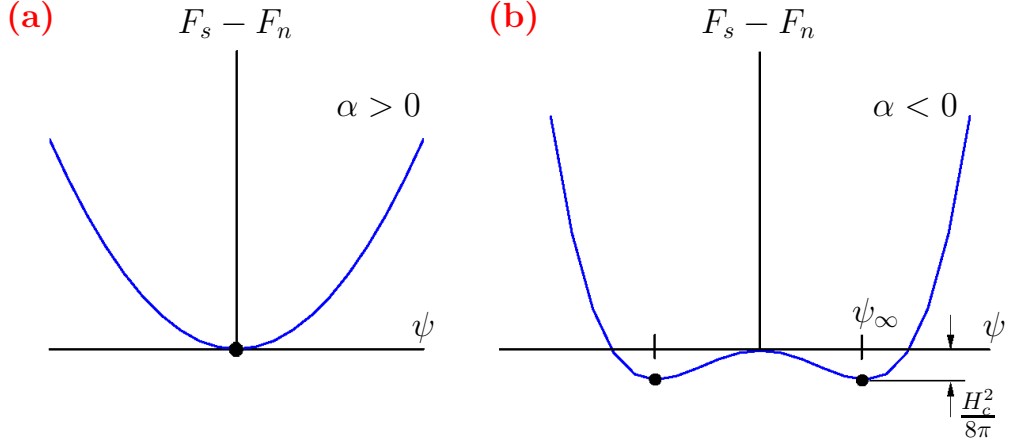


Figure 1.2: The free energy density difference between the normal state and superconducting state: (a) for $\alpha > 0$ at $T > T_c$; (b) for $\alpha < 0$ at $T < T_c$. Solid dots correspond to equilibrium states. The order parameter is taken real for, simplicity. The figure is adapted from [28].

Eq. (1.1) is presented as it done originally by Ginzburg and Landau [27]. The form of the kinetic energy density in Eq. (1.1) was constructed in analogy with the quantum mechanical kinetic energy of a particle with the mass m^* as $\frac{1}{2m^*}|\hbar\nabla\psi|^2$. Then for a carrier of charge e^* moving in a field with the vector potential \mathbf{A} , the kinetic energy should be modified to $-\hbar\nabla - \frac{e^*}{c}\mathbf{A}$, where $-\frac{i\hbar}{m^*} - \frac{e^*}{cm^*}\mathbf{A}$ becomes the velocity operator. At the time when the GL functional was proposed, it was not yet known that two electrons participate in the formation of a bound state. Later, when the microscopic BCS theory was developed and the idea about electron-phonon interaction was suggested, it was clear that in Eq. (1.1) the mass m^* should be replaced by $2m$, where m is the mass of electron, and the charge by $2e$, where e is the electron charge. Therefore, the kinetic energy density in Eq. (1.1) modifies to

$$\frac{1}{4m}\left|\frac{\hbar}{i}\nabla\psi - \frac{2e}{c}\mathbf{A}\psi\right|^2. \quad (1.2)$$

Now the question arises: how the phenomenological coefficients α and β depend on temperature? One can address this question by considering

the simplest case, i. e., a homogeneous superconductor without external magnetic field, for which ψ is spatially uniform. Then one can find the value of $|\psi|^2$ which minimizes the free energy F_s , after differentiating $dF_s/d|\psi|^2$, as

$$|\psi|^2 = \frac{-\alpha}{\beta}, \quad (1.3)$$

the free energy density difference between the normal and superconducting states becomes

$$F_s - F_n = -\frac{\alpha^2}{2\beta}. \quad (1.4)$$

This difference equals also to $-H_c^2/8\pi$, which is nothing else but the condensation energy of the superconducting state with H_c being the thermodynamic critical field. Accordingly, one obtains that $\alpha = H_c \sqrt{\frac{\beta}{4\pi}}$. Expansion of the thermodynamic critical field into the Taylor series to the first order in temperature around T_c shows that $\alpha \propto (T - T_c)$. Then one concludes that $\alpha = 0$ at $T = T_c$, otherwise ψ will not vanish at T_c . In order to obtain finite ψ for $T < T_c$, it follows from Eq. (1.3) that α should be negative in the superconducting state. Coefficient β is in turn positive and temperature-independent, therefore it can be assumed to be constant. In Fig. 1.2 two kinds of solutions of Eq. (1.4) are illustrated schematically for the order parameter ψ , depending on the sign of α . If α is positive, then a specimen is in the normal state [Fig. 1.2(a)]. When α is negative, Eq. (1.4) hosts two equilibrium solutions ψ_∞ [Fig. 1.2(b)] showing that the system is in the superconducting state, for order parameter approaching ψ_∞ .

1.2.2 Ginzburg-Landau equations

By integrating the free energy density given by Eq. (1.1) over the entire volume of superconductor and the environment, we arrive at the free energy functional:

$$\mathcal{F}_s = \mathcal{F}_n + \int d^3r \left[\alpha |\psi|^2 + \frac{\beta}{2} |\psi|^4 + \frac{1}{4m} \left| \left(\frac{\hbar}{i} \nabla \psi - \frac{2e}{c} \mathbf{A} \psi \right) \right|^2 + \frac{\mathbf{B}^2}{8\pi} \right], \quad (1.5)$$

where \mathcal{F}_n is the free energy of the normal state. In order to find an equilibrium value of ψ which minimizes the free energy functional, one has to variate Eq. (1.5) with respect to ψ^* . The variation yields:

$$\delta_{\psi^*} \mathcal{F}_s = \int d^3r \left[\alpha \psi \delta \psi^* + \beta \psi |\psi|^2 \delta \psi^* + \frac{1}{4m} \left(\frac{\hbar}{i} \nabla \psi - \frac{2e}{c} \mathbf{A} \psi \right) \left(-\frac{\hbar}{i} \nabla \delta \psi^* - \frac{2e}{c} \mathbf{A} \delta \psi^* \right) \right]. \quad (1.6)$$

We have to modify the last term in Eq. (1.6) in order to take $\delta\psi^*$ out of $(\hbar/i)\nabla\delta\psi^*$ and then out of brackets. Therefore, we write

$$\mathbf{d} = \frac{\hbar}{i}\nabla\psi - \frac{2e}{c}\mathbf{A}\psi, \quad (1.7)$$

and use the identity $\nabla(\delta\psi^*\mathbf{d}) = \mathbf{d}\nabla\delta\psi^* + \delta\psi^*\nabla\mathbf{d}$, to obtain

$$\int d^3r \nabla\delta\psi^*\mathbf{d} = - \int d^3r \delta\psi^*\nabla\mathbf{d} + \int d^3r \nabla(\delta\psi^*\mathbf{d}). \quad (1.8)$$

Applying the Gauss' theorem to the last integral, which is converted into a surface integral, one obtains

$$\int d^3r \nabla(\delta\psi^*\mathbf{d}) = \oint_S d^2r \delta\psi^*\mathbf{d}. \quad (1.9)$$

Substituting Eq. (1.9) into Eq. (1.6), we obtain

$$\begin{aligned} \delta_{\psi^*}\mathcal{F}_s = \int d^3r \left[\alpha\psi + \beta\psi|\psi|^2 + \frac{1}{4m} \left(\frac{\hbar}{i}\nabla - \frac{2e}{c}\mathbf{A} \right)^2 \psi \right] \delta\psi^* \\ + \oint d^2r \left[\frac{\hbar}{i}\nabla\psi - \frac{2e}{c}\mathbf{A}\psi \right] \delta\psi^*. \end{aligned} \quad (1.10)$$

To reach $\delta_{\psi^*}\mathcal{F}_s = 0$ for an arbitrary $\delta\psi^*$, both integrals in Eq. (1.10) should tend to zero. Thus, we arrive at the first Ginzburg-Landau (GL) equation from the volume integral:

$$\alpha\psi + \beta\psi|\psi|^2 + \frac{1}{4m} \left(\frac{\hbar}{i}\nabla - \frac{2e}{c}\mathbf{A} \right)^2 \psi = 0, \quad (1.11)$$

and the surface integral in Eq. (1.10) gives the boundary condition for Eq. (1.11):

$$\mathbf{n} \left(\frac{\hbar}{i}\nabla\psi - \frac{2e}{c}\mathbf{A}\psi \right) = 0, \quad (1.12)$$

where \mathbf{n} is the unit vector normal to the superconductor surface. The boundary condition given by Eq. (1.12) means that superconducting current across the boundary of a superconductor is zero. One can easily verify that minimization of Eq. (1.5) with respect to ψ leads to the complex-conjugate of Eq. (1.11).

Variation of the free energy in Eq. (1.5) with respect to \mathbf{A} produces the GL equation for the vector potential. Recalling that $\mathbf{B} = \text{rot}\mathbf{A}$ one obtains:

$$\begin{aligned} \delta_{\mathbf{A}}\mathcal{F}_s = \int d^3r \left\{ \frac{1}{4m} \delta_{\mathbf{A}} \left[\left(\frac{\hbar}{i}\nabla\psi - \frac{2e}{c}\mathbf{A}\psi \right) \left(-\frac{\hbar}{i}\nabla\psi^* - \frac{2e}{c}\mathbf{A}\psi^* \right) \right] \right. \\ \left. + \frac{1}{4\pi} \text{rot}\mathbf{A} \text{rot}\delta\mathbf{A} \right\} = \end{aligned}$$

$$\begin{aligned}
 = \int d^3r \left\{ \frac{1}{4m} \left(-\frac{2e}{c} \psi^* \delta \mathbf{A} \right) \left(\frac{\hbar}{i} \nabla \psi - \frac{2e}{c} \mathbf{A} \psi \right) + \frac{1}{4m} \left(-\frac{\hbar}{i} \nabla \psi^* - \frac{2e}{c} \mathbf{A} \psi^* \right) \right. \\
 \left. \times \left(-\frac{2e}{c} \psi \delta \mathbf{A} \right) + \frac{1}{4\pi} \text{rot} \mathbf{A} \text{rot} \delta \mathbf{A} \right\}. \quad (1.13)
 \end{aligned}$$

Using the following property

$$\begin{aligned}
 \int d^3r \text{rot} \mathbf{A} \text{rot} \delta \mathbf{A} &= \int d^3r \delta \mathbf{A} \text{rot} \text{rot} \mathbf{A} - \int d^3r \text{div} [\delta \mathbf{A} \times \text{rot} \mathbf{A}] \\
 &= \int d^3r \delta \mathbf{A} \text{rot} \text{rot} \mathbf{A} - \oint_S d^2r [\delta \mathbf{A} \times \text{rot} \mathbf{A}], \quad (1.14)
 \end{aligned}$$

one then modifies the last term $\text{rot} \mathbf{A} \text{rot} \delta \mathbf{A}$ in Eq. (1.13) to $\text{rot} \text{rot} \mathbf{A} \delta \mathbf{A}$. Since $\delta \mathbf{A}|_S = 0$, the surface integral of Eq. (1.14) turns to zero. Subsequently, one obtains:

$$\delta_{\mathbf{A}} \mathcal{F}_s = \int d^3r \left\{ \frac{i\hbar e}{2mc} (\psi^* \nabla \psi - \psi \nabla \psi^*) + \frac{2e^2}{mc^2} \mathbf{A} |\psi|^2 + \frac{1}{4\pi} \text{rot} \text{rot} \mathbf{A} \right\} \delta \mathbf{A}. \quad (1.15)$$

By leading $\delta_{\mathbf{A}} \mathcal{F}_s = 0$ for an arbitrary $\delta \mathbf{A}$, we arrive at the second GL equation for the vector potential \mathbf{A} :

$$\mathbf{j}_s = -\frac{i\hbar e}{2m} (\psi^* \nabla \psi - \psi \nabla \psi^*) - \frac{2e^2}{mc} \mathbf{A} |\psi|^2, \quad (1.16)$$

where, by Maxwell's equation, the current density in the superconductor is $\mathbf{j}_s = \frac{c}{4\pi} \text{rot} \text{rot} \mathbf{A}$.

1.2.3 Two characteristic length scales in the GL theory

There are two fundamental characteristic lengths associated with the GL equations (1.11) and (1.16). Let us recast those equations by introducing a dimensionless function $f = \psi/\psi_\infty$, where $\psi_\infty = |\alpha|/\beta$, and assuming one-dimensional case, i. e. $f(x)$, such that $f(x) \rightarrow 1$, when $x \rightarrow \infty$. Then dimensionless first GL equation will take the form:

$$-\xi^2 \frac{d^2 f}{dx^2} - f + f^3 = 0, \quad (1.17)$$

where $\xi^2 = \frac{\hbar^2}{4m|\alpha|}$, and the equation for the vector potential becomes:

$$\text{rot rot } \mathbf{A} = -i \frac{\Phi_0}{4\pi\lambda^2} (f^* \nabla f - f \nabla f^*) - \frac{|f|^2}{\lambda^2} \mathbf{A}, \quad (1.18)$$

where $\Phi_0 = \frac{hc}{2e}$ is the flux quantum, and $\lambda^2 = \frac{mc^2\beta}{8\pi|\alpha|e^2}$.

Let us consider the case of a superconductor in absence of external magnetic field. The function f becomes real, because the vector potential $\mathbf{A} = 0$. Substituting $f(x)$ by $1 - \varepsilon(x)$, where $\varepsilon(x) \ll 1$, Eq. (1.17) modifies to:

$$\xi^2 \frac{d^2 \varepsilon(x)}{dx^2} - 2\varepsilon(x) = 0, \quad (1.19)$$

where only linear term in $\varepsilon(x)$ was kept. When $x \rightarrow \infty$, $\varepsilon(\infty) \rightarrow 0$, therefore the solution of Eq. (1.19) is:

$$\varepsilon(x) = \varepsilon(0) e^{-\sqrt{2}x/\xi}. \quad (1.20)$$

The solution given by Eq. (1.20) shows that ξ is the characteristic scale over which f varies. This length is called the coherence length. Since ξ depends on α , therefore it also depends on temperature as

$$\xi \propto (T_c - T)^{-1/2}. \quad (1.21)$$

From this dependence follows that the coherence length is discontinuous at $T = T_c$.

Another quantity λ , introduced in Eq. (1.18), is the London magnetic field penetration depth. This characteristic length shows how the magnetic field falls off inside the superconductor, measured from the surface. In GL theory, the penetration depth depends on α , hence also temperature, as

$$\lambda \propto (T_c - T)^{-1/2}. \quad (1.22)$$

It is also discontinuous at $T = T_c$. Therefore, it is convenient to introduce the ratio of the two length scales $\kappa = \lambda/\xi$, which is finite at $T = T_c$. This ratio is called the GL parameter.

Introduction of the GL parameter κ allows to conveniently classify superconductors according to their response to the external magnetic field. If one considers the normal metal(N)-superconductor(S) interface, and how the order parameter $\psi(x)$ and the magnetic field \mathbf{H} vary in the vicinity of the interface, then one can distinguish two cases: $\kappa \ll 1$ ($\lambda \ll \xi$) [Fig. 1.3(a)]

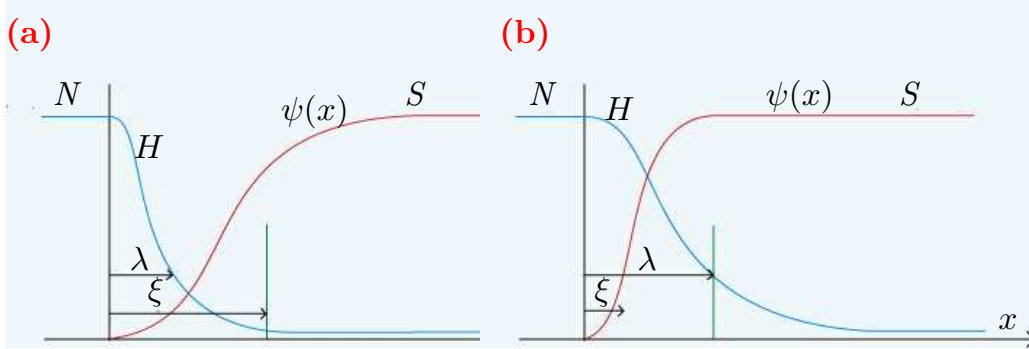


Figure 1.3: Spatial variations of the order parameter $\psi(x)$ and the magnetic field H in the vicinity of the normal metal (N) - superconductor (S) interface for: (a) $\kappa \ll 1$; (b) $\kappa \gg 1$. Adapted from [86].

and $\kappa \gg 1$ ($\lambda \gg \xi$) [Fig. 1.3(b)]. When $\kappa \ll 1$ [Fig. 1.3 (a)], it implies that the magnetic field penetrates into superconductor on a small length λ and falls over this length rapidly. The surface energy of the NS interface is positive for $\kappa \ll 1$, and negative for $\kappa \gg 1$ and equals zero exactly at $\kappa = 1/\sqrt{2}$. Accordingly, if $\kappa \ll 1/\sqrt{2}$, then a superconductor is of type I, otherwise ($\kappa \gg 1/\sqrt{2}$) it is of type II.

The Ginzburg-Landau theory is a phenomenological theory and was proposed before the microscopic BCS theory for superconductivity was formulated [32]. The exact expressions for the phenomenological coefficients α and β were unknown. At first the theory was accepted with skepticism. Seven years later the microscopic BCS theory was proposed, and two years after that Gor'kov developed the Green's function technique [36] to show that the Ginzburg-Landau theory is the limiting case of the BCS theory in the proximity of the critical temperature and for slowly varying electromagnetic fields. In the next Section, we introduce the BCS theory, its Hamiltonian and show how the GL equation can be derived from the BCS theory based on the Green's function technique.

1.3 The BCS theory

Although superconductivity was discovered in 1911, the explanation on how the superconducting state arises was given only 46 years after. In understanding the phenomenon, the experimental discovery of the isotope effect was instrumental. Different isotopes of the same superconducting metals were found to have different critical temperatures $T_c \propto M^{-\alpha}$, where M is the mass of an isotope and α is the isotope coefficient. For Hg, Pb, Sn, and

Zn the isotope coefficient α was found experimentally to be close to $1/2$. Then it became clear that the ion lattice participated in the formation of superconducting state, which was beyond understanding of the theoretical approaches at that time, since superconductivity occurred at low temperatures, and it was difficult to believe that at such low temperatures the ion lattice can contribute.

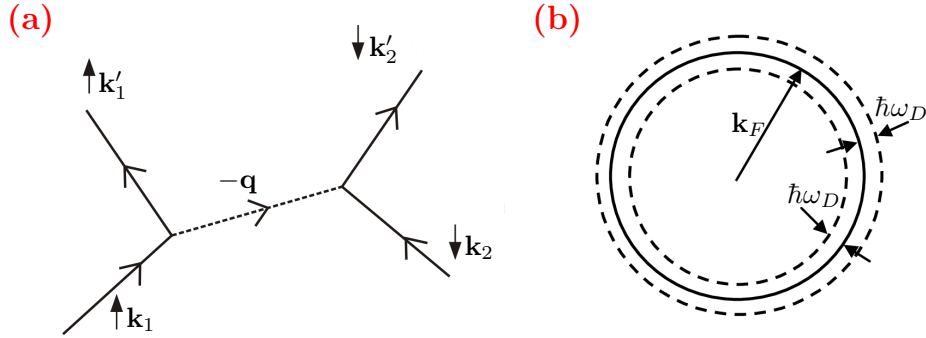


Figure 1.4: (a) Diagram showing electron-electron interaction by emitting and subsequent absorbing of a phonon with momentum \mathbf{q} ; (b) Fermi sphere of radius k_F near to which electron-phonon interaction occurs in the band layer proportional to $\hbar\omega_D$ above and below of the surface.

Indeed, if we consider a metal at $T = 0K$, then ions of the crystalline lattice cannot oscillate. However, free electrons can transport freely through the lattice, and nothing prevents electrons from creating regions of increased negative charge in a metal after some time. Suppose an electron with momentum \mathbf{k}_1 causes an excess negative charge. The surrounding ions feel the negative charge and will be attracted to the location of increased electron density trying to compensate the negative charge. The positive ions moving towards the negative charge will create an excess positive charge. As a result, another electron with \mathbf{k}_2 passing by the positive charge will be attracted to it. This results in two electrons with momenta \mathbf{k}_1 and \mathbf{k}_2 to be attracted to each other via lattice movement (i.e. phonon) with momentum \mathbf{q} . The electron with momentum \mathbf{k}_1 will transit to another state with momentum \mathbf{k}'_1 , while the second electron with momentum \mathbf{k}_2 will transit to the state with \mathbf{k}'_2 due to the phonon exchange. The first electron emits the phonon $\mathbf{k}_1 - \mathbf{q} = \mathbf{k}'_1$, while the second absorbs it $\mathbf{k}_2 + \mathbf{q} = \mathbf{k}'_2$. Thus, the electron-phonon interaction proceeds with the momentum conservation:

$$\mathbf{k}_1 + \mathbf{k}_2 = \mathbf{k}'_1 + \mathbf{k}'_2. \quad (1.23)$$

This process is illustrated in Fig. 1.4(a). Such attraction arises only if the

lattice vibrations are in phase with the electron density oscillation with the frequency $\omega = (\bar{\varepsilon}_{\mathbf{k}_1} - \bar{\varepsilon}_{\mathbf{k}'_1})/\hbar$. The characteristic frequency of the ion lattice vibration is the Debye frequency ω_D . Therefore, two electrons will attract each other if the electron density oscillation has frequency $\omega < \omega_D$.

The idea about electron interacting with another electron via phonon was a major breakthrough in understanding of superconductivity. The question left to address was which electrons participate in the electron-phonon interaction? At $T = 0$ K electrons occupy all the states up to the Fermi level with \mathbf{k}_F in the Fermi sphere in the momentum space. Since all the states with $\mathbf{k} < \mathbf{k}_F$ are occupied, the electrons can scatter only to the states above the Fermi level with $\mathbf{k} > \mathbf{k}_F$, due to the Pauli exclusion principle. Hence, it was proposed that electrons with energies that differ from the Fermi energy by no more than $\hbar\omega_D$ are attracted to each other and participate in the phonon mediated electron-electron interaction. This forms the foundation of the BCS theory [32]. The interaction between electrons is replaced by a potential $V_{\mathbf{k}\mathbf{k}'}$ in the BCS theory, where

$$V_{\mathbf{k}\mathbf{k}'} = \begin{cases} -V, & |\bar{\varepsilon}_{\mathbf{k}} - \varepsilon_F| \leq \hbar\omega_D, \quad |\bar{\varepsilon}_{\mathbf{k}'} - \varepsilon_F| \leq \hbar\omega_D \\ 0, & |\bar{\varepsilon}_{\mathbf{k}} - \varepsilon_F| > \hbar\omega_D, \quad |\bar{\varepsilon}_{\mathbf{k}'} - \varepsilon_F| > \hbar\omega_D \end{cases}, \quad (1.24)$$

i. e. it is attractive in the layer of thickness $\sim \hbar\omega_D$ above and below of the Fermi level [Fig. 1.4(b)], otherwise it is zero. Attraction between electrons near the Fermi surface arises even at a very weak V causing the instability of the ground state of the Fermi sea. This attractive interaction will decrease the ground state energy of previously non-interacting electrons leading to a new state. In order to find the ground state energy of the emerged state, one needs to construct a Hamiltonian which incorporates electron-electron interaction satisfying Eqs. (1.23) and (1.24).

1.3.1 Emergence of an energy gap

Hamiltonian of free electrons is known and it contains only the kinetic energy which can be written in terms of operators of the second quantization as

$$H_0 = \sum_{\mathbf{k}\alpha} \frac{\hbar^2 k^2}{2m} a_{\mathbf{k}\alpha}^+ a_{\mathbf{k}\alpha}, \quad (1.25)$$

where $\frac{\hbar^2 k^2}{2m}$ is the energy of an electron in the state \mathbf{k} , and α denotes the spin index in the summation. The operators $a_{\mathbf{k}\alpha}^+$ and $a_{\mathbf{k}\alpha}$ are the second quantization operators. Operating by $a_{\mathbf{k}\alpha}^+$ on a vacuum state $|\psi_0\rangle$ creates an electron

in the state $\mathbf{k}\alpha$, while the operator $a_{\mathbf{k}\alpha}$ will annihilate an electron in the state $\mathbf{k}\alpha$. The creation and annihilation operators satisfy the anticommuting rules:

$$\begin{aligned} a_{\mathbf{k}\alpha}^+ a_{1\beta}^+ + a_{1\beta}^+ a_{\mathbf{k}\alpha}^+ &= 0, \\ a_{\mathbf{k}\alpha}^+ a_{1\beta} + a_{1\beta} a_{\mathbf{k}\alpha}^+ &= \delta_{\mathbf{k}1} \delta_{\alpha\beta}, \\ a_{\mathbf{k}\alpha} a_{1\beta} + a_{1\beta} a_{\mathbf{k}\alpha} &= 0. \end{aligned} \quad (1.26)$$

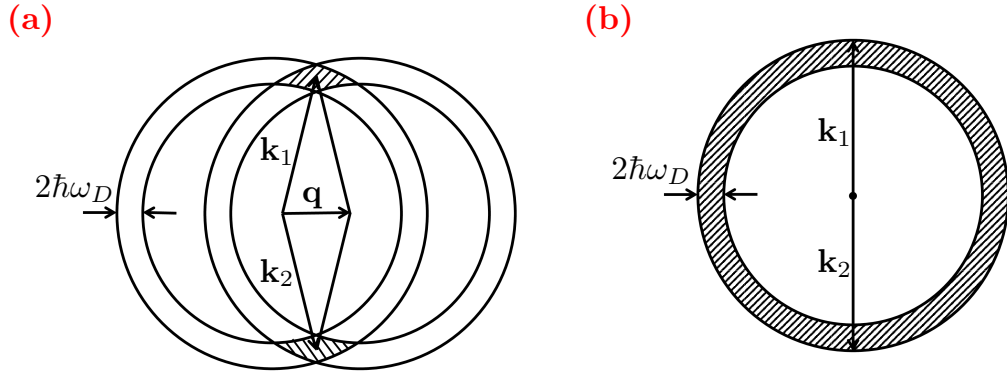


Figure 1.5: (a) The diagram shows that if the total momentum of coupled electrons is \mathbf{q} , then the interaction occurs only between the electrons in the dashed area; (b) If $\mathbf{q} = 0$, then the interaction area increases significantly meaning that electrons with the same magnitude but oppositely directed momenta couple near the Fermi surface in the band of thickness $2\hbar\omega_D$.

However, when a small attraction arises between the electrons occupying the states near the Fermi surface, the electrons cannot be considered free anymore, and Hamiltonian, given by Eq. (1.25) needs modifying to describe the emerged instability. On the other hand, Eq. (1.23) implies that electron-electron scattering occurs with the momentum conservation. If we consider two electrons with oppositely directed momenta \mathbf{k}_1 and \mathbf{k}_2 , and associate a sphere with each electron as shown in Fig. 1.5(a), then only electrons occupying the states in dashed regions can satisfy Eq. (1.23). If we decrease \mathbf{q} , the dashed areas will grow thus increasing the interaction region. Two spheres will tend to coincide when $\mathbf{q} \rightarrow 0$ [Fig. 1.5(b)]. It is not difficult to see that $\mathbf{k}_2 = -\mathbf{k}_1$, when $\mathbf{q} = 0$. Thus, we conclude that electrons with the same magnitude but oppositely directed momenta \mathbf{k} and $-\mathbf{k}$ pair near

the Fermi surface in the band of thickness $\sim \hbar\omega_D$ and they scatter to a new state $(\mathbf{k}', -\mathbf{k}')$ in the band $\sim \hbar\omega_D$. By instability of the Fermi sea one means pairing of electrons, i. e. formation of so-called Cooper pairs.

Taking into account the foundation of the BCS theory given by Eq. (1.24), and that electrons with oppositely momenta pair, the corresponding interaction energy can be formulated as

$$H_{int} = \frac{1}{2} \sum_{\mathbf{k}, \mathbf{k}', \alpha, \beta} V_{\mathbf{k}\mathbf{k}'} a_{\mathbf{k}, \alpha}^+ a_{\mathbf{k}', \beta}^+ a_{\mathbf{k}', \beta} a_{\mathbf{k}, \alpha}, \quad (1.27)$$

where β is the spin index. Then the full Hamiltonian of the system is:

$$H = \sum_{\mathbf{k}\alpha} \frac{\hbar^2 k^2}{2m} a_{\mathbf{k}\alpha}^+ a_{\mathbf{k}\alpha} + \frac{1}{2} \sum_{\mathbf{k}, \mathbf{k}', \alpha, \beta} V_{\mathbf{k}\mathbf{k}'} a_{\mathbf{k}, \alpha}^+ a_{\mathbf{k}', \beta}^+ a_{\mathbf{k}', \beta} a_{\mathbf{k}, \alpha}. \quad (1.28)$$

Eq. (1.28) shows that pairing is energetically favorable, because it leads to rearrangement of the ground state and decreases its energy. The system should spend a finite energy to excite electrons, allowing them to pair. Due to this an energy gap appears in the energy spectrum which is equal to the pairing energy. By operating Hamiltonian given by Eq. (1.28) on the ground state, one can find the energy gap.

The trial function of the interacting electrons can be chosen in the form as it was introduced by Bardeen, Cooper and Schrieffer in their seminal paper of 1957 [32, 29]:

$$\tilde{\psi} = \prod_{\mathbf{k}} (u_{\mathbf{k}} + v_{\mathbf{k}} a_{\mathbf{k}\uparrow}^+ a_{-\mathbf{k}\downarrow}^+) \psi_0, \quad (1.29)$$

with

$$\frac{v_{\mathbf{k}}}{u_{\mathbf{k}}} = g_{\mathbf{k}}, \quad u_{\mathbf{k}}^2 + v_{\mathbf{k}}^2 = 1, \quad (1.30)$$

where Eqs. (1.30) assure the normalization of $\tilde{\psi}$, i. e. $\int_V |\tilde{\psi}|^2 d\mathbf{r} = N$, where N is the number of electrons in the system. With the choice of the trial function given by Eq. (1.29), one has to minimize a Lagrange multiplier:

$$E_s = \langle \tilde{\psi} | H | \tilde{\psi} \rangle - E_F \langle \tilde{\psi} | N | \tilde{\psi} \rangle, \quad (1.31)$$

because the number of particles is not fixed in this case, and the Fermi energy E_F serves as the Lagrange multiplier.

The contribution of the kinetic energy along with the Lagrange multiplier in Eq. (1.31) is:

$$\langle \tilde{\psi} | H_0 | \tilde{\psi} \rangle - E_F \langle \tilde{\psi} | N | \tilde{\psi} \rangle = \sum_{\mathbf{k}\alpha} v_{\mathbf{k}}^2 \zeta_{\mathbf{k}} = \sum_{\mathbf{k}} 2 v_{\mathbf{k}}^2 \zeta_{\mathbf{k}}, \quad (1.32)$$

where $\zeta_{\mathbf{k}} = \frac{\hbar^2 k^2}{2m} - E_F$ is the energy of an electron in the state \mathbf{k} measured from the Fermi level E_F (the summation over the spin index was done, and counted in the sum as factor 2). This matrix element means that in the state $\tilde{\psi}$ the probability to find a state with \mathbf{k} occupied is $v_{\mathbf{k}}^2$.

The matrix element for the interaction part is:

$$\langle \tilde{\psi} | H_{int} | \tilde{\psi} \rangle = \frac{1}{2} \sum_{\mathbf{k}, \mathbf{k}', \alpha, \beta} V_{\mathbf{k}\mathbf{k}'} v_{\mathbf{k}'} u_{\mathbf{k}} v_{\mathbf{k}} u_{\mathbf{k}'} = \sum_{\mathbf{k}, \mathbf{k}'} V_{\mathbf{k}\mathbf{k}'} v_{\mathbf{k}'} u_{\mathbf{k}} v_{\mathbf{k}} u_{\mathbf{k}'}, \quad (1.33)$$

where summation over the spin indices was done. In Eq. (1.33) we considered only matrix elements which give contribution into transition of a pair from the state $(\mathbf{k} \uparrow, -\mathbf{k} \downarrow)$ to the state $(\mathbf{k}' \uparrow, -\mathbf{k}' \downarrow)$.

Thus, we find that the total energy of a superconductor in the state described by Eq. (1.29) is:

$$E_s = \sum_{\mathbf{k}} 2 v_{\mathbf{k}}^2 \zeta_{\mathbf{k}} + \sum_{\mathbf{k}, \mathbf{k}', \mathbf{q}} V_{\mathbf{k}\mathbf{k}'} v_{\mathbf{k}'} u_{\mathbf{k}} v_{\mathbf{k}} u_{\mathbf{k}'}. \quad (1.34)$$

Minimizing Eq. (1.34) with respect to $v_{\mathbf{k}}^2$ leads to the equation:

$$2\zeta_{\mathbf{k}} - V \frac{(1 - 2v_{\mathbf{k}}^2)}{v_{\mathbf{k}} u_{\mathbf{k}}} \sum_{\mathbf{k}'} u_{\mathbf{k}'} v_{\mathbf{k}'} = 0, \quad (1.35)$$

where the summation occurs only over the states near the Fermi surface satisfying Eq. (1.24). Therefore the matrix element $V_{\mathbf{k}\mathbf{k}'}$ was replaced by its approximation value $-V$. As a result from the previous equation it follows

$$\frac{v_{\mathbf{k}} u_{\mathbf{k}}}{(1 - 2v_{\mathbf{k}}^2)} = \frac{\Delta_{\mathbf{k}}}{2\zeta_{\mathbf{k}}}, \quad (1.36)$$

where

$$\Delta_{\mathbf{k}} = V \sum_{\mathbf{k}'} u_{\mathbf{k}'} v_{\mathbf{k}'} \quad (1.37)$$

defines the energy gap. Expressing $v_{\mathbf{k}}^2$ from Eq. (1.36) leads to a quadratic equation for it:

$$v_{\mathbf{k}}^4 - v_{\mathbf{k}}^2 + \frac{\Delta_{\mathbf{k}}^2}{4E_{\mathbf{k}}^2} = 0, \quad (1.38)$$

where

$$E_{\mathbf{k}} = \sqrt{\zeta_{\mathbf{k}}^2 + \Delta_{\mathbf{k}}^2}, \quad (1.39)$$

is the energy of excitation showing that the occupied states are separated from the first excited state by the energy gap $\Delta_{\mathbf{k}}$. Then

$$v_{\mathbf{k}}^2 = \frac{1}{2} \left(1 - \frac{\zeta_{\mathbf{k}}}{E_{\mathbf{k}}} \right). \quad (1.40)$$

The minus sign in Eq. (1.40) stems from a general argument that, as $\mathbf{k} \rightarrow 0$, $v_{\mathbf{k}}^2 \rightarrow 1$, while $\zeta_{\mathbf{k}} \rightarrow -E_F$. Eq. (1.40) shows that the total energy of the system reaches its minimum when the electron distribution in the vicinity of the Fermi level is “smeared out” over the energy interval $\sim 2\Delta$. This occurs at 0 K.

Inserting Eq. (1.40) into Eq. (1.37) and taking into account Eq. (1.39), one obtains:

$$\Delta_{\mathbf{k}} = V \sum_{\mathbf{k}'} \frac{\Delta_{\mathbf{k}'}}{2(\zeta_{\mathbf{k}'}^2 + \Delta_{\mathbf{k}'}^2)}. \quad (1.41)$$

This equation always has the trivial solution $\Delta_{\mathbf{k}'}$, corresponding to

$$v_{\mathbf{k}'} = \begin{cases} 1, & \xi_{\mathbf{k}'} < 0 \\ 0, & \xi_{\mathbf{k}'} > 0 \end{cases}. \quad (1.42)$$

Then

$$\Delta_{\mathbf{k}'} = 0 \quad \text{for } |\xi_{\mathbf{k}'}| > \hbar\omega_D, \quad (1.43)$$

$$\Delta_{\mathbf{k}'} = \Delta \quad \text{for } |\xi_{\mathbf{k}'}| < \hbar\omega_D. \quad (1.44)$$

We can then rewrite Eq. (2.26) as

$$1 = V \sum_{\mathbf{k}'} \frac{1}{2(\zeta_{\mathbf{k}'}^2 + \Delta^2)}. \quad (1.45)$$

Using the formula

$$\sum_{\mathbf{k}} \dots = \int_{-\hbar\omega_D}^{\hbar\omega_D} \dots N(\zeta) d\zeta, \quad (1.46)$$

to go from the summation over \mathbf{k} to an integration over ζ , where $N(\zeta)$ is the density of states at the energy ζ . Since we are interested in an energy interval of width $\hbar\omega_D \ll E_F$, we can replace $N(\zeta)$ by its value at the Fermi level $N(0) = mk_F/2\pi^2\hbar^2$. Then Eq. (1.45) reduces to:

$$1 = \frac{N(0)V}{2} \int_{-\hbar\omega_D}^{\hbar\omega_D} (\zeta^2 + \Delta^2)^{-1/2} d\zeta. \quad (1.47)$$

We are interested in the weak coupling limit $N(0)V \ll 1$, therefore the solution of Eq. (1.47) is:

$$\Delta \simeq 2\hbar\omega_D \exp\left(-\frac{1}{N(0)V}\right). \quad (1.48)$$

This is the fundamental result of the BCS theory stating that the energy gap is proportional to the Debye temperature $\hbar\omega_D = k_B\theta$, and depends only on the point like interaction V and the density of states at the Fermi level $N(0)$.

Once Δ is known explicitly, we can calculate the kinetic and potential energies. Then, one obtains that the kinetic energy is equal to:

$$\langle\tilde{\psi}|H_0|\tilde{\psi}\rangle = 2 \sum_{\mathbf{k}<\mathbf{k}_F} \xi_{\mathbf{k}} + \frac{\Delta^2}{V} - \frac{N(0)\Delta^2}{2}, \quad (1.49)$$

where the first term is the energy of the normal state where $\Delta = 0$. Inserting Δ into Eq. (1.33) gives the interaction energy:

$$\langle\tilde{\psi}|H_{int}|\tilde{\psi}\rangle = -\frac{\Delta^2}{V}. \quad (1.50)$$

Then the energy difference between the normal and the superconducting state is:

$$\langle\tilde{\psi}|H|\tilde{\psi}\rangle - \langle\psi_n|H|\psi_n\rangle = -\frac{N(0)\Delta^2}{2}, \quad (1.51)$$

from which follows that the energy of the condensed state is lower than that of the normal state. Thus, instability in the Fermi sea due to pairing of electrons leads to emerging of a new state with lower total energy and a gap in the energy spectrum.

1.3.2 The GL equation from the BCS theory

In this Subsection we demonstrate how the GL equation for a single band superconductor can be derived from the BCS theory. We recall that the GL formalism works near T_c , therefore we use the assumption that the energy gap is small and varies slowly near to the critical temperature T_c . The derivation is founded on the method proposed by Gor'kov [36] and based on the Green's function formalism at arbitrary temperatures and fields.

First we rewrite Hamiltonian given by Eq. (1.28) in terms of new operators $\Psi_\alpha(\mathbf{r})$ and $\Psi_\alpha^\dagger(\mathbf{r})$ by performing transformation from the second quanti-

zation operators to new operators as

$$\begin{aligned}\Psi_\alpha(\mathbf{r}) &= \sum_{\mathbf{k}} e^{i\mathbf{k}\mathbf{r}} a_{\mathbf{k}\alpha}, \\ \Psi_\alpha^\dagger(\mathbf{r}) &= \sum_{\mathbf{k}} e^{-i\mathbf{k}\mathbf{r}} a_{\mathbf{k}\alpha}^\dagger.\end{aligned}\quad (1.52)$$

Basically, this is a transformation from the momentum representation to the real space. The new operators satisfy anticommuting rules:

$$\begin{aligned}\Psi_\alpha(\mathbf{r})\Psi_\beta(\mathbf{r}') + \Psi_\beta(\mathbf{r}')\Psi_\alpha(\mathbf{r}) &= 0, \\ \Psi_\alpha^\dagger(\mathbf{r})\Psi_\beta^\dagger(\mathbf{r}') + \Psi_\beta^\dagger(\mathbf{r}')\Psi_\alpha^\dagger(\mathbf{r}) &= 0, \\ \Psi_\alpha^\dagger(\mathbf{r})\Psi_\beta(\mathbf{r}') + \Psi_\beta(\mathbf{r}')\Psi_\alpha^\dagger(\mathbf{r}) &= \delta_{\alpha\beta}\delta(\mathbf{r} - \mathbf{r}').\end{aligned}\quad (1.53)$$

After substituting Eqs. (1.52) into Eq. (1.28), Hamiltonian of the superconducting state modifies to:

$$H_S = \int \left\{ - \sum_{\alpha} \Psi_\alpha^\dagger(\mathbf{r}) \frac{\nabla^2}{2m} \Psi_\alpha(\mathbf{r}) + \frac{\Lambda}{2} \sum_{\alpha\beta} \Psi_\alpha^\dagger(\mathbf{r}) \Psi_\beta^\dagger(\mathbf{r}) \Psi_\alpha(\mathbf{r}) \Psi_\beta(\mathbf{r}) \right\} d\mathbf{r}, \quad (1.54)$$

where we replaced the interaction term $V_{\mathbf{k}\mathbf{k}'}$ by Λ and further we assume that $\Lambda < 0$. The new operators do not incorporate time-dependence, therefore one has to carry out a new transformation to the Heizenberg representation, in which operators acquire the time-dependence:

$$\tilde{\Psi}_{\alpha'}(\mathbf{r}) = e^{iH_S t} \Psi_{\alpha'}(\mathbf{r}) e^{-iH_S t}. \quad (1.55)$$

The new operators $\tilde{\Psi}_{\alpha'}(\mathbf{r})$ and $\tilde{\Psi}_{\alpha'}^\dagger(\mathbf{r})$ satisfy the equation:

$$\begin{aligned}i \frac{\partial \tilde{\Psi}_{\alpha'}(\mathbf{r})}{\partial t} &= [\tilde{\Psi}_{\alpha'}(\mathbf{r}), H_S], \\ i \frac{\partial \tilde{\Psi}_{\alpha'}^\dagger(\mathbf{r})}{\partial t} &= [\tilde{\Psi}_{\alpha'}^\dagger(\mathbf{r}), H_S].\end{aligned}\quad (1.56)$$

Inserting Eqs. (1.55) and (1.54) into Eq. (1.56) and using the anticommuting rules given by Eq. (1.53), one arrives at the equation of motion for the operators $\tilde{\Psi}_{\alpha'}$ and $\tilde{\Psi}_{\alpha'}^\dagger$:

$$\begin{aligned}\left(i \frac{\partial}{\partial t} + \frac{\nabla^2}{2m} \right) \tilde{\Psi}_{\alpha'} - \Lambda \tilde{\Psi}_{\alpha'}^\dagger \tilde{\Psi}_{\alpha'} \tilde{\Psi}_{\alpha'} &= 0, \\ \left(i \frac{\partial}{\partial t} - \frac{\nabla^2}{2m} \right) \tilde{\Psi}_{\alpha'}^\dagger + \Lambda \tilde{\Psi}_{\alpha'}^\dagger \tilde{\Psi}_{\alpha'}^\dagger \tilde{\Psi}_{\alpha'} &= 0.\end{aligned}\quad (1.57)$$

One can obtain the Green's function from Eq. (1.57) by multiplying the first equation, for example, by $-i\tilde{\Psi}_\beta^\dagger(\mathbf{r}')$ and applying the time-ordering operator T as

$$\left(i\frac{\partial}{\partial t} + \frac{\nabla^2}{2m}\right)G_{\alpha\beta}(\mathbf{r}, \mathbf{r}') + i\Lambda\langle T(\tilde{\Psi}_\alpha^\dagger\tilde{\Psi}_\alpha\tilde{\Psi}_{\alpha'}\tilde{\Psi}_\beta^\dagger)\rangle = \delta(\mathbf{r} - \mathbf{r}'), \quad (1.58)$$

where $G_{\alpha\beta}(\mathbf{r}, \mathbf{r}') = -i\langle T(\tilde{\Psi}_{\alpha'}(\mathbf{r})\tilde{\Psi}_\beta^\dagger(\mathbf{r}'))\rangle$ is the Green's function.

The term $\langle T(\tilde{\Psi}_\alpha^\dagger\tilde{\Psi}_\alpha\tilde{\Psi}_{\alpha'}\tilde{\Psi}_\beta^\dagger)\rangle$ in Eq. (1.58) represents an average of four-fermion attractive potential. We can apply the Wick's theorem to the term and find this average. According to the Wick's theorem, the average of four operators generates averaged pairs of operators $\tilde{\Psi}^\dagger$ and $\tilde{\Psi}$. From all the generated pairs we are interested only in pairs which correspond to creation of a pair $\langle T(\tilde{\Psi}^\dagger\tilde{\Psi}^\dagger)\rangle$ and annihilation of a pair $\langle T(\tilde{\Psi}\tilde{\Psi})\rangle$. As a result, the average splits into:

$$\langle T(\tilde{\Psi}_\alpha^\dagger\tilde{\Psi}_\alpha\tilde{\Psi}_{\alpha'}\tilde{\Psi}_\beta^\dagger)\rangle = \tilde{\Psi}_\alpha^\dagger\tilde{\Psi}_\beta^\dagger\langle T(\tilde{\Psi}_\alpha\tilde{\Psi}_{\alpha'})\rangle + \langle T(\tilde{\Psi}_\alpha^\dagger\tilde{\Psi}_\beta^\dagger)\rangle\tilde{\Psi}_\alpha\tilde{\Psi}_{\alpha'}. \quad (1.59)$$

Moreover, $\langle T(\tilde{\Psi}^\dagger\tilde{\Psi}^\dagger)\rangle$ corresponds to $\langle N + 2|T(\tilde{\Psi}^\dagger\tilde{\Psi}^\dagger)|N\rangle$, where N is the number of electrons in the system, while $\langle T(\tilde{\Psi}\tilde{\Psi})\rangle$ satisfies $\langle N|T(\tilde{\Psi}\tilde{\Psi})|N+2\rangle$. One can rewrite the pair averages as

$$\begin{aligned} \langle N|T(\tilde{\Psi}_\alpha(\mathbf{r})\tilde{\Psi}_\beta(\mathbf{r}'))|N+2\rangle &= e^{-2i\mu t}F_{\alpha\beta}(\mathbf{r} - \mathbf{r}'), \\ \langle N+2|T(\tilde{\Psi}_\alpha^\dagger(\mathbf{r})\tilde{\Psi}_\beta^\dagger(\mathbf{r}'))|N\rangle &= e^{2i\mu t}F_{\alpha\beta}^\dagger(\mathbf{r} - \mathbf{r}'), \end{aligned} \quad (1.60)$$

where $\langle T(\tilde{\Psi}_\alpha(\mathbf{r})\tilde{\Psi}_\beta(\mathbf{r}'))\rangle = F_{\alpha\beta}(\mathbf{r} - \mathbf{r}')$ is the anomalous Green's function [87] and μ is the chemical potential. After inserting Eq. (1.59) into Eq. (1.58) and employing the expression for the anomalous Green's function, Eq. (1.58) modifies to

$$\left(i\frac{\partial}{\partial t} + \frac{\nabla^2}{2m}\right)G_{\alpha\beta}(\mathbf{r}, \mathbf{r}') - i\Lambda F_{\alpha\beta}(0+)F_{\alpha\beta}^\dagger(\mathbf{r}, \mathbf{r}') = \delta(\mathbf{r} - \mathbf{r}'), \quad (1.61)$$

where $F_{\alpha\beta}(0+) = e^{2i\mu t}\langle N|(\tilde{\Psi}_\alpha\tilde{\Psi}_\beta)|N+2\rangle$. Performing similar arithmetical operation with respect to the second equation of Eq. (1.57), one obtains equation for the anomalous Green's function $F_{\alpha\beta}(\mathbf{r}, \mathbf{r}')$:

$$\left(i\frac{\partial}{\partial t} - \frac{\nabla^2}{2m} - 2\mu\right)F_{\alpha\beta}^\dagger(\mathbf{r}, \mathbf{r}') + i\Lambda F_{\alpha\beta}^\dagger(0+)G_{\alpha\beta}(\mathbf{r}, \mathbf{r}') = 0. \quad (1.62)$$

The properties of $G_{\alpha\beta}(\mathbf{r}, \mathbf{r}')$ and $F_{\alpha\beta}(\mathbf{r}, \mathbf{r}')$ are described in detail in Ref. [87].

We can apply the Wick's theorem to the four-fermion attractive potential in Eq. (1.54) and rewrite the interaction term in Hamiltonian via averaged pairs $\langle T(\tilde{\Psi}^\dagger\tilde{\Psi}^\dagger) \rangle$ and $\langle T(\tilde{\Psi}\tilde{\Psi}) \rangle$ as

$$H_{BCS} = H_0 - \int \left\{ \tilde{\Psi}_\alpha^\dagger(\mathbf{r})\tilde{\Psi}_\beta^\dagger(\mathbf{r})\Delta(\mathbf{r}) + \Delta(\mathbf{r})^*\tilde{\Psi}_\alpha(\mathbf{r})\tilde{\Psi}_\beta(\mathbf{r}) \right\} d\mathbf{r}, \quad (1.63)$$

where we introduced the gap $\Delta(\mathbf{r}) = |\Lambda|\langle T(\tilde{\Psi}_\alpha(\mathbf{r})\tilde{\Psi}_\beta(\mathbf{r})) \rangle = |\Lambda|F_{\alpha\beta}(\mathbf{r}, \mathbf{r}')$, and replaced the kinetic energy by H_0 . Eq. (1.63) represents the **BCS Hamiltonian**.

Eqs. (1.61) and (1.62) were derived in absence of the magnetic field. In order to study the response of superconductor to the magnetic field, we have to include the magnetic field into Eqs. (1.61) and (1.62). Therefore, we modify the kinetic term in the equations as

$$\frac{\nabla^2}{2m} \rightarrow \frac{1}{2m} \left(\partial_{\mathbf{r}} - ie\mathbf{A}(\mathbf{r}) \right)^2.$$

It is also convenient to perform the Fourier transform of the Green's functions from the time dependence in Eqs. (1.61) and (1.62) to the summation over frequency. After those alterations [87], we can rewrite Eqs. (1.61) and (1.62) as

$$\begin{cases} i\omega + \frac{1}{2m} \left(\partial_{\mathbf{r}} - ie\mathbf{A}(\mathbf{r}) \right)^2 + \mu \} \mathcal{G}_\omega(\mathbf{r}, \mathbf{r}') + \Delta(\mathbf{r})\mathcal{F}_\omega^\dagger(\mathbf{r}, \mathbf{r}') = \delta(\mathbf{r} - \mathbf{r}'), \\ \left\{ -i\omega + \frac{1}{2m} \left(\partial_{\mathbf{r}} + ie\mathbf{A}(\mathbf{r}) \right)^2 + \mu \right\} \mathcal{F}_\omega^\dagger(\mathbf{r}, \mathbf{r}') - \Delta^*(\mathbf{r})\mathcal{G}_\omega(\mathbf{r}, \mathbf{r}') = 0, \end{cases} \quad (1.64)$$

where $\mathcal{G}_\omega(\mathbf{r}, \mathbf{r}')$ and $\mathcal{F}_\omega^\dagger(\mathbf{r}, \mathbf{r}')$ are Fourier components of the Green's functions. We redefined the gap function in Eq. (1.64) as

$$\Delta^*(\mathbf{r}) = |\Lambda|T \sum_{\omega} \mathcal{F}_\omega^\dagger(\mathbf{r}, \mathbf{r}'). \quad (1.65)$$

It was shown by Gor'kov [36] that Eq. (1.65) can be expanded in powers of Δ in the vicinity of the critical temperature $1 - T/T_c \ll 1$, since as $\Delta(\mathbf{r})$ is small near T_c . We assume that the characteristic length scale is the correlation radius of electrons $\xi_0 \sim v_F/T_c$, where v_F is the velocity of electrons at the Fermi level, and this length scale is much smaller than the magnetic penetration depth δ . Thus, all the quantities, including the field, vary on the length scales exceeding the principal length scale of the theory.

Fourier components $\mathcal{G}_\omega(\mathbf{r}, \mathbf{r}')$ and $\mathcal{F}_\omega^\dagger(\mathbf{r}, \mathbf{r}')$ are unknown. Assuming that the magnetic field is small near T_c , we can find the expressions for them by

expanding the components as [36, 87]

$$\begin{aligned}\mathcal{G}_\omega(\mathbf{r}, \mathbf{r}') &= \mathcal{G}_\omega^{(0)}(\mathbf{r}, \mathbf{r}') - \int \mathcal{G}_\omega^{(0)}(\mathbf{r}, \mathbf{l}) \Delta(\mathbf{l}) \mathcal{F}_\omega^\dagger(\mathbf{l}, \mathbf{r}') d\mathbf{l}, \\ \mathcal{F}_\omega^\dagger(\mathbf{r}, \mathbf{r}') &= \int \mathcal{G}_{-\omega}^{(0)}(\mathbf{l}, \mathbf{r}) \Delta^*(\mathbf{l}) \mathcal{G}_\omega(\mathbf{l}, \mathbf{r}') d\mathbf{l},\end{aligned}\quad (1.66)$$

where $\mathcal{G}_\omega^{(0)}$ and $\mathcal{F}_\omega^\dagger$ are the known Fourier components in the absence of the magnetic field [87]. Substituting the first equation of Eq. (1.66) into the second equation, and afterwards inserting the obtained expression into Eq. (1.65), one arrives at the expansion [36, 87]:

$$\begin{aligned}\Delta^*(\mathbf{r}) &= |\Lambda|T \sum_\omega \int \mathcal{G}_\omega^{(0)}(\mathbf{l}, \mathbf{r}) \Delta^*(\mathbf{l}) \mathcal{G}_{-\omega}^{(0)}(\mathbf{l}, \mathbf{r}) d\mathbf{l} - |\Lambda|T \sum_\omega \int \int \int \mathcal{G}_\omega^{(0)}(\mathbf{l}, \mathbf{m}) \\ &\quad \times \Delta(\mathbf{m}) \mathcal{G}_\omega^{(0)}(\mathbf{s}, \mathbf{r}) \Delta^*(\mathbf{s}) \mathcal{G}_{-\omega}^{(0)}(\mathbf{s}, \mathbf{m}) \Delta^*(\mathbf{l}) \mathcal{G}_{-\omega}^{(0)}(\mathbf{l}, \mathbf{r}) d\mathbf{l} d\mathbf{m} d\mathbf{s}.\end{aligned}\quad (1.67)$$

In fact, the expansion given by Eq. (1.67) represents a long series of integrals. However, we are interested only in two first terms shown in the expansion, because they produce at the end the final result in the form of the GL equation. The first integral in Eq. (1.67) generates the result [36, 87]:

$$\left(\frac{1}{4m} \left(\partial_{\mathbf{r}} + 2ie\mathbf{A}(\mathbf{r}) \right)^2 + \frac{1}{\eta} \frac{(T_c - T)}{T_c} \right) \Delta^*(\mathbf{r}), \quad (1.68)$$

where $\eta = \frac{7\zeta(3)}{6(\pi T_c)^2} \varepsilon_F$. The second integral in Eq. (1.67) yields [36, 87]:

$$\frac{7\zeta(3)}{8(\pi T_c)^2 \eta} \Delta^*(\mathbf{r}) |\Delta(\mathbf{r})|^2. \quad (1.69)$$

Combining the results for both integrals leads to equation:

$$\left\{ \frac{1}{4m} \left(\partial_{\mathbf{r}} + 2ie\mathbf{A}(\mathbf{r}) \right)^2 + \frac{1}{\eta} \left(\frac{T_c - T}{T_c} - \frac{7\zeta(3)}{8(\pi T_c)^2} |\Delta(\mathbf{r})|^2 \right) \right\} \Delta^*(\mathbf{r}) = 0. \quad (1.70)$$

Eq. (1.70) describes the behavior of a superconductor in the vicinity of the critical temperature $1 - T/T_c \ll 1$.

Let us now introduce a new function $\psi(\mathbf{r})$ proportional to $\Delta(\mathbf{r})$ as

$$\psi(\mathbf{r}) = \sqrt{\frac{7\zeta(3)N(0)}{8(\pi T_c)^2}} \Delta(\mathbf{r}), \quad (1.71)$$

where $N(0)$ is the density of states at the Fermi level [36, 87]. By taking the complex conjugate of Eq. (1.70) and inserting $\psi(\mathbf{r})$ into the equation, Eq. (1.70) modifies to a new form as

$$\left\{ \frac{1}{4m} \left(\partial_{\mathbf{r}} - 2ie\mathbf{A}(\mathbf{r}) \right)^2 + \frac{1}{\eta} \left(\frac{T_c - T}{T_c} - \frac{1}{N(0)} |\psi(\mathbf{r})|^2 \right) \right\} \psi(\mathbf{r}) = 0. \quad (1.72)$$

Eq. (1.72) is the Ginzburg-Landau equation and we can rewrite it in a more familiar way:

$$\alpha\psi(\mathbf{r}) + \beta\psi(\mathbf{r})|\psi(\mathbf{r})|^2 + \frac{1}{4m} \left(\frac{\hbar}{i} \nabla - \frac{2e}{c} \mathbf{A} \right)^2 \psi(\mathbf{r}) = 0, \quad (1.73)$$

where we found explicit expressions for the previous phenomenological coefficients α and β :

$$\alpha = \frac{(T - T_c)}{\eta T_c}, \quad \beta = \frac{1}{\eta N(0)}. \quad (1.74)$$

Eq. (1.72) acquired the form similar to the quantum mechanical equation characterizing behavior of a particle with the mass $2m$ and the charge $2e$. Then the gap function $\Delta(\mathbf{r})$ can be interpreted as the quantity which is proportional to the wave function of the paired electrons or the wave function with respect to the center of inertia of the pair.

This remarkable result was important, because it proved the correctness of the phenomenological Ginzburg-Landau theory, showed that superconductors are well described by the Ginzburg-Landau equations near T_c , and provided the microscopic expressions for the previously phenomenological coefficients in the GL theory.

1.4 Multiband superconductors

The fundamentals of the BCS theory are established on the facts that electrons near the Fermi surface form Cooper pairs and then condense into a common quantum state, with which an energy gap is associated. However, a real superconducting specimen can comprise more than one Fermi surface resulting in appearance of multiple energy gaps. Each of these gaps is associated with charge carriers which form Cooper pairs. If in the BCS theory pairing was due to electron-phonon interaction near the Fermi surface and the Debye frequency ω_D was dependency range over which the interaction occurred, for multiband superconductors formation of the Cooper pairs does

not necessarily occur only due to the electron-phonon interaction and ω_D is no longer the single characteristic quantity for the pairing.

The idea that a superconductor can possess multiple gaps was suggested by Moskalenko [88] and simultaneously by Suhl [89] in 1959, shortly after the BCS theory was proposed, by generalizing the BCS theory for a two-gap superconductor. Afterwards, in 1966 Leggett suggested existence of a new kind of collective excitations for two-gap superconductors [90]. His idea was that if a system contains two coupled gaps then a Cooper pair of one gap can scatter into a Cooper pair of the second gap thus causing a counterflow between these two gaps. The counterflow of the two gaps leads to small oscillations of the relative phase of the two condensates. The Leggett mode is gapped. Although these collective excitations were predicted in 1966, the experimental observation of the Leggett mode was achieved only in 2007 [62], after the discovery of a two-gap superconductor MgB_2 [51]. In the experiment the gap of these oscillations was measured [62].

This discovery of MgB_2 was the result of the search for higher T_c values motivated by a basic desire to find an intrinsic limiting temperature and by technological interest to make superconducting devices. In conventional superconductors, there are three parameters on which the value of critical temperature depends: the phonon energy, the density of states, and the electron-phonon coupling strength. Experimentally, it is possible to tune the density of states by varying the chemical composition in an isostructural series of compounds. In addition, using light elements can raise ω_D . Based on these features, labs around the world pursued superconductivity in ternary or quaternary compounds that were rich in light elements such as lithium, boron, carbon, and magnesium. In 2001 it was reported that MgB_2 , having four electronic bands crossing the Fermi level and two distinct gaps, entered superconducting regime at $T_c = 39$ K [51].

A few years later iron-pnictide superconductors were discovered [63, 64, 66, 52, 73, 100, 67, 101, 102, 65, 103, 104, 72, 105] which are also multiband superconductors [73, 74]. Unlike MgB_2 , iron-arsenides are not intermetallic compounds and there is evidence that superconductivity co-exists with antiferromagnetism in these compounds. Thus, iron-based superconductors present an even richer platform for further study [68, 69].

However, it had been the discovery of MgB_2 that gave initial rise to a new epoch in superconductivity stemming from the multigap nature. The concept of two gaps in a single superconductor has been considered theoretically earlier [88, 89] but MgB_2 was the first example of distinct two-gap superconductivity found in experiment. Over the last decade multiband superconductors have been intensely studied, and were found to exhibit significantly richer characteristics compared to their single-band counterparts [91]. Therefore,

in what follows, we discuss the crystal structure of MgB_2 and an iron-based superconductor, their complex Fermi surface appearance, the isotope effect measurements, evidence of existence of multiple gaps in those materials and pairing mechanisms.

1.4.1 The crystal structure of MgB_2 and some of pnictides

Magnesium diboride undergoes the transition to superconducting state at $T_c = 39$ K [51]. MgB_2 is a binary intermetallic compound with a simple crystal structure incorporating hexagonal Mg planes interlayered with honeycomb B sheets, as shown in Fig. 1.6(a). This crystal structure leads to non-trivial links between the arrangement of the Mg atoms and the B atoms and the resulting band structure and the electronic states [56]. MgB_2 incorporates two distinct bands: a two-dimensional σ band and a three-dimensional π one. The σ band involves electrons of the B plane creating a two-dimensional network of delocalised electrons which can conduct only in the basal plane of B. On the other hand, the π band forms a three-dimensional network and links neighboring B layers through the inert Mg ions allowing electrons to conduct perpendicularly to the B planes as well as parallel to the B sheets [56].

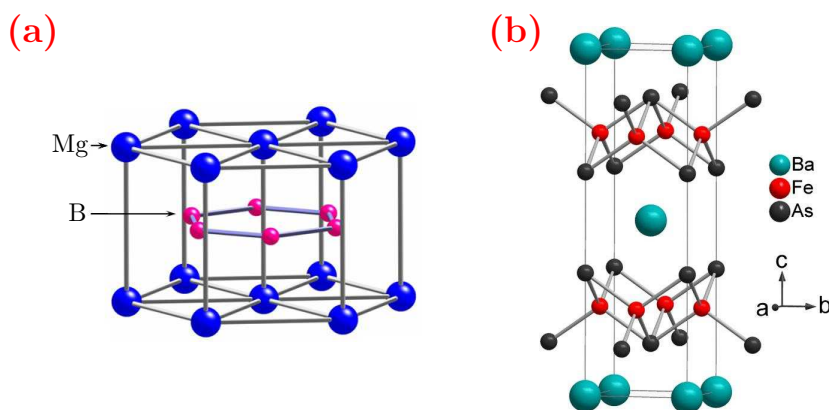


Figure 1.6: (a) Crystal structure of MgB_2 : hexagonal planes of magnesium (blue) interlayered with honeycomb layers of boron (pink) (adapted from [51]); (b) Charged $(\text{Ba})^{\delta+}$ layers alternating with layers of $(\text{FeAs})^{\delta-}$ in the crystal structure of BaFe_2As_2 (adapted from [66]).

Iron-based layered pnictide superconductors exhibit more complex crystal structure. The superconductivity has first been discovered in oxygen containing compounds like RFeAsO , where R can be La, Nd or Sm, as well

as in oxygen-free compounds $A\text{Fe}_2\text{As}_2$ (where $A=\text{Ba},\text{Sr},\text{Ca}$). The critical temperature of these compounds ranges from 26 to 52 K. For example, the crystal structure of BaFe_2As_2 is shown in Fig. 1.6(b). BaFe_2As_2 has a quasi-two-dimensional tetragonal structure, which consists of charged $(\text{Ba})^{\delta+}$ layers alternating with layers of $(\text{FeAs})^{\delta-}$ as shown in Fig. 1.6(b). The parent materials of iron-based superconductors show antiferromagnetic long-range order below 150 K [64, 100, 67, 102], and superconductivity occurs upon doping of either electrons [64, 65, 103, 104] or holes [66] into the FeAs layers.

1.4.2 The Fermi surface of multiband superconductors

Since the exemplified multiband superconductors incorporate intricate crystal structure, it is not surprising that they do not exhibit an individual Fermi surface but rather an intricate collection of Fermi sheets separated in the momentum space and centered around the symmetry points of the Brillouin zone. The Fermi sheets corresponding to MgB_2 are shown in Fig. 1.7(a). The vertical sections of cylinders at the corners are associated with the σ band of MgB_2 while the three-dimensional network of tunnels and caves in the center of the zone is linked with the π band. The letters designate the symmetry points of the hexagonal Brillouin zone in momentum space.

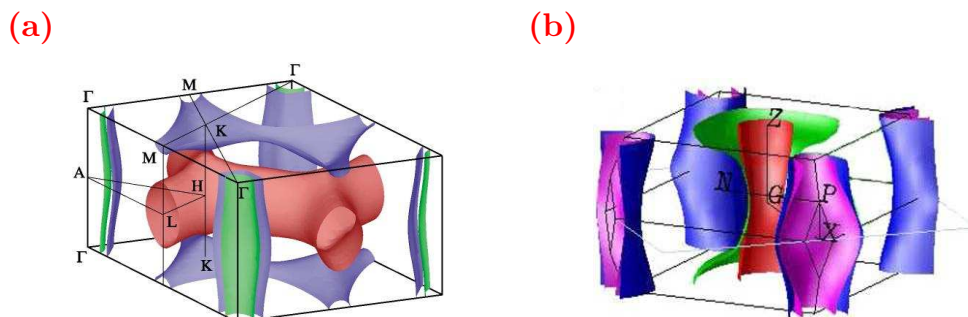


Figure 1.7: (a) Fermi surface of MgB_2 . The vertical sections of cylinders at the corners are associated with the σ bands; the 3D network of tunnels and caves in the center of the zone is associated with the π bands. The letters designate the symmetry points of the hexagonal Brillouin zone in momentum space (adapted from [55]); (b) Fermi surface of BaFe_2As_2 (adapted from [72]).

The Fermi surface of BaFe_2As_2 is shown in Fig. 1.7(b). It consists of an inner and outer hole pockets centered at Γ (denoted by G in Fig. 1.7(b)) point of the Brillouin zone, and four pairs of inner and outer electron pockets at X points.

1.4.3 The isotope effect measurements

The next important ingredient in understanding multiband superconductors is the presence of the isotope effect as in the case of the single band superconductors. The isotope coefficient α_i , where i is the index of the elemental component in the compound, is defined as

$$\alpha_i = -\frac{d \ln T_c}{d \ln M_i}, \quad (1.75)$$

where M_i is the magnetization of a component. For the conventional superconductors for the full isotope effect $\alpha = 1/2$, and is the characteristic of electron-phonon pairing mechanism.

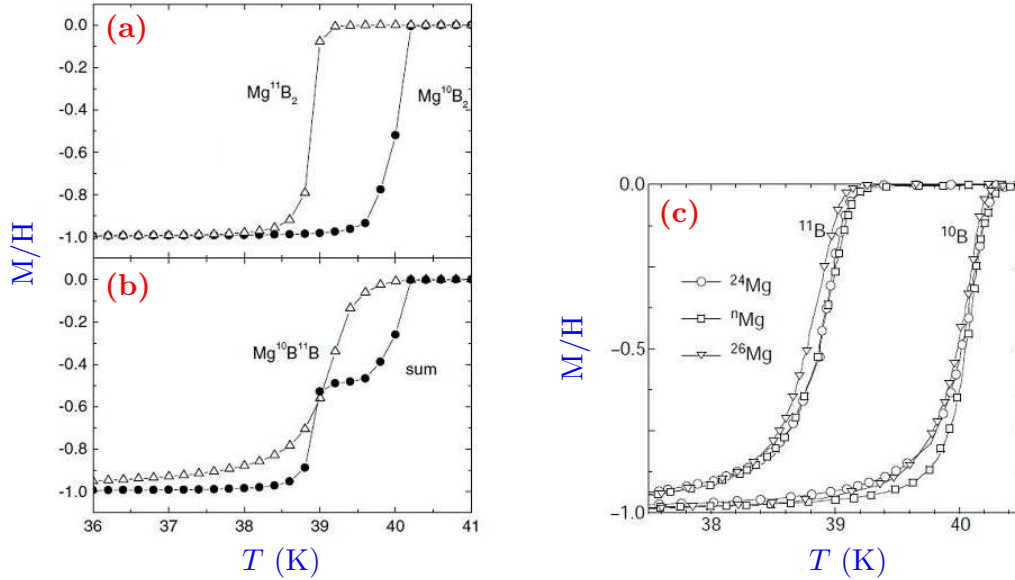


Figure 1.8: Isotope effect in MgB₂. (a) Magnetization divided by applied field as a function of temperature for Mg¹⁰B₂ and Mg¹¹B₂ (adapted from [52]); (b) Magnetization divided by applied field as a function of temperature for Mg¹⁰B¹¹B and sum of Mg¹⁰B₂ and Mg¹¹B₂ data shown in panel (a) (adapted from [52]); (c) Magnetization divided by applied field as a function of temperature for combination of ^aMg^bB₂ where $a = 24, n, 26$ and $b = 10, 11$; ⁿMg indicates samples with natural Mg (adapted from [53]).

The first measurements of the isotope effect in MgB₂ [52, 57, 58, 59, 60] showed that when ¹¹B was replaced by ¹⁰B the critical temperature was increased by 1 K, as shown in Fig. 1.8(a). The isotope coefficient for B was

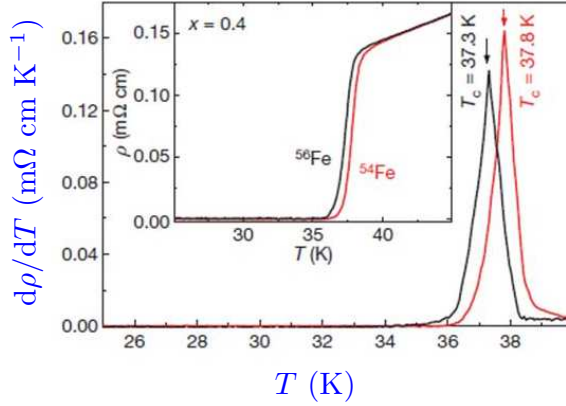


Figure 1.9: The temperature dependence of derivative of the resistivity $d\rho/dT$ in $\text{Ba}_{1-x}\text{K}_x\text{Fe}_2\text{As}_2$ (with $x = 0.4$) showing the increase of critical temperature upon substitution of ^{56}Fe atoms by ^{54}Fe . Inset features the temperature dependence of the resistivity (adapted from [105]).

found to be $\alpha_B = 0.26(3)$ [52]. However, substitution of ^{24}Mg for ^{26}Mg showed almost no shift in T_c [53] [Fig. 1.8(c)]. α_{Mg} was found to be 0.02(1). The total isotope effect for Mg and B together also exhibited a small effect in the temperature shift [52] [Fig. 1.8(b)]. We recall that there are three deterministic quantities for the critical temperature: the characteristic phonon energy $\hbar\omega_D$, the density of states at the Fermi level $N(E_F)$, and the strength of the electron-phonon interaction V . The phonon energies of MgB_2 were found to be high but not especially different from other diboride compounds that have much lower values of T_c . MgB_2 does not have d -electrons resulting in low density of states. There is only one key characteristic left which is the electron-phonon coupling strength, prompting the idea of a selective electron-phonon interaction in MgB_2 . The large isotope effect for B indicates that phonon associated with B vibrations play a more significant role in the superconductivity of MgB_2 .

The isotope effect was also measured in iron-pnictide superconductor $\text{Ba}_{1-x}\text{K}_x\text{Fe}_2\text{As}_2$ at substitution of ^{56}Fe by ^{54}Fe , as depicted in Fig. 1.9 [105]. This substitution showed a significant isotope effect with $\alpha_{Fe} = 0.35$. Although the isotope effect is a feature of electron-phonon pairing in a superconductor, theoretical calculations indicated that the electron-phonon interaction is not strong enough in this compound to give rise to such high transition temperatures observed in numerous experiments [63, 64, 66, 52, 73, 100, 67, 101, 102, 65, 103, 104, 72, 105]. The exact pairing mechanism in

iron-pnictides is currently in dispute. However, it is evident that superconductivity in these compounds emerges from specific structural and electronic conditions in the $(\text{FeAs})^{\delta-}$ layer.

1.4.4 Experimental evidence of multiple gaps

The knowledge of the symmetry and shape of the superconducting gap in momentum space is essential for constructing the correct model of the pairing mechanism and further theoretical considerations.

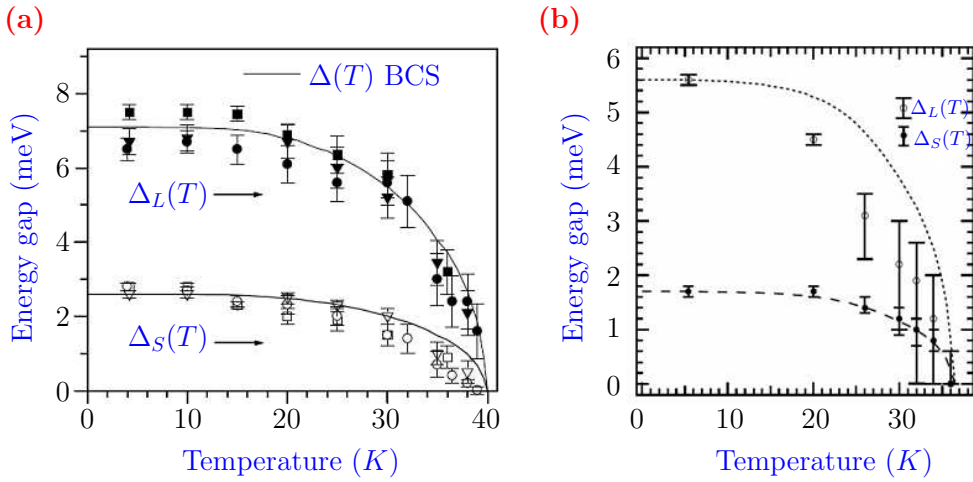


Figure 1.10: Temperature dependence of two energy gaps in MgB₂. (a) Symbols stand for the experimental data. $\Delta_S(T)$ denoted by solid symbol corresponds to the π band, while $\Delta_L(T)$ designated by open symbols is associated with the σ band. The solid lines represent BCS predictions. The sample entered the superconducting regime at $T_c = 39.5$ K (adapted from [93]); (b) Filled and open circles represent the smaller $\Delta_S(T)$ and larger $\Delta_L(T)$ gaps respectively. Broken and dotted lines show the predicted temperature dependence of superconducting gaps from BCS theory. MgB₂ underwent the transition at $T_c = 36.5$ K (adapted from [95]).

The multigap nature of superconductivity in MgB₂ had been first theoretically predicted [54] and then experimentally established by a number of spectroscopies [93, 94, 95]. The two gaps in MgB₂ arise naturally from the different strengths of the electron-phonon coupling in the σ and π bands. The gaps were observed in the superconducting tunneling behavior measurements [93, 94, 95]. Fig. 1.10 shows the experimental results taken with a

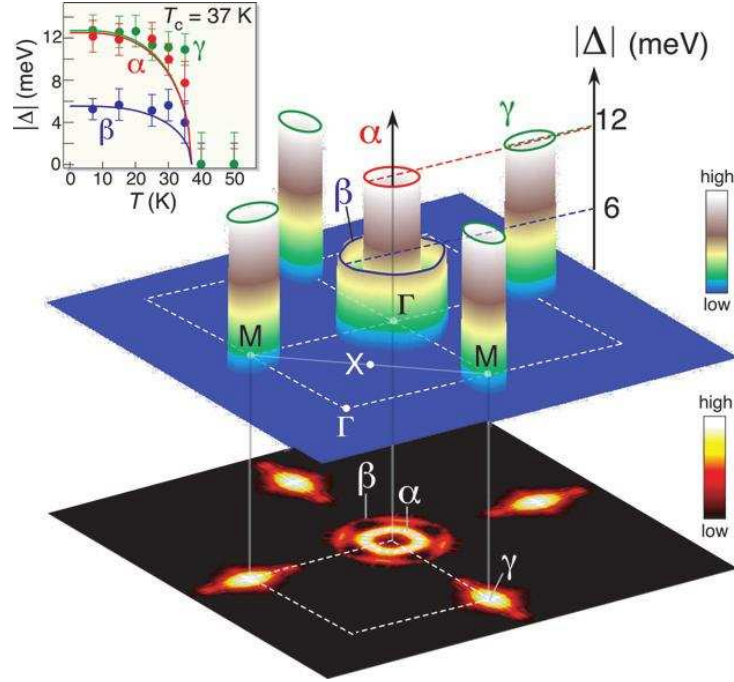


Figure 1.11: The image illustrates the evidence of three distinct gaps in $\text{Ba}_{0.6}\text{K}_{0.4}\text{Fe}_2\text{As}_2$ shown in inset, all gaps appear at the same temperature $T_c = 37$ K. Experimental data shown by dots, while solid lines are predicted by the theory. The main image demonstrates the complex structure of Fermi surfaces in this compound (adapted from [73]).

scanning tunneling microscope on a polycrystalline sample of MgB_2 . Both gaps arise at the same critical temperature [93, 94, 95], which indicates significant interaction between them. The two gaps are however not increasing equally at lower temperature, since there is a weaker gap denoted by $\Delta_S(T)$ which corresponds to the weak π band, and a larger gap $\Delta_L(T)$ associated with the σ band. As shown in Fig. 1.10, the temperature dependence of both gaps follows the BCS behavior.

The situation becomes somewhat more complicated with respect to the iron-based superconductors. One of the most vital questions is whether the mechanism of superconductivity in these materials is similar to that in conventional superconductors or the cuprate high temperature superconductors. Or this family of materials offers a completely new route to the superconducting state? On the experimental side, angle-resolved photoelectron spectroscopy (ARPES) for $\text{Ba}_{0.6}\text{K}_{0.4}\text{Fe}_2\text{As}_2$ indicated three nearly isotropic and nodeless superconducting gaps of different values [73] [shown in Fig. 1.11].

Similar ARPES measurements of the superconducting gap in $\text{NdFeAsO}_{0.9}\text{F}_{0.1}$ single crystals [106] showed a nodeless superconducting gap in the hole pocket around the Γ point of Brillouin zone. A nodeless gap was also observed in $\text{SmFeAsO}_{0.85}\text{F}_{0.15}$ measured by Andreev spectroscopy [107]. On the other hand, NMR studies of the superconducting properties of iron-arsenide based compound $\text{PrFeAsO}_{0.89}\text{F}_{0.11}$ showed two gaps opening below T_c , with nodes in the gap function [74].

1.4.5 The pairing symmetry

Specific heat measurements [96, 97] and the isotope effect [52] indicate that MgB_2 is a conventional superconductor with s -wave pairing. In conventional superconductors, the electron-phonon interaction creates Cooper pairs of approximately equal pairing strength, distributed uniformly over the Fermi surface. However, in MgB_2 there is one high-energy phonon (≈ 570 meV), associated with the in-plane motion of the B atoms, coupling strongly to electrons of σ band. Therefore, the σ band hosts more Cooper pairs becoming the stronger band, while the π band will host lower density of Cooper pairs. Thus, MgB_2 involves two bands with different electron-phonon coupling [57, 58, 59, 60, 53, 98]. This explains the isotope effect stemming mostly from the B atoms. Moreover, the electron-phonon coupling strength in the σ band exceeds significantly the characteristic phonon energy $\hbar\omega$. The latter feature sheds light on the found high critical temperature $T_c = 39$ K for a conventional superconductor. The temperature behavior of gaps in MgB_2 nevertheless follows the BCS trend.

In case of the iron-based superconductors, the pairing mechanism and the gap symmetry are still in dispute. There is experimental evidence of the isotope effect in $\text{Ba}_{1-x}\text{K}_x\text{Fe}_2\text{As}_2$ [105], but the electron-phonon pairing cannot explain the observed high critical temperatures of iron-pnictide superconductors. The NMR measurements in $\text{LaFeAs}(\text{O}_{1-x}\text{F}_x)$ indicated that the spin-lattice relaxation rate changed with temperature as $1/T_1 \propto T^3$, which is the evidence of a d -wave, unconventional superconductor [68, 69]. T_1 is the longitudinal (or spin-lattice) relaxation time, the characteristics of NMR being the mechanism by which the component of the magnetization vector along the direction of the static magnetic field reaches thermodynamic equilibrium with its surroundings (by which a lattice are meant) in nuclear magnetic resonance. In superconductivity the quantity $1/T_1$ is measured. If the behaviour of $1/T_1$ follows the T^3 trend in a superconducting material, where T is the temperature, then the superconductor has the d -wave pairing symmetry. If $1/T_1$ follows the exponential trend, then the superconductor is conventional. However, d -wave superconductors do not host nodeless gaps

nor multiple gaps [73, 74]. On the other hand, the theoretical result of the gap calculation [70, 71] showed that the T dependence of $1/T_1$ in a dirty s_{\pm} superconductor mimics T^3 behavior over a wide range of T , and becomes exponential (the BCS behavior) only at very low temperatures. It was also shown in Ref. [70] that the gap changes sign between different parts of the Fermi surface suggesting presence of electron- and hole-like pockets. Such gap behavior follows s_{\pm} -wave symmetry and is considered to be unconventional.

Albeit pairing in iron-based superconductors does not follow the s -wave symmetry, we can generalize the BCS theory for superconductors with s_{\pm} -wave symmetry and associate a scalar function $\Delta_{\mathbf{k}}$ with each gap, i. e. with the gap which corresponds to the singlet pairing and involving a unique temperature transition. Then one can introduce BCS Hamiltonian for a multi-band superconductor similar as in Ref. [88, 89]:

$$H_{\text{BCS}} = H_c + \sum_i \int d^3r \left[\sum_{\sigma} \hat{\psi}_{i\sigma}^{\dagger}(\mathbf{r}) T_i(\mathbf{r}) \hat{\psi}_{i\sigma}(\mathbf{r}) + \hat{\psi}_{i\uparrow}^{\dagger}(\mathbf{r}) \hat{\psi}_{i\downarrow}^{\dagger}(\mathbf{r}) \Delta_i(\mathbf{r}) + \text{h.c.} \right], \quad (1.76)$$

where $T_i(\mathbf{r})$ is the single-electron energy, $\hat{\psi}_{i\downarrow}^{\dagger}(\mathbf{r})$ is the creation operator, and $\hat{\psi}_{i\downarrow}(\mathbf{r})$ is annihilation operator. H_c represents the c-number term [75], which is a quadratic form of anomalous averages $\langle \hat{\psi}_{i\uparrow}(\mathbf{r}) \hat{\psi}_{i\downarrow}(\mathbf{r}) \rangle$. We also introduced in Eq. (1.76) the gap definition for a multi-band superconductor as

$$\Delta_i(\mathbf{r}) = \sum_{j=1,2,\dots} g_{ij} \langle \hat{\psi}_{i\uparrow}(\mathbf{r}) \hat{\psi}_{j\downarrow}(\mathbf{r}) \rangle, \quad (1.77)$$

where g_{ij} is the coupling matrix and the gap was defined through anomalous pairing as usual in the BCS theory. The coupling matrix is the analogue of the electron-phonon interaction matrix in the BCS theory defined by Eq. (1.24). The coupling matrix assumes an interval within which pairing takes place. The diagonal elements of the coupling matrix are associated with the pairing inside of each band, while the non-diagonal elements are accounting for the interband interaction.

Hamiltonian given by Eq. (1.76) along with the gap definition (1.77) will be employed in subsequent derivation of the Ginzburg-Landau theory for the multi-band superconductors in Chapter 2 .

1.5 Superconductors under quantum confinement

When superconductors are under strong quantum confinement, the electronic motion in the direction in which the confinement is applied (vertical in the case of nanothin superconducting film) is restricted. This leads to quantized quasi-momentum component corresponding to the motion perpendicular to the film plane. As the result, the Fabri-Pérot modes (or, in other words, the quantum-well states (QWSs)) are formed, as indicated first by Blatt and Thompson [76]. In the presence of the QWSs the band gap can separate into several two-dimensional (sub)band gaps, the number of which changes with decreasing or increasing the film thickness [76, 108]. The emergence of (sub)band gaps can be explained in the following way. In films, the energetic positions of the QWSs exhibit the scaling $1/d^2$, where d is the film thickness [21]. When the film thickness is varied, QWSs can cross the Fermi surface.

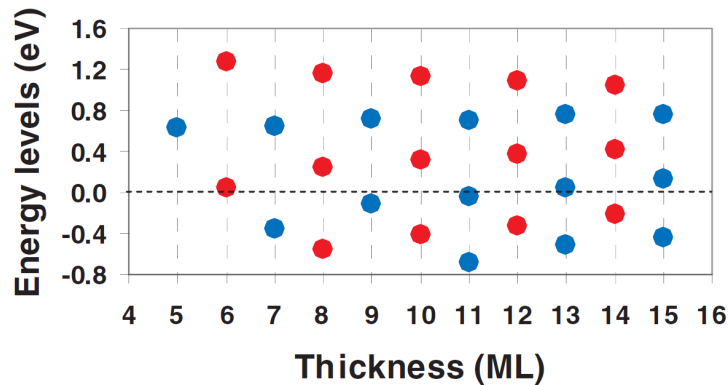


Figure 1.12: Illustration of the locations of quantum-well states for various thicknesses (5-18 ML) in Pb film. The dashed line shows the position of the Fermi level. The red color is for even numbers of MLs and the blue is for odd numbers of MLs (adapted from [109]).

Each time when a QWS crosses the Fermi surface, the relevant density of states (DOS) increases, and a new 2D band emerges. At each resonance, a new 2D gap starts to contribute. For example, figure 1.12 illustrates QWSs which were observed in Pb film in Ref. [109]. The dashed line in Fig. 1.12 indicates the position of the Fermi surface. As seen in Fig. 1.12 three QWSs cross the Fermi surface at 6, 11 and 13 ML, while the QWS at 9 ML approaches the Fermi surface, thus creating three additional (sub)bands and

the resonance should occur at 9 ML thickness. The corresponding oscillations of DOS are depicted in Fig. 1.13. It was also shown in Ref. [109] that gaps for 5 and 7 ML have the same gap value but the gap for 6 ML is larger. Afterwards the three gaps at 5, 6 and 7 ML were probed at the temperature $T = 6.24$ K which resulted in vanishing gaps at 5 and 7 ML, while the gap at 6 ML still persisted. Note that the oscillations of DOS in Fig. 1.13 are shifted with respect to the positions where QWSs cross the Fermi surface. This phase shift was generated by the interface film-substrate on which the film was grown [109].

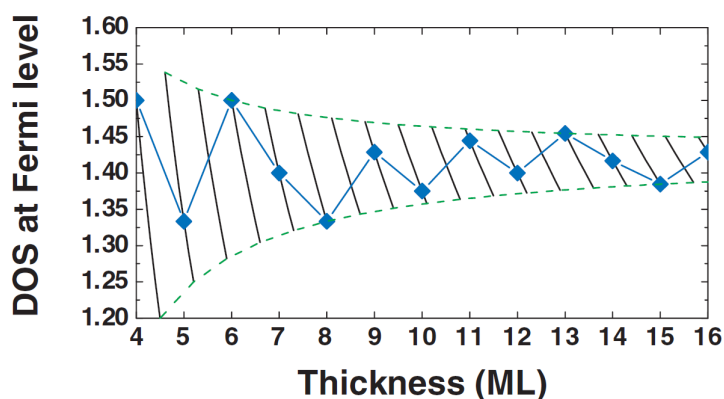


Figure 1.13: Estimated density of states (DOS) near the Fermi level as a function of the film thickness in Pb film (adapted from [109]).

The oscillations of DOS lead to quantum-size resonance effects in superconducting characteristics, i. e., oscillations of the critical temperature T_c as shown in Fig. 1.14, enhancement of the critical magnetic field H_c (thermodynamic, but upper and lower), and the excitation gap. Such size-dependent enhancement in the mean-field characteristics is termed superconductive quantum-size oscillations [21].

The quantum-size effects on the energy gap and the critical temperature were in focus of intensive theoretical works in 60s [76, 77, 78, 79, 80, 81]. Experimentally, the oscillations of the energy gap on variation of the film thickness were observed in early experiments on tin films [110, 111]. However, subsequent experiments on metallic films could not confirm those results [21]. Recent advances in nano-fabrication allowed to produce single-crystalline metallic nanofilms with atomically uniform thickness [112, 113, 114, 115, 116, 117, 118, 119, 120], in which quantum-size oscillations were reported.

The fabrication of such nanofilms was not without difficulties. Most of the

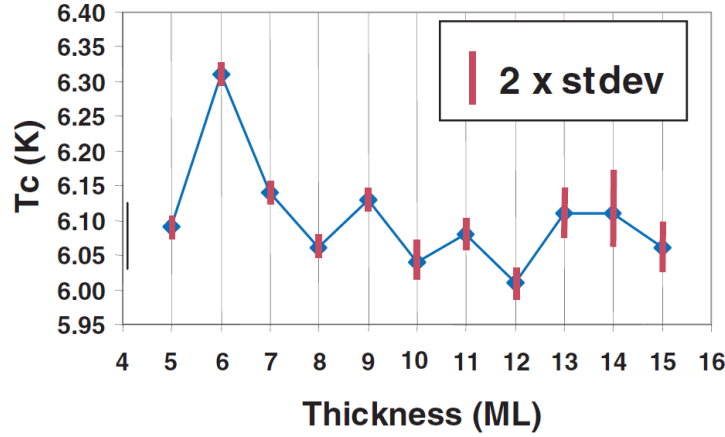


Figure 1.14: Variation of critical temperatures T_c from the film thickness in Pb film. Determined from temperature-dependent gap measurements for the film in ultra thin regime of 5-18 ML (adapted from [109]).

metallic films grow in a polycrystalline fashion, in forms of coupled grains. Typically, dimensions of the grains are significantly smaller than the film thickness d . If the coupling between grains is strong enough, the characteristic size of such grains restricts the electronic mean free path l . If the grains are too small, with the diameters of order $\sim \lambda_F$, where λ_F is the Fermi wavelength, then it can happen that due to $l \sim \lambda_F$ the system becomes an insulator before reaching the quasi-2D regime. However, Pb was found to grow into smooth single-crystalline nanofilms. This valuable finding opened completely new prospects in fabrication of ultrathin metallic films and led eventually to first results on the coherent behavior of Pb single-crystalline nanofilms [112]. For Pb films growing in $\langle 111 \rangle$ -direction one monolayer (ML) corresponds to thickness of 0.287 nm. If the thickness of a fabricated film is $d \approx 5 - 9$ nm, then the film has $d = 17 - 30$ ML.

Today many experimental groups around the world work with atomically flat nano-thin superconductors. In particular, a number of experiments have been performed for Pb single-crystalline nanofilms with the number of atomic layers varying from 1 to 30 ML. As a consequence, many important achievements were reported, such as appearance of the multiple subbands [112, 109, 119], quantum-size oscillations of T_c [112, 113, 109, 119] [shown in Fig. 1.14], and the upper critical field H_{c2} (perpendicular to a nanofilm) [113]. Vortices were also observed by mapping the zero-bias tunneling conductance in the presence of a magnetic field [114, 115, 118].

1.6 Multi-component Bose-Einstein condensation

In this Section we outline another example of a multi-component quantum system - the multi-component Bose-Einstein condensates. Those were created shortly after the experimental realization of Bose-Einstein condensation (BEC). Therefore, we begin with a short historical overview of Bose-Einstein condensation, difficulties in the experimental realization, the first successful experimental realizations of Bose-Einstein condensate, the theory applicable to study BEC and then move to fundamentals of multi-component Bose-Einstein condensation.

1.6.1 Achievement of Bose-Einstein condensation

Superconductivity and superfluidity are intimately related to the macroscopic occupation of a single quantum state by bosons. Electrons are fermions, thus cannot condense into a single quantum state. For bosons, the appearance of a condensate is natural, because bosons can occupy the same ground state at low temperatures. This phenomenon was pointed out by Einstein after studying Satyendra Nath Bose's statistical derivation of Planck's law for photons [121] to extend it to systems with a conserved number of particles [122, 123]. According to this theory, when a gas of bosonic atoms is cooled below a critical temperature T_c , a phase transition would occur and a large fraction of the atoms would occupy the lowest-energy quantum state. This phenomenon was subsequently termed Bose-Einstein condensation. The reasoning for occurrence of BEC was straightforward and based on the wave-particle duality, when particles with mass m at temperature T can be considered as quantum-mechanical wave packets with a spatial extent of the order of a thermal de Broglie wavelength $\lambda_{dB} = \left(\frac{2\pi\hbar^2}{mk_B T}\right)^{1/2}$. Accordingly, the value of λ_{dB} is the position uncertainty associated with the thermal momentum distribution which increases with decreasing temperature. When atoms are cooled to the temperature where λ_{dB} is comparable to the inter-atomic separation $n^{-1/3}$ (where n is the number of atoms per unit volume), the atomic wave packets start to overlap creating a system of indistinguishable particles. At this point, bosons undergo a quantum-mechanical phase transition and form a Bose-Einstein condensate. Thus, the task on creation of Bose-Einstein condensation was very simple to cool bosonic particles until the wave packets start to overlap. However, it was not experimentally feasible with the experimental techniques at hand at that time.

In 1938 London suggested the connection between the then recently discovered superfluid ^4He [124, 264] and the Bose-Einstein condensation [126, 127]. Superfluid ^4He is considered as the prototype of Bose-Einstein condensation. However, the interaction between helium atoms is strong, reducing the number of atoms in the lowest-energy state. As a result, it was difficult to measure directly the occupancy of the lowest-energy state. The latter led to the conclusion that Bose-Einstein condensation should be sought in weakly interacting Bose gases with higher condensate fraction. It required, however, to find an atomic system which would stay gaseous until it undergoes the transition, and to develop the cooling and trapping techniques in order to reach the required temperatures and densities.

As an example of such weakly interacting bosonic system, spin-polarized hydrogen atoms were proposed by Hecht in 1959 [128]. The conclusion of the study done by Hecht was that this system would be a good candidate, because the attractive interaction between two hydrogen atoms with their aligned electronic spins was estimated to be so weak that they do not tend to create a bound state. Thus, the spin-polarized hydrogen atoms would not form a liquid but remain gaseous at sufficiently low temperatures. Stwalley and Nosanow also studied the same system in 1976 [129], and argued that hydrogen atoms would be a superfluid as well as Bose-Einstein condensate. This theoretical prediction stimulated several experimental groups over the world to experimentally achieve Bose-Einstein condensation in hydrogen atoms. After more than two decades of experimental work, Bose-Einstein condensation of spin-polarized hydrogen atoms was achieved in 1998 [130].

As it was remarked by Ketterle [131], those studies of spin-polarized hydrogen atoms were important because they showed that hydrogen atoms can remain in a metastable gaseous state close to Bose-Einstein condensate conditions. The theory of cold collision processes developed for hydrogen atoms was used afterwards for alkali atoms, and advanced technique in evaporative cooling of spin-polarized hydrogen atoms contributed to the achievement of Bose-Einstein condensation in dilute alkali atoms in 1995 [172, 133, 134]. The initial experiments were performed on magnetically trapped ultracold vapours of alkali metals ^{87}Rb [172], ^{23}Na [133], and ^7Li [134]. Also the atoms of ^{39}K , ^{41}K , ^{52}Cr , ^{85}Rb , ^{133}Cs , ^{170}Yb , ^{174}Yb have been demonstrated to undergo Bose-Einstein condensation [135].

By dilute gases one means systems with a very low particle density. For comparison, the density of air at room temperatures and atmospheric pressure is about 10^{19} cm^{-3} . In liquids and solids the density of atoms is of order 10^{22} cm^{-3} . The density at the center of Bose-Einstein condensate is typically $10^{13}\text{-}10^{15}\text{ cm}^{-3}$ atoms. Therefore, in order to reach Bose-Einstein condensation in dilute alkali atoms, the temperature must be reached of order 10^{-5}

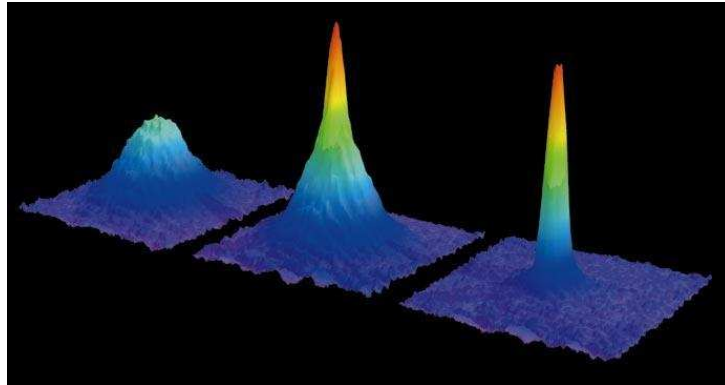


Figure 1.15: Observation of Bose-Einstein condensation by absorption imaging. The figure shows absorption vs. two spatial dimensions. From left to right the atomic distribution in the cloud is shown, when cooled to just above the transition point, after the condensate is formed, and after further evaporative cooling stabilizing an almost pure condensate. The total number of atoms at the phase transition was about 7×10^5 , and transition occurred at $T_c = 2 \mu\text{K}$ (adapted from [131]).

K or even less. In a typical experiment, the number of atoms is of order 10^6 while the radius of the cloud is about 10-100 μm (density $\approx 10^{14} \text{ cm}^{-3}$), and the transition temperature is of order $T_c \approx 1 \mu\text{K}$. Bose-Einstein condensation is usually obtained by combination of different laser cooling techniques and forced evaporative cooling [131, 135], as debated in the next Section.

1.6.2 Experimental technique

Alkali atoms are bosons, having odd atomic number Z and odd mass number A . The ground-state electronic structure of alkali atoms is simple, i. e. all electrons but one occupy closed shells, and the remaining electron is in s orbital in a higher shell. The total spin of an alkali atom is an integer consisting of the nuclear spin, which is a half-integer, and the electron spin, which is equal to $1/2$. Because of the s orbital electron, alkali atoms can be easily manipulated by employing a magneto-optical trap (MOT) [Fig. 1.16], which was used in the pioneering experiments on trapping ultracold alkali atoms [172, 133].

Usually, in the experiment a beam of alkali atoms emerged from an oven at a temperature of about 600 K, corresponding to a speed of $\approx 800 \text{ m s}^{-1}$. The beam is then transmitted through a so-called Zeeman slower, in which the velocity of atoms in the beam is significantly reduced, to about 30 m

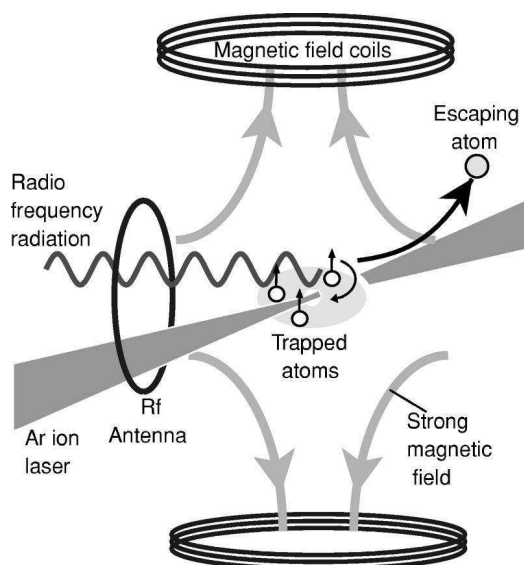


Figure 1.16: Experimental setup which was used for cooling sodium atoms to achieve Bose-Einstein condensation by Ketterle group at MIT in 1995 (adapted from [131]).

s^{-1} . This velocity corresponds to 1 K. After passing the Zeeman slower, atoms are slow enough to be trapped in MOT. The scheme of the magneto-optical trap which was used at MIT is shown in Fig. 1.16. In MOT atoms are trapped by a strong magnetic field, generated by two coils. In the center of MOT the magnetic field vanishes causing the atoms to flip the spin and further escape. Therefore, the atoms should be held away from the center of the trap and a strong argon ion laser beam is used for that purpose. The final step of achieving Bose-Einstein condensation is evaporative cooling to remove relatively energetic atoms from the cloud. The evaporative cooling is controlled by radiofrequency radiation from an antenna by selectively flipping the spins of the most energetic atoms. The remaining atoms are cooled down further by collisions among themselves [131].

1.6.3 Gross-Pitaevskii theory for a Bose-Einstein condensate

In the previous two Subsections, we considered preconditioning for Bose-Einstein condensation (BEC), and the experimental methods to achieve Bose gases. In this Subsection, we consider the mean-field theory for BEC.

The theory for the Bose-Einstein condensation is based on the Gross-

Pitaevskii equation [136, 137, 138], which describes the zero-temperature evolution of the nonuniform Bose gas. In fact, Pitaevskii [136] and Gross [137, 138] independently considered a nonuniform dilute Bose gas, generalizing Bogoliubov's treatment of a uniform Bose gas at zero temperature [139] to comprise nonuniform states, particularly quantized vortices.

In the fully condensed state all bosons occupy the same single-particle state $\phi(\mathbf{r})$. As a result one can write the N -particle wave function as

$$\Psi(\mathbf{r}_1, \mathbf{r}_2, \dots, \mathbf{r}_N) = \prod_{i=1}^N \phi(\mathbf{r}_i), \quad (1.78)$$

which is symmetric under interchange of the coordinates of any two particles. The single-particle wave function $\phi(\mathbf{r}_i)$ is normalized as

$$\int d\mathbf{r} |\phi(\mathbf{r})|^2 = 1. \quad (1.79)$$

Since we consider a dilute Bose gas, only binary collisions are relevant at low energies. Then we can approximate the effective interaction between two atoms by a short-range interaction $\approx g\delta(\mathbf{r} - \mathbf{r}')$, where \mathbf{r} and \mathbf{r}' are positions of two particles, and g is a coupling constant with the dimension of energy \times volume. g depends on the s -wave scattering length a as $g = 4\pi\hbar^2 a/m$ [135, 140]. For example, the scattering length for ^{23}Na is $a = 2.75$ nm [141], for ^{87}Rb is $a = 5.77$ nm [142], and for ^7Li is $a = -1.45$ nm [143]. By means of the scattering length a we can introduce another characteristic of dilute gases such as $\bar{n}|a|^3 \ll 1$, where \bar{n} is the mean particle density.

In a uniform bulk system, the scattering length must be positive (corresponds to a repulsive interaction between atoms) to prevent an instability leading to a collapse. However, a Bose condensate in an external confining trap can remain stable even for $a < 0$ (corresponds to an attractive interaction between atoms) as long as the number of condensed atoms is below a critical value $N_{cr} \sim a_r/|a|$, where a_r is the oscillator length.

To investigate the energy of the condensed state, we adopt a mean-field approach assuming that the wave function is a symmetrized product of single-particle wave functions. This wave function does not contain the correlations produced by the interaction when two atoms are close to each other. The effects are taken into account in the effective interaction $g\delta(\mathbf{r} - \mathbf{r}')$. One can write the effective Hamiltonian as

$$H = \sum_{i=1}^N \left[\frac{\mathbf{p}_i^2}{2m} + V(\mathbf{r}_i) \right] + g \sum_{i < j} \delta(\mathbf{r}_i - \mathbf{r}_j), \quad (1.80)$$

where $V(\mathbf{r}_i)$ is the external potential. Then the energy of the state (1.78) is given by

$$E = N \int d\mathbf{r} \left[\frac{\hbar^2}{2m} |\nabla \phi(\mathbf{r})|^2 + V(\mathbf{r}) |\phi(\mathbf{r})|^2 + \frac{(N-1)}{2} g |\phi(\mathbf{r})|^4 \right]. \quad (1.81)$$

In the interaction term, $N(N-1)/2$ is the number of terms in the interaction energy, that is the number of ways of making pairs of bosons, times $\int d\mathbf{r} g |\phi(\mathbf{r})|^4$, the interaction energy of two particles in the state $\phi(\mathbf{r})$.

An essential feature of a dilute Bose gas at zero temperature is the existence of a order parameter $\psi(\mathbf{r})$ that characterizes the condensed state. One can introduce the order parameter for the uniform Bose gas of volume V as

$$\psi(\mathbf{r}) = N^{1/2} \phi(\mathbf{r}). \quad (1.82)$$

After inserting Eq. (1.82) in Eq. (1.81), the energy of the ground state modifies to

$$E(\psi) = \int d\mathbf{r} \left[\frac{\hbar^2}{2m} |\nabla \psi(\mathbf{r})|^2 + V(\mathbf{r}) |\psi(\mathbf{r})|^2 + \frac{1}{2} g |\psi(\mathbf{r})|^4 \right], \quad (1.83)$$

where we neglected the term of order $1/N$ assuming that $N \gg 1$. In order to find the solution for $\psi(\mathbf{r})$, one has to minimize Eq. (1.83) with respect to $\psi^*(\mathbf{r})$ with the constraint that the total number of particles should be constant

$$N = \int d\mathbf{r} |\psi(\mathbf{r})|^2, \quad (1.84)$$

where $n(\mathbf{r}) = |\psi(\mathbf{r})|^2$ is the particle density. The constraint can be applied in the form $\delta E - \mu \delta N$, where μ is the Lagrange multiplier that ensures the conservation of the particle number. Then the minimization of Eq. (1.83) with the condition (1.84) leads to the equation:

$$-\frac{\hbar^2}{2m} \nabla^2 \psi(\mathbf{r}) + V(\mathbf{r}) \psi(\mathbf{r}) + g |\psi(\mathbf{r})|^2 \psi(\mathbf{r}) - \mu \psi(\mathbf{r}) = 0. \quad (1.85)$$

The variation of the kinetic energy term was done by performing an integration in parts by using the Gauss-Ostrogradskii's theorem $\int dV \nabla \psi \nabla \delta \psi = \oint \delta \psi \nabla \psi dS - \int dV (\nabla \nabla \psi) \delta \psi$. The surface integral vanishes for systems of finite extent or when periodic boundary conditions are imposed [135]. Eq. (1.85) is the time-independent Gross-Pitaevskii equation (GP) [136, 137, 138]. It has the form of the Schrödinger equation in which the potential

acting on particles is the sum of the external potential $V(\mathbf{r})$ and a non-linear term $g|\psi(\mathbf{r})|^2$ that takes into account the mean field produced by the other bosons. The eigenvalue of Eq. (1.83) is not the energy per particle, as it is for the Schrödinger equation, but the chemical potential [140, 135].

Let us consider harmonically trapped condensate with the external potential being the anisotropic three-dimensional harmonic oscillator

$$V(x, y, z) = \frac{1}{2}m(\omega_x^2 x^2 + \omega_y^2 y^2 + \omega_z^2 z^2), \quad (1.86)$$

where ω_i ($i = x, y, z$) are the three oscillator frequencies, which can differ from each other in general. Then, when there is no interparticle interaction, the third term in Eq. (1.85) can be omitted, the solution of Eq. (1.85) has the form [135]:

$$\phi_0(\mathbf{r}) = \frac{1}{\pi^{3/4}(a_x a_y a_z)^{1/2}} e^{-x^2/2a_x^2} e^{-y^2/2a_y^2} e^{-z^2/2a_z^2}, \quad (1.87)$$

where a_i ($i = x, y, z$) are the oscillator lengths given by $a_i^2 = \hbar/m\omega_i$. In that case, the density distribution $n(\mathbf{r}) = N\phi_0(\mathbf{r})^2$ is Gaussian.

When a large number of particles is trapped in the cloud (starting with $\approx 10^3$ atoms in the cloud), then the kinetic energy term can be neglected in Eq. (1.85), and one arrives at the equation:

$$(V(r) + g|\psi(\mathbf{r})|^2)\psi(\mathbf{r}) = \mu\psi(\mathbf{r}). \quad (1.88)$$

Eq. (1.88) acquires the solution:

$$n(\mathbf{r}) = |\psi(\mathbf{r})|^2 = (\mu - V(\mathbf{r}))/g. \quad (1.89)$$

Eq. (1.89) gives the condition for the cloud which exists when the right-hand side of Eq. (1.89) is positive, and $\psi(\mathbf{r}) = 0$ otherwise. The boundary of the cloud is therefore given by $V(\mathbf{r}) = \mu$. The physical content of this approximation is that the energy to add a particle at any point in the cloud is the same everywhere. This energy is given by the sum of the external potential $V(\mathbf{r})$ and an interaction contribution $gn(\mathbf{r})$ which is the chemical potential of a uniform gas having density equal to the local density $n(\mathbf{r})$. Since this approximation is reminiscent of the Thomas-Fermi approximation in the theory of atoms, it is referred to by the same name.

One more term can be added to Eq. (1.85) - angular momentum energy which corresponds to the rotation of the condensate along the z -axis. Then the solution of Eq. (1.85) will represent topological defects such as vortices.

1.6.4 Multi-component Bose-Einstein condensates

Bosons of a single component Bose-Einstein condensate occupy a single quantum state. What happens if two or more quantum states are occupied simultaneously? In such case, one deals with a multi-component Bose-Einstein condensation. The simplest example of such a multi-component BEC is a mixture of two different kind of bosons, for example two isotopes of the same element, or two different atoms. Since alkali atoms have a spin, it allows to make mixtures of the same isotope but in different internal spin states.

The first multi-component condensate was composed of two hyperfine states of ^{87}Rb , created by the group led by Wieman and Cornell at JILA in 1997 [9]. ^{87}Rb has nuclear spin $I = 3/2$, which combines with the single valence electron spin ($S = 1/2$). The total spin is the quantum number $F = I \pm 1/2$ corresponding to the total angular momentum operator $\mathbf{F} = \mathbf{I} + \mathbf{J}$, where \mathbf{I} and \mathbf{J} are the operators of the nuclear spin and the electronic angular momentum, respectively in units of \hbar [135]. In the common notation a hyperfine spin state is $|F, m_F\rangle$, meaning that in the hyperfine ground spin states of a given alkali atom $J = S = 1/2$ and I are fixed, while F and m_F can take values $|I - J| \leq F \leq I + J$ and $-F \leq m_F \leq F$, respectively, in integer steps. ^{87}Rb has two manifolds, a lower one with $F = 1$ and an upper one with $F = 2$. To trap ^{87}Rb atoms, one needs weak-field states as $|1, -1\rangle$, $|2, 1\rangle$ and $|2, 2\rangle$, which are only stable states. In the experiment a state $|1, -1\rangle$ was cooled evaporatively and by the intercomponent interaction the state $|2, 2\rangle$ was cooled through sympathetic cooling.

Following the creation of binary condensate in ^{87}Rb , the group of Ketterle at MIT confined a BEC of sodium atoms in all spin projections of the $F = 1$ hyperfine level [144]. Up to now two-component BECs were created of two hyperfine spin states of atoms of the same species [10, 145, 146, 147, 148, 149, 150] and two-component BECs composed of two different kind of atoms [151, 152, 153, 154, 155, 156]. Mixtures of hyperfine spin states of the same isotope differ from mixtures of distinct isotopes, because atoms can undergo transitions between hyperfine states, while transitions that convert one isotope into another may be neglected [135].

Multi-component BEC is a favorable platform to study emergent novel physics in mixtures of generally different superfluids. An important feature of superfluids is their ability to support vortices. Multi-component BEC offers a rich variety of topological defects such as vortex lattices [15, 157, 16], vortex sheets [17] and skyrmions [18, 158, 159]. We shall discuss some of these topological defects in more detail in Section 1.7. In the following Subsection we outline the Gross-Pitaevskii formalism for the multicomponent BEC.

1.6.5 Theory for multicomponent Bose-Einstein condensates

Having derived the Gross-Pitaevskii theory for single-component BECs, we now generalize the Gross-Pitaevskii theory for multicomponent Bose-Einstein condensates. We start the consideration of theory for a multi-component BEC with a two-component case.

The generalization of the wave function given by Eq. (1.78) to two components (with N_1 and N_2 particles respectively) is:

$$\Psi(\mathbf{r}_1, \mathbf{r}_2, \dots, \mathbf{r}_{N_1}; \mathbf{r}'_1, \mathbf{r}'_2, \dots, \mathbf{r}'_{N_2}) = \prod_{i=1}^{N_1} \phi_1(\mathbf{r}_i) \prod_{j=1}^{N_2} \phi_2(\mathbf{r}'_j), \quad (1.90)$$

where the bosons of component 1 are denoted by \mathbf{r}_i and of component 2 by \mathbf{r}'_j . The corresponding single-particle wave functions are ϕ_1 and ϕ_2 , respectively. The atomic interactions generally depend on the species, and we denote the effective intercomponent interaction by g_{ij} . For a uniform system of volume V , one can write the interaction energy as

$$E = \frac{N_1(N_1 - 1)g_{11}}{2V} + \frac{N_1N_2g_{12}}{V} + \frac{N_2(N_2 - 1)g_{22}}{2V}. \quad (1.91)$$

In the zero-temperature mean-field approximation, one can introduce an order parameter associated with each component as $\Psi_j(\mathbf{r}) = |\Psi_j|e^{i\varphi_j}$. Then the free energy of the two-component BEC can be written as

$$E_M(\mathbf{r}) = \int d\mathbf{r} \left\{ \sum_{j=1}^2 \left(\frac{\hbar^2}{2m_j} |\nabla \Psi_j|^2 + V_j(\mathbf{r}) |\Psi_j|^2 + \frac{1}{2} g_{jj} |\Psi_j|^4 \right) + g_{12} |\Psi_1|^2 |\Psi_2|^2 \right\}, \quad (1.92)$$

where m_j is the mass of the bosons in component j , and as in the case of the single component BEC we neglected the terms of order $1/N_j$, assuming $N_j \gg 1$. The first term in Eq. (1.92) is the kinetic energy of component j , the second term is the trapping potential experienced by component j , the third term is the self-interaction energy of component j with the interaction parameter g_{jj} , and the last term is the intercomponent interaction energy between components 1 and 2 with the interaction strength g_{12} . The interaction parameter g_{jj} depends on the s -wave scattering length a_{jj} as $g_{jj} = 4\pi\hbar^2 a_{jj}/m_j$, while the intercomponent interaction parameter is $g_{12} = 4\pi\hbar^2 a_{12}/m_{12}$, with $m_{12} = m_1 m_2 / (m_1 + m_2)$ being the reduced mass.

The intercomponent interaction can be either attractive or repulsive between the components depending on the sign of the scattering length a_{12} which can be manipulated by using the Feshbach resonance [160]. However, one can distinguish two regimes for two-component BECs. If $g_{12}^2 > g_1 g_2$, then the two components are immiscible and separate into nonoverlapping phases [161]. Otherwise, when $g_{12}^2 < g_1 g_2$ the two components form interpenetrating BECs [161]. Interestingly, in the experiment performed by Myatt at JILA [9], the interaction parameters approximately satisfied $g_{12}^2 \lesssim g_1 g_2$ [162], implying that two such uniform BECs would overlap. However, the two trapped condensates were spatially separated due to the differences in the two trapping potentials and interaction parameters [9]. Usually, in order to avoid phase separation in an experiment, two hyperfine spin states are used so that the difference in the angular momentum is $\Delta m = 2$ (for example, states $|1, -1\rangle$ and $|2, 1\rangle$) [161].

The order parameters are normalized such that

$$\int |\psi_j(\mathbf{r})|^2 d\mathbf{r} = N_j, \quad (1.93)$$

where N_j is the total number of particle in component j .

Minimizing Eq. (1.92) with respect to Ψ_1^* and Ψ_2^* leads to two coupled time-independent GP equations:

$$\left(-\frac{\hbar^2}{2m_j} \nabla^2 + V_j(\mathbf{r}) - \mu_j + g_{jj} |\Psi_j|^2 + g_{12} |\Psi_{3-j}|^2 \right) \Psi_j = 0, \quad (1.94)$$

where $j \in \{1, 2\}$ and μ_j is the chemical potential of component j being introduced as the Lagrange multiplier to ensure the particle number conservation in each component separately. These two coupled Gross-Pitaevskii equations describe the evolution of the two order parameters, embodying a rich variety of physics, and can be used to predict many features of two-component BECs, e.g. the dependence of ground-state wave functions on the nonlinear interactions, and the nature of exotic topological features, such as vortices, vortex lattices and skyrmions.

Generalization of Eqs. (1.92) and (1.94) to a more general case is straightforward and will be given in Chapter 4, Section 4.2 concerning the physics of a three-component coherently coupled BEC.

1.6.6 Dimensionless GP equations

In our study of multi-component BECs, we solved numerically the coupled Gross-Pitaevskii equations (1.94). Before we present the numerical method

used to solve Eqs. (1.94), we need to recast the equations to a dimensionless form. We choose the units of the harmonic oscillator of component 1, so that $\hbar\omega_1$ and $a_r = \sqrt{\hbar/m_1\omega_1}$ are the units of energy and length, respectively. The new wave functions $\Psi'_j = a_r\Psi_j/\sqrt{N_j}$ are normalized to unity. Then the two recast GP equations take the form:

$$\begin{aligned} \left(-\frac{1}{2}\nabla^2 + \frac{1}{2}r^2 + \frac{1}{2}\frac{\omega_{z,1}^2}{\omega_1^2}z^2 + g'_{11}|\Psi'_1|^2 + g'_{12}|\Psi'_2|^2 - \mu_1 \right) \Psi'_1 &= 0, \\ \left(-\frac{1}{2}\frac{m_1}{m_2}\nabla^2 + \frac{1}{2}\frac{m_2}{m_1}\frac{\omega_2^2}{\omega_1^2}r^2 + \frac{1}{2}\frac{m_2}{m_1}\frac{\omega_{z,2}^2}{\omega_1^2}z^2 + g'_{22}|\Psi'_2|^2 \right. \\ &\quad \left. + g'_{21}|\Psi'_1|^2 - \mu_2 \right) \Psi'_2 = 0, \end{aligned} \quad (1.95)$$

where $r^2 = x^2 + y^2$, and we assumed in Eq. (1.95) that the x - and y -components of the oscillator frequency of component j are equal to $\omega_{x,j} = \omega_{y,j} = \omega_j$. We consider a mass-imbalanced case with $m_1 \neq m_2$. When $N_1 \neq N_2$ the parameters in the recast equations are:

$$\begin{aligned} g'_{11} &= \frac{m_1 N_1 g_{11}}{\hbar^2}, & g'_{22} &= \frac{N_2}{N_1} \frac{g_{22}}{g_{11}} g'_{11}, \\ g'_{12} &= \frac{N_2}{N_1} \frac{g_{12}}{g_{11}} g'_{11}, & g'_{21} &= \frac{g_{12}}{g_{11}} g'_{11}. \end{aligned} \quad (1.96)$$

In the case of an anisotropic trapping potential with $\omega_z \gg \omega_x = \omega_y \equiv \omega_\perp$, the condensates will be pancake-shaped, and can effectively be described by a two-dimensional (2D) GP equations. The dependence of the z coordinate can be integrated out from Eq. (1.95) by employing an ansatz wave function $\Psi_j(x, y, z) = R_j(x, y)Z_j(z)$ [163, 164], where the functions $R_j(x, y)$ and $Z_j(z)$ are normalized to unity. After substituting the ansatz into Eq. (1.95) and multiplying it by Z_j^* , one can subsequently perform the integration over the z coordinate in the obtained equation. After the integration, we arrive at the following two-dimensional GP equations:

$$\begin{aligned} \left(-\frac{1}{2}\nabla_{2D}^2 + \frac{1}{2}r^2 - \mu_1 + E_{z,1} \right) R_1 + g'_{11}|R_1|^2 R_1 \int |Z_1(z)|^4 dz \\ + g'_{12}|R_2|^2 R_1 \int |Z_2(z)|^2 |Z_1(z)|^2 dz = 0, \\ \left(-\frac{1}{2}\frac{m_1}{m_2}\nabla_{2D}^2 + \frac{1}{2}\frac{m_2}{m_1}\frac{\omega_2^2}{\omega_1^2}r^2 - \mu_2 + E_{z,2} \right) R_2 + g'_{22}|R_2|^2 R_2 \int |Z_2(z)|^4 dz \\ + g'_{21}|R_1|^2 R_2 \int |Z_1(z)|^2 |Z_2(z)|^2 dz = 0, \end{aligned} \quad (1.97)$$

where we introduced the integrals

$$E_{z,j} = \int dz Z^*(z) \left(-\frac{1}{2} \frac{\partial^2}{\partial z^2} + \frac{1}{2} \frac{\omega_{z,j}^2}{\omega_1^2} \right) Z(z), \quad (1.98)$$

which can be incorporated into the chemical potential as $\mu_j^{2D} = \mu_j + E_{z,j}$. The function $Z_j(z)$ can be chosen as:

$$Z_j = \exp \left(-\frac{z^2}{2a_{z,j}^2} \right) \left(\pi a_{z,j}^2 \right)^{-1/4}, \quad (1.99)$$

where $a_{z,j} = \sqrt{\frac{\hbar}{m_j \omega_{z,j}}}$ is the z -component oscillator length. Inserting Eq. (1.99) and performing integration of the last two integrals in Eqs. (1.97) leads to the equations:

$$\begin{aligned} \left(-\frac{1}{2} \nabla_{2D}^2 + \frac{1}{2} r^2 - \mu_1^{2D} + g_{11}^{2D} |R_1|^2 + g_{12}^{2D} |R_2|^2 \right) R_1 &= 0, \\ \left(-\frac{1}{2} \frac{m_1}{m_2} \nabla_{2D}^2 + \frac{1}{2} \frac{m_2}{m_1} \frac{\omega_2^2}{\omega_1^2} r^2 - \mu_2^{2D} + g_{22}^{2D} |R_2|^2 + g_{21}^{2D} |R_1|^2 \right) R_2 &= 0, \end{aligned} \quad (1.100)$$

where we introduced $g_{jj}^{2D} = \frac{g'_{jj}}{a_{z,j} \sqrt{2\pi}}$, $g_{12}^{2D} = \frac{g'_{12}}{\sqrt{\pi}} (a_{z,1}^2 + a_{z,2}^2)^{-1/2}$ and

$$g_{21}^{2D} = \frac{g'_{21}}{\sqrt{\pi}} (a_{z,1}^2 + a_{z,2}^2)^{-1/2}.$$

It is convenient to replace the function R_j by Ψ_j and re-write the dimensionless 2D Gross-Pitaevskii equations as

$$\begin{aligned} \left(-\frac{1}{2} \nabla^2 + \frac{1}{2} r^2 + g_{11}^{2D} |\Psi_1|^2 + g_{12}^{2D} |\Psi_2|^2 - \mu_1 \right) \Psi_1 &= 0, \\ \left(-\frac{1}{2} \frac{m_1}{m_2} \nabla^2 + \frac{1}{2} \frac{m_2}{m_1} \frac{\omega_2^2}{\omega_1^2} r^2 + g_{22}^{2D} |\Psi_2|^2 + g_{21}^{2D} |\Psi_1|^2 - \mu_2 \right) \Psi_2 &= 0. \end{aligned} \quad (1.101)$$

1.6.7 Introduction of link-variables to the GP equations

In order to introduce the discretization scheme which was used in the numerical calculations, we consider a rotating two-component Bose-Einstein condensate by introducing the angular momentum energy $-\Omega \Psi_j^* L_z \Psi_j$ in each equation (1.101), where $L_z = -i\hbar[\mathbf{e}_z \cdot (\mathbf{r} \times \nabla)]$ is the z component of the angular momentum operator in the position representation. Both condensates

are subjected to rotate along the z -axis with the same rotating velocity Ω . z coordinate was integrated out in the angular momentum energy, and energy is scaled in units of $\hbar\omega_1$. Then the equations (1.101) modify to:

$$\begin{aligned} & \left(-\frac{1}{2}\nabla^2 + \frac{1}{2}r^2 - \Omega L_z + g_{11}^{2D}|\Psi_1|^2 + g_{12}^{2D}|\Psi_2|^2 - \mu_1 \right) \Psi_1 = 0, \\ & \left(-\frac{1}{2}\frac{m_1}{m_2}\nabla^2 + \frac{1}{2}\frac{m_2}{m_1}\frac{\omega_2^2}{\omega_1^2}r^2 - \Omega L_z + g_{22}^{2D}|\Psi_2|^2 + g_{21}^{2D}|\Psi_1|^2 - \mu_2 \right) \Psi_2 = 0. \end{aligned} \quad (1.102)$$

The kinetic energy can be combined with the trap potential and with the angular momentum energy in Eq. (1.102) leading to further recast equations:

$$\left(\frac{1}{2}\left(\frac{\nabla}{i} - \mathbf{A}\right)^2 + \frac{1}{2}\left(1 - \frac{\Omega^2}{\omega_1^2}\right)r^2 + g_{11}^{2D}|\Psi_1|^2 + g_{12}^{2D}|\Psi_2|^2 - \mu_1 \right) \Psi_1 = 0, \quad (1.103)$$

$$\begin{aligned} & \left(\frac{1}{2}\left(\frac{\nabla}{i} - \mathbf{A}'\right)^2 + \frac{1}{2}\frac{m_2^2}{m_1^2}\left(\frac{\omega_2^2}{\omega_1^2} - \frac{\Omega^2}{\omega_1^2}\right)r^2 + g_{22}^{2D}\frac{m_2}{m_1}|\Psi_2|^2 \right. \\ & \quad \left. + g_{21}^{2D}\frac{m_2}{m_1}|\Psi_1|^2 - \mu_2\frac{m_2}{m_1} \right) \Psi_2 = 0, \end{aligned} \quad (1.104)$$

where $\mathbf{A} = (y\Omega, -x\Omega)$ and $\mathbf{A}' = (y(m_1/m_2)\Omega, -x(m_1/m_2)\Omega)$. From newly recast Eqs. (1.103) and (1.104), conditions follow for the trapping potential of component 1 and 2, respectively as $\left(1 - \frac{\Omega^2}{\omega_1^2}\right) > 0$ and $\left(\frac{\omega_2^2}{\omega_1^2} - \frac{\Omega^2}{\omega_1^2}\right) > 0$, otherwise the confinement is lost.

We can treat vectors \mathbf{A} and \mathbf{A}' as effective gauge fields and introduce link variables

$$U_{\alpha=x,y}^{m,n} = \exp \left[-i \int_{\mathbf{r}_m}^{\mathbf{r}_n} A_\alpha d\alpha \right], \quad (1.105)$$

for component 1 and

$$U_{\alpha=x,y}^{\prime m,n} = \exp \left[-i \int_{\mathbf{r}_m}^{\mathbf{r}_n} A'_\alpha d\alpha \right], \quad (1.106)$$

for component 2. The link variables given by Eqs. (1.105) and (1.106) connect the m point of the discretized grid with the nearest n point of the

same grid separated by the mesh $d\alpha$ of the grid on which the computation is done. The link-variable method is used in order to provide fast convergence of the solver at a high magnetic field and to preserve the gauge invariance under discretization [165, 166, 167]. In the case of Bose-Einstein condensation the analogue of the high magnetic field is the fast rotation. Therefore, it is convenient to introduce the link-variables to solve numerically the GP equations thus facilitating the fast convergence of our solver.

In our calculation, the whole system is mapped on a square grid with the uniform mesh h , where $h = \frac{\text{computation area}}{\text{grid size}}$. Then first term in Eq. (1.103) can be discretized as

$$\begin{aligned} \left(\frac{\nabla_\alpha}{i} - A_\alpha\right)^2 \Psi_{m,k} &= -\nabla_\alpha^2 \Psi_{m,k} + i\nabla_\alpha(A_\alpha \Psi_{m,k}) + A_\alpha^2 \Psi_{m,k} \\ &+ iA_\alpha \nabla_\alpha \Psi_{m,k} = \frac{1}{U_\alpha^{m,n}} \left(-2iA_\alpha U_\alpha^{m,n} \nabla_\alpha \Psi_{m,k} \right. \\ &\left. -iU_\alpha^{m,n} \Psi_{m,k} (\nabla_\alpha A_\alpha - iA_\alpha^2) + U_\alpha^{m,n} \nabla_\alpha^2 \Psi_{m,k} \right), \end{aligned} \quad (1.107)$$

where the index (m, n) denotes the lattice point of interest. Substitution of equations $\nabla_\alpha U_\alpha^{m,n} = -iA_\alpha U_\alpha^{m,n}$ and $\nabla_\alpha^2 U_\alpha^{m,n} = -iU_\alpha^{m,n} (\nabla_\alpha A_\alpha - iA_\alpha^2)$ into Eq. (1.107) leads to:

$$\left(\frac{\nabla_\alpha}{i} - A_\alpha\right)^2 \Psi_{m,k} = \frac{1}{U_\alpha^{m,n}} \nabla_\alpha (\nabla_\alpha (U_\alpha^{m,n} \Psi_{m,k})). \quad (1.108)$$

If $\alpha = x$, one obtains:

$$\begin{aligned} \left(\frac{\nabla_x}{i} - A_x\right)^2 \Psi_{m,k} &= \frac{1}{U_x^{m,n}} \frac{1}{h} \left(\frac{U_x^{m+1,n} \Psi_{m+1,k} - U_x^{m,n} \Psi_{m,k}}{h} \right. \\ &\quad \left. - \frac{U_x^{m,n} \Psi_{m,k} - U_x^{m-1,n} \Psi_{m-1,k}}{h} \right) \\ &= \frac{U_x^{m+1,n} \Psi_{m+1,k} - 2\Psi_{m,k} + U_x^{m-1,n} \Psi_{m-1,k}}{h^2}, \end{aligned} \quad (1.109)$$

where we assumed that $\frac{U_x^{m+1,n} \Psi_{m+1,k}}{U_x^{m,n}} \approx U_x^{m+1,n} \Psi_{m+1,k}$. In analogy, we can do the same transformation for $\alpha = y$.

The discretized GP equation for component 1 can be now written in full

as:

$$\begin{aligned} & \frac{U_x^{i-1,i}\Psi_1^{i-1,j}}{h^2} + \frac{U_x^{i+1,i}\Psi_1^{i+1,j}}{h^2} + \frac{U_y^{j-1,j}\Psi_1^{i,j-1}}{h^2} + \frac{U_y^{j+1,j}\Psi_1^{i,j+1}}{h^2} \\ &= \left(\frac{4}{h^2} - \frac{1}{2} \left(1 - \frac{\Omega^2}{\omega_1^2} \right) r^2 - g_{11}^{2D} |\Psi_1|^2 - g_{12}^{2D} |\Psi_2|^2 + \mu_1 \right) \Psi_1^{i,j}. \end{aligned} \quad (1.110)$$

For the GP equation of the second component similar discretization scheme leads:

$$\begin{aligned} & \frac{U_x^{i-1,i}\Psi_2^{i-1,j}}{h^2} + \frac{U_x^{i+1,i}\Psi_2^{i+1,j}}{h^2} + \frac{U_y^{j-1,j}\Psi_2^{i,j-1}}{h^2} + \frac{U_y^{j+1,j}\Psi_2^{i,j+1}}{h^2} \\ &= \left(\frac{4}{h^2} - \frac{1}{2} \frac{m_2^2}{m_1^2} \left(\frac{\omega_2^2}{\omega_1^2} - \frac{\Omega^2}{\omega_1^2} \right) r^2 - g_{22}^{2D} \frac{m_2}{m_1} |\Psi_2|^2 - g_{21}^{2D} \frac{m_2}{m_1} |\Psi_1|^2 + \mu_2 \right) \Psi_2^{i,j}. \end{aligned} \quad (1.111)$$

1.6.8 Numerical simulation of the coupled GP equations

In this Subsection we describe the numerical method which we used to solve the discretized GP equations (1.110) and (1.111). In the previous Subsection, we introduced link-variables into the coupled GP equations to ensure the fast convergence. The numerical method is based on Euler time steps being performed to let the solution relax to a stable state. The taken boundary condition was $\Psi_j = 0$ at the boundary of the computation area, and each Ψ_j has to be normalized to unity separately ($j \in \{1, 2\}$ for a two component case). Therefore, after every time step each chemical potential μ_j has to be adapted to ensure the proper normalization of corresponding Ψ_j .

To find the chemical potential μ_j that features Ψ_j normalized to unity in the case of two coupled Gross-Pitaevskii equations, six quantities are relevant for the algorithm: (1) $N_j(t) = \int dx dy |\Psi_j(t)|^2$, the current normalization at time t of Ψ_j , (2) $\delta N_j(t) = N_j(t) - N_j(t - \delta t)$, the change of the normalization $N_j(t)$ over the last time step δt , and (3) $r_j(t) = |\delta N_j(t)/(N_j(t) - 1)|$ the rate at which the normalization N_j approaches 1. The rate r_j we want to keep lower than a threshold rate r_t to avoid overshooting the correct μ_j . r_t is optionally chosen to ensure the minimization of the convergence time. In every time step, μ_j is adjusted by an amount of the order of $\delta \mu_j = |N_j(t) - 1|$. As one can see from the GP equations, increasing (decreasing) μ_j leads to increase (decrease) of N_j .

Algorithm for solving the coupled GP equations

```

1: procedure SolveCoupledGP
2:   repeat
3:      $\psi_1 \leftarrow \psi_1 + \delta t \cdot \text{GP}_1(\psi_1, \psi_2, \mu_1)$             $\triangleright$  Do one (or more) time step(s)
        $\psi_2 \leftarrow \psi_2 + \delta t \cdot \text{GP}_2(\psi_2, \psi_1, \mu_2)$ 
4:      $N_j \leftarrow \int dx dy |\psi_j|^2$                                 $\triangleright$  Compute the normalization
5:      $\delta N_j \leftarrow N_j - N_j^{prev}$ 
6:      $\delta \mu_j \leftarrow (N_j - 1)$ 
7:      $r_j \leftarrow |\delta N_j / \delta \mu_j|$ 
8:     if  $\delta N_j \cdot \delta \mu_j < 0$  then                                $\triangleright$  If  $N_j$  evolves in the right direction
9:       if  $r_j < r_t$  then                                          $\triangleright$  If convergence rate is slow
10:         $\mu_j \leftarrow \mu_j - \delta \mu_j$                              $\triangleright$  Speed up the change of  $N_j$ 
11:       else                                                          $\triangleright$  Convergence rate is too fast
12:         $\mu_j \leftarrow \mu_j + \frac{1}{2} \delta \mu_j$                      $\triangleright$  Slow down the change of  $N_j$ 
13:       end if
14:     else                                                          $\triangleright$   $N_j$  evolves in the wrong direction
15:        $\mu_j \leftarrow \mu_j - \delta \mu_j$                              $\triangleright$  Change  $\mu_j$  to counteract this
16:     end if
17:      $N_j^{prev} \leftarrow N_j$ 
18:   until  $|\text{GP}_1(\psi_1, \psi_2, \mu_1) / \psi_1| < e_\psi$             $|N_1 - 1| < e_N$ 
       and  $|\text{GP}_2(\psi_2, \psi_1, \mu_2) / \psi_2| < e_\psi$             $|N_2 - 1| < e_N$ 
19: end procedure

```

Table 1.1: The algorithm used in the numerical computation of the coupled GP equations (1.110) and (1.111).

To outline the algorithm, we begin with assumption of initially high normalization $N_j > 1$. Then two scenarios can occur: either the normalization is decreasing, as it should, or it is increasing. In the latter case the chemical potential μ_j should be lowered by an amount $\delta \mu_j$. In the former case one should avoid, or at least counteract, possible overshooting the solution. One can do the latter by following the rate r_j : when $r_j > r_t$, the solver approaches $N_j = 1$ too fast. Therefore, one needs precautionary measure to decrease μ_j by $\delta \mu_j / 2$. When $r < r_t$, we will speed up the rate by increasing μ_j by $\delta \mu_j$. The case of a too low normalization ($N_j < 1$) is analogous, only the signs in front of $\delta \mu_j$ are reversed. We compute Ψ_j and μ_j self-consistently until both quantities are below a predefined error threshold. At that, Ψ_1 and Ψ_2 are updated simultaneously in the same loop. The pseudocode is depicted in Table 1.1.

1.7 Skyrmions in multi-component systems

Superfluidity, superconductivity and Bose-Einstein condensation are examples of systems with quantum phase coherence. On the microscopic scale this coherence is manifested through existence of quantized vortices, which are localized phase singularities with integer topological charge. These topological defects are readily observed in liquid helium [168, 169, 170], in superconductors [85, 171], and in dilute atomic gases BEC [10, 172]. The occurrence of quantized vortices in superfluids has been the focus of fundamental theoretical [173, 174, 175, 85, 140] and experimental work [176, 177, 170, 10]. Vortex-like excitations exist even in the Earth's atmosphere [140], in superfluid hadronic matter (neutron stars) [140], and in rotating nuclei [140].

Recently, multi-band superconductors and multi-component BECs have been demonstrated to exhibit another kind of topological defect termed skyrmion [178, 179], which was predicted in early 50s in nuclear physics [180, 181, 182, 183]. Search for the skyrmions in multi-component BECs offers an advantage to study their physical behaviour in much greater detail, because this kind of a multi-component system can be easily created, manipulated, and tuned, enabling direct comparison between theory and experiment.

This Section gives an outline of main topological excitations such as vortices and skyrmions which will be used later in the presentation of the main research results.

1.7.1 Vortices

Studying the superconductors of type II with the dimensionless Ginzburg-Landau parameter $\kappa > 1/\sqrt{2}$, Abrikosov was first to derive that the magnetic field would penetrate the superconducting sample in forms of separate single flux quantum filaments (or vortex lines) [85]. He noticed that the resulting pattern would be similar to one arising in vortex matter in superfluid helium II, proposed earlier by Onsager [173] and Feynman [175]. Analyzing the behavior of the order parameter in the neighborhood of the vortex cores at the field close to the upper critical field H_{c2} , Abrikosov found that the order parameter Ψ vanishes in the vortex core, while the field becomes maximal there, and the phase θ of Ψ changes by 2π when encircling the vortex. He found that a single filament will carry exactly one quantum of flux

$$\Phi_0 = \frac{hc}{2e} = 2.07 \times 10^{-7} \text{ G} \cdot \text{cm}^2, \quad (1.112)$$

where h is Planck's constant, c is the speed of light and e is the electron charge. Although Abrikosov initially predicted that vortices would form a

square lattice, it was soon realized that the triangular vortex lattice has lower free energy.

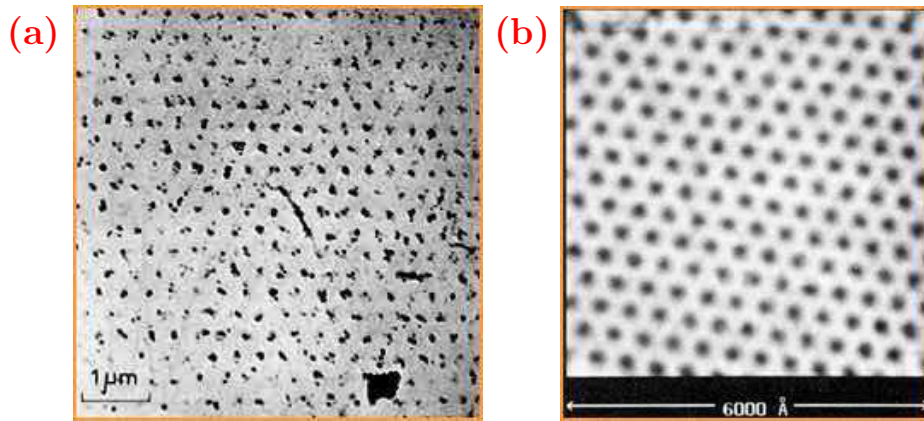


Figure 1.17: (a) First triangular vortex lattice observation in Pb at $T = 1.1$ K by using Bitter decoration technique (adapted from [176]); (b) Abrikosov flux lattice in NbSe₂ at $T = 1.8$ K measured by STM (adapted from [184]).

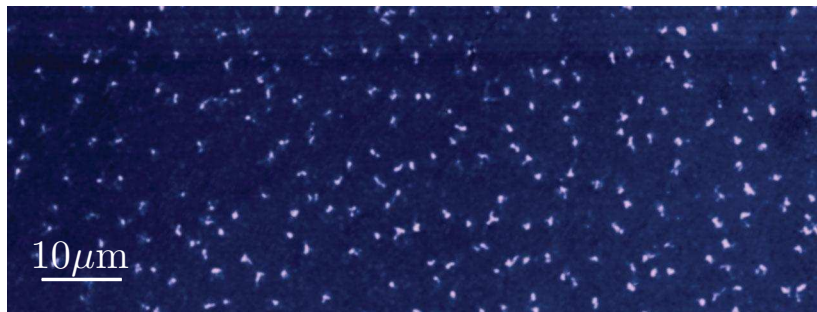


Figure 1.18: Unusual vortex pattern observed in MgB₂ at $T = 4.2$ K. The density of vortices in the decoration experiment represents the internal field (adapted from [1]).

The first direct observation of Abrikosov lattice was on samples of lead (shown in Fig. 1.17(a)) and niobium by employing magnetic decoration technique by Essmann and Träuble in 1967 [176]. Subsequent experiments confirmed that magnetic field penetrates the superconducting materials of type II as singly quantized vortices forming the triangular lattice [177, 184]. Singly quantized vortices were also observed in HTS superconductors [185, 186] and in films [187, 188]. Unusual vortex pattern, disobeying a particular lattice,

was recently observed in the two-gap superconductor MgB_2 [1], shown in Fig. 1.18. This is one of the first manifestations of novel physics in multi-component superconductors.

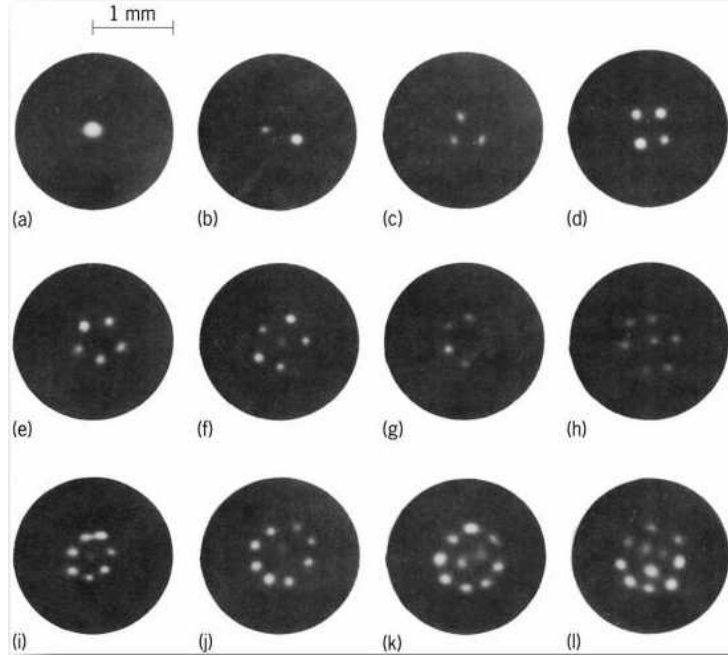


Figure 1.19: Photographs of stable vortex arrays in the rotating helium II. The pictures are placed in the order of the angular velocity applied to the sample: (a) 0.30 s^{-1} ; (b) 0.30 s^{-1} ; (c) 0.40 s^{-1} ; (d) 0.37 s^{-1} ; (e) 0.45 s^{-1} ; (f) 0.47 s^{-1} ; (g) 0.47 s^{-1} ; (h) 0.45 s^{-1} ; (i) 0.86 s^{-1} ; (j) 0.55 s^{-1} ; (k) 0.58 s^{-1} ; (l) 0.59 s^{-1} (adapted from [170]).

In the context of superfluid ^4He , Onsager and Feynman proposed independently that when superfluid is rotated, the circulation will be quantized in the form of whirlpools [173, 174, 175]. Indeed, if we consider a rotating condensate with which we can associate a complex-valued order parameter $\Psi = |\psi|e^{i\varphi}$ (where $|\psi|$ is the amplitude, and φ is the phase), then we can define the velocity of the condensate as the gradient of a scalar

$$\mathbf{v} = \frac{\hbar}{m} \nabla \varphi, \quad (1.113)$$

where m is the particle mass. Applying the operation circulation to this gradient yields that

$$\nabla \times \mathbf{v} = 0, \quad (1.114)$$

i. e. the velocity field of the superfluid is irrotational, unless the phase of the order parameter has a singularity. Superfluid supports the rotation only in these singularities. From the single-valuedness of the order parameter it follows that the change in the phase of the order parameter around a closed contour must be a multiple of 2π

$$\Delta\varphi = \oint \nabla\varphi \cdot d\mathbf{l} = 2\pi l, \quad (1.115)$$

where l is an integer. Then the circulation of the superfluid velocity around a closed contour is given by

$$\oint \mathbf{v} \cdot d\mathbf{l} = \frac{\hbar}{m} 2\pi l = l \frac{h}{m}, \quad (1.116)$$

demonstrating that the circulation of the superfluid velocity is quantized in units of h/m . These whirlpools were termed vortices. The order parameter drops to zero inside of the vortex, while the phase changes by 2π around it.

The first experimental vortex imaging in superfluids was performed in the rotating helium II in 1979 by Yarmchuk, Gordon and Packard [170] [shown in Fig. 1.19]. Shortly after Bose-Einstein condensation was realized experimentally in trapped dilute alkali atoms, the first experiment on vortex observation in BEC was performed [10]. Since then plenty of vortex experiments in the trapped dilute BECs were implemented, providing important information on the coherence and superfluid properties of dilute atomic gases. An exhaustive list of experiments on vortices in BECs is given in Ref. [172].

1.7.2 Skyrmions

Vortices in superfluids, BECs and superconductors are topological defects and considered to be manifestation of quantum phase coherence on microscopic length scales. They are supported in both single component BECs and superconductors as well as in multi-component BECs and multi-band superconductors. However, multi-component quantum systems differ from single component counterparts by exhibiting dependence on the phase-difference between the condensates, leading to nontrivial topological defects such as skyrmions [180].

Skyrmion was first introduced by a British theorist Skyrme [180, 181, 182, 183, 190, 191, 192] representing an extended baryon, being considered as a topological soliton created from bosons but exhibiting fermion features. While solving the sine-Gordon equation for a field with components $\phi_0 = \cos\theta$ and $\phi_1 = \sin\theta$

$$\partial_{xx}^2 \theta - \partial_{tt}^2 \theta = \varkappa^2 \sin\theta, \quad (1.117)$$

where θ is angular variable and \varkappa is an inverse length, Skyrme found that this equation has three solutions a 2π -kink, a 4π -kink, and a breather [190]. These solutions were already known by that time but Skyrme was not aware of the existence of corresponding works [193]. He was able to show that solitons of the sine-Gordon equation arising from the bosonic field model, are in fact fermions. Skyrme also showed that these solitonic solutions possess conserved current with components $j^0 = \frac{1}{2\pi}\partial_x\theta$ and $j^1 = -\frac{1}{2\pi}\partial_t\theta$. The integral of the component j^0 of the conserved current

$$Q_{1D} = \int j^0 dx = \frac{1}{2\pi} \int \partial_x \theta = \frac{1}{2\pi} (\theta(\infty, t) - \theta(-\infty, t)), \quad (1.118)$$

he termed *topological charge* (or topological index). The generalization of the topological index to the three spatial dimensions acquires the form [194]:

$$Q_{3D} = \frac{1}{24\pi^2} \epsilon_{\alpha\beta\gamma} \int d^3x \operatorname{tr}(U^\dagger \partial_\alpha U \partial_\beta U^\dagger \partial_\gamma U), \quad (1.119)$$

where $\epsilon_{\alpha\beta\gamma}$ is the 3-component Levi-Civita tensor and U is an $SU(2)$ -valued field. The minimal energy solutions for each Q_{3D} are called skyrmions. Skyrmions in their original sense are smooth, topologically stable extremal field configurations which are trivial at spatial infinity and have a finite energy. Moreover, skyrmions are characterized by a non-zero and integer-valued topological charge Q_{3D} .

Although initially skyrmion was introduced in the context of baryonic number, the term is widely used nowadays in the condensed matter theory for a broad range of defects with corresponding topology. For example, skyrmionic texture was predicted to exist in a spinor Bose-Einstein condensate based on two or more hyperfine states of an atom, where the spin degree of freedom becomes relevant [179]. Skyrmionic defects are also found in superconductors [178, 197], in thin magnetic films [195], and in chiral nematic liquid crystals [196]. In the case of a two-component field $\Psi^\dagger = (\psi_1^*, \psi_2^*)$, one can always construct a pseudospin field $\mathbf{n} \equiv (n_x, n_y, n_z) = \frac{\Psi^\dagger \hat{\sigma} \Psi}{\Psi^\dagger \Psi}$ with $\hat{\sigma}$ being the Pauli matrices. Then the components of pseudospin \mathbf{n} are:

$$n_x = \frac{\psi_1^* \psi_2 + \psi_2^* \psi_1}{\Psi^\dagger \Psi}, \quad n_y = \frac{i(\psi_2^* \psi_1 - \psi_1^* \psi_2)}{\Psi^\dagger \Psi}, \quad n_z = \frac{|\psi_1|^2 - |\psi_2|^2}{\Psi^\dagger \Psi}. \quad (1.120)$$

Then when the pseudospin \mathbf{n} winds from 0 to 2π , it describes a continuous closed surface as shown in Fig. 1.20. The topological charge associated with the skyrmion in that case can be calculated as [197]

$$Q_{2cf} = \frac{1}{4\pi} \int_{\mathbb{R}^2} \mathbf{n} \cdot \partial_x \mathbf{n} \times \partial_y \mathbf{n} dx dy. \quad (1.121)$$

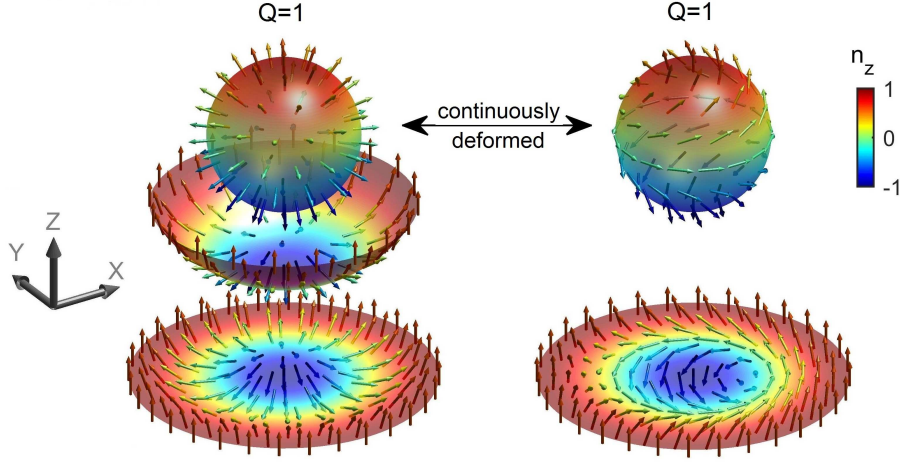


Figure 1.20: Skyrmion model. Sphere represents 3D velocity field of the average spin $\mathbf{n} = (n_x, n_y, n_z)$. n_z denotes the length of the average spin. 2D surface is the projection of 3D pseudospin field to two dimensions. Courtesy of Lingfeng Zhang, CMT group, University of Antwerp.

The meaning of the topological charge becomes clearer here: when the average spin winds once around the closed surface, the topological index is equal to one. In other words, the topological charge counts how many times the average spin winds the closed surface. As Fig. 1.20 demonstrates, the topological charge is $Q = 1$ when the average spin winds the sphere once.

In a more general case of a multi-component field $\Psi^\dagger = (\psi_1^*, \psi_2^*, \psi_3^*, \dots)$ and a two-dimensional system one can extend the topological charge given by Eq. (1.121) as [178]

$$Q_{mcf} = \int \frac{i\epsilon_{\alpha\beta}}{2\pi|\Psi|^4} \left(|\Psi|^2 \partial_\alpha \Psi^\dagger \partial_\beta \Psi + \Psi^\dagger \partial_\alpha \Psi \partial_\beta \Psi^\dagger \Psi \right) d^2r, \quad (1.122)$$

where $\alpha, \beta \in \{x, y\}$, $\epsilon_{\alpha\beta}$ is the 2-component Levi-Civita tensor. In fact, if one inserts the components of the pseudospin \mathbf{n} into Eq. (1.121), after carrying out simple arithmetical calculations the topological charge given by Eq. (1.121) modifies to Eq. (1.122), where the field $\Psi^\dagger = (\psi_1^*, \psi_2^*)$ has two components.

A detailed derivation of the topological index given by Eq. (1.122) from the Ginzburg-Landau functional for a multi-component system is presented in Ref. [178]. It was also shown in Ref. [178] that the topological index Q_{mcf} takes integer values. The proof is based on the assumption that the magnetic

flux is carried by an integer number of m fractional-flux vortices emerging in the system.

1.8 Goals of the thesis

One of the main aims of this thesis is to revisit long-established and widely used theoretical models and tools in superconductivity in the context of multiband superconductors. One of such tools is the Ginzburg-Landau theory [27], being regarded as the most convenient tool for conventional single-band superconductors. The generalization of the Ginzburg-Landau theory to multiband superconductors represents a system of nonlinear Ginzburg-Landau equations, one for each band gap, coupled via the linear Josephson-type terms. Albeit this generalization appears intuitively justified, partially by a familiar structure of the equations, it contains several fundamental shortcomings. First, it has to be reconciled with the phenomenological Landau theory of phase transitions [198]. Second, the earlier analysis of the two-component model [19, 20] revealed that the accuracy of a solution to the formalism exceeds the accuracy of its derivation. Therefore, the objective of this thesis is to construct a convenient and simple tool for the study of the properties of multiband superconductors which eliminates aforementioned fundamental inconsistencies. The subsequent goal is to point out the new physics stemming from the multi-component nature of the system, with particular attention to the chiral regime of three-band superconductors.

Furthermore, nano and atomically thin films are of great current interest, and were proven to be multiband superconductors, where the multiband structure is dictated by the nanofilm thickness through the size quantization of the electron motion perpendicular to the film. However, a serious limitation here is the absence of a convenient theoretical tool to access new physical phenomena in such quasi-two-dimensional systems. For example, investigating complex configurations of vortices in nanofilms by employing a microscopic model, e.g., the Bogoliubov-de Gennes equations, is a difficult and time consuming task. On the other hand, the standard Ginzburg-Landau model is not valid in nanofilms, since the nanofilm thickness is much smaller than the bulk BCS coherence length and the band gaps vary significantly in this scale. Therefore, the objective of this thesis is to derive the appropriate multiband Ginzburg-Landau theory for nano-thin superconductors, and point out the consequences on emergent physics.

The third objective is to study numerically exotic vortex structures in the rotating harmonically trapped two- and three-component Bose-Einstein condensates. The underlying goal of these investigations is to extend our un-

derstanding of vortex phenomena in the gaseous condensates but also to link the findings to the ones of multiband superconductivity - particularly in the chiral regime and novel vortex matter. Although the research carried out in the thesis addresses a wide range of problems, it is important to stress that superconductivity and Bose-Einstein condensation are closely related, representing condensation of bosonic particles. The advantage of BECs is that they can be easily created and manipulated experimentally, and to support quantized vortices when being rotated, which allows to study the rich emergent vortex physics and thereby prove some theoretical hypotheses. We note that despite the research is theoretical, it is strongly motivated by current experimental prospects.

CHAPTER 2

The chiral regime of three-band superconductors

In the previous Chapter the Ginzburg-Landau and BCS theories for single band superconductors were reviewed, the concept of multiband superconductor was defined, main properties of the multiband superconductors were considered and the generalization of the BCS theory for the multiband superconductors was given. In this Chapter, by using the Gor'kov technique developed for the single band superconductors and outlined in the previous Chapter, the generalization of Ginzburg-Landau theory for the multiband superconductors is derived.

2.1 Introduction

Studies of multiband (or multigap) superconducting systems, where more than one carrier band contributes to the formation of the condensate, have now more than a half-century history [88, 89, 19, 199]. In the last decade, clear experimental evidences of multigap condensates were observed in a rich variety of materials such as magnesium diboride [51, 56], oxypnictides [64], iron arsenides [66] and iron pnictides [99, 200]. The string of discoveries continues today so that the number of multiband superconductors increases almost yearly.

There are different physical mechanisms responsible for the formation of multiple carrier bands. For example, in bulk specimens the multi-gap structure can be related to the appearance of separate pockets in the Fermi surface centered around some points of the Brillouin zone. However, it was

recently shown that multiband superconductivity can also arise in nanoscale specimens (e.g. in nanofilms) made of ordinary single-band superconducting materials, where the geometrical size quantization creates distinct carrier subbands [112, 109, 119, 120, 201]. These and similar findings broadened the interest in the physics of multiband coherent phenomena, and that interest has given a strong impetus to theoretical investigations. One of the focal points of such investigations is revisiting long-established and widely used theoretical models and methods in superconductivity in the context of multiband superconductors. One of such methods is the Ginzburg-Landau (GL) theory [27], which is commonly regarded as one of the most general and yet simple mean-field approaches for conventional single-band superconductors. Surprisingly, the generalization of the GL theory to the multiband case is still a highly debated issue.

On the microscopic level, a multiband superconductor is modeled by the multicomponent generalization of the BCS theory [88, 89]. The corresponding GL equations are derived using a straightforward application of the original single-band recipe by Gor'kov [36] (see, e.g., Refs. [202] and [75]). In this approach, superconducting gap functions in each carrier band, hereafter referred to as band gaps, are regarded as the order parameters. Similarly to the single-band case, the anomalous Green's function is expanded in powers of the corresponding band gaps and its spatial gradients [36], and then the expansion is truncated to keep the same terms as in the single-band GL theory. This procedure yields a system of nonlinear GL-type equations, one for each band gap, coupled via the linear Josephson-type terms, and the corresponding multicomponent functional. This is often referred to as the *multi-component* GL model and is widely used in the analysis of multiband superconductors [202, 75, 203, 204, 205, 206, 178, 6, 207, 208, 209, 210, 211, 212, 213].

Although this formulation of GL theory appears intuitively justified, partially by a familiar structure of the obtained equations, it possesses several fundamental inconsistencies. First, it has to be reconciled with the Landau theory of phase transitions, according to which the order parameter must be associated with a particular irreducible representation of the relevant symmetry group. Following this prescription, Volovik and Gor'kov developed a classification of the exotic superconducting phases within the GL theory [214] (a systematic classification of the GL theories based on the symmetry analysis can be found in Ref. [215]). It is important that the number of independent order parameters in the GL theory, given by the dimensionality of the irreducible representation, is typically lower than the number of bands, which is certainly different from the multicomponent model mentioned above.

Secondly, the analysis of the multicomponent GL theory presented by Geilikman, Zaitsev and Kresin [19, 199] and more recently by Kogan and

Schmalian [20] revealed another inconsistency: the accuracy of a solution to the formalism *exceeds* the accuracy of its derivation. This discrepancy is intrinsic in the multiband generalization of the Gor'kov procedure and can only be eliminated by invoking an additional truncating *reconstruction*, which removes the artificial higher-order contributions [19, 199, 20, 216, 217].

Without additional symmetries, such reconstruction yields a *strict proportionality* of all band gaps, i. e., the GL theory has a single order parameter. This conclusion agrees with the phenomenological classification that predicts a single-component GL theory in this case. (Deviations from this result appear only in higher-order corrections to the ordinary GL theory [216, 217, 218]).

This analysis did not consider the case of a degenerate solutions for T_c which appears due to an additional symmetry of the system. Furthermore, the calculations in Ref. [19] for an arbitrary number of bands employed a rather restrictive ansatz for the band gaps, while Refs. [20] and [216] utilize the separability specific to the two-band case. The microscopic derivation of the multiband GL theory has not been yet achieved in the general case. Notice that a mechanical merge of the symmetry analysis with the Gor'kov truncating procedure, in which the outcome of the Gor'kov procedure is simply rewritten in terms of the basis states of the relevant symmetry group representations, does not solve the problem. It yields a mixture of different irreducible representations, which should not happen in the standard GL formalism [5].

In this Chapter, we derive the reconstructed GL theory from the microscopic Hamiltonian for a multiband superconductor in a general case with an arbitrary number of bands as well as with an arbitrary symmetry (reflected in the degeneracy of the solutions for T_c). The origin of the symmetry is not important here. We note that it can appear not only due to the lattice structure of the material, as discussed in Ref. [214] and [215] but also due to other reasons, e.g., the geometrical shape of the sample as in superconducting single-crystalline nanofilms [219, 220, 220]. A detailed analysis of the obtained equations is then performed for the three-band system treated as a prototype of a multiband superconductor. In particular, we consider a simple three-band model of pnictides with dominant interband couplings which allows for the twofold degeneracy of the solitons for T_c . We demonstrate that in full agreement with the phenomenological GL theory, this system has two order parameters, related to the two-dimensional irreducible representation of the relevant symmetry group. However, unlike the phenomenological analysis based on the symmetry considerations, the derivation from the microscopic theory offers the explicit expressions for the coefficients of the GL theory. These expressions are highly nontrivial in the case of multiband supercon-

ductors because they contain important information about contributions of different bands that can not be obtained from the symmetry arguments. The corresponding ground state of the system is found to be a chiral state with nontrivial phase difference between the band gaps. Such states in multigap superconductors have attracted much interest [6, 207, 208, 209, 210, 211, 213] as they could lead to unconventional phenomena such as the formation of antiferromagnetic domains or noninteger vortices (see, e.g., Ref. [215]). Notice that in this consideration we do not go beyond the standard GL domain (i.e., band gaps are proportional to $\tau^{1/2}$, with $\tau = 1 - T/T_c$ the proximity to the critical temperature).

The Chapter is organized as follows. In Section 2.2, the GL theory for multiband superconductors is derived starting from the standard multiband BCS model. The derivation is performed in three steps: (i) the truncated multiband gap equation is obtained in matrix form by following the Gor'kov procedure adapted for the case of multiple bands, (ii) the truncating reconstruction is then applied by invoking the τ -expansion, and (iii) an explicit form of the resulting GL equations is obtained by keeping terms of order $\tau^{1/2}$ in the band gaps. In Section 2.3, we recast the final formalism in a more explicit form, for both the nondegenerate and degenerate cases. In Section 2.4, we consider a three-band model, for which expressions for the coefficients of the GL equations can be calculated analytically for an arbitrary interaction matrix. Then, we investigate the case of a degenerate solution for T_c for a simple variant of the model with strong interband couplings and demonstrate analytically that the degeneracy in this model leads to a chiral ground state. Our summary and conclusions can be found in Section 2.5.

2.2 Derivation of the GL theory

2.2.1 Truncated gap equation

Following Gor'kov [36], the GL theory is usually derived from the gap self-consistency equation, using an expansion of the anomalous Green's function in powers of the order parameter and its spatial derivatives. We outline this derivation for multiple bands, starting from the multiband BCS Hamiltonian [88, 89] with s-wave singlet pairing, which reads as

$$H_{\text{BCS}} = H_c + \sum_i \int d^3r \left[\sum_{\sigma} \hat{\psi}_{i\sigma}^{\dagger}(\mathbf{r}) T_i(\mathbf{r}) \hat{\psi}_{i\sigma}(\mathbf{r}) + \hat{\psi}_{i\uparrow}^{\dagger}(\mathbf{r}) \hat{\psi}_{i\downarrow}^{\dagger}(\mathbf{r}) \Delta_i(\mathbf{r}) + \text{h.c.} \right], \quad (2.1)$$

where i enumerates different bands, $\hat{\psi}_{i\sigma}(\mathbf{r})$ and $\hat{\psi}_{i\sigma}^\dagger(\mathbf{r})$ are the carrier field operators, $\Delta_i(\mathbf{r})$ are the band gap functions, or simply band gaps, H_c is the c -number term (see, e.g., Ref. [75]), and $T_i(\mathbf{r})$ stands for the single-electron energy. Equation (2.1) is supplemented with by the self-consistent gap equation

$$\vec{\Delta} = \check{g}\vec{R}, \quad (2.2)$$

where we introduce \check{g} , the matrix of the coupling constants g_{ij} , and use the vector notations $\vec{\Delta}^T = (\Delta_1, \Delta_2, \dots)$ and $\vec{R}^T = (R_1, R_2, \dots)$, with $R_i = \langle \hat{\psi}_{i\uparrow}(\mathbf{r})\hat{\psi}_{i\downarrow}(\mathbf{r}) \rangle$ being the anomalous Green's function of the i -th band [222].

Using Eq. (2.1), we expand the anomalous Green's functions in the vicinity of T_c into a series in powers of the band gaps and their spatial gradients. As the Hamiltonian (2.1) is diagonal over the band index, the series is obtained independently for each band yielding the same expressions as in the single-band case. The derivation of the expansion in powers of the gap function is given in **Chapter 1**, Section 1.3, Subsection 1.3.2, therefore we quote here the final expansion for R_i , where only the leading nonlinear and gradient terms are retained,

$$R_i[\Delta_i] \simeq N_i(0)\mathcal{A}\Delta_i + \Omega_i[\Delta_i], \quad (2.3)$$

where $N_i(0)$ is the band density of states (DOS), $\mathcal{A} = \ln(2e^\Gamma \hbar\omega_c/\pi T_c)$, and

$$\Omega_i[\Delta_i] = -a_i\Delta_i - b_i|\Delta_i|^2\Delta_i + \mathcal{K}_i\nabla^2\Delta_i. \quad (2.4)$$

In Eqs. (2.3) and (2.4) ω_c is the cut-off frequency, $\Gamma = 0.577$ is the Euler constant and the coefficients are calculated as

$$a_i = -N_i(0)\tau, \quad b_i = N_i(0)\frac{7\zeta(3)}{8\pi^2 T_c^2}, \quad \mathcal{K}_i = \frac{b_i}{6}\hbar^2 v_i^2, \quad (2.5)$$

with $\zeta(\dots)$ the Riemann zeta function and v_i the band Fermi velocity. Although here only results for the clean limit are quoted, we note that the structure of the equations will be the same for dirty systems, as is usually the case in the standard GL formalism.

We note that the magnetic field is not included in Eq. (2.4). The generalization to the nonzero-field case is trivial and will be done at a later stage by using the standard prescription of inserting the gauge invariant gradients $\mathbf{D} = \nabla - i\frac{2e}{\hbar c}\mathbf{A}$, where \mathbf{A} is the vector potential. One should remember, however, that this recipe is valid only in the standard GL domain when only

terms of order $\tau^{1/2}$ are kept in the gap functions. A more involved and complicated procedure is needed when higher-order corrections to the band gaps are considered [218].

Substituting Eq. (2.3) into Eq. (2.2), we obtain the following system of coupled equations:

$$(\mathcal{A}_i + a_i)\Delta_i + b_i\Delta_i|\Delta_i|^2 - \mathcal{K}_i\nabla^2\Delta_i + \sum_{j\neq i}\gamma_{ij}\Delta_j = 0, \quad (2.6)$$

where γ_{ij} is the element of the inverted interaction matrix \check{g}^{-1} and the constants \mathcal{A}_i are defined as

$$\mathcal{A}_i = \gamma_{ii} - N_i(0)\mathcal{A}. \quad (2.7)$$

The truncated set of equations given by Eq. (2.6) are commonly referred to as the generalization of the GL theory to the multiband case, or the *multi-component GL theory*. This interpretation is suggestive, especially given that in the limit of zero interband couplings Eq. (2.6) yields N uncoupled GL equations for Δ_i 's that are the true Landau order parameters for the uncoupled bands. Thus, the coupling is commonly assumed to be a weak perturbation that does not significantly alter this physical picture.

However, already this trivial limit highlights shortcomings of the interpretation of Eq. (2.6) as a consistent multiband GL formalism. In the absence of coupling each band has its own critical temperature T_{ci} , while the T_c of the entire system is the largest of those. In the vicinity of T_c , which is the usual validity domain of the GL theory, only the band with $T_{ci} = T_c$ develops a superconductive state and, therefore, the system is in fact described by a single-band GL theory with the single order parameter (here we assume that the T_{ci} 's are well separated). One can also imagine a degenerate situation where $M \leq N$ gaps have the same largest critical temperature T_c . Here, in the zero-coupling limit, the system is described by the theory with $M \leq N$ order parameters corresponding to M uncoupled components. Thus, in the zero interband-coupling limit, the GL theory *always* has fewer active order parameters than the number of available bands. This conclusion is of course trivial in the noninteracting case. However, in what follows we demonstrate that it holds also in the general case of a nonzero coupling within the accuracy of the GL approach.

2.2.2 Reconstructed GL theory

Deriving the GL theory for the general case of nonzero interband interactions starts by noting that as discussed previously, Eq. (2.6) is inconsistent because

the accuracy of its solution exceeds the accuracy of its derivation. One can see this (details can be found in Refs. [19, 199, 20, 216, 217]) by taking into account that the coefficients $\mathcal{A}_i + a_i$ and γ_{ij} are not zero in the limit $\tau \rightarrow 0$ ($T \rightarrow T_c$). This implies that a solution to Eq. (2.6), when being expanded in τ , comprises terms of arbitrarily high orders, i.e., all Δ_i 's are given by infinite series in powers $\tau^{n+1/2}$, with integer n . At the same time the Gor'kov truncation neglects terms that contribute to orders higher than $\tau^{1/2}$ in the band gap functions. The only situation when this inconsistency does not happen is the single-band GL theory where the coefficient of the linear term in the GL equation is proportional to τ and, as a result, the solution comprises a single contribution of order $\tau^{1/2}$.

In order to reconcile the accuracy of a solution for Δ_i with the accuracy of the derivation of Eq. (2.6), we use the reconstruction procedure that abandons incomplete higher-order contributions from the band gaps. This procedure is nothing more than a systematic perturbation expansion in τ , which gives the GL theory and its corrections in a systematic way [218]. Following this procedure, the solution to Eq. (2.6) is sought in the form of a series in odd powers of $\tau^{1/2}$ as

$$\Delta_i = \Delta_i^{(0)} + \Delta_i^{(1)} + \mathcal{O}(\tau^{5/2}), \quad (2.8)$$

where $\Delta_i^{(0)} \propto \tau^{1/2}$ and $\Delta_i^{(1)} \propto \tau^{3/2}$. This series is inserted into Eq. (2.6) and then terms of the same order are collected. A simple power-counting shows that making a solution to Eq. (2.6) consistent with the Gor'kov truncation, one should keep the two lowest orders in the resulting τ -expansion of Eq. (2.6) and the leading order term $\propto \tau^{1/2}$ in Eq. (2.8).

Notice that one must also take into account that spatial derivatives of the difference $\delta\Delta_i = \Delta_i - \Delta_i^{(0)}$ do not contribute to these lowest orders. In an earlier consideration [19] it was assumed that $\delta\Delta_i$ is independent of the coordinates, see Eq. (14) in Ref. [199]. Subsequent works [216, 217, 218] have demonstrated that such a restrictive ansatz is not needed. The GL theory introduces the coherence length, $\xi \propto \tau^{-1/2}$ so that *all* spatial derivatives of *all* contributing terms in the band gaps scale as $\propto \tau^{1/2}$. In other words, each gradient operator ∇ introduces a factor $\propto \tau^{1/2}$. Counting powers of τ in the expansion confirms that the higher-order gradients of $\Delta_i^{(0)}$ as well as the lowest gradients of $\delta\Delta_i$ do not contribute to the two lowest orders of the τ expansion of Eq. (2.6).

Substituting Eq. (2.8) into Eq. (2.6) and collecting terms of order $\tau^{1/2}$, we obtain the first equation in the reconstructed theory

$$\check{L}\vec{\Delta}^{(0)} = 0, \quad (2.9)$$

where the elements of the matrix \check{L} are written as

$$L_{ij} = \delta_{ij}\mathcal{A}_i + (1 - \delta_{ij})\gamma_{ij}, \quad (2.10)$$

with δ_{ij} being the Kronecker symbol. The condition of solvability of Eq. (2.9),

$$\det\check{L} = 0, \quad (2.11)$$

is the equation for the critical temperature T_c that generally has N solutions. Clearly, one has to choose the solution with the maximal T_c as it yields the minimal value of the free energy. Equation (2.9) is commonly referred to as the linearized gap equation as it can also be obtained by simply neglecting all the nonlinear contributions in Eq. (2.6).

When $N > 2$, one may encounter a situation with $M < N$ degenerate solutions to Eq. (2.11) that correspond to the same maximal value of T_c . In this case the matrix \check{L} has M eigenvectors ξ_α , with $\alpha = 1, \dots, M$, corresponding to the zero eigenvalue of \check{L} at $T = T_c$. Without loss of generality these eigenvectors can be chosen orthogonal, and their normalization is not important.

A general solution to Eq. (2.9) is then represented as a sum of M terms (i.e. $M = 1$ for the nondegenerate case), one for each eigenvector, as

$$\vec{\Delta}^{(0)}(\mathbf{r}) = \sum_{\alpha} \psi_{\alpha}(\mathbf{r})\vec{\xi}_{\alpha}. \quad (2.12)$$

Here, M functions ψ_{α} are specified by the equation that is obtained from Eq. (2.6) by matching terms of order $\tau^{3/2}$ as

$$\check{L}\vec{\Delta}^{(1)} = \vec{\Omega}[\vec{\Delta}^{(0)}], \quad (2.13)$$

where the components $\Omega_i[\Delta_i^{(0)}]$ of $\vec{\Omega}[\vec{\Delta}^{(0)}]$ are given by Eq. (2.4) with Δ_i replaced by $\Delta_i^{(0)}$. A closed set of M equations for $\psi_{\alpha}(\mathbf{r})$ is derived by projecting Eq. (2.13) to the eigenvectors $\vec{\xi}_{\alpha}$, which yields M equations given by

$$\sum_i \xi_{\alpha i} \Omega_i[\Delta_i^{(0)}] = 0, \quad (2.14)$$

where $\xi_{\alpha i}$ is the i -th component of $\vec{\xi}_{\alpha}$.

2.3 Explicit form of the GL equations

2.3.1 Nondegenerate case

Here, we recast Eq. (2.14) in a more explicit and familiar form. In the nondegenerate, case a single function $\psi(\mathbf{r}) \equiv \psi_1(\mathbf{r})$ controls the same spatial

profile of all band condensates. Rewriting Eq. (2.14) for $\psi(\mathbf{r})$ one obtains

$$a\psi + b|\psi|^2\psi - \mathcal{K}\mathbf{D}^2\psi = 0, \quad (2.15)$$

where we include a nonzero magnetic field by replacing $\nabla \rightarrow \mathbf{D}$. The coefficients a , b and \mathcal{K} in Eq. (2.15) are given by

$$a = \sum_i a_i \xi_i^2, \quad b = \sum_i b_i \xi_i^4, \quad \mathcal{K} = \sum_i \mathcal{K}_i \xi_i^2, \quad (2.16)$$

where ξ_i is the band component of $\vec{\xi} \equiv \vec{\xi}_1$. The corresponding free-energy functional reads as

$$\mathcal{F} = \int d^3r \left[a|\psi|^2 + \frac{b}{2}|\psi|^4 + \mathcal{K}|\mathbf{D}\psi|^2 + \frac{\mathbf{B}^2}{8\pi} \right]. \quad (2.17)$$

Using this functional, one derives the accompanying Maxwell equation for the gauge field in the form

$$\frac{1}{4\pi} \text{rot} \mathbf{B} = i \frac{2e}{\hbar c} \mathcal{K} (\psi \mathbf{D}^* \psi^* - \psi^* \mathbf{D} \psi). \quad (2.18)$$

As seen, Eqs. (2.15), (2.17) and (2.18) have the form of the ordinary single-band GL theory. In fact, however, this is an *effectively* single-band GL theory as the coefficients a , b and \mathcal{K} comprise contributions of all bands. It is also important to remember that ψ itself cannot be interpreted as an excitation gap: it is related to the band gap functions via Eq. (2.12).

The single-band representation of the reconstructed GL theory allows one to define the characteristic lengths of a multiband superconductor in a unique way. In particular, the coherence length ξ , the magnetic penetration depth λ , and their ratio κ are given by the standard GL expressions as

$$\xi = \sqrt{\frac{\mathcal{K}}{|a|}}, \quad \lambda = \frac{\hbar c}{|e|} \sqrt{\frac{b}{32\pi \mathcal{K} |a|}}, \quad \kappa = \Phi_0 \sqrt{\frac{b}{32\pi^3 \mathcal{K}^2}}, \quad (2.19)$$

where Φ_0 is the flux quantum. However, the multiband origin of Eqs. (2.15)-(2.18) is still reflected in some properties of the system. For example, following Eqs. (2.16) and (2.19), one concludes that b, \mathcal{K} can be roughly estimated as linearly proportional to N . Taking into account the relation $\kappa \propto \sqrt{b/\mathcal{K}^2}$ one arrives at the trend $\kappa \sim 1/\sqrt{N}$, which means that a multiband superconductor approaches a type-I superconducting behaviour when the number of bands is large enough.

2.3.2 Degenerate case

When the maximal solution to Eq. (2.11) is degenerate, i.e., $M > 1$, Eq. (2.12) yields a set of coupled nonlinear equations, an explicit form of which is obtained as

$$\sum_{\beta} (a_{\alpha\beta} - \mathcal{K}_{\alpha\beta} \mathbf{D}^2) \psi_{\beta} + \sum_{\beta\gamma\delta} b_{\alpha\beta\gamma\delta} \psi_{\beta} \psi_{\gamma}^* \psi_{\delta} = 0, \quad (2.20)$$

where the coefficients are defined as

$$\begin{aligned} a_{\alpha\beta} &= \sum_i a_i \xi_{\alpha i} \xi_{\beta i}, & \mathcal{K}_{\alpha\beta} &= \sum_i \mathcal{K}_i \xi_{\alpha i} \xi_{\beta i}, \\ b_{\alpha\beta\gamma\delta} &= \sum_i b_i \xi_{\alpha i} \xi_{\beta i} \xi_{\gamma i} \xi_{\delta i}. \end{aligned} \quad (2.21)$$

The corresponding free-energy functional is now obtained in the form

$$\begin{aligned} \mathcal{F} = \int d^3r & \left[\sum_{\alpha\beta} (a_{\alpha\beta} \psi_{\alpha}^* \psi_{\beta} + \mathcal{K}_{\alpha\beta} \mathbf{D}^* \psi_{\alpha}^* \mathbf{D} \psi_{\beta}) \right. \\ & \left. + \frac{1}{2} \sum_{\alpha\beta\gamma\delta} b_{\alpha\beta\gamma\delta} \psi_{\alpha}^* \psi_{\beta} \psi_{\gamma}^* \psi_{\delta} + \frac{\mathbf{B}^2}{8\pi} \right]. \end{aligned} \quad (2.22)$$

By calculating the functional derivative with respect to the vector potential, we obtain from Eq. (2.22) the accompanying Maxwell equation as

$$\frac{1}{4\pi} \text{rot} \mathbf{B} = i \frac{2e}{\hbar c} \sum_{\alpha\beta} \mathcal{K}_{\alpha\beta} (\psi_{\alpha} \mathbf{D}^* \psi_{\beta}^* - \psi_{\beta}^* \mathbf{D} \psi_{\alpha}). \quad (2.23)$$

The number of components in the reconstructed GL theory is $1 \leq M < N$, unlike in the original system of equations given by Eq. (2.6). Another important difference is that all coefficients of the linear terms in the reconstructed GL theory are now proportional to τ , which dictates that $\psi_{\alpha} \propto \tau^{1/2}$. This eliminates the problem of the mismatch between the accuracy of the solutions and the equations, which was the reason to seek the reconstruction.

Notice that the reconstructed GL formalism, obtained here by the τ -expansion, recovers the standard Landau theory of phase transitions. In particular, the degeneracy of the linearized gap equation is related to an extra symmetry between the bands, hidden in the relevant coupling matrix. The degree of degeneracy M is defined by the dimensionality of the corresponding irreducible representation with the M basis vectors ξ_{α} 's. Equation (2.22) is interpreted as the Landau free-energy functional with the ψ_{α} 's being a

Landau order parameters. The reconstruction can thus be regarded as the procedure of finding the true Landau order parameter of the system, in the form of linear combinations of the band gaps [see Eq. (2.12)]. However, Eqs. (2.17) and (2.22) are derived by matching all relevant terms in the τ -expansion, rather than through the phenomenological approach based on the group-theory analysis [215].

In agreement with the Landau recipe, the reconstructed GL theory is based on a single irreducible representation. However, if one continues the τ -expansion to next orders, admixtures of other irreducible representations will appear in the formalism. Within the symmetry analysis, it is often argued that such terms should arise because the appearance of the condensate at $T < T_c$ already changes the symmetry of the system [215]. The reconstruction yields a clear quantitative estimate for such admixtures. It is easy to see from Eq. (2.8) that the order parameters related to extra irreducible representations will be of order $\tau^{3/2}$ and higher, which must be neglected in the present analysis concerning the standard GL formalism.

2.4 Three-band system

2.4.1 Eigenvectors

As a prototype of multiband superconductors, we now consider a physically relevant case of a three-band system, the analysis of which can be done analytically. In order to obtain the eigenvectors ξ_α , we write Eq. (2.9) as a system of linear algebraic equations

$$\mathcal{A}_i \Delta_i^{(0)} + \sum_{j \neq i} \gamma_{ij} \Delta_j^{(0)} = 0. \quad (2.24)$$

It is easy to verify that the following relations hold:

$$\eta_1 \Delta_1^{(0)} = \eta_2 \Delta_2^{(0)} = \eta_3 \Delta_3^{(0)}, \quad (2.25)$$

where

$$\begin{aligned} \eta_1 &= \mathcal{A}_1 \gamma_{23} - \gamma_{12} \gamma_{13}, & \eta_2 &= \mathcal{A}_2 \gamma_{13} - \gamma_{12} \gamma_{23}, \\ \eta_3 &= \mathcal{A}_3 \gamma_{12} - \gamma_{13} \gamma_{23}, \end{aligned} \quad (2.26)$$

and \mathcal{A}_i is defined by Eq. (2.7).

We now investigate the following possibilities. Let us first assume that $\eta_1, \eta_2, \eta_3 \neq 0$. Then, from Eq. (2.25) we immediately find that

$$\xi_i \propto 1/\eta_i, \quad (2.27)$$

which implies that the gaps in all three bands are nonzero. When one of the η_i 's is zero, say $\eta_1 = 0$, then Eq. (2.25) dictates that $\Delta_2^{(0)} = \Delta_3^{(0)} = 0$, and therefore the condensate is formed only in one band. When two of the η_i 's vanish, the gap is nonzero in the corresponding two bands. In all these cases, we deal with the nondegenerate scenario governed by the single-component GL equation (2.15) with the coefficients given by Eq. (2.16). However, the eigenvector $\vec{\xi}$, whose band components appear in Eq. (2.16), is dependent on the particular situation. As mentioned above, for $\eta_1, \eta_2, \eta_3 \neq 0$ we obtain Eq. (2.27), whereas for, say, $\eta_1 = \eta_2 = 0$ we have $\vec{\xi}^T = (1, -\gamma_{13}/\gamma_{23}, 0)$.

The case when all η_i 's are equal to zero requires a bit more algebra. Expressing \mathcal{A}_i in terms of γ_{ij} from Eq. (2.26) and then inserting the result into Eq. (2.24), we find that in this case Eqs. (2.24) are reduced to a single equation that reads as

$$\gamma_{12}\gamma_{13}\Delta_1^{(0)} + \gamma_{12}\gamma_{23}\Delta_2^{(0)} + \gamma_{13}\gamma_{23}\Delta_3^{(0)} = 0. \quad (2.28)$$

A general solution to Eq. (2.28) can be written as

$$\vec{\Delta}^{(0)}(\mathbf{r}) = \vartheta_1(\mathbf{r})\vec{u}_1 + \vartheta_2(\mathbf{r})\vec{u}_2, \quad (2.29)$$

where

$$\vec{u}_1 = \begin{pmatrix} 0 \\ -\gamma_{13}/\gamma_{12} \\ 1 \end{pmatrix}, \quad \vec{u}_2 = \begin{pmatrix} 1 \\ -\gamma_{13}/\gamma_{23} \\ 0 \end{pmatrix} \quad (2.30)$$

are linearly independent and $\vartheta_{1,2}(\mathbf{r})$ are unknown functions to be specified later. Comparing Eq. (2.29) with Eq. (2.12), we conclude that this case represents the degenerate scenario with $M = 2$. Equation (2.29) can be rewritten in terms of two orthogonal eigenvectors $\vec{\xi}_{1,2}$ by applying the orthogonalization procedure to $\vec{u}_{1,2}$, which gives

$$\vec{\xi}_1 = \vec{u}_1, \quad \vec{\xi}_2 = \vec{u}_2 - \frac{\gamma_{13}^2\gamma_{12}}{(\gamma_{12}^2 + \gamma_{13}^2)\gamma_{23}}\vec{u}_1. \quad (2.31)$$

One can then express the functions $\vartheta_{1,2}$ through $\psi_{1,2}$ introduced earlier as $\vartheta_1(\mathbf{r}) = \psi_1(\mathbf{r}) - \gamma_{13}^2\gamma_{12}/[(\gamma_{12}^2 + \gamma_{13}^2)\gamma_{23}]\psi_2(\mathbf{r})$ and $\vartheta_2(\mathbf{r}) = \psi_2(\mathbf{r})$. The band gaps are then defined by the two Landau order parameters $\psi_{1,2}$ according to

$$\begin{aligned} \Delta_1^{(0)} &= \psi_2, \\ \Delta_2^{(0)} &= -\frac{\gamma_{13}}{\gamma_{12}}\psi_1 - \frac{\gamma_{12}^2\gamma_{13}}{(\gamma_{13}^2 + \gamma_{12}^2)\gamma_{23}}\psi_2, \\ \Delta_3^{(0)} &= \psi_1 - \frac{\gamma_{13}^2\gamma_{12}}{(\gamma_{13}^2 + \gamma_{12}^2)\gamma_{23}}\psi_2. \end{aligned} \quad (2.32)$$

Finally we note that the derivation of Eqs. (2.28)-(2.32) assumes that $\gamma_{12}, \gamma_{13}, \gamma_{23} \neq 0$. If some of these interband couplings is zero while $\eta_1 = \eta_2 = \eta_3 = 0$, the problem reduces to a trivial example of the nondegenerate case where some of the available bands are uncoupled.

2.4.2 Chiral state with phase frustration

Under certain conditions, the ground state of a three-band superconductor may develop a nontrivial phase difference between different band gaps, referred to as the state with phase frustration or the chiral solution. This state is of particular interest as it breaks time-reversal invariance in the system, leading to many unconventional superconducting properties [215]. Following, we analytically demonstrate the possibility of such a state in the three-band system within the simple variant of the model with strong interband couplings, i.e., $g_{ii} = 0$ and $g_{i \neq j} > 0$ and $N_1(0) = N_2(0) = N_3(0)$. Our analytical calculation compliments numerical investigations in the recent Ref. [6]. Such a model describes an interesting example of a system where the superconducting pairing is caused by interband coupling and, as it is believed, may be relevant for the pnictides [6]. We are interested in the special case when different interband couplings are equal to one another, which may be dictated by some symmetry between bands [5] but is not necessarily limited to only this particular physical situation. Please note that many different combinations of intraband and interband couplings can lead to a degeneracy of T_c and possible phase frustration (see, e.g. Ref. [207, 208, 209]). However, in the absence of physical justifications for such coupling matrices, we refrain from their analysis.

Using the orthogonality conditions for $\vec{\xi}_\alpha$'s and the fact that the band DOS's are equal, we obtain $a_{12} = a_{21} = 0$ in Eq. (2.20). Furthermore, it is obvious that the tensor $b_{\alpha\beta\gamma\delta}$ is symmetric with respect to permutation of each pair of indices so that it is convenient to introduce new notations

$$\begin{aligned} \beta_1 &= b_{1111}, & \beta_2 &= b_{1112} = b_{1121} = b_{1211} = b_{2111}, \\ \beta_3 &= b_{1122} = b_{1212} = b_{2112} = b_{2121} = b_{1221} = b_{2211}, \\ \beta_4 &= b_{1222} = b_{2122} = b_{2212} = b_{2221}, & \beta_5 &= b_{2222}. \end{aligned} \quad (2.33)$$

Then, for the homogeneous case without magnetic field, Eq. (2.20) yields

$$\alpha_1 = -\beta_1|\psi_1|^2 - \beta_2(2\psi_1^*\psi_2 + \psi_1\psi_2^*) - \beta_3\left(2|\psi_2|^2 + \psi_2^2\frac{\psi_1^*}{\psi_1}\right) - \beta_4|\psi_2|^2\frac{\psi_2}{\psi_1}, \quad (2.34a)$$

$$\alpha_2 = -\beta_2|\psi_1|^2\frac{\psi_1}{\psi_2} - \beta_3\left(2|\psi_1|^2 + \psi_1^2\frac{\psi_2^*}{\psi_2}\right) - \beta_4(2\psi_1\psi_2^* + \psi_1^*\psi_2) - \beta_5|\psi_2|^2, \quad (2.34b)$$

where we also denote $\alpha_1 = a_{11}$, $\alpha_2 = a_{22}$. As usual, it is convenient to search for a solution to Eq. (2.34) in the form $\psi_i = |\psi_i| \exp(i\phi_i)$. Then, matching the imaginary parts in Eq. (2.34a) [or in Eq. (2.34b), which gives the same result], we obtain

$$[\beta_2r + 2\beta_3 \cos(\delta\phi) + \beta_4r^{-1}] \sin(\delta\phi) = 0, \quad (2.35a)$$

where the notations $\delta\phi = \phi_2 - \phi_1$ and $r = |\psi_1|/|\psi_2|$ are introduced. Matching the real parts in Eqs. (2.34a) and (2.34b) yields, respectively,

$$-\frac{\alpha_1}{|\psi_1|^2} = \beta_1 + (3\beta_2 + \beta_4r^{-2})r^{-1} \cos(\delta\phi) + \beta_3r^{-2}[2 + \cos(2\delta\phi)], \quad (2.35b)$$

$$-\frac{\alpha_2}{|\psi_1|^2} = (\beta_2r + 3\beta_4r^{-1}) \cos(\delta\phi) + \beta_3[2 + \cos(2\delta\phi)] + \beta_5r^{-2}. \quad (2.35c)$$

To check the thermodynamic stability of different solutions to Eqs. (2.35), one needs to calculate the free energy from the functional in Eq. (2.22). It can be rewritten, using the new notations, as

$$\mathcal{F} = \int d^3r \left\{ |\psi_1|^2(\alpha_1 + \alpha_2 r^{-2}) + \frac{1}{2}|\psi_1|^4 \left(\beta_1 + 4 \cos(\delta\phi)r^{-1}(\beta_2 + \beta_4r^{-2}) + 2\beta_3r^{-2}[2 + \cos(2\delta\phi)] + \beta_5r^{-4} \right) \right\}. \quad (2.36)$$

To proceed further, we substitute the chosen model parameters into the obtained equations. Inverting the coupling matrix yields $\gamma_{ii} = -1/(2g)$ and $\gamma_{i \neq j} = 1/(2g)$. Then, using Eq. (2.31), we obtain the eigenvectors as $\vec{\xi}_1^T = (0, -1, 1)$ and $\vec{\xi}_2^T = (2, -1, -1)$, where $\vec{\xi}_2$ is now multiplied by 2 for the sake of convenience of our further calculations. Substituting these eigenvectors into Eq. (2.21), we find

$$\alpha_1 = 2\tilde{a}, \quad \alpha_2 = 6\tilde{a}, \quad \beta_1 = 2\tilde{b}, \quad \beta_2 = 0, \quad \beta_3 = 2\tilde{b}, \quad \beta_4 = 0, \quad \beta_5 = 18\tilde{b}, \quad (2.37)$$

where $\tilde{a} = a_1 = a_2 = a_3$ and $\tilde{b} = b_1 = b_2 = b_3$, and a_i and b_i are given by Eq. (2.5). Finally, based on Eq. (2.37), we can rewrite Eq. (2.35a) as

$$\sin(2\delta\phi) = 0, \quad (2.38)$$

which yields the obvious solution for the phase difference $\delta\phi = \pi n/2$, with n being an integer.

One can identify two solution classes. The first one is given by $\delta\phi = 0, \pi, 2\pi, \dots$ for which $\cos(2\delta\phi) = 1$. Here, a sign difference can occur between the band components but there is no nontrivial phase difference. In this case, Eqs. (2.35b) and (2.35c) are reduced to

$$|\psi_1|^2 = |\tilde{a}|/[\tilde{b}(1 + 3r^{-2})]. \quad (2.39)$$

The complete homogeneous solution for the band gaps is then given by

$$\vec{\Delta}^{(0)} = \sqrt{\frac{|\tilde{a}|}{\tilde{b}(3 + r^2)}} \begin{pmatrix} 2 \\ -r - 1 \\ r - 1 \end{pmatrix}, \quad (2.40)$$

where $r = |\psi_1|/|\psi_2|$ serves as a parameter. The corresponding free-energy density $f = \mathcal{F}/V$ is obtained as

$$f = -\tilde{a}^2/\tilde{b}. \quad (2.41)$$

Notice that since Eq. (2.41) does not depend on r , this quantity is not fixed and therefore we obtain a continuous family of solutions with the same free-energy density.

The second solution class is obtained when n is odd, i.e., $\delta\phi = \pi/2, 3\pi/2, \dots$ and $\cos(2\delta\phi) = -1$. In this case, Eqs. (2.35b) and (2.35c) yield the system of two equations

$$-\tilde{a}/|\psi_1|^2 = \tilde{b}(1 + r^{-2}), \quad (2.42a)$$

$$-3\tilde{a}/|\psi_1|^2 = \tilde{b}(1 + 9r^{-2}). \quad (2.42b)$$

This system is solved trivially giving $|\psi_1|^2 = 3\tilde{a}/(4\tilde{b})$ and $r = \sqrt{3}$. Then, using Eqs. (2.42) and taking $\delta\phi = \pi/2, 5\pi/2, \dots$ and $\delta\phi = 3\pi/2, 7\pi/2, \dots$ we obtain two different solutions as

$$\vec{\Delta}^{(0)} = i\sqrt{\frac{|\tilde{a}|}{\tilde{b}}} \begin{pmatrix} 1 \\ e^{i2\pi/3} \\ e^{-i2\pi/3} \end{pmatrix}; \quad -i\sqrt{\frac{|\tilde{a}|}{\tilde{b}}} \begin{pmatrix} 1 \\ e^{-i2\pi/3} \\ e^{i2\pi/3} \end{pmatrix}. \quad (2.43)$$

These are chiral solutions with a nontrivial phase difference between the band gaps. The free-energy density for both of them reads as

$$f = -3\tilde{a}^2/(2\tilde{b}). \quad (2.44)$$

Comparing this with Eq. (2.41) reveals that the chiral solution is more favorable energetically and thus three-band model with strong interband couplings supports the formation of the chiral state.

Note that Eqs. (2.40) and (2.43) are the two solution classes of Eq. (2.38). They arise due to the fact that the solution for the critical temperature is twofold degenerated which leads to Eq. (2.32) for the band gaps. As seen from Eq. (2.32) the band gaps scale differently already at $T = T_c$, i. e., when the system enters the superconducting regime. This difference in the band gaps can arise either from a difference of amplitude gaps or an emergent phase difference between the band gaps. Therefore, it is logical that Eq. (2.40) gave rise to two sorts of solution, i.e., the first one with difference in amplitude gaps given by Eq. (2.40), while the second class corresponds to the solution with the non-trivial phase difference between the band gaps given by Eq. (2.43). Both these solution classes were obtained as a consequence of the symmetry of the chosen coupling matrix with the strong interband interaction.

This conclusion agrees with the numerical simulations of Eq. (2.6) for the three-band case [6], which showed that the chiral state with the phase shifts $\pm 2\pi/3$ is found at $T \rightarrow T_c$ only in the limit $g_{23} \rightarrow g_{12} = g_{13}$. The phase shift obtained in our work is independent of temperature, which differs from the numerical simulations of Ref. [6]. We note, however, that these simulations employed the unreconstructed GL equations, where a solution does not account for all relevant terms of the τ -expansion. A correct temperature dependence of the phase shift must be calculated with the help of the extended multiband GL formalism that should be constructed in the spirit of the approach of Ref. [217].

As already mentioned above, the appearance of the chiral state may indicate the symmetry of the model, reflected in the structure of the coupling matrix. In particular, the matrix investigated in this Section can be realized by choosing the bands as the pockets of the Fermi surface centered around the \mathbf{X} points of the Brillouin zone of the *fcc* lattice (see Ref. [5]). The band gaps are then transformed according to a three dimensional representation of the O_h cubic symmetry group. This representation splits into one dimensional A_g and two-dimensional E_g irreducible representations. The two-dimensional representation E_g , which corresponds to the highest critical temperature, can have its basis chosen as two vectors in Eq. (2.43). Constructing the Landau theory from this irreducible representation, one recovers the reconstructed GL formalism discussed above, which additionally proves its validity.

Here, we stress that recasting the multicomponent GL theory (2.6) in terms of the basis functions of the symmetry-group representations does not eliminate admixtures of different irreducible representations in the free-energy functional [5]. However, following our analysis, such admixtures must

be neglected as they exceed the accuracy of the GL theory, in full agreement with the standard Landau approach. The proper accounting of the admixture terms can be done only by employing the extended GL theory which collects all relevant higher-order terms in the expansion of the band gaps.

Finally, as the chiral state is related to the degeneracy of a solution for T_c that can be caused by, e.g., the crystalline symmetry, the existence of any simple relation between the chiral state and signs of the interband coupling $\gamma_{i \neq j}$, as suggested in Refs. [211, 207, 208, 209] appears to be very questionable at least in the GL domain. Notice that this conclusion is also supported by numerical solutions of Eqs. (2.6) performed in Ref. [6].

2.5 Summary and conclusions

In this Chapter, we have derived the consistent multiband GL theory from the multiband BCS Hamiltonian. The derivation applies a reconstruction procedure to the conventional Gor'kov truncation of the matrix gap equation. This reconstruction invokes the expansion in powers of τ and removes incomplete contributions to band gaps of orders higher than $\tau^{1/2}$, thus matching the accuracy of the gap with that of the Gor'kov truncation.

When the solution for T_c is not degenerate, we recover the earlier results of Ref. [19, 20, 216, 217] that the GL theory of a multiband superconductor maps onto a single-component GL formalism in which the spatial profiles of all band gaps are equivalent. However, this result is valid only in the standard GL domain, i.e., to the accuracy $\Delta_i \propto \tau^{1/2}$. Differences between the spatial profiles of the band gaps appears already in the leading correction to the GL theory [216, 217].

If the solution for T_c is degenerate, which appears due to a symmetry of the system, the GL theory acquires several order parameters. We have carried out a detailed analysis for the three-band system treated as a prototype of a multiband superconductor. For the simple three-band model of pnictides with dominant interband couplings, the solution for T_c is twofold degenerate and the GL theory has two order parameters ψ_α which correspond to the two-dimensional irreducible representation of the relevant symmetry group, in full agreement with the Landau theory. We have shown that the band energy gaps themselves can not be interpreted as the Landau order parameters in a multiband superconductor due to the Josephson-type coupling between bands.

Our approach yields explicit expressions for the coefficients of the GL theory. Also, the formalism provides a solid basis for further extensions of the theory and, in particular, offers the correct way to account for the

influence of other irreducible representations not inherent in the ordinary GL approach.

It is worth noting that the origin of the degeneracy of T_c is not always due to the crystalline symmetry. It can arise, e.g., in the atomically flat superconducting nanofilms, where the size quantization of the perpendicular motion of electrons results in the formation of multiple single-electron subbands [112, 109, 201, 119, 120]. Such superconducting nanofilms can be regarded as effectively multiband superconductors with the interaction matrix [219, 220, 221] $g_{ij} = g(1 + \delta_{ij}/2)/d$, where d is the nanofilm thickness and g is the coupling constant for the material of the nanofilm. The structure of this matrix is similar to that of \tilde{g} investigated in Subsection 2.4.2 and, as a result, a degenerate solution for T_c also appears in this case. The developed formalism thus provides a general link between the multiband BCS theory and the phenomenological Landau model for multiband superconductors, irrespective of the origin of the symmetry.

We conclude by noting that the degenerate regime manifests itself in several important physical consequences such as the formation of the chiral ground state and the appearance of different spatial length scales of the band condensates, which can be observed at $T \rightarrow T_c$. This may result in a plethora of new phenomena, i.e., fractional vortices [210], flux-carrying topological solitons [178], and other exotic states [223, 224, 225, 226]. So far, those phenomena have been studied using the unreconstructed multicomponent GL model given by Eq. 2.6, and so we suggest revisiting these problems in the framework of the true GL formalism.

The author contributed significantly to the main ideas, performed all analytical calculations starting from the first truncation, suggested a method on restoration of the Ginzburg-Landau functional from the Ginzburg-Landau equation, analyzed the data and the literature.

*The results presented in this Chapter were published as: N. V. Orlova, A. A. Shanenko, A. V. Vagov, M. V. Milošević, and F. M. Peeters, Ginzburg-Landau theory for multiband superconductors: Microscopic derivation, Phys. Rev. B **87**, 134510 (2013).*

CHAPTER 3

Nanofilms as multiband superconductors

In Chapter 1, it was shown that nanofilms (or superconductors under quantum confinement) can also evolve multiband structure when the nanofilm thickness is varied. In this Chapter, a corresponding BCS theory for such nanofilms is developed and a Ginzburg-Landau theory which can be suitable to study such systems is derived. At the derivation, the same problem with higher order contributions in the band gaps arises. Therefore, the elegant method on removing the higher order contributions from the band gaps which was developed in Chapter 2 is vitally needed here.

3.1 Introduction

Recent advances in nano-fabrication resulted in superconducting single crystalline metallic nanofilms with atomically uniform thickness (see e.g., [112, 109, 201, 119, 120]), including world-thinnest one-atomic-layer superconductors made of In and Pb [114, 227]. Another exciting development in the field of superconductivity is an avalanche of novel compounds (e.g., metallic borides, iron pnictides and chalcogenides) that constitute a new class: the multiband superconductors [56, 99, 228, 229]. At first sight, superconducting metallic nanofilms bear little similarity to the multiband superconducting compounds. However, there exists an important common feature. The single-particle energy spectrum in a perfectly uniform high-quality nanofilm is tightly bound in the perpendicular quantum-confined direction due to the formation of quantum-well states (QWS), similar to the Fabry-Pérot

modes in an optical interferometer. This leads to the formation of a series of single-particle subbands, where the bottom of each subband coincides with the corresponding QWS. As a result, the superconducting condensate in the nanofilm becomes a coherent mixture of different subband condensates, i.e. *the superconducting metallic single-crystalline nanofilms are effectively multi(sub)band superconductors*.

Multiband materials are believed to harbor new superconducting phenomena, such as the highly-debated exotic vortex configurations in MgB_2 [1, 206, 230, 212, 223, 224, 225, 2], solitonic solutions [231, 210], chiral states [5, 6, 213], hidden criticality [7], and the recently observed crossover from the Bardeen-Cooper-Schrieffer (BCS) regime to the Bose-Einstein condensation (BEC) in $\text{FeSe}_x\text{Te}_{1-x}$ [3]. However, an important property of a bulk material is that its multiband structure is always fixed. As opposed to that, the number of contributing subbands in an atomically flat nanofilm is *controllable* by the nanofilm thickness. Moreover, even for a fixed thickness of the sample, energetic positions of the subbands and, as a result, their microscopic parameters (such as e.g., the densities of states and the subband Fermi velocity) can still be changed: the formation of the QWS depends on the presence of a protective cover, on a particular substrate, on the character of the interface between the film and substrate etc. Therefore, single-crystalline metallic nanofilms are *quantum-engineered multiband superconductors*, and as such present a prime candidate for further investigations of exciting physics of multi-coupled superconducting condensates. Moreover, being atomically flat, these films are well suited for scanning-probe experimentation of their superconducting gap or vortex structure [114].

Superconductivity in atomically flat single-crystalline nanofilms is clearly an extremely interesting subject, but was scarcely investigated to date¹. One of the main reasons for this is the absence of a reliable and solvable formalism such as, e.g., the Ginzburg-Landau (GL) theory [27]. Successive applications of the GL functional range from condensed-matter theory (e.g., phase transitions and fluctuation phenomena, superconductivity and superfluidity) to high-energy physics (e.g., Higgs mechanism). However, neither 3D nor 2D variants of the ordinary GL functional are justified for single-crystalline nanofilms. Here the system size perpendicular to the film is much smaller than the bulk Cooper-pair radius and therefore the Gor'kov derivation [29, 87, 222] of the 3D GL formalism does not hold. Furthermore, due to the size-quantization the superconducting order parameter exhibits fast spatial variations in the direction perpendicular to the nanofilm [232] and

¹Only a few theoretical works, that are mainly focused on the superconducting quantum-size effects, see, e.g., [76, 81, 220, 232], have been published to date.

therefore it is not possible to employ the ordinary 2D GL formalism that is usually well justified in films with thickness smaller than the GL coherence length but larger than the bulk Cooper-pair size, i.e., when the order parameter can be assumed almost spatially uniform in the perpendicular direction.

In this Chapter, we derive the GL theory appropriate for single-crystalline metallic nanofilms and demonstrate that the presence of the size quantization indeed leads to a multiband formalism. This formalism is computationally convenient and efficient, and will present a powerful theoretical tool for further studies of the effects of the multiple-subband structure on, e.g., vortex configurations, critical phenomena and superconducting fluctuations in nanothin single-crystalline systems.

3.2 Multiband BCS Hamiltonian for nano-films

According to recent experiments, superconducting fluctuations play a minor role in single-crystalline metallic nanofilms with thicknesses $> 5-8$ atomic layers where it was shown that the energy gap as a function of temperature follows almost perfectly the BCS temperature trend (see, e.g., in [109]). Even for thicknesses under 5 atomic layers, coherent behavior and vortices were found, e.g., see [114] for such results in one-atomic-layer Pb and In nanofilms. Fluctuations become important in the latter regime (first serious evidences are reported in [233]) but a convenient and reliable theoretical platform to study them is still lacking². With all these facts in mind, we construct the appropriate GL functional for single-crystalline metallic nanofilms starting from the general expression for the BCS mean-field Hamiltonian of s-wave superconductors

$$H_{\text{BCS}} = \mathcal{C} + \int d^3x \left\{ \sum_{\sigma} \hat{\psi}_{\sigma}^{\dagger}(\mathbf{x}) T_{\mathbf{x}} \hat{\psi}_{\sigma}(\mathbf{x}) + [\hat{\psi}_{\uparrow}^{\dagger}(\mathbf{x}) \hat{\psi}_{\downarrow}^{\dagger}(\mathbf{x}) \Delta(\mathbf{x}) + \text{h.c.}] \right\}. \quad (3.1)$$

Here $T_{\mathbf{x}}$ is the single-electron Hamiltonian absorbing the chemical potential μ and the relevant confinement potential; $\Delta(\mathbf{x}) = g \langle \hat{\psi}_{\uparrow}(\mathbf{x}) \hat{\psi}_{\downarrow}(\mathbf{x}) \rangle$ (with $g > 0$ the coupling constant) is the superconducting order parameter; \mathcal{C} stands for a c -number term that is not important for the present analysis. In atomically uniform nanofilms it is natural to introduce the perpendicular and parallel

²As is well-known, the easiest and reliable approach to probe effects due to superconducting fluctuations is to employ the partition function constructed from the GL functional. The appropriate GL functional for single-crystalline atomically uniform metallic nanofilms is derived here.

spatial degrees of freedom, i.e.,

$$T_{\mathbf{x}} = T_{\perp} + T_{\parallel} - \mu, \quad \hat{\psi}_{\sigma}(\mathbf{x}) = \sum_j \vartheta_j(x_{\perp}) \hat{\psi}_{j\sigma}(x_{\parallel}), \quad (3.2)$$

where $\mathbf{x} = (x_{\perp}, x_{\parallel})$, with x_{\perp} the perpendicular coordinate and x_{\parallel} the set of coordinates associated with the in-plane motion; $\vartheta_j(x_{\perp})$ denotes the wave function of the j th QWS; and the new field operators $\hat{\psi}_{j\sigma}^{\dagger}(x_{\parallel})$ and $\hat{\psi}_{j\sigma}(x_{\parallel})$ obey the canonical anti-commutation relations typical of fermions and, so, can be viewed as the subband field operators.

In nanofilms $\Delta(\mathbf{r})$ exhibits fast oscillations with a period of $\lambda_F/2$ (with λ_F the 3D Fermi wavelength) as a function of x_{\perp} [232]. As known from textbooks [29, 222], such fast variations do not allow the ordinary Gor'kov derivation of the GL theory. To construct a proper generalization, we need to integrate out the “fast” perpendicular coordinates. This makes it possible to express the reduced BCS Hamiltonian of Eq. (3.1) in terms of $\hat{\psi}_{j\sigma}^{\dagger}(x_{\parallel})$ and $\hat{\psi}_{j\sigma}(x_{\parallel})$. The resulting expression can be considerably simplified when keeping in mind the relevant energy scales in superconducting nanofilms: the energy spacing δ between the neighboring QWS (between the neighboring subbands) is much larger than the pairing energy. For δ we have $\delta \sim \frac{\hbar^2}{2m} \left(\frac{\pi}{d}\right)^2$, with d the nanofilm thickness, whereas the pairing energy is of order Δ_{bulk} , the zero-temperature bulk excitation gap. One easily finds $\delta = 200\text{-}400$ meV for $d = 1\text{-}2$ nm, which is a few orders of magnitude larger than the typical metallic values of the bulk gap, i.e., $\Delta_{\text{bulk}} = 0.1\text{-}2$ meV. Therefore, one can expect that the pairing between electrons from different single-electron subbands is strongly suppressed, i.e., two electrons from different subbands are not able to form a Cooper pair. The same conclusion follows from a numerical study of the Bogoliubov-de Gennes equations [234]. This allows one to invoke *the intraband-pairing approximation*, i.e.,

$$\int d^3x \hat{\psi}_{\uparrow}^{\dagger}(\mathbf{x}) \hat{\psi}_{\downarrow}^{\dagger}(\mathbf{x}) \Delta(\mathbf{x}) \simeq \sum_j \int dx_{\parallel} \hat{\psi}_{j\uparrow}^{\dagger}(x_{\parallel}) \hat{\psi}_{j\downarrow}^{\dagger}(x_{\parallel}) \Delta_j(x_{\parallel}), \quad (3.3)$$

where

$$\Delta_j(x_{\parallel}) = \int dx_{\perp} [\vartheta_j^*(x_{\perp})]^2 \Delta(\mathbf{x}) \quad (3.4)$$

can be interpreted as the subband order parameter. Plugging Eq. (3.3) into Eq. (3.1), we obtain the intraband-approximation to the BCS Hamiltonian,

i.e.,

$$H_{\text{BCS}} \simeq \mathcal{C} + \sum_j \int dx_{\parallel} \left\{ \sum_{\sigma} \hat{\psi}_{j\sigma}^{\dagger}(x_{\parallel}) T_{j,\parallel} \hat{\psi}_{j\sigma}(x_{\parallel}) + [\hat{\psi}_{j\uparrow}^{\dagger}(x_{\parallel}) \hat{\psi}_{j\downarrow}^{\dagger}(x_{\parallel}) \Delta_j(x_{\parallel}) + \text{h.c.}] \right\}, \quad (3.5)$$

where we introduce $T_{j,\parallel} = \varepsilon_j + T_{\parallel} - \mu$, with the QWS-energy

$$\varepsilon_j = \int dx_{\perp} \vartheta_j^*(x_{\perp}) T_{\perp} \vartheta_j(x_{\perp}).$$

As seen, Eq. (3.5) represents the multiband generalization of the BCS two-band model [88, 89]. Note that we adopt the set-up of a perpendicular external magnetic field that is most interesting for experimental applications. Inside the nanofilm we assume $\mathbf{B} = \mathbf{B}_{\perp}(x_{\parallel})$ and choose $\mathbf{A} = \mathbf{A}_{\parallel}(x_{\parallel})$.

The self-consistency equation $\Delta(\mathbf{x}) = g \langle \hat{\psi}_{\uparrow}(\mathbf{x}) \hat{\psi}_{\downarrow}(\mathbf{x}) \rangle$ can also be expressed in terms of the subband-dependent variables as

$$\Delta_i(x_{\parallel}) \simeq \sum_j g_{ij} \langle \hat{\psi}_{j\uparrow}(x_{\parallel}) \hat{\psi}_{j\downarrow}(x_{\parallel}) \rangle, \quad (3.6)$$

where we again neglect the pairing of electrons from different subbands, i.e.,

$$\langle \hat{\psi}_{\uparrow}(\mathbf{x}) \hat{\psi}_{\downarrow}(\mathbf{x}) \rangle \simeq \sum_j \vartheta_j^2(x_{\perp}) \langle \hat{\psi}_{j\uparrow}(x_{\parallel}) \hat{\psi}_{j\downarrow}(x_{\parallel}) \rangle, \quad (3.7)$$

and the coupling-matrix element reads as

$$g_{ij} = g \int dx_{\perp} [\vartheta_i^*(x_{\perp})]^2 \vartheta_j^2(x_{\perp}). \quad (3.8)$$

We notice again that the intraband-pairing approximation, i.e., Eqs. (3.3), (3.5), (3.6) and (3.7), is relevant when $\delta/\Delta_{\text{bulk}} \gg 1$ and exact in the limit $\delta/\Delta_{\text{bulk}} \rightarrow \infty$.

3.3 Gor'kov truncation for multiband superconductors

The second step in our derivation is to employ the known procedure of the Gor'kov truncation for multiple bands, see, e.g., [75]. First, one assumes that the subband order parameters and their spatial gradients are small enough (which is always valid in the vicinity of the critical temperature). Then, the

anomalous Green function of each subband can be represented as an infinite series in powers of the corresponding subband order parameter and its spatial gradients. When truncating this series in the manner of Gor'kov [29, 222, 75, 20, 216, 218], we obtain

$$\langle \hat{\psi}_{j\uparrow}(x_{\parallel}) \hat{\psi}_{j\downarrow}(x_{\parallel}) \rangle = (\mathcal{A}_j - a_j) \Delta_j - b_j \Delta_j |\Delta_j|^2 + \mathcal{K}_j \mathbf{D}^2 \Delta_j, \quad (3.9)$$

with \mathbf{D} the gauge-invariant gradient and

$$\mathcal{A}_j = N_j(0) \ln \left(\frac{2e^{\Gamma} \hbar \omega_D}{\pi T_c} \right), \quad a_j = -N_j(0) \tau, \quad b_j = N_j(0) \frac{7\zeta(3)}{8\pi^2 T_c^2}, \quad \mathcal{K}_j = \frac{b_j}{4} \hbar^2 v_j^2, \quad (3.10)$$

where $\tau = 1 - T/T_c$ is the proximity to the critical temperature; the Boltzmann coefficient k_B is set to unity; $N_j(0)$ and v_j are the subband density of states and Fermi velocity, respectively; $\zeta(\dots)$ is the Riemann zeta-function and $\Gamma = 0.577$ stands for the Euler constant. Note that the factor $\frac{1}{4}$ in the expression for \mathcal{K}_j appears because of the 2D character of the single-electron subbands. For 3D systems $\frac{1}{4}$ is replaced by $\frac{1}{6}$, see e.g., Refs. [222, 29, 75, 20, 216, 218]. Inserting Eq. (3.9) into Eq. (3.6), we find the following equations for the subband order parameters:

$$\alpha_j \Delta_j + b_j \Delta_j |\Delta_j|^2 - \mathcal{K}_j \mathbf{D}^2 \Delta_j + \sum_{i \neq j} \phi_{ji} \Delta_i = 0, \quad (3.11)$$

where ϕ_{ji} is the inverse of the interaction matrix g_{ji} , and $\alpha_j = \phi_{jj} - \mathcal{A}_j + a_j$. We remark that the last term in the l.h.s. of Eq. (3.11) is the Josephson-like coupling responsible for the ‘‘tunneling’’ of Cooper pairs from one subband to another. The free-energy functional (measured from the normal-state free energy at $\mathbf{B} = 0$) corresponding to Eq. (3.11) reads

$$\mathcal{F} = \int d^3x \left\{ \frac{\mathbf{B}^2}{8\pi} + \delta(x_{\perp}) \left[\sum_j (\alpha_j |\Delta_j|^2 + \frac{b_j}{2} |\Delta_j|^4 + \mathcal{K}_j |\mathbf{D} \Delta_j|^2) + \sum_{i \neq j} \phi_{ji} (\Delta_i \Delta_j^* + \text{c.c.}) \right] \right\}, \quad (3.12)$$

and the stationary point $\frac{\delta \mathcal{F}}{\delta \mathbf{A}} = 0$ yields the supplemental Maxwell equation.

Note that the coefficients of Eq. (3.10) have been derived for the case when all the contributing QWS are far below the Fermi level, i.e., $\varepsilon_j \ll \mu$. However, as already mentioned, the energetic positions of the subbands vary significantly when changing the nanofilm thickness and details of fabrication.

It may therefore occur that one of the QWS will be situated in the vicinity of μ which corresponds to a shape Blatt-Thompson superconducting resonance [235, 236]. In that case Eq. (3.11) remains the same but some of the coefficients related to such a resonant subband will be different. In particular, when the bottom of the resonant subband (with the quantum number k) touches exactly μ , i.e., $\varepsilon_k = \mu$, we find

$$\mathcal{A}_k = \frac{N_k(0)\mathcal{A}}{2}, \quad a_k = \frac{N_k(0)\tau}{2}, \quad \mathcal{K}_k = N_k(0)\frac{\hbar^2}{16mT_c}, \quad (3.13)$$

while b_k is unaltered and given by Eq. (3.10). Note that the coefficient for the gradient term in the equation for the gap in the resonant subband has a completely different dependence on T_c and, of course, does not contain the subband Fermi velocity that is exactly equal to zero for the case $\varepsilon_k = \mu$. Interestingly, it resembles the dirty-limit expression for $\mathcal{K}_j \propto D_j/T_c$, with D_j the subband diffusion coefficient (see e.g., [237]). As recently found, the superconducting nanofilm approaches the BCS-BEC crossover when one of the contributing single-electron subbands crosses μ [238] (see also [239]). The qualitative change in the temperature dependence of \mathcal{K}_k in Eq. (3.13) is a signature of this phenomenon. Indeed, \mathcal{K}_j is proportional to the Cooper-pair size $\xi_{0,j}$ associated with the given subband. Based on Eq. (3.10) we obtain $\xi_{0,j} \sim \hbar v_j/T_c$ while Eq. (3.13) yields $\xi_{0,k} \sim \hbar/(mT_c)^{1/2}$ for the resonant subband. Thus, we have $\xi_{0,j}/\xi_{0,k} \sim (\mu/T_c)^{1/2}$, which means that $\xi_{0,k}$ becomes smaller by two orders of magnitude, i.e. we obtain a clear signature of approaching the BCS-BEC crossover in the resonant subband in agreement with the recent finding of [238].

Equation (3.10) has been derived for a clean system and therefore the effects of scattering on imperfections are not included (e.g., on the interface between the nanofilm and the substrate). Though single-crystalline metallic nanofilms are usually characterized by an extraordinary purity (see, e.g., discussion about the mean-free path in In nanofilms in [240]), it is important to outline how to incorporate effects of moderate disorder. In the presence of an extremely large energy scale induced by the perpendicular quantum confinement, we can take impurity scattering into account as a perturbation, preserving, to a first approximation, the separation of the in-plane and perpendicular electronic motion. This will produce a similar multiband formalism but with in-plane motion specified by quasi-randomly distributed levels in an almost equidistant manner, i.e., the in-plane motion will acquire a diffusive character. Then, in the simplest approach, one may replace (see e.g., [202, 203]) \mathcal{K}_j of Eq. (3.10) by its dirty-limit 2D expression $3\pi D_j/(16T_c)$ (\mathcal{A}_j , a_j and b_j will remain the same). In addition, a step-like

jump in the subband-dependent density of states at the energy of the corresponding perpendicular level will be smoothed due to the broadening of the QWS. Such a broadening can be estimated as c.a. 30-40 meV (at zero temperature and for the QWS close to the Fermi level) [241], which is much smaller than the interband energy spacing δ in metallic nanofilms.

3.4 Reconstructed truncation and the GL theory

The above straightforward application of the Gor'kov truncation in the case of multiple (sub)bands is a well established procedure. However, it has significant and well-hidden problems. It was recently shown [20, 216] (but also known from 1960's, see [19]) that the theory constructed in this manner includes incomplete higher-order terms in powers of τ . In other words, the accuracy of a solution to this formalism exceeds the accuracy of the Gor'kov truncation. Indeed, α_j in Eqs. (3.11) and (3.12) does not approach zero when $\tau \rightarrow 0$: T_c is unique in the system and so ϕ_{jj} cannot be equal to \mathcal{A}_j for all subband condensates. The consequence of this fact is that a solution to Eq. (3.11) is not proportional to $\tau^{1/2}$ (as it is in the single-band case and should be in the Landau theory) but includes higher-order terms $\propto \tau^{3/2}, \tau^{5/2}$ etc. (Here we refer an interested reader to detailed calculations in Refs. [20, 216, 218].) These higher-order terms are incomplete because Eq. (3.9) does not keep all contributions relevant for such higher orders. Thus, the incomplete terms must be avoided to obtain a trustworthy formalism.

With this in mind, we rewrite Eq. (3.11) in the matrix form

$$\check{L}\vec{\Delta} = \vec{R}, \quad (3.14)$$

where $\vec{\Delta} = (\Delta_1, \dots, \Delta_n)^T$, \check{L} is the matrix with elements $L_{ij} = \phi_{ij} - \mathcal{A}_i \delta_{ij}$, and \vec{R} has components $R_j = -a_j \Delta_j - b_j \Delta_j |\Delta_j|^2 + \mathcal{K}_j \mathbf{D}^2 \Delta_j$. Next, we introduce the expansion

$$\vec{\Delta} = \vec{\Delta}^{(0)} + \vec{\Delta}^{(1)} + \mathcal{O}(\tau^{5/2}), \quad (3.15)$$

where $\Delta_i^{(0)} \propto \tau^{1/2}$ and $\Delta_i^{(1)} \propto \tau^{3/2}$. Inserting Eq. (3.15) into Eq. (3.14) and matching terms of the order $\tau^{1/2}$, we obtain

$$\check{L}\vec{\Delta}^{(0)} = 0. \quad (3.16)$$

For a nontrivial solution of Eq. (3.16), we should have $\det \check{L} = 0$ which gives the equation for T_c . To go further, we need to specify the interaction matrix: $g_{ij} = g(1 + \delta_{ij})/d$, for infinite confining interaction [235, 236]. The matrix

ϕ_{ij} has a similar structure: $\phi_{ii} = \zeta$ and $\phi_{ij}|_{i \neq j} = \chi$, where $\zeta > 0$ and $\chi < 0$ are proportional to d/g (e.g., for the case of three contributing subbands $\vartheta = 10d/(7g)$ and $\chi = -4d/(7g)$). Then, given the concrete form of ϕ_{ij} , the solution to Eq. (3.16) reads ³

$$\vec{\Delta}^{(0)}(x_{\parallel}) = \psi(x_{\parallel})\vec{\eta}, \quad \eta_j = N(0)(\zeta - \chi - \mathcal{A}_j)^{-1}, \quad (3.17)$$

with $N(0) = \sum_j N_j(0)$ the total density of states. As seen, all subband gaps are proportional to $\psi(x_{\parallel})$, and it remains to determine $\psi(x_{\parallel})$.

Selecting terms of the order $\tau^{3/2}$ in Eq. (3.14), we find $\check{L}\vec{\Delta}^{(1)} = \vec{R}^{(0)}$, where $R_j^{(0)}$ can be obtained from R_j by substituting $\Delta_j^{(0)}$ for Δ_j . We rewrite this result as $[\vec{\Delta}^{(0)}]^\dagger \vec{R}^{(0)} = 0$, which can further be rearranged to the familiar GL form

$$a\psi + b\psi|\psi|^2 - \mathcal{K}\mathbf{D}^2\psi = 0, \quad (3.18)$$

with $a = \sum_j \eta_j^2 a_j$, $b = \sum_j \eta_j^4 b_j$, $\mathcal{K} = \sum_j \eta_j^2 \mathcal{K}_j$. The corresponding GL free energy reads

$$\mathcal{F}_{\text{GL}}^{(\text{nano})} = \int d^3x \left\{ \frac{\mathbf{B}^2}{8\pi} + \delta(x_{\perp}) \left[a|\psi|^2 + \frac{b}{2}|\psi|^4 + \mathcal{K}|\mathbf{D}\psi|^2 \right] \right\}, \quad (3.19)$$

and the variation of $\mathcal{F}_{\text{GL}}^{(\text{nano})}$ with respect to \mathbf{A} gives the accompanying Maxwell equation in the form

$$\frac{c}{4\pi} \text{rot} \mathbf{B} = \delta(x_{\perp}) \mathbf{j}_{2D}, \quad (3.20)$$

where

$$\mathbf{j}_{2D} = i \frac{2e\mathcal{K}}{\hbar} (\psi \mathbf{D}\psi^* - \psi^* \mathbf{D}\psi) \quad (3.21)$$

is the 2D current density in the film plane, referred to as the sheet current density.

Equations (3.17)-(3.21) constitute the GL formalism for nano-thin superconductors where the formation of the QWS strongly influences the properties of the system. As seen, this formalism maps effectively onto the single-band 2D GL theory. However, the coefficients a , b and \mathcal{K} are specified by completely different microscopic expressions, involving the summation over the contributing subbands. In addition, ψ is not an excitation gap: the subband gaps Δ_j are proportional to ψ . In fact ψ is the true Landau order parameter for nano-thin superconductors.

³As shown in [220], the equation for T_c has more than one solution. One must select the maximal T_c for which $\zeta - \chi - \mathcal{A}_i \neq 0$ for all species, and the use of Eq. (3.17) is fully justified.

The equations have two characteristic lengths, the GL coherence length ξ and the 2D magnetic screening length Λ , given by

$$\xi = \sqrt{\frac{\mathcal{K}}{|a|}}, \quad \Lambda = \left(\frac{\Phi_0^2}{2\pi}\right)^2 \frac{b}{4\pi\mathcal{K}|a|}, \quad (3.22)$$

with Φ_0 is the flux quantum. Λ can be roughly estimated as inversely proportional to the number of contributing subbands N . In the limit $N \gg 1$ the quantum-size effects are weakened and eventually washed out. In this case one can estimate the number of subbands as $N \approx d/\lambda_F$, where d is the film thickness. This yields $\Lambda \propto 1/d$, which is the well known Pearl result for superconducting films [242].

Notice that for the diffusive in-plane motion Eqs. (3.17)-(3.21) remain the same but, as already mentioned above, \mathcal{K}_j given by Eq. (3.10) should be replaced by its dirty-limit expression (a_j and b_j are not altered).

We also note that the GL formalism given by Eqs. (3.17)-(3.19) represents the theory to the leading-order in τ (see [216, 218]). However, due to the scaling given in Eq. (3.17), this formalism will not capture the physics based on the interplay of the different length scales of the different subband condensates [243]. To shed light on that phenomenon one should construct an extended GL formalism by accurately including terms of the order $\tau^{3/2}$ in Δ_j , see, e.g., [216, 218].

3.5 Applicability domain of the GL theory for nanofilms

We now address the important issue about the applicability domain of the GL theory for nano-thin superconductors. For single-band superconducting materials this domain is $\tau \ll 1$. However, for multiband superconductors it can shrink in the presence of (sub)bands that have significantly different properties [203, 244, 245]. This observation follows from the applicability of the gradient expansion involved in the derivation of the GL theory, which requires the condition $\xi \gg \xi_{0,i}$, where ξ is the GL coherence length and $\xi_{0,i}$ controls the spatial variations of the kernels in the integral expansion of the anomalous Greens function in powers of the band excitation gap ($\xi_{0,i}$ can be viewed as the Cooper-pair radius in a given band). Then, e.g., for the clean limit, one has $\xi_{0,i} = \hbar v_i / (2\pi T_c)$ and the condition of the applicability of the gradient expansion becomes:

$$\tau \ll \gamma = \min_i \sum_j v_j^2 \rho_j / v_i^2, \quad (3.23)$$

where $\rho_i = N_0(0)\eta_i^2 / \sum_j N_j(0)\eta_j^2$. One can have a situation when the band with the largest Fermi velocity does not make a significant contribution to γ . In this case $\gamma < 1$ and, consequently, the validity domain of the gradient expansion shrinks, which recovers the arguments of Refs. [203, 244, 245]. This point should always be taken into account in studies of bulk multiband superconductors.

However, simple arguments demonstrate that the validity domain of the GL theory for nano-thin superconductors is essentially the same as for bulk single-band materials. For a regular case, when all contributing QWS are well below the Fermi level, η_j s and v_j s in all contributing subbands are of the same order of magnitude and thus $\gamma \sim 1$. Changes in γ can be expected only in the vicinity of a shape resonance (here Eq. (3.23) should be altered to take into account Eq. (3.13). In this case $\xi_{0,i}$ associated with the resonant subband decreases, in some cases by orders of magnitude, as discussed above, see Eq. (3.13). However, the corresponding drop in ξ is much less pronounced. The short-length contribution of the resonant subband to ξ is almost negligible as compared to the long-length contributions of the other subbands. The resonant decreasing factor for ξ can be estimated as $1 - 1/N$, where, we recall that N is the number of the contributing subbands. Then, γ decreases by a factor of $(1 - 1/N)^2$. In all practical situations the nanofilm has many contributing subbands with $N \gg 1$, which implies $\gamma \sim 1$. Thus, the validity domain of the GL theory for the nano-thin superconductors remains $\tau \ll 1$.

3.6 Summary and conclusions

Single-crystalline metallic nanofilms with thickness down to a few atomic layers constitute a new class of superconductors, i.e., quantum-engineered multiband superconductors. As opposed to bulk multiband superconductors, the number of subbands in nano-thin superconductors, but also their energetic positions and thus the properties, can be coarsely varied via the thickness, a chosen substrate, the character of the interface, the presence/absence of a protective cover etc. Future experiments using the electrostatic doping [246, 247, 248] are expected to provide a way to fine-tune subbands in nanofilms by giving the method on how to increase or decrease charge carrier density without causing structural disorder in nanofilms. Such outstanding flexibility opens new prospects for the experimental studies of multiband coherent phenomena but also rises significant theoretical challenges. One of them is the formulation of the GL theory for high-quality metallic nanofilms that has been constructed in this work. This convenient theoretical tool will

enable further analytical and numerical calculations of the critical parameters, vortex matter in applied magnetic field, and exploration of the impact of phase fluctuations, all as a function of the number of multiple contributing subbands (thickness). We have also provided the GL formalism for studies of a superconducting shape resonance and/or dirty samples, which are bound to host different physics from their clean and non-resonant counterparts. With these scientific prospects, we conclude that our results can give a new impetus to interest in nanoscale superconductivity.

The author contributed substantially to the main ideas, suggested a method on restoration of the Ginzburg-Ladnau functional from the Ginzburg-Landau equation.

*The results presented in this Chapter were published as: A. A. Shanenko, N. V. Orlova, A. Vagov, M. V. Milošević, V. M. Axt and F. M. Peeters, Nanofilms as quantum-engineered multiband superconductors: the Ginzburg-Landau theory, EPL **102**, 27003 (2013).*

CHAPTER 4

Skyrmionic vortex lattices in three-component BECs

The study presented in this Chapter, was motivated by the results of Chapter 2, in which the chiral solutions were found in the case of three-band superconductivity. Those solutions arise as consequence of non-trivial phase difference between the band gaps. It is known that such non-trivial phase difference can lead to existence of novel topological defects, such as skyrmions [178, 197]. The needed parametric regimes in which skyrmions should be stable are not achieved in available superconducting materials. However, they are reachable in three-component BECs, where components can be experimentally tuned in a broad parametric range. Therefore, the aim of the present work was to study a regime in which a non-trivial phase difference arises between the condensates of a three-component Rabi-coupled BEC, and report the consequent novel vortical and skyrmionic lattices that can be observed as the smoking gun for the underlying chiral phenomena.

4.1 Introduction

Since the experimental creation of large vortex lattices in rotating single-component Bose–Einstein condensates (BECs) of atomic gases [249, 250, 251], there has been growing interest in studying the rotational response of BECs with multiple components¹. The physics of such superfluid mixtures is more intricate because the competing effects enter not only via the

¹For a review, see [252]

self-interaction of a single component but also through intercomponent interactions [135, 161]. In terms of finding the energy-minimizing vortex configuration, this means that the relative positioning of vortices in different components also profoundly affects the total energy. In addition, two different regimes can be distinguished: the immiscible regime, where the components separate into nonoverlapping phases, and the miscible regime with interpenetrating BECs [161].

The versatility of the emerging ground-state vortex structures is apparent already in the simplest multicomponent case, the two-component BEC, which has been realized experimentally, e.g., with two hyperfine spin states of atoms of the same species [10, 145, 146, 147, 148, 149, 150]. A rapidly rotating miscible two-component BEC with equally populated and repulsively interacting components was shown to form vortex lattices whose geometry can change from triangular to rectangular, with the lattice unit cells of the two components displaced relative to each other [15, 157]. Subsequently, a two-component mass-imbalanced BEC with attractive intercomponent interactions was shown to host vortex lattices that vary from a square lattice to a triangular lattice of vortex pairs (dimers) [16]. In the immiscible regime corresponding to strong intercomponent repulsion, rotating harmonically trapped two-component BECs undergo a phase separation leading to serpentine vortex sheets [17] or, when the components are unequally populated, to a giant vortex surrounded by a ring of single-quantum vortices [158]. The ground state of a rotating two-component BEC can also host spin-texture skyrmions [179, 158, 159, 253] or a solitary multiquantum vortex [253].

Moreover, a two-component BEC consisting of two hyperfine spin states of the same atom can be coupled not only by density–density interactions but also coherently, so that the complex phases of the condensate wave functions are no longer independent of each other. When rotated, such Rabi-coupled two-component BECs were found to contain vortex dimers (also called meron pairs [254, 255]), and multidimer bound states made up of four or six individual vortices from different components [256]. The dimer and multidimer bound states were shown to emerge due to the Rabi coupling giving rise to energy-costing domain walls in the relative phase between the two components [257, 256]. In effect, the domain walls confine vortices in different components into bound vortex molecules [257, 256]. With increasing strength of the Rabi coupling, the domain wall between the bound vortices shrinks and eventually vanishes, merging the constituent vortices into an “integer vortex” (with the same phase winding in each component) [257, 210, 256]. Thus, the Rabi coupling induces an attractive interaction between same-sign vortices in different components. For a more detailed study of vortex–vortex interactions in multicomponent BECs, we refer to the work of Dantas *et*

al. [258].

The sign of the Rabi coupling does not play a role in the ground state of the Rabi-coupled two-component BEC, since one can always multiply either of the condensate wave functions by a global $U(1)$ phase factor to obtain a ground-state solution with an attractive Rabi energy. However, the situation becomes significantly more involved when there are more than two coherently coupled components in the system. Such a case, with three Rabi-coupled BEC components, has been studied earlier in Ref. [259] but only in the unfrustrated parameter regime where all three pairwise Rabi energies can be simultaneously attractive at the same point in space. In this work, we investigate coherently coupled three-component BECs in the other regime where the Rabi energies necessarily exhibit intrinsic phase frustration. Specifically, we show that the interplay of the intrinsic Rabi frustration with the other interactions and superfluidity of the system can result in the emergence of exotic ground-state vortex lattices when the system is rotated. Fixing the relative phases of two pairs already fixes the relative phase of the remaining pair. This can result in the suppression of some of the three pairwise Rabi couplings and generally leads to the existence of phase-frustrated vortex lattices with unconventional features such as zig-zag patterns, vortex chains, and doubly quantized vortices. In the limit of strong Rabi coupling, the phase frustration causes the three-component BEC to behave effectively as a two-component BEC with only density–density interactions. Consequently, we also observe a triangular-to-square transition in the ground-state vortex lattice in agreement with previous results for the two-component system [15, 157, 159].

The overall repulsive interaction between different components tends to favor interlacing of vortices in different components, splitting composite integer vortices into separate entities. Although each component has, on average, the same overall circulation determined by the external rotation frequency, the vortices of the system can no longer be satisfactorily described by a single winding number. For this reason, we invoke a topological index defined in terms of a CP^2 invariant [178] and use it to classify the observed nontrivial states. This classification has a broader scope in multicomponent quantum physics, since the relative phase frustration appears not only in coherently coupled three-component BECs but also in multiband superconductors [207, 6, 208, 209, 260], where it accounts for, i.a., fractional vortices [261], solitons [210], skyrmions [178, 197, 262], and vortex sheets [263].

The Chapter is organized as follows: In Section 4.2, the theoretical description of the coherently coupled rotating three-component BECs is outlined. Section 4.3 presents the main results, summarized in two vortical-skyrmionic lattice phase diagrams, with the discovered domains illustrated

with representative ground-state solutions. The physical interpretation of the obtained lattices is given in terms of the topological index (Section 4.3.1), intrinsic phase suppression of the Rabi coupling (Section 4.3.2), and domain walls (Section 4.3.3). Finally, we summarize our findings and discuss the outlook in Section 4.4.

4.2 Theoretical framework

Our starting point is a harmonically trapped three-component BEC consisting of three different spin states of a single atomic species, coupled coherently to each other. We use the standard zero-temperature mean-field approach [135] and describe the condensate with three complex-valued wave functions Ψ_i , where $i \in \{1, 2, 3\}$. For simplicity, we focus on the case of a highly oblate cylindrically symmetric trapping potential with the harmonic trap frequencies satisfying $\omega_z \gg \omega_x = \omega_y \equiv \omega$, which implies that the BEC is quasi-two-dimensional and the z dependence can be integrated out. Assuming that the system is set into rotation about the z axis with angular frequency Ω , we write the two-dimensional Gross-Pitaevskii (GP) energy functional [259] in the rotating frame of the system as

$$E = \int \left[\sum_{i=1}^3 \left(\frac{\hbar^2}{2m} |\nabla \Psi_i|^2 + \frac{1}{2} m \omega^2 r^2 |\Psi_i|^2 - \Omega \Psi_i^* L_z \Psi_i \right) + \frac{1}{2} \sum_{i=1}^3 \sum_{j=1}^3 g_{ij} |\Psi_i|^2 |\Psi_j|^2 - \hbar \sum_{i \neq j} \omega_{ij} \Psi_i^* \Psi_j \right] d^2r, \quad (4.1)$$

where m is the mass of the atoms, $r^2 = x^2 + y^2$, and $L_z = -i\hbar(y\partial_x - x\partial_y)$ is the angular momentum operator. The local density–density interactions are characterized by the intra- and intercomponent coupling constants g_{ii} and g_{ij} ($= g_{ji}$), respectively. We assume that $g_{11} = g_{22} = g_{33}$ and $g_{12} = g_{13} = g_{23}$. The additional effective coupling constants ω_{ij} ($= \omega_{ji} \in \mathbb{R}$) in Eq. (4.1) are known as the Rabi frequencies that interlink the phases of the components [264, 265]. They can be experimentally realized and their values controlled by externally applied electromagnetic fields. Accordingly, we call the last term in Eq. (4.1) the Rabi energy and denote the corresponding energy density as $\varepsilon_R = \sum_{i < j} \varepsilon_{ij}$, where $\varepsilon_{ij} = -\hbar \omega_{ij} (\Psi_i^* \Psi_j + \Psi_j^* \Psi_i)$ are the pairwise Rabi energy densities. Variation of Eq. (4.1) with respect to Ψ_i^*

leads to three coupled time-independent GP equations:

$$\begin{aligned} \left(-\frac{\hbar^2}{2m}\nabla^2 + \frac{1}{2}m\omega^2r^2 - \Omega L_z - \mu + \sum_{j=1}^3 g_{ij}|\Psi_j|^2 \right) \Psi_i \\ - \hbar \sum_{j \neq i} \omega_{ij} \Psi_j = 0, \end{aligned} \quad (4.2)$$

where $i \in \{1, 2, 3\}$. Here μ is a chemical potential ensuring that

$$\int \sum_i |\Psi_i(\mathbf{r})|^2 d^2r = N, \quad (4.3)$$

since we consider coherently coupled states where the Hamiltonian conserves only the total particle number $N = \sum_i N_i$ but not the componentwise num-

bers $N_i = \int |\Psi_i|^2 d^2r$.

In order to obtain dimensionless quantities for the numerics, we measure length in units of the radial harmonic oscillator length $a_r = \sqrt{\hbar/m\omega}$ and energy in units of $\hbar\omega$. We parametrize the interactions by the two dimensionless quantities $g = g_{11}mN/3\hbar^2$ and $\sigma = g_{12}/g_{11}$ and consider only the repulsively interacting miscible system with $0 < \sigma \leq 1$. Then dimensionless GP equations take the form

$$\begin{aligned} \left(-\frac{1}{2}\tilde{\nabla}^2 + \frac{1}{2}\tilde{r}^2 + g|\tilde{\Psi}_i|^2 - \frac{\Omega}{\omega}\tilde{L}_z - \frac{\mu}{\hbar\omega} + \sigma g \sum_{j \neq i} |\tilde{\Psi}_j|^2 \right) \tilde{\Psi}_i \\ - \sum_{j \neq i} \frac{\omega_{ij}}{\omega} \tilde{\Psi}_j = 0, \end{aligned} \quad (4.4)$$

where $\tilde{\Psi}_i = N^{-1/2}\sqrt{3}a_r\Psi_i$ and $\tilde{r} = r/a_r$. The numerical analysis of the three-component BEC is based on solving Eqs. (4.4) with the link-variable discretization scheme and the numerical method given in **Chapter 1**, Subsections 1.6.7 and 1.6.8.

4.3 Numerical results

We have numerically solved the GP equations of the rotating three-component BEC in the presence of both density–density and Rabi couplings [Eqs. (4.4)]. In all the states we present, we have fixed the intracomponent coupling strength to $g = g_{11}mN/3\hbar^2 = 2115$ and the rotation frequency to $\Omega = 0.97\omega$.

On the other hand, we treat the relative intercomponent density–density coupling strength σ and the Rabi frequency ω_{12} as variables in the intervals $0 < \sigma \leq 1$ and $-0.12\omega \leq \omega_{12} \leq -0.01\omega$ in order to study their effect on the ground-state vortex lattices of the system. We assume the other two Rabi frequencies ω_{13} and ω_{23} to be equal and consider two different fixed values, $\omega_{13} = \omega_{23} = 0.01\omega$ and $\omega_{13} = \omega_{23} = 0.05\omega$, since these already convey many of the key phenomena related to the Rabi coupling. Hence, we end up with two different fixed parameter sets $(g, \Omega, \omega, \omega_{13}, \omega_{23})$ and the dimensionless variables σ and ω_{12}/ω . The results for the two parameter sets are presented as two phase diagrams in the plane of σ and ω_{12}/ω in Figs. 4.7 and 4.13. In the remainder of this Section, we will analyze the phase diagrams in detail (Section 4.3.1) and discuss the emerging phenomena of Rabi suppression (Section 4.3.2) and domain walls (Section 4.3.3). We recall from Ref. [266] that when the Rabi couplings are not present, only triangular lattices were observed in the rotating ground states in the range $0 \leq \sigma < 1$.

4.3.1 Lattice phase diagrams

Let us first consider the fixed Rabi frequencies $\omega_{13} = \omega_{23} = 0.01\omega$, and vary the interspecies interaction strength and the remaining Rabi frequency in the ranges $0 \leq \sigma \leq 1$ and $0.01 \leq -\omega_{12} \leq 0.12\omega$, respectively. This results in a diverse set of ground-state vortex lattices, examples of which are depicted in Figs. 4.1–4.6. For each solution, we present the density $|\Psi_i|^2$ of each component, the total density $n_{\text{tot}} = \sum_i |\Psi_i|^2$, and the Rabi energy density ε_{R} ; we also locate the vortices and present the relative complex phases between the components using the quantities $\text{sgn}(\omega_{ij}) \cos(\varphi_i - \varphi_j)$, where sgn is the sign function, $i < j$, and $\varphi_i = \arg(\Psi_i)$. We will refer to these figures when discussing the related phenomena in the subsequent sections.

For $0 \leq \sigma \leq 0.7$ and $-\omega_{12} \leq 0.04\omega$, and also in the small region where $0.7 < \sigma \leq 0.9$ and $-\omega_{12} \leq 0.03\omega$, all three components host triangular vortex lattices as shown in Figs. 4.1(a)–(c). For $-\omega_{12} > 0.04\omega$ and $\sigma \geq 0.3$, the three triangular lattices are interlaced with one another. However, for $-\omega_{12} > 0.03\omega$ and $\sigma < 0.3$, vortices in components 1 and 2 move on top of each other to form overlapping triangular vortex lattices [Figs. 4.2(a)–(c)], which are in turn interlaced by the triangular lattice in component 3. Together they constitute a honeycomb lattice of local minima in the total density n_{tot} as shown in Fig. 4.2(d).

For $\sigma \geq 0.3$ and increased $|\omega_{12}|$, the triangular vortex lattices in components 1 and 2 are replaced by overlapping *square lattices of vortex dimers*, while component 3 hosts an interlacing square lattice of solitary vortices.

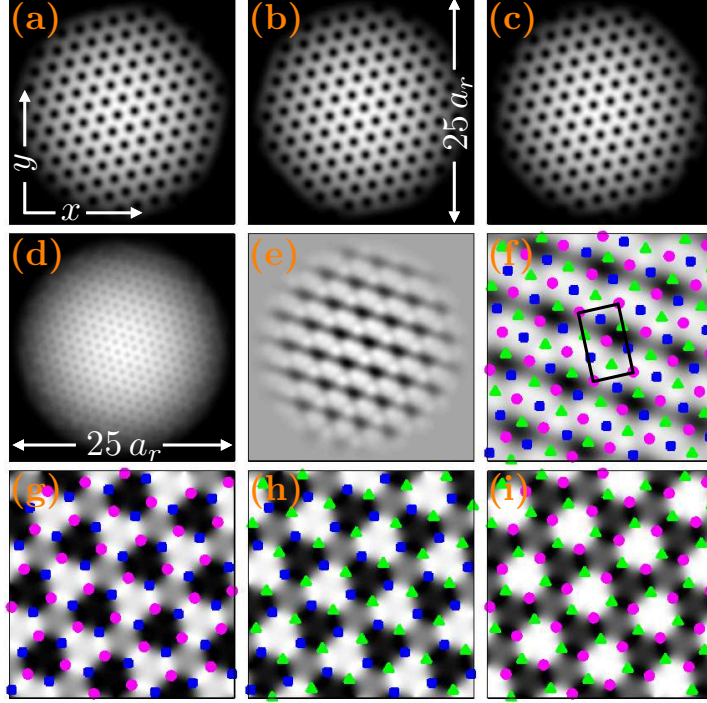


Figure 4.1: Rotating ground state for the intercomponent interaction strength $\sigma = g_{12}/g_{11} = 0.2$ and the dominant Rabi frequency $\omega_{12}/\omega = -0.01$. The panels show (a)–(c) atomic densities $|\Psi_1|^2$, $|\Psi_2|^2$, and $|\Psi_3|^2$, respectively; (d) total density n_{tot} ; (e) negative Rabi energy density $-\varepsilon_R$; (f) vortices of each component on top of $-\varepsilon_R$, with (blue) squares, (pink) dots, and (green) triangles denoting vortices in the wave functions Ψ_1 , Ψ_2 , and Ψ_3 , respectively; (g) $-\cos \varphi_{12}$, where $\varphi_{ij} = \arg(\Psi_i) - \arg(\Psi_j)$; (h) $\cos \varphi_{13}$; (i) $\cos \varphi_{23}$. Panel (f) also indicates the elementary cell of the combined vortex lattice. The average topological index $\tilde{Q} = 2$ for this state [see Eq. (4.6)]. In the grayscale images, white (black) is used for largest (smallest) values. This state corresponds to the intracomponent interaction strength $g = g_{11}mN/3\hbar^2 = 2115$, rotation frequency $\Omega/\omega = 0.97$, and Rabi frequencies $\omega_{13} = \omega_{23} = 0.01\omega$. The field of view in panels (f)–(i) is $11a_r \times 11a_r$, where $a_r = \sqrt{\hbar/m\omega}$, showing the central portion of the harmonic trap.

In the range $0.3 \leq \sigma \leq 0.7$, the alignment of the dimers exhibits small distortions in the center region of the lattice as shown in Figs. 4.3(a)–(b). However, with a further increase in the intercomponent repulsion to $\sigma = 0.8$, the dimers become globally tilted with respect to the square cell of their underlying lattice [Figs. 4.4(a) and 4.4(b)]. Both the vortex lattice in com-

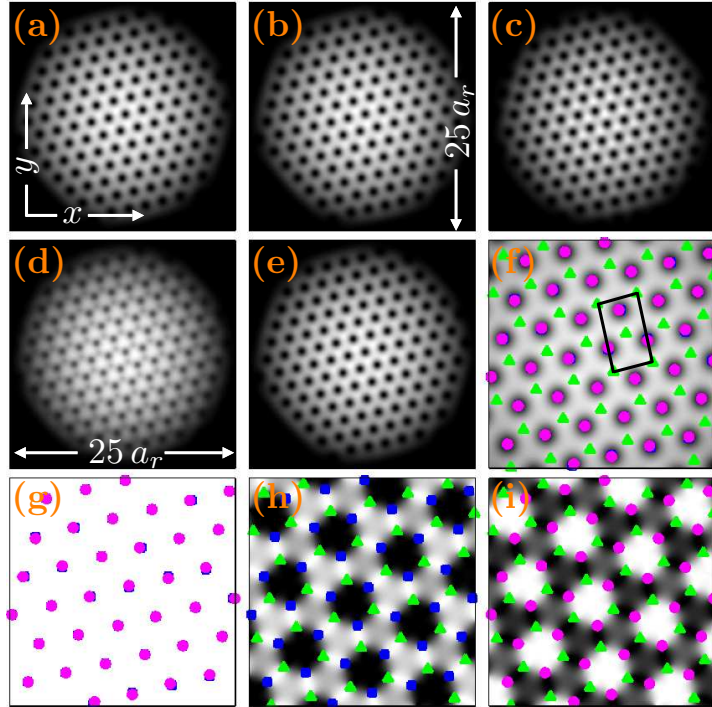


Figure 4.2: Rotating ground state for $\sigma = g_{12}/g_{11} = 0.2$ and $-\omega_{12}/\omega = 0.09$. Other parameter values are the same as in Fig. 4.1. The panels depict (a) $|\Psi_1|^2$; (b) $|\Psi_2|^2$; (c) $|\Psi_3|^2$; (d) n_{tot} ; (e) $-\varepsilon_{\text{R}}$; (f) vortices superposed on $-\varepsilon_{\text{R}}$; (g) $-\cos \varphi_{12}$; (h) $\cos \varphi_{13}$; (i) $\cos \varphi_{23}$. Panel (f) also indicates the elementary cell of the combined vortex lattice. The average topological index $\tilde{Q} = 4/3$ for this state. The field of view in panels (f)–(i) is $11a_r \times 11a_r$.

ponent 3 and the lattice of minima in n_{tot} [Figs. 4.3(d) and 4.4(d)] remain square throughout this region. Note in particular that at $\sigma = 0.7$, neither n_{tot} [Fig. 4.3(d)] nor the Rabi energy density ε_{R} [Fig. 4.3(e)] shows the lattice distortions appearing in components 1 and 2.

Finally, the region $\sigma = 1$, corresponding to strong intercomponent repulsion, can be considered as the border that separates miscible and immiscible regimes. Here, two phases can be distinguished with varying ω_{12} . For $0.01\omega \leq -\omega_{12} \leq 0.04\omega$, we obtain interlacing triangular vortex-dimer lattices in components 1 and 2, while a triangular lattice of doubly quantized fused-core vortices forms in component 3 [Figs. 4.5(a)–(c)]. A fused-core vortex comprises two singly quantized vortices practically coalesced into a single, doubly quantized defect, or at least to within a distance smaller than the core diameter of the constituent vortices. The apparent elliptical shape of

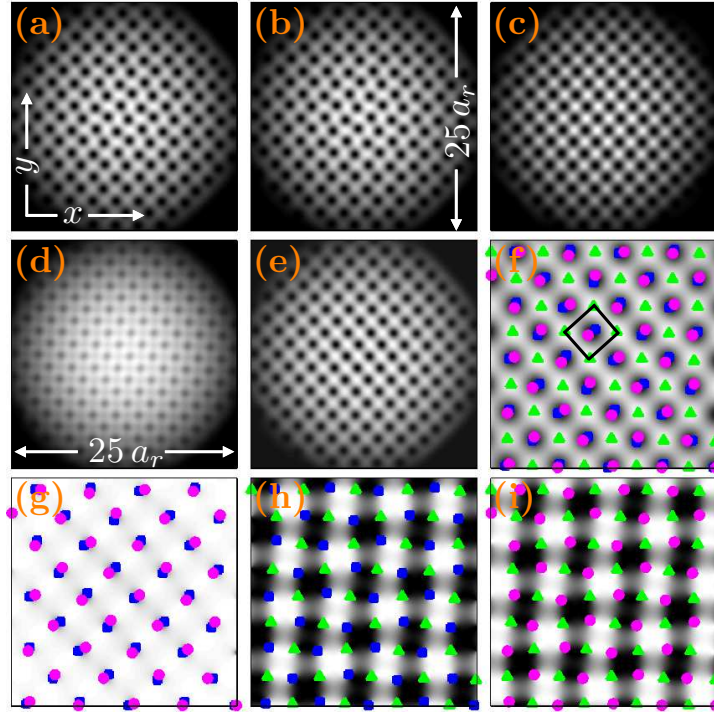


Figure 4.3: Rotating ground state for $\sigma = g_{12}/g_{11} = 0.7$ and $-\omega_{12}/\omega = 0.09$. Other parameter values are the same as in Fig. 4.1. The panels depict (a) $|\Psi_1|^2$; (b) $|\Psi_2|^2$; (c) $|\Psi_3|^2$; (d) n_{tot} ; (e) $-\varepsilon_R$; (f) vortices superposed on $-\varepsilon_R$; (g) $-\cos \varphi_{12}$; (h) $\cos \varphi_{13}$; (i) $\cos \varphi_{23}$. Panel (f) also shows the elementary cell of the combined vortex lattice. The average topological index $\tilde{Q} = 2/3$ for this state. The field of view in panels (f)–(i) is $11a_r \times 11a_r$.

the combined defect is due to the small separation of the phase singularities. In the second phase at $\sigma = 1$, which occurs for $0.5\omega \leq -\omega_{12} \leq 0.12\omega$, component 1 hosts a honeycomb vortex lattice, component 2 a triangular lattice of vortex dimers, and component 3 a triangular lattice of fused-core vortices [Figs. 4.6(a)–(c), respectively]. Furthermore, we note that the Rabi energy density exhibits a honeycomb spatial structure [Fig. 4.6(e)].

All these states can actually be topologically characterized as containing two-dimensional skyrmions. According to Ref. [178], skyrmions in a K -component model in two spatial dimensions can be defined by the $\mathbb{C}P^{K-1}$ topological invariant

$$\mathcal{Q} = \int \frac{i\epsilon_{\alpha\beta}}{2\pi|\Psi|^4} \left(|\Psi|^2 \partial_\alpha \Psi^\dagger \partial_\beta \Psi + \Psi^\dagger \partial_\alpha \Psi \partial_\beta \Psi^\dagger \Psi \right) d^2r, \quad (4.5)$$

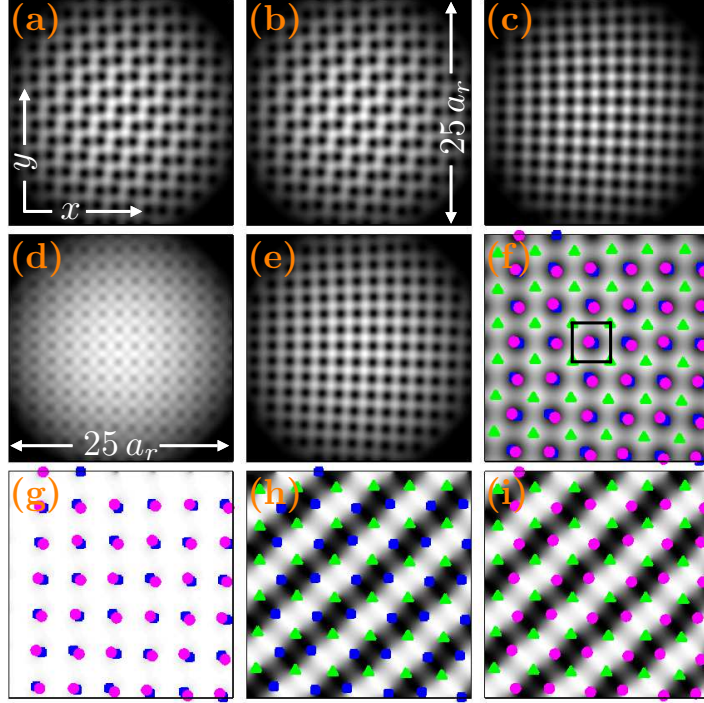


Figure 4.4: Rotating ground state for $\sigma = 0.9$ and $-\omega_{12}/\omega = 0.09$. Other parameter values are the same as in Fig. 4.1. The panels show (a) $|\Psi_1|^2$; (b) $|\Psi_2|^2$; (c) $|\Psi_3|^2$; (d) n_{tot} ; (e) $-\varepsilon_{\text{R}}$; (f) vortices superposed on $-\varepsilon_{\text{R}}$; (g) $-\cos \varphi_{12}$; (h) $\cos \varphi_{13}$; (i) $\cos \varphi_{23}$. Panel (f) also indicates the elementary cell of the combined vortex lattice. The average topological index $\tilde{Q} = 2/3$ for this state. The field of view in panels (f)–(i) is $11a_r \times 11a_r$.

termed the topological index. In Eq. (4.5), $\epsilon_{\alpha\beta}$ is the Levi-Civita symbol, $\alpha, \beta \in \{x, y\}$, and $\Psi^\dagger = (\Psi_1^*, \Psi_2^*, \dots, \Psi_K^*)$. We note that $\mathbb{C}P^{K-1}$ is the complex projective space whose points label the complex lines through the origin of the space \mathbb{C}^K [178]. The dimensionality of the space \mathbb{C}^K is defined by the number K of $U(1)$ fields (components) in the system. The K fields can be collected into a complex K vector $\Phi : M \rightarrow \mathbb{C}^K$, where $M = \mathbb{R}^2$ is physical space. The space \mathbb{C}^K can be mapped into a new space $\mathbb{C}P^{K-1}$ by projecting a point in \mathbb{C}^K to the complex line in $\mathbb{C}P^{K-1}$.

For our states, the integration is carried over the elementary cell of the combined three-component vortex lattice. The topological index is zero for an integer vortex, i.e., when the vortices reside on top of each other in all components. In our case, we deal with two types of states: in the first type, three interlacing lattices form in all three component at small values of $|\omega_{12}|$,

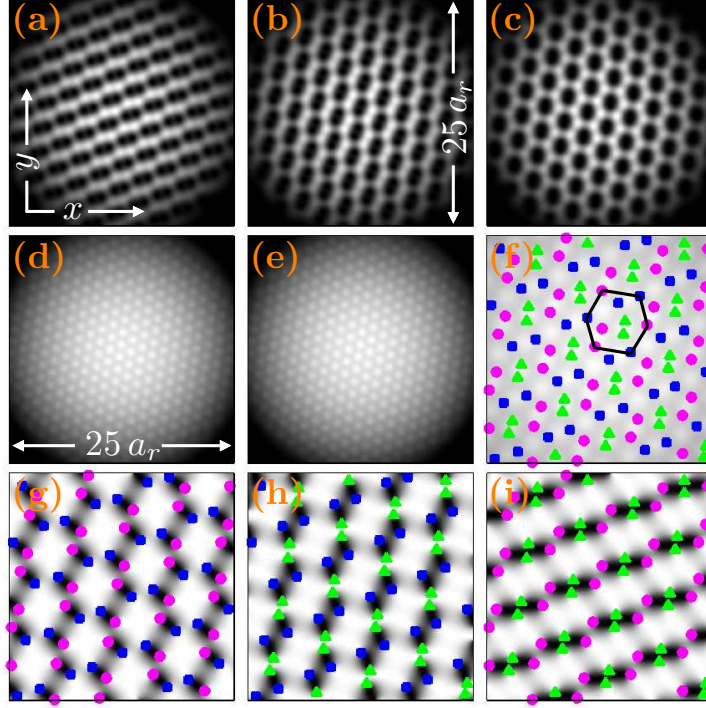


Figure 4.5: Rotating ground state for $\sigma = 1.0$ and $-\omega_{12}/\omega = 0.01$. Other parameter values are the same as in Fig. 4.1. The panels correspond to (a) $|\Psi_1|^2$; (b) $|\Psi_2|^2$; (c) $|\Psi_3|^2$; (d) n_{tot} ; (e) $-\varepsilon_{\text{R}}$; (f) vortices superposed on $-\varepsilon_{\text{R}}$; (g) $-\cos \varphi_{12}$; (h) $\cos \varphi_{13}$; (i) $\cos \varphi_{23}$. Panel (f) also shows the elementary cell of the combined vortex lattice. The average topological index $\tilde{Q} = 2$ for this state. The field of view in panels (f)–(i) is $11a_r \times 11a_r$.

while in the second type, when $|\omega_{12}|$ is increased, we find overlapping vortex lattices in component 1 and 2. Examples of states of each type are presented in Figs. 4.1 and 4.2, respectively. If we calculate the $\mathbb{C}P^2$ topological index for each of these two states by using Eq. (4.5), where $\Psi^\dagger = (\Psi_1^*, \Psi_2^*, \Psi_3^*)$, we obtain the same $Q = 2$ per combined-lattice elementary cell, although they clearly constitute two different phases. Therefore, in order to better distinguish different phases, we instead calculate pairwise $\mathbb{C}P^1$ topological indices Q_{ij} , by using Eq. (4.5), where $\Psi^\dagger = (\Psi_i^*, \Psi_j^*)$ and $i \neq j$ ($i, j = 1, 2, 3$), separately for each pair of the components, and then calculate an average topological index \tilde{Q} for the entire three-component state as

$$\tilde{Q} = \frac{Q_{12} + Q_{13} + Q_{23}}{3}. \quad (4.6)$$

We stress that each Q_{ij} is calculated over the same elementary cell of the

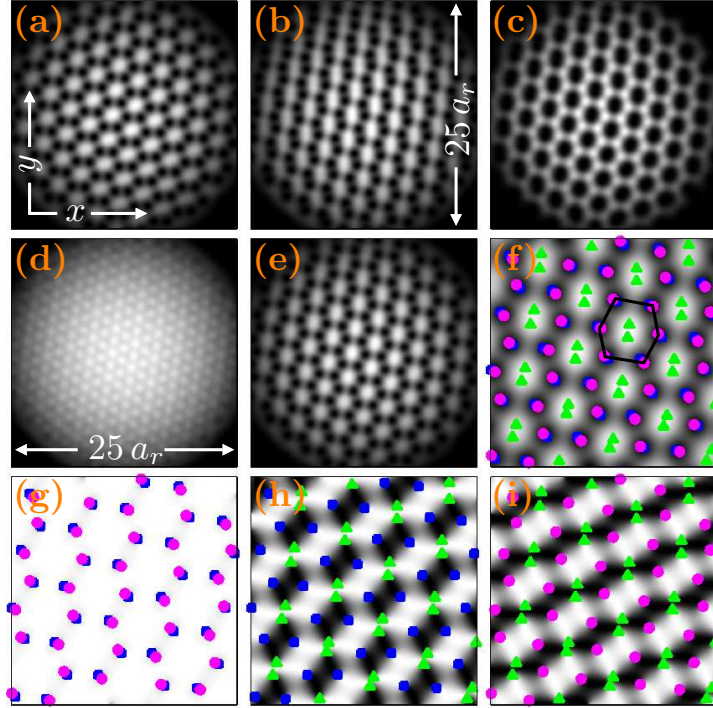


Figure 4.6: Rotating ground state for $\sigma = 1.0$ and $-\omega_{12}/\omega = 0.09$. Other parameter values are the same as in Fig. 4.1. The panels correspond to (a) $|\Psi_1|^2$; (b) $|\Psi_2|^2$; (c) $|\Psi_3|^2$; (d) n_{tot} ; (e) $-\varepsilon_{\text{R}}$; (f) vortices superposed on $-\varepsilon_{\text{R}}$; (g) $-\cos \varphi_{12}$; (h) $\cos \varphi_{13}$; (i) $\cos \varphi_{23}$. Panel (f) also indicates the elementary cell of the combined vortex lattice. The average topological index $\tilde{Q} = 4/3$ for this state. The field of view in panels (f)–(i) is $11a_r \times 11a_r$.

three-component lattice. In panel (f) of Figs. 4.1–4.6, we mark vortices of each component on top of the Rabi energy density ε_{R} and also indicate the lattice elementary cell (by black solid line). To illustrate the use of Eq. (4.6), let us consider, for example, the state shown in Fig. 4.1, for which the elementary cell is the rectangle that connects four vortices of component 2 [denoted by (pink) dots]. The rectangle encloses two vortices of each component. As a result, the pairwise topological indices are $\mathcal{Q}_{12} = 2$, $\mathcal{Q}_{13} = 2$, and $\mathcal{Q}_{23} = 2$. The average topological index for the state is $\tilde{Q} = 2$. On the other hand, calculating the average topological index for the state shown in Fig. 4.2 in the same manner gives $\tilde{Q} = 4/3$, because the individual vortices of component 1 and 2 reside on top of each other and hence $\mathcal{Q}_{12} = 0$.

By calculating the average topological index \tilde{Q} from Eq. (4.6) for all the obtained states and collecting the results, we obtain the phase diagram

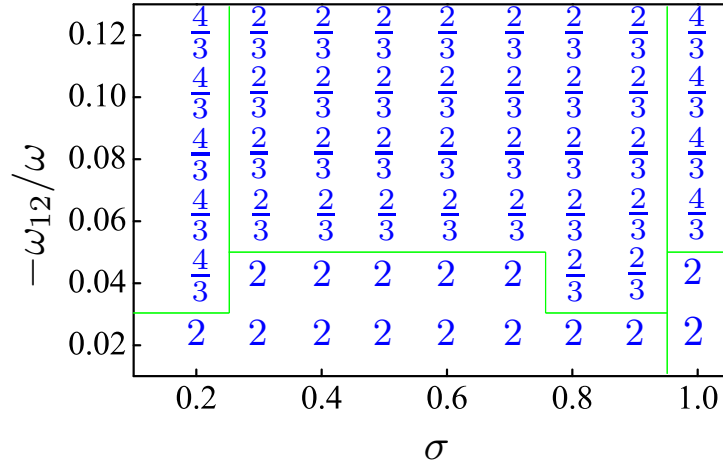


Figure 4.7: Skyrmionic-lattice phase diagram as a function of the inter-component interaction strength σ and the Rabi frequency ω_{12} , for fixed intracomponent interaction strength $g = 2115$, external rotation frequency $\Omega/\omega = 0.97$, and Rabi frequencies $\omega_{13} = \omega_{23} = 0.01\omega$. Each number corresponds to a numerically solved ground state of the three-component Bose-Einstein condensate and indicates the corresponding average topological index \tilde{Q} [Eq. (4.6)] per elementary cell of the combined three-component vortex lattice. The (green) solid lines are guides to the eye for separating different phases.

shown in Fig. 4.7. It classifies the different types of ground-state skyrmionic lattices for the fixed Rabi couplings $\omega_{13} = \omega_{23} = 0.01\omega$ in the two-dimensional domain $0 \leq \sigma \leq 1$ and $0.01\omega \leq -\omega_{12} \leq 0.14\omega$. The states with $\tilde{Q} = 2$ in the range $0 \leq \sigma < 1$ correspond to skyrmionic lattices with two vortices per component in a rectangular cell resulting from an interlacing triangular vortex lattice in each component (Fig. 4.1). The states with $\tilde{Q} = 4/3$ have a parallelogram cell and overlapping triangular lattices in components 1 and 2 (Fig. 4.2). The states with $\tilde{Q} = 2/3$ correspond to overlapping square lattices of vortex dimers in components 1 and 2, an interlacing square vortex lattice in component 3, and a square cell that contains one vortex of each component (Figs. 4.3 and 4.4). The states with $\tilde{Q} = 2$ at $\sigma = 1$ have a hexagonal cell which includes two vortices of each component. At larger $|\omega_{12}|$, this phase changes into a skyrmionic lattice with $\tilde{Q} = 4/3$ because of overlapping lattices in components 1 and 2.

We now turn to the second parameter set, which differs from the first by having $\omega_{13} = \omega_{23} = 0.05\omega$, and the Rabi coupling ω_{12} changes in the range

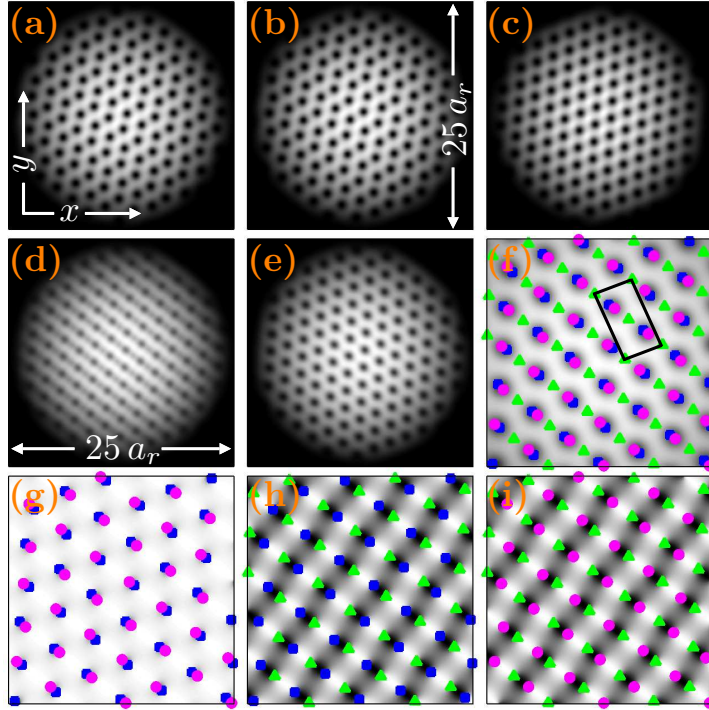


Figure 4.8: Rotating ground state for the intercomponent interaction strength $\sigma = g_{12}/g_{11} = 0.2$ and the dominant Rabi frequency $\omega_{12}/\omega = -0.09$. The panels show (a)–(c) atomic densities $|\Psi_1|^2$, $|\Psi_2|^2$, and $|\Psi_3|^2$, respectively; (d) total density n_{tot} ; (e) negative Rabi energy density $-\varepsilon_{\text{R}}$; (f) vortices of each component on top of $-\varepsilon_{\text{R}}$; (g) $-\cos \varphi_{12}$; (h) $\cos \varphi_{13}$; (i) $\cos \varphi_{23}$. Panel (f) also shows the elementary cell of the combined vortex lattice. The average topological index $\tilde{Q} = 2$ for this state. This state corresponds to the intra-component interaction strength $g = g_{11}mN/3\hbar^2 = 2115$, rotation frequency $\Omega/\omega = 0.97$, and Rabi frequencies $\omega_{13}/\omega = \omega_{23} = 0.05\omega$. The field of view in panels (f)–(i) is $11a_r \times 11a_r$.

$0.03\omega \leq -\omega_{12} \leq 0.14\omega$. For this given parameter set, in the range $0 < \sigma \leq 0.4$ and $-\omega_{12} < 0.09\omega$, components 1 and 2 host interlacing zig-zag vortex lattices, which are in turn both interlaced by a triangular vortex lattice in component 3, similar to ones shown in Figs. 4.8(a)–(c). For $-\omega_{12} \gtrsim 0.09\omega$, the zig-zag lattices in components 1 and 2 start to overlap, while the interlacing triangular lattice in component 3 remains unchanged. An example of the state with overlapping zig-zag lattices in components 1 and 2 is shown in Fig. 4.8. The total density for both kinds of states exhibits a plane-wave-like modulation [Fig. 4.8(d)].

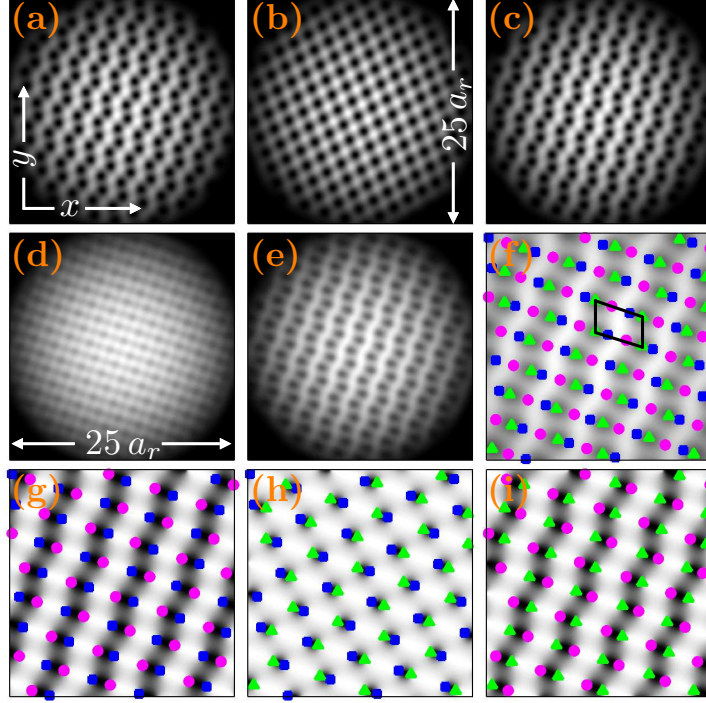


Figure 4.9: Rotating ground state for $\sigma = 0.7$ and $-\omega_{12}/\omega = 0.03$. Other parameter values are the same as in Fig. 4.8. The panels show (a) $|\Psi_1|^2$; (b) $|\Psi_2|^2$; (c) $|\Psi_3|^2$; (d) n_{tot} ; (e) $-\varepsilon_{\text{R}}$; (f) vortices superposed on $-\varepsilon_{\text{R}}$; (g) $-\cos \varphi_{12}$; (h) $\cos \varphi_{13}$; (i) $\cos \varphi_{23}$. Panel (f) also indicates the elementary cell of the combined vortex lattice. The average topological index $\bar{Q} = 1$ for this state. The field of view in panels (f)–(i) is $11a_r \times 11a_r$.

The states occurring for $0.5 \leq \sigma \leq 0.8$ and $0.03\omega \leq \omega_{12} < 0.1\omega$ correspond to components 1 and 3 exhibiting zig-zag vortex lattices and component 2 forming a square vortex lattice that interlaces both zig-zag lattices. An example from this range is shown in Fig. 4.9. The corresponding total density is depicted in Fig. 4.9(d) and exhibits a square pattern. In the same range of intercomponent repulsion, $0.5 \leq \sigma \leq 0.8$, but for $-\omega_{12} > 0.1\omega$, zig-zag lattices instead form in components 1 and 2, which are interlaced by a square vortex lattice in component 3 (Fig. 4.10). Both n_{tot} and ε_{R} have a square pattern [Figs. 4.10(d) and (e)].

For $\sigma = 0.9$ and $0.03\omega \leq -\omega_{12} < 0.1\omega$, the system hosts triangular dimer lattices in components 1 and 2 and parallel straight chains of vortices in component 3. An example from this region is shown in Fig. 4.11. With further increasing $|\omega_{12}|$, the vortices in components 1 and 2 eventually move

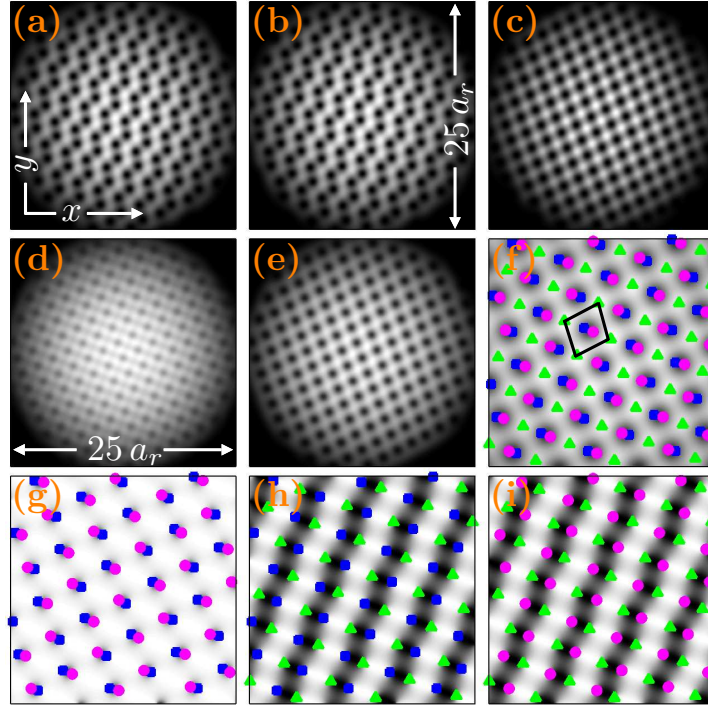


Figure 4.10: Rotating ground state for $\sigma = 0.7$ and $-\omega_{12}/\omega = 0.12$. Other parameter values are the same as in Fig. 4.8. The panels show (a) $|\Psi_1|^2$; (b) $|\Psi_2|^2$; (c) $|\Psi_3|^2$; (d) n_{tot} ; (e) $-\varepsilon_{\text{R}}$; (f) vortices superposed on $-\varepsilon_{\text{R}}$; (g) $-\cos \varphi_{12}$; (h) $\cos \varphi_{13}$; (i) $\cos \varphi_{23}$. Panel (f) also shows the elementary cell of the combined vortex lattice. The average topological index $\tilde{Q} = 2/3$ for this state. The field of view in panels (f)–(i) is $11a_r \times 11a_r$.

on top of each other and form fully overlapping triangular dimer lattices for $0.1\omega < -\omega_{12} \leq 0.14\omega$.

At $\sigma = 1$, we identify two different phases. For $0.03\omega \leq -\omega_{12} < 0.1\omega$, the system hosts mutually interlaced triangular lattices of dimers in all three components (Fig. 4.12). The other phase occurs for $-\omega_{12} \gtrsim 0.1\omega$ and has overlapping triangular lattices of dimers in components 1 and 2 and an interlacing triangular lattice of dimers in component 3.

The states shown in Figs. 4.8–4.12 are also amenable to skyrmionic classification in terms of the average topological index per elementary cell of the total lattice [Eq. (4.6)]. The corresponding phase diagram of appropriate skyrmionic lattices for these states is shown in Fig. 4.13. For the states with $\tilde{Q} = 2$ in the range $0 < \sigma \leq 0.4$, the elementary cell is a rectangle that contains two vortices of each component [Fig. 4.8(f)]. The skyrmionic

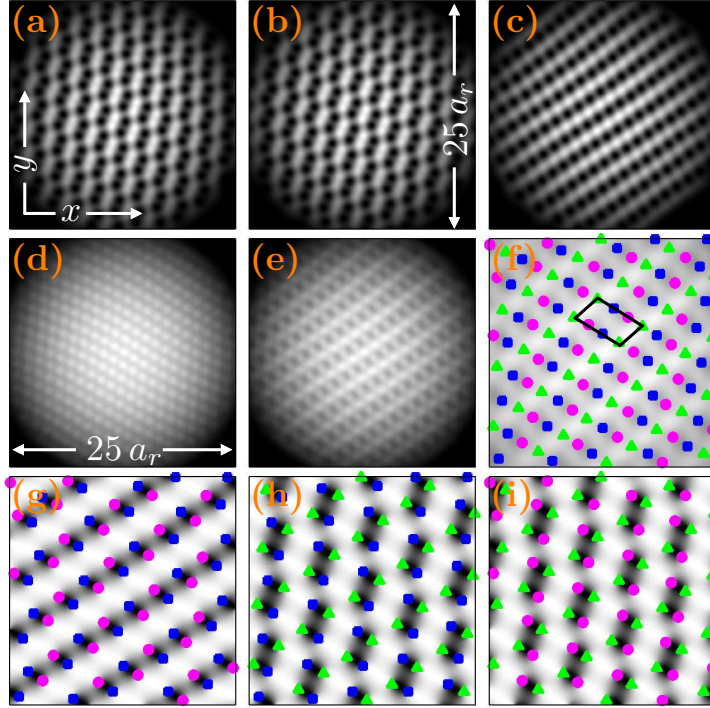


Figure 4.11: Rotating ground state for $\sigma = 0.9$ and $-\omega_{12}/\omega = 0.06$. Other parameter values are the same as in Fig. 4.8. The panels depict (a) $|\Psi_1|^2$; (b) $|\Psi_2|^2$; (c) $|\Psi_3|^2$; (d) n_{tot} ; (e) $-\varepsilon_{\text{R}}$; (f) vortices superposed on $-\varepsilon_{\text{R}}$; (g) $-\cos \varphi_{12}$; (h) $\cos \varphi_{13}$; (i) $\cos \varphi_{23}$. Panel (f) also shows the elementary cell of the combined vortex lattice. The average topological index $\tilde{Q} = 1$ for this state. The field of view in panels (f)–(i) is $11a_r \times 11a_r$.

lattices with $\tilde{Q} = 4/3$ in the same range of σ correspond to the states with overlapping zig-zag vortex lattices in component 1 and 2, so that the pairwise topological index $Q_{12} = 0$. The region with $\tilde{Q} = 1$ in $0.4 < \sigma \leq 0.8$ corresponds to a skyrmionic lattice with a parallelogram cell containing one vortex of each component [Fig. 4.9(f)]. With increasing $|\omega_{12}|$ this phase changes into a skyrmionic lattice with $\tilde{Q} = 2/3$ [Fig. 4.10(f)]. At $\sigma = 0.9$, we distinguish two phases, with $\tilde{Q} = 1$ and $\tilde{Q} = 2/3$, where in both cases the elementary cell encloses one vortex of each component and is similar to the one shown in Fig. 4.11(f). Finally, the region at $\sigma = 1.0$ also shows two phases with the average topological indices $\tilde{Q} = 2$ and $\tilde{Q} = 4/3$. The elementary cell contains two vortices of each component and is as shown in Fig. 4.12(f). The latter phase with $\tilde{Q} = 4/3$ emerges due to overlapping triangular lattices of dimers in components 1 and 2, which reduces Q_{12} to zero.

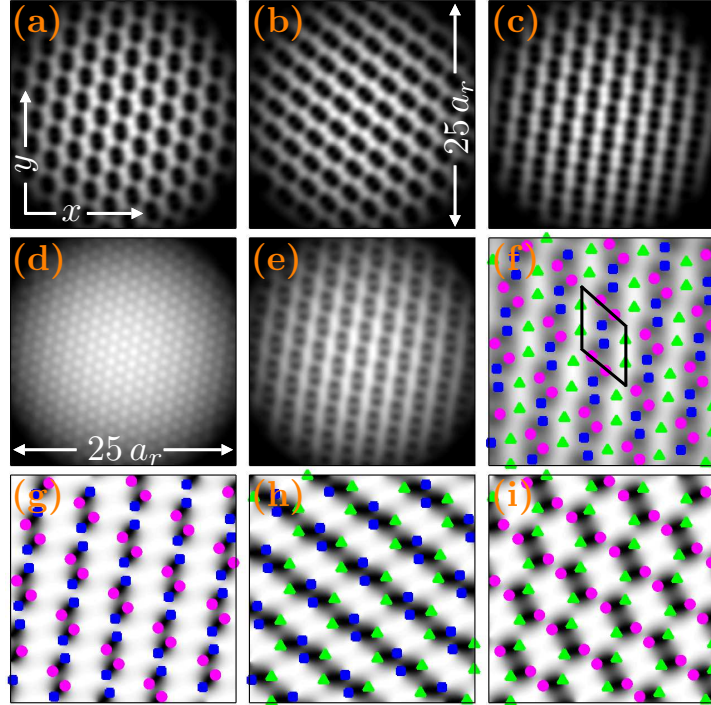


Figure 4.12: Rotating ground state for $\sigma = 1.0$ and $-\omega_{12}/\omega = 0.09$. Other parameter values are the same as in Fig. 4.8. The panels are for (a) $|\Psi_1|^2$; (b) $|\Psi_2|^2$; (c) $|\Psi_3|^2$; (d) n_{tot} ; (e) $-\varepsilon_{\text{R}}$; (f) vortices superposed on $-\varepsilon_{\text{R}}$; (g) $-\cos \varphi_{12}$; (h) $\cos \varphi_{13}$; (i) $\cos \varphi_{23}$. Panel (f) also shows the elementary cell of the combined vortex lattice. The average topological index $\tilde{Q} = 2$ for this state. The field of view in panels (f)–(i) is $11a_r \times 11a_r$.

4.3.2 Rabi suppression in the three-component system

In the Rabi-coupled *two-component* BEC, the sign of the Rabi frequency ω_{12} is irrelevant for the ground-state energetics because the system can freely adjust the global phase difference between Ψ_1 and Ψ_2 to minimize the Rabi energy. Consequently, $\omega_{12} = \omega_0$ and $\omega_{12} = -\omega_0$ ($\omega_0 \in \mathbb{R}$) will yield physically identical ground-state solutions with attractive Rabi energy $E_{\text{R}} \leq 0$ that favors the overlap of same-sign vortices between the two components. In the three-component counterpart, however, the signs of ω_{ij} make a difference, and can result in intrinsic frustration and consequent suppression of some or all of the three pairwise Rabi couplings.

In order to heuristically see how the Rabi suppression emerges in the three-component BEC, consider the wave functions in the vicinity of a vortex,

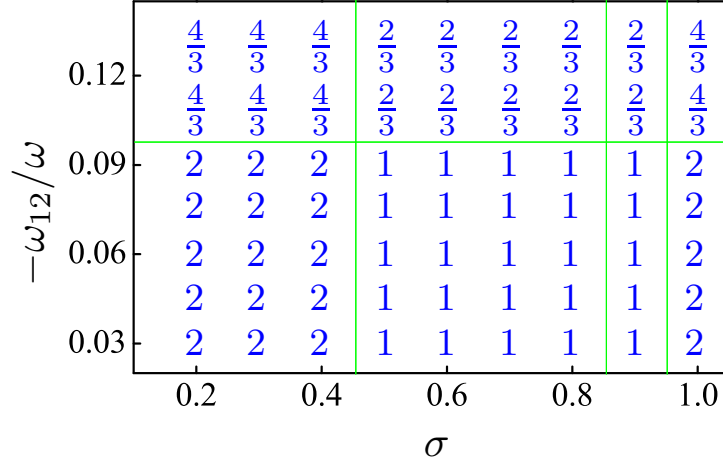


Figure 4.13: Skyrmionic-lattice phase diagram in the plane of the inter-component interaction strength σ and the Rabi frequency ω_{12} for fixed intracomponent interaction strength $g = 2115$, external rotation frequency $\Omega/\omega = 0.97$, and Rabi frequencies $\omega_{13} = \omega_{23} = 0.05\omega$. The numbers correspond to the average topological index \tilde{Q} given by Eq. (4.6) for the elementary cell of the ensuing three-component lattice. The green solid lines are guides to the eye.

for example, in component 1. In local polar coordinates (r', ϕ') with the vortex at $r' = 0$, we write the wave functions as

$$\Psi_j(r', \phi') = \exp[i(\kappa_j \phi' + C_j)] f_k(r'),$$

where the constants $C_j \in \mathbb{R}$ set the local relative phases and only affect the Rabi term in Eq. (4.1). The Rabi energy density then becomes

$$\frac{E_{\text{R}}^{\text{loc}}}{\pi r_0^2} = -\frac{2}{r_0^2} \sum_{i < j} \sum \omega_{ij} \delta_{\kappa_i, \kappa_j} \cos C_{ij} \int_0^{r_0} f_i f_j r' dr', \quad (4.7)$$

where $\delta_{\kappa_i, \kappa_j}$ is the Kronecker delta, $C_{ij} = C_i - C_j$, and r_0 defines the small disk over which the local Rabi energy $E_{\text{R}}^{\text{loc}}$ is averaged. In the case $\kappa_1 = \kappa_2 = \kappa_3$, i.e., superposed same-sign vortices in all components or no vortices at all, all three terms in the sum can be nonzero. If we further assume $f_1 = f_2 = f_3$, the minimization of the above Rabi energy density implies maximization of the function $h(C_{12}, C_{13}) = \sum_{i < j} \sum \omega_{ij} \cos C_{ij} = \omega_{12} \cos C_{12} + \omega_{13} \cos C_{13} + \omega_{23} \cos(C_{12} - C_{13})$. This function has an upper bound of $\sum_{i < j} |\omega_{ij}|$. How-

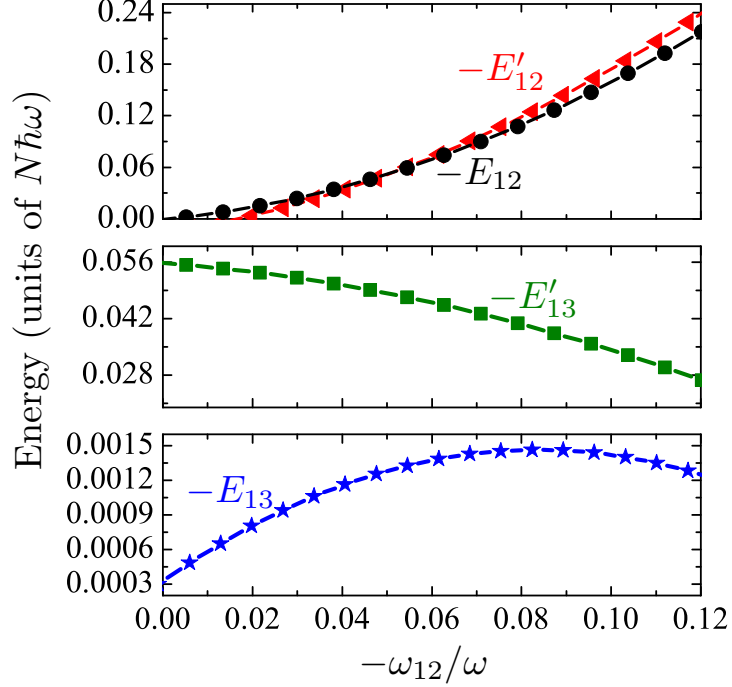


Figure 4.14: Pairwise Rabi energies $E_{ij} = -\omega_{ij} \int (\tilde{\Psi}_i^* \tilde{\Psi}_j + \tilde{\Psi}_j^* \tilde{\Psi}_i) d^2r$ as functions of the Rabi frequency ω_{12}/ω for fixed $g = 2115$, $\sigma = 0.7$, $\Omega/\omega = 0.97$. Here E_{ij} are for $\omega_{13} = \omega_{23} = 0.01\omega$ and E'_{ij} for $\omega_{13} = \omega_{23} = 0.05\omega$.

ever, depending on the values of ω_{ij} , $\max_{C_{ij}} h(C_{12}, C_{13})$ may be significantly below this upper bound, indicating that some or all of the Rabi couplings are suppressed by the relative phase frustration between the particular components. In general, the upper bound can be reached if and only if $\omega_{12}\omega_{13}\omega_{23} \geq 0$, which is never satisfied by the parameter values used in this work (all the presented states have $\omega_{12} < 0 < \omega_{13} = \omega_{23}$). For the parameter set used in Fig. 4.7, the phase frustration occurs symmetrically between all three pairs at $\omega_{12} = -0.01\omega$ (Fig. 4.1 shows an example of this type) for which the maximization yields $\cos C_{12} = -0.5$ and $\cos C_{13} = \cos C_{23} = 0.5$. At $\omega_{12} = -0.09\omega$ (Figs. 4.2–4.6), the optimal phases yield $\cos C_{12} = -0.99$ and $\cos C_{13} = \cos C_{23} = 0.056$, so that $\max_{C_{ij}} h(C_{12}, C_{13}) = 0.091\omega < 0.11\omega =$

$\sum_{i<j} \sum |\omega_{ij}|$. Hence, the Rabi couplings within pairs 1–3 and 2–3 are strongly suppressed, whereas the coupling within pair 1–2 is almost maximal. For the parameter set used in Fig. 4.13, the phase frustration is symmetric between

all three pairs at $\omega_{12} = -0.05\omega$ and occurs dominantly within pairs 1–3 and 2–3 at $\omega_{12} = -0.09\omega$ (Figs. 4.8 and 4.12) and at $\omega_{12} = -0.12\omega$ (Fig. 4.10).

Figure 4.14 shows the behavior of the pairwise Rabi energies E_{12} and E_{13} as functions of $-\omega_{12}$ for fixed $\sigma = 0.7$, $g = 2115$, and $\Omega/\omega = 0.97$. Unprimed quantities are for $\omega_{13} = \omega_{23} = 0.01\omega$ and primed quantities for $\omega_{13} = \omega_{23} = 0.05\omega$. We observe that $-E_{12}$ and $-E'_{12}$ are superlinearly increasing functions of $-\omega_{12}$, whereas $-E_{13}$ and $-E'_{13}$ have a maximum at a finite $-\omega_{12}$. The decrease of $-E_{13}$ and $-E'_{13}$ with $-\omega_{12}$ is a direct consequence of the relative phase suppression between the particular components. The Rabi energies for other values of σ show qualitatively similar behavior.

4.3.3 Domain walls in the relative phases

The Rabi coupling leads to well-defined complex relative phases between the condensates, and therefore, to the possibility of domain walls, i.e., one-dimensional defects, in the relative phase field [257]. The Rabi term breaks the U(1) symmetry of the relative phases $\varphi_{ij} \equiv \varphi_i - \varphi_j$, where $\varphi_i = \arg(\Psi_i)$ and $i < j$, by rendering the value for which $\text{sgn}(\omega_{ij}) \cos \varphi_{ij} = 1$ energetically favorable. This enables us to define a domain wall to lie along the path that connects two oppositely charged vortices in φ_{ij} (i.e., same-sign vortices in φ_i and φ_j) and satisfies $\cos \varphi_{ij} = -\text{sgn}(\omega_{ij})$, i.e., maximizes the phase-dependent part of the pairwise Rabi energy. Together, the repulsive density–density coupling $g_{ij} > 0$ and the Rabi coupling ω_{ij} give rise to an energy minimum at a finite domain-wall length [157]. Increasing $|\omega_{ij}|$ decreases this optimal length until the two vortices in φ_{ij} merge and the domain wall vanishes.

Let us now investigate the behavior of domain walls in the states discussed in the preceding sections (Figs. 4.1–4.6 and 4.8–4.12). For convenience, we consider the three components in pairs and their corresponding pairwise relative phases φ_{12} , φ_{23} and φ_{13} . The relative phases are presented in panels (g)–(i) of said figures using the quantities $\text{sgn}(\omega_{ij}) \cos \varphi_{ij}$, with domain walls shown in black; the positions of vortices of the relevant components are also indicated.

The properties of the domain walls depend on the strength of the Rabi coupling. For example, their characteristic width (analogous to the core size of vortices) is proportional to $|\omega_{ij}|^{-1/2}$ [257]. In Fig. 4.15, we show how the domain walls change when ω_{12} is varied in the range $0.01\omega \leq -\omega_{12} \leq -0.12\omega$ while the other parameters are kept constant. At $|\omega_{ij}| = 0.01\omega$, the domain walls are fairly delocalized, appearing wide between the oppositely charged vortices in each φ_{ij} [Fig. 4.15(a)]. Increasing $|\omega_{ij}|$ to 0.03ω narrows the domain walls in φ_{12} , while φ_{23} and φ_{13} remain nearly unchanged [Fig.

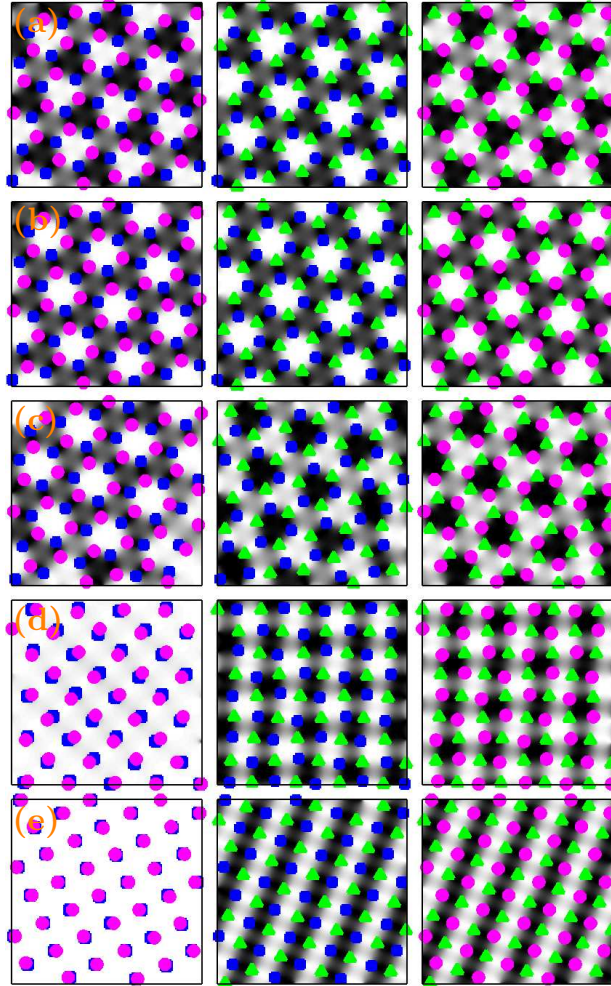


Figure 4.15: Relative complex phases between components shown in terms of $\text{sgn}(\omega_{ij}) \cos \varphi_{ij}$, where $\varphi_{ij} = \arg(\Psi_i) - \arg(\Psi_j)$ and the sgn function makes small values (shown in black) correspond to maximal pairwise Rabi energy density. First column is for $-\cos \varphi_{12}$, second for $\cos \varphi_{13}$ and third for $\cos \varphi_{23}$. The rows correspond to different values of ω_{12}/ω : (a) -0.01 , (b) -0.03 , (c) -0.04 , (d) -0.06 , and (e) -0.12 . Other parameters are fixed at $\sigma = 0.7$, $\Omega/\omega = 0.97$, $g = 2115$, and $\omega_{13} = \omega_{23} = 0.01\omega$. The field of view in each panel is $11a_r \times 11a_r$, and the vortices in Ψ_1 , Ψ_2 , and Ψ_3 are marked with (blue) squares, (pink) dots, and (green) triangles, respectively.

4.15(b)]. In this region, the pairwise Rabi energies $-E_{12}$, $-E_{13}$ and $-E_{23}$ all increase with increasing $-\omega_{12}$ as shown in Fig. 4.14. At $\omega_{12} = -0.06\omega$,

the strong Rabi coupling between components 1 and 2 shrinks the domain walls in φ_{12} , with vortices in φ_1 and φ_2 almost coinciding [Fig. 4.15(d)]. Simultaneously, the Rabi energies $-E_{13}$ and $-E_{23}$ reach their maximum and gradually start decreasing due to the phase frustration occurring for these pairs [Fig. 4.14]. Finally, at $\omega_{12} = -0.12\omega$, the domain walls have vanished completely in φ_{12} [Fig. 4.15(e)]. Thus, we arrive at a unique state in which the domain walls persist in φ_{23} and φ_{13} but vanish completely in φ_{12} . The effective interlocking of components 1 and 2 with $\varphi_{12} \simeq \pi$ implies that $\varphi_{13} \equiv \varphi_{23} + \varphi_{12} \simeq \varphi_{23} + \pi$, as can be observed from Figs. 4.15(d) and 4.15(e).

4.3.4 Vortex phases revisited

Equipped with the insight gained from the previous two subsections, let us return to the phase diagrams in Figs. 4.7 and 4.13, and the various skyrmionic lattice phases therein. The skyrmionic lattices emerge from the combinations of the diverse set of single-component vortex lattices appearing in the three-component system. One can see that both phase diagrams exhibit a triangular-to-square transition in the underlying vortex-lattice geometry, which is qualitatively similar to that of two-component BECs. In order to understand how it comes about in the three-component system, note that when ω_{12} is large enough to overcome the density–density repulsion due to $g_{12} > 0$ and dominate over the other Rabi couplings, components 1 and 2 effectively become locked together such that $\Psi_1 = \text{sgn}(\omega_{12}) \Psi_2 = -\Psi_2$. At the same time, the Rabi coupling becomes very weak for the pairs 1–3 and 2–3 because of the suppression effect; in fact, since we have $\omega_{13} = \omega_{23}$, $\Psi_1 = -\Psi_2$ implies that $\varepsilon_{13} = -\varepsilon_{23}$, leading to cancellation of these Rabi couplings from the energy functional. As a consequence, in this phase-locked limit components 1 and 2 can be viewed as a single component, and the system starts to behave like a repulsive two-component system with only density–density interactions. Then the triangular-to-square transition is expected in the overall lattice geometry, and the ensuing ground states can be classified according to the results of Refs. [15, 157]. Figure 4.2 presents an example from the two-component-like regime with triangular lattices (with $\sigma = 0.7$), while Fig. 4.4 shows a state with square lattice geometry and components 1 and 2 nearly locked together ($\sigma = 0.9$) and which, with a further increase $|\omega_{12}|$, would attain the square-geometry two-component limit.

The states containing zig-zag vortex lattices in some of the components (Figs. 4.8–4.10) emerged in the region where all $|\omega_{ij}|$ were comparable with each other and with the density–density repulsions. The zig-zag lattices can be viewed as deformed triangular Abrikosov lattices where vortices originally in a straight row have been displaced in alternating directions. In

the state shown in Fig. 4.8, with $\tilde{Q} = 2$, these displacements are in opposite directions in components 1 and 2 [Fig. 4.8(g)]. As observed from Figs. 4.8(g)-(i), this vortex configuration can efficiently accommodate relatively tightly bound dimers in all three components, which are energetically favoured due to the interplay of the comparable density–density repulsion and Rabi-mediated attraction. It also follows from the zig-zag pattern that these dimers are arranged in an antiferromagnetic order within each pair, maximizing the intracomponent vortex distances. The origin of the phases illustrated in Figs. 4.9 and 4.10 (with $\tilde{Q} = 1$ and occurring in the range $0.4 < \sigma \leq 0.8$) can be understood in a similar way but with the underlying lattice geometry being square instead of triangular. This again reflects the triangle-to-square transition discussed above. We note that the zig-zag vortex patterns have previously been found for single-component BECs in highly eccentric harmonic trap potentials [267].

4.4 Summary and Conclusions

In this Chapter, we have shown that Rabi-coupled three-component BECs can host unconventional vortex lattices in the rotating ground state of the system. Based on the elementary cell of the total lattice pattern in each state, we also interpreted and classified the states as skyrmionic lattices. We argued that emerging lattice configurations can no longer be classified only by the winding numbers of three components, and that the average topological index of the corresponding elementary cell must be invoked. Using the latter, we collected our results in two phase diagrams in the plane of the intercomponent interaction strength σ and Rabi frequency ω_{12} . We found that at certain combinations of signs and values of the Rabi frequencies ω_{ij} , some of the pairwise Rabi energies become heavily suppressed due to relative phase frustration. For example, when $\omega_{12}\omega_{13}\omega_{23} < 0$ and $|\omega_{12}| \gg |\omega_{13}| \approx |\omega_{23}|$, the Rabi coupling is significant only between components 1 and 2. Such Rabi suppression results in an effective reduction of the three-component BEC to a density–density-coupled two-component BEC. Similarly, a three-component multiband superconductor, for which the Josephson-type coupling serves as an analog of the Rabi coupling in BECs, also reduces to a two-gap superconductor at a particular choice of the coupling matrix [6].

When the Rabi coupling becomes suppressed between two pairs of components, the three-component system exhibits the triangular-to-square vortex-lattice transition in agreement with the previous results for the repulsively coupled two-component BECs and the classification given in Refs. [15, 157]. Although we have limited our study to a particular subset of the large param-

eter space, we expect the rotating ground state of the Rabi-coupled three-component BEC to harbor many more unforeseen vortex-lattice structures for other values of σ and the intracomponent interaction strength g .

In light of the Rabi suppression, it might be interesting to compare and contrast the present system with a hybrid three-component system in which two components are different spin states of the same atom coherently coupled to each other, whereas the third component is a different species with different atomic mass and coupled only through density–density interactions to the other two components. In the limit of strong Rabi coupling, the hybrid system would reduce to a mass-imbalanced two-component BEC, whose rotating ground state exhibits a variety of unconventional ground-state vortex structures [16, 253]. This more intricate limiting behavior suggests that when the Rabi coupling is of intermediate strength, rotation of the hybrid system will likely produce novel ground-state vortex lattices that do not exist in our equal-mass system.

To realize the exotic vortex lattices experimentally, one could use, e.g., ^{87}Rb atoms in the hyperfine ground level $5^2\text{S}_{1/2}$. Two-component BECs have already been realized using mixtures of the $|F = 1, m_F = -1\rangle$ and $|2, 1\rangle$ states [10], the $|1, 1\rangle$ and $|2, 2\rangle$ states [149], and the $|2, 1\rangle$ and $|2, 2\rangle$ states [147] from this manifold. The Rabi-coupled three component BEC could be created by optically trapping a mixture of any three of these states and using microwave and radiofrequency radiation to coherently couple them via two-photon processes. The vortex lattices could then be produced by inducing rotation in the system and letting it relax to its minimum-energy state. Measurement of the relative phase between the BEC components should also be feasible [268]. We also note that many of the discovered phases could be distinguished by imaging only the profile of the total density n_{tot} .

The author contributed significantly to the central ideas of the research, constructed the model, implemented and carried out all numerical simulations, analyzed the data.

The results of this Chapter were submitted to Phys. Rev. A as: N. V. Orlova, P. Kuopanportti, and M. V. Milošević, Skyrmionic vortex lattices in coherently coupled three-component BoseEinstein condensates.

CHAPTER 5

Multiquantum vortices in two-component BEC

The results of the previous Chapter demonstrate the potential of the coupling between multiple condensates to create emergent physics that is not available otherwise. We prove that point further in this Chapter, on example of a two-component BEC. Namely, it is shown here that a rotating and harmonically trapped mixture of two Bose-Einstein-condensed superfluids can host a multiply quantized vortex in the ground state. Those so-called giant vortices are not stable in rotating and harmonically confined single-component BECs, and are thus a unique property of two-(or multi-)component BECs.

5.1 Introduction

According to the conventional paradigm [173, 175], the ground state in a rotating superfluid will involve only singly quantized vortices (SQVs). Vortices with larger quantum numbers are energetically unfavorable and do not occur—not even for rapid rotation, which instead spawns a triangular Abrikosov lattice of SQVs [85]. Although this is well established [170, 249, 251] for a solitary superfluid described by a single \mathbb{C} -valued order parameter Ψ , vortex physics becomes much more diverse when *multiple* mutually interacting superfluids are rotated simultaneously in the same container.

Already for the simplest mixture, which consists of two superfluid species and is described by two \mathbb{C} -valued order parameters Ψ_1 and Ψ_2 , a myriad of unusual ground-state vortex structures have been found in experimental and theoretical studies [252]. Experimentally, a versatile platform to study

vortices is provided by atomic Bose–Einstein condensates (BECs) [269, 172, 10], in which two-component superfluid mixtures have been realized using two different spin states of the same isotope [11, 9, 12, 10, 13, 14], two different isotopes of the same element [270, 271], or two distinct elements [151, 152, 153, 154, 155, 156, 272, 273, 274]. The unconventional vortex structures that were detected in these experiments comprise coreless SQVs [10] and square vortex lattices [11]. Theoretical studies, however, have furnished the two-species BECs with many more ground-state vortex configurations than the aforementioned two [254, 255, 159, 15, 157, 275, 276, 16]: Predicted but hitherto unobserved ones include serpentine vortex sheets [17], triangular lattices of vortex pairs [16], and, in a pseudospin-1/2 representation, giant skyrmions [158, 159] and meron pairs [254, 255].

One peculiar feature of the two-species mixture, which goes against the traditional paradigm, is the appearance of multiply quantized vortices (MQV) in the rotating ground state of the harmonically trapped system [158, 159, 16]. So far, the MQVs, also known as giant vortices, have been predicted only in complicated states involving a number of accompanying SQVs and a large total circulation, thereby requiring rotation frequencies close to the maximum set by the harmonic trap frequency. Consequently, the states have eluded experimental observation and, due to the accompanying SQVs, might not be suitable for investigating the rarely encountered ground-state MQV in a controlled fashion. Besides being exotic and interesting in their own right, MQVs could also be used to realize bosonic quantum Hall states [277], initiate quantum turbulence [278, 279, 280], or implement a ballistic quantum switch [281].

In this investigation, we make the ground-state MQVs more accessible to experiments by showing theoretically that an interacting mixture of two dilute superfluids, when rotated at moderate speed, exhibits ground states that contain a *solitary* MQV in one of the superfluids. We find such states both for mutually attractive mixtures, where the MQV has a completely empty core, and for mutually repulsive mixtures, where the core is occupied by the other, vortex-free superfluid species. These states represent a rare instance of a stable, solitary MQV in an atomic BEC and, as such, constitute a robust, well-isolated, and tunable environment for the experimental exploration of MQV physics, in complement to earlier observations in mesoscopic superconductors [282, 283, 284, 285].

All the discovered states share the property that the two superfluid species carry unequal numbers of circulation quanta under the same external rotation. This requires the two superfluids to be composed of particles with

sufficiently different masses¹. For concreteness, we will focus on the harmonically trapped two-species BEC of ⁸⁷Rb and ⁴¹K because it has already been realized in several experiments [151, 152, 153, 154, 155, 156], it enables a flexible control over its interaction strengths [154], and it has a suitable atomic mass ratio of ~ 2 . Although we present ground states only for this particular system, the essential features of our results apply generally to mass-imbalanced binary mixtures of dilute superfluids.

5.2 Model

We assume that the two-species BEC is rotated with angular velocity $\Omega \hat{\mathbf{z}}$. In the zero-temperature mean-field regime, the ground-state order parameters Ψ_1 (assigned to ⁸⁷Rb) and Ψ_2 (⁴¹K) satisfy the coupled time-independent Gross–Pitaevskii equations in the rotating reference frame [252]:

$$(\mathcal{H}_j + g_{jj}|\Psi_j|^2 + g_{12}|\Psi_{3-j}|^2 - \mu_j) \Psi_j(r, \phi) = 0, \quad (5.1)$$

where $j \in \{1, 2\}$,

$$\mathcal{H}_j = -\frac{\hbar^2}{2m_j} \nabla^2 + \frac{1}{2} m_j \omega_j^2 r^2 + i\hbar \Omega \frac{\partial}{\partial \phi}, \quad (5.2)$$

and the chemical potentials μ_j ensure that $\int |\Psi_j|^2 d^2r = N_j$. Here N_j , m_j , and ω_j denote, respectively, the total number, the mass, and the radial harmonic trapping frequency of species j atoms. We only consider quasi-two-dimensional configurations pertaining to, e.g., highly oblate (prolate) traps with strong (weak) axial confinement and Ψ_j approximately Gaussian (constant) in the axial direction. The intraspecies interaction strengths g_{jj} are assumed to be positive, whereas for the interspecies parameter g_{12} we also consider negative values.

We parametrize the interactions by the three dimensionless quantities $U = (g_{11} + g_{12}) m_1 N_1 / \hbar^2$, g_{22}/g_{11} , and $\Gamma = g_{12} / \sqrt{g_{11} g_{22}} > -1$. The ground states, i.e., the lowest-energy solutions of Eqs. (5.1), are then uniquely specified by these three and the following four other parameters: m_2/m_1 , N_2/N_1 , ω_2^2/ω_1^2 , and Ω/ω_1 . Focusing on the ⁸⁷Rb–⁴¹K BEC, we fix $m_2/m_1 = 0.471$. The dimensionless equations, the discretization scheme, and the numerical method which we used to solve Equations (5.1) are given in details in **Chapter 1**, Subsections 1.6.6, 1.6.7 and 1.6.8.

¹Essentially, this is because the circulation $\oint \mathbf{v}(\mathbf{r}) \cdot d\mathbf{r}$ of the superfluid velocity $\mathbf{v} = \hbar \nabla \text{Arg}(\Psi) / m$ is quantized in units of $2\pi\hbar/m$, where m is the mass of the superfluid particles.

5.3 Ground-state multiquantum vortices

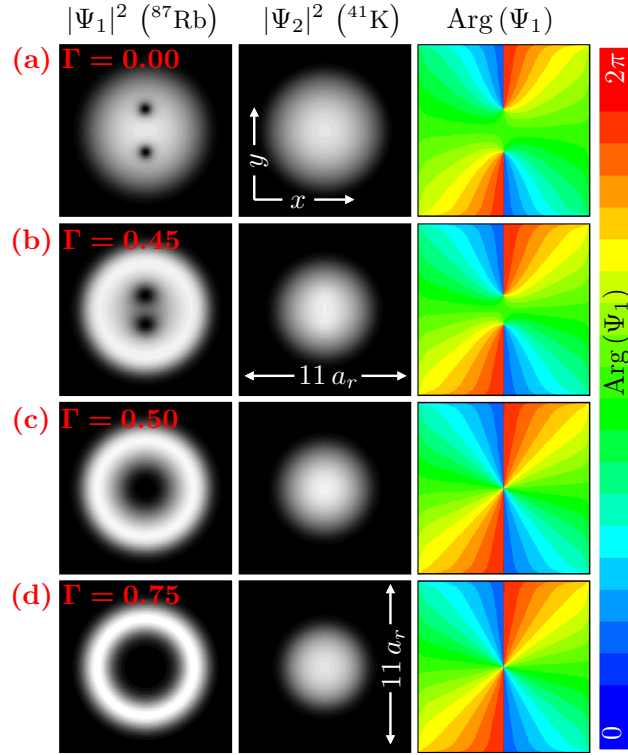


Figure 5.1: Emergence of a ground-state two-quantum vortex in a rotating, mutually repulsive two-species ^{87}Rb – ^{41}K BEC. (a)–(d) Atomic densities $|\Psi_1|^2$ and $|\Psi_2|^2$ and the complex phase of the order parameter Ψ_1 in the ground state at the indicated value of the interspecies interaction strength $\Gamma = g_{12}/\sqrt{g_{11}g_{22}}$. In all four cases, $\text{Arg}(\Psi_2) \equiv \text{const}$ (not shown). The parameters in the Gross–Pitaevskii equations are set to $m_2/m_1 = 0.471$, $g_{22}/g_{11} = 4$, $\omega_2^2/\omega_1^2 = 10$, $N_2/N_1 = 1$, $\Omega/\omega_1 = 0.4$, and $U = (g_{11} + g_{12})m_1N_1/\hbar^2 = 300$. The chosen value of U corresponds approximately to 10^3 atoms in the system. The length unit is $a_r = \sqrt{\hbar/m_1\omega_1}$.

In order to understand why MQVs emerge in the rotating two-species BEC, we begin with a scenario where only Γ is varied while the other parameters are held constant. Furthermore, for $\kappa_j \in \mathbb{Z}$, let $\langle \kappa_1, \kappa_2 \rangle$ denote a sufficiently pointlike phase defect about which $\arg(\Psi_1)$ winds by $\kappa_1 \times 2\pi$ and $\arg(\Psi_2)$ by $\kappa_2 \times 2\pi$. For interspecies repulsion ($\Gamma > 0$), the simplest MQV state appearing as the ground state is a $\langle 2, 0 \rangle$ vortex, whereas for $\Gamma < 0$, the simplest one corresponds to $\langle 2, 1 \rangle$. In this quasi-2D system, the $\langle 2, 0 \rangle$ state

is a pointlike vortex defect that carries two quanta of phase circulation in the first component and none in the second component. Respectively, the $\langle 2, 1 \rangle$ vortex can be defined as a state in which the first component hosts two quanta of circulation while the second component carries one quantum of circulation. Below, we investigate these two cases separately.

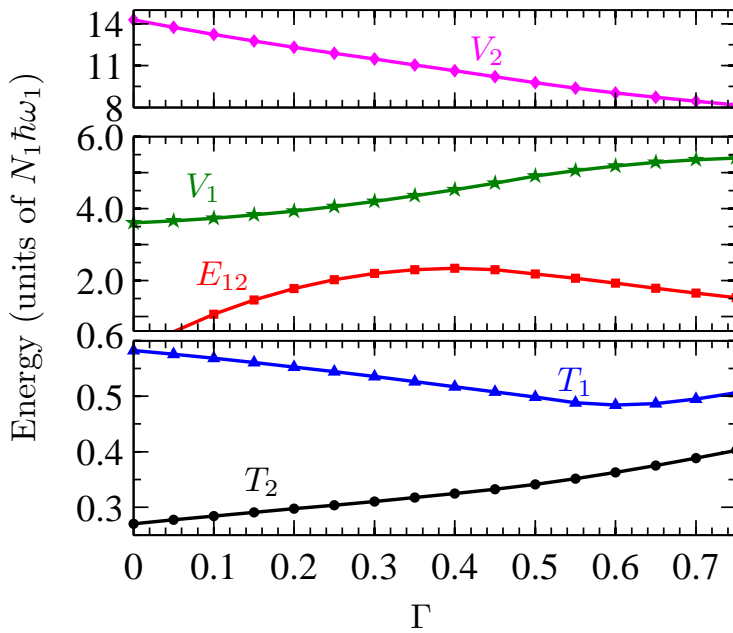


Figure 5.2: Interspecies interaction energy $E_{12} = g_{12} \int |\Psi_1 \Psi_2|^2 d^2r$, kinetic energies $T_j = \hbar^2 \int |\nabla \Psi_j|^2 d^2r / 2m_j$, and trap energies $V_j = m_j \omega_j^2 \int r^2 |\Psi_j|^2 d^2r / 2$ as functions of Γ for the same ground states. The parameters in the Gross–Pitaevskii equations are the same as ones given in Fig. 5.1.

Consider first the mutually repulsive mixture. Figures 5.1(a)–5.1(d) depict ground states at different $\Gamma \geq 0$ for a rotating ^{87}Rb – ^{41}K BEC in which there are two circulation quanta in Rb and none in K. Figure 5.2 shows the relevant energy terms as a function of Γ . When $\Gamma = 0$ [Fig. 5.1(a)], the two off-centered $\langle 1, 0 \rangle$ vortices are separated by a distance of ~ 10 times their core radius. As Γ increases, the condensates move apart, with Rb shifting outward and K inward; this behavior is manifested in the trap potential energy, which increases for Rb and decreases for K. Consequently, Rb is depleted

from the region between the two $\langle 1, 0 \rangle$ vortices, enabling them to merge into a $\langle 2, 0 \rangle$ vortex without the kinetic-energy increase typical of MQV formation; indeed, the kinetic energy T_1 of Rb decreases with $\Gamma \in [0, 0.6]$. Hence, for $\Gamma \geq 0.5$, we observe an axisymmetric $\langle 2, 0 \rangle$ vortex, about which $\arg(\Psi_1)$ winds by $2 \times 2\pi$. It is a coreless vortex [254, 255, 159, 286, 287, 288, 289] in the sense that the total atomic density $n_{\text{tot}} = |\Psi_1|^2 + |\Psi_2|^2$ does not vanish at the phase singularity. We stress that the $\langle 2, 0 \rangle$ vortex is a unique example of a ground-state MQV in a purely harmonic trap that occurs as a solitary topological defect without any accompanying SQVs.

The emergence of the ground-state $\langle 2, 1 \rangle$ vortex for $\Gamma < 0$ is illustrated in Fig. 5.3. For uncoupled condensates [Fig. 5.3(a)], there are two off-centered $\langle 1, 0 \rangle$ vortices and one central $\langle 0, 1 \rangle$ vortex. As Γ approaches -1 , the two $\langle 1, 0 \rangle$ vortices move closer to each other, so that at $\Gamma = -0.98$, all three phase singularities lie at the origin and make up an axisymmetric $\langle 2, 1 \rangle$ vortex. To explain the movement, we note that the kinetic energy T_1 increases when the two vortices approach each other, whereas the interspecies interaction energy E_{12} decreases due to the increasing overlap $\int n_1 n_2 d^2r$. Since E_{12} gains in importance when the attraction becomes stronger, it eventually begins to dominate over T_1 , and thus the $\langle 2, 1 \rangle$ vortex forms [Fig. 5.3(d)].

The ground-state $\langle 2, 1 \rangle$ vortex constitutes a rare instance of a stable MQV with a genuinely empty, self-supporting core. Typically, such vortices are rendered unstable against splitting by quasiparticle excitations that are highly localized within the core [290, 291, 292, 293, 294, 295, 296, 297, 298, 299, 300, 301, 302]. In our case, however, the doubly quantized vortex in Ψ_1 is held together by the indivisible SQV in Ψ_2 .

The $\langle 2, 1 \rangle$ vortices are most readily found for relatively small values of U . This is because small U implies a large size of the vortex cores, which suppresses the kinetic energy near the phase singularities and leads to strong dependence of E_{12} on the vortex positions.

To produce the MQVs of Figs. 5.1 and 5.3, it is desirable to have control over the parameter $\Gamma = g_{12}/\sqrt{g_{11}g_{22}}$. In experiments, g_{jk} may be tuned with Feshbach resonances [160], which have been demonstrated for ^{87}Rb – ^{87}Rb [303, 304, 305], ^{41}K – ^{41}K [306, 307], and ^{87}Rb – ^{41}K [154] interactions. However, ground-state MQVs can also be obtained in the ^{87}Rb – ^{41}K BEC without employing Feshbach resonances. To demonstrate this for an axially uniform system, we use the bare s -wave scattering lengths $a_{11}/a_B = 99$ [308], $a_{22}/a_B = 60$ [309], and $a_{12}/a_B = 163$ [151], where a_B is the Bohr radius, and accordingly set $g_{22}/g_{11} = 1.29$ and $\Gamma = 2.27$. The remaining parameters are fixed after the ^{87}Rb – ^{41}K experiment of Ref. [156].

Figure 5.4 shows the resulting ground states at two different rotation

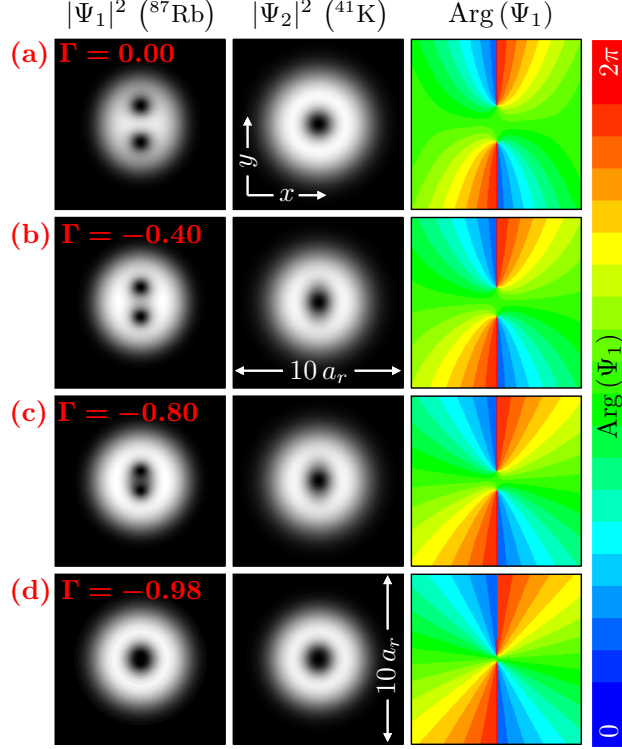


Figure 5.3: Formation of a ground-state vortex with specieswise quantum numbers $\langle \kappa_1, \kappa_2 \rangle = \langle 2, 1 \rangle$ in a rotating, mutually attractive ^{87}Rb - ^{41}K BEC. (a)–(d) Atomic densities $|\Psi_1|^2$ and $|\Psi_2|^2$ and the complex phase of Ψ_1 in the ground state at the indicated value of $\Gamma = g_{12}/\sqrt{g_{11}g_{22}}$; $\text{Arg}[\Psi_2(r, \phi)] \simeq \phi$ for all Γ (not shown). Here $g_{22}/g_{11} = \omega_2^2/\omega_1^2 = N_2/N_1 = 1$, $\Omega/\omega_1 = 0.7$, and $U = 50$. The chosen value of U corresponds approximately to 10^2 atoms in the system.

frequencies, $\Omega/\omega_1 = 0.7$ and 0.8 . At $\Omega/\omega_1 = 0.7$ (0.8), the Rb species hosts a central 9-quantum (12-quantum) giant vortex surrounded by a ring of 13 (16) SQVs. In both cases, the K species is vortex-free and occupies the core of the central giant vortex. However, due to high rotation frequency and strong self-interaction, the first component triggers more vortices. The vortices which did not enter the giant vortex formed in the center, arrange into a ring of vortices instead, because the second component located in the center and this configuration minimizes the free energy. At larger Ω , the giant vortex becomes surrounded by a triangular lattice of SQVs; similar profiles have been found earlier for rapidly rotating single-component BECs in anharmonic trap potentials [310, 311, 312, 313, 314, 315, 316, 317, 318].

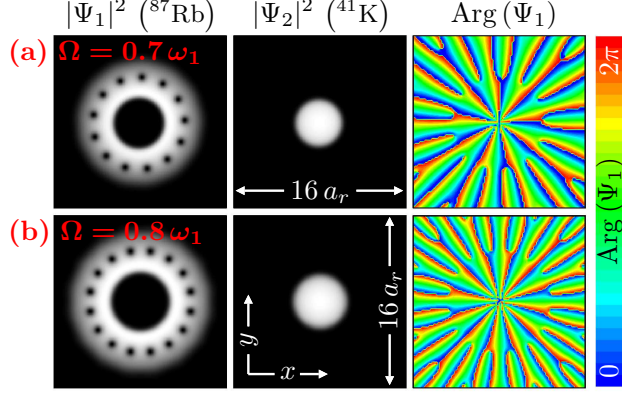


Figure 5.4: Ground states of a ^{87}Rb - ^{41}K BEC with interaction parameters $\Gamma = 2.27$ and $g_{22}/g_{11} = 1.29$ corresponding to the unmodified scattering lengths in a highly prolate trap, shown for two different rotation frequencies. In both states, $\text{Arg}(\Psi_2) \equiv \text{const}$ (not shown). Furthermore, $\omega_2^2/\omega_1^2 = 2.12$, $N_2/N_1 = 0.27$, and $U = 2800$ after the experiment of Ref. [156]. The chosen value of U corresponds approximately to 10^6 atoms in the system.

5.4 Pseudospin textures

In this Section, we analyze our results in the pseudospin-1/2 representation [145, 319, 254, 255]. At points where $n_{\text{tot}} \neq 0$, we define the local unit-length pseudospin

$$\hat{\mathbf{s}}(r, \phi) = \frac{1}{n_{\text{tot}}(r, \phi)} \sum_{jk} \Psi_j^*(r, \phi) \boldsymbol{\sigma}_{jk} \Psi_k(r, \phi), \quad (5.3)$$

where $\boldsymbol{\sigma}$ is a vector of the three Pauli matrices. Now consider a $\langle \kappa_1, \kappa_2 \rangle$ vortex about which the atomic densities are locally axisymmetric. After transforming to shifted polar coordinates (r', ϕ') with the vortex core at $r' = 0$, we can write Ψ_j , for small r' , in terms of a spin rotation Z and a $U(1)$ gauge transformation acting on a unit-length reference spinor $\chi \in \mathbb{C}^2$:

$$\begin{aligned} \Psi_j(r', \phi') &= |\Psi_j(r')| e^{i(\kappa_j \phi' + C_j)} \\ &= \sqrt{n_{\text{tot}}(r')} e^{\frac{i}{2} \kappa_g \phi'} \sum_k Z_{jk}(\kappa_s \phi') \chi_k(r'), \end{aligned} \quad (5.4)$$

where $\kappa_s = \kappa_2 - \kappa_1$ and $\kappa_g = \kappa_1 + \kappa_2$ are integers that determine, respectively, the number of 2π rotations of $\hat{\mathbf{s}}$ about the unit vector $\hat{\mathbf{z}}$ and the number of π windings of the $U(1)$ gauge along a contour enclosing the core, $Z(\kappa_s \phi') = \exp(-i\kappa_s \phi' \sigma_z/2)$, and $C_j \in \mathbb{R}$ are constants.

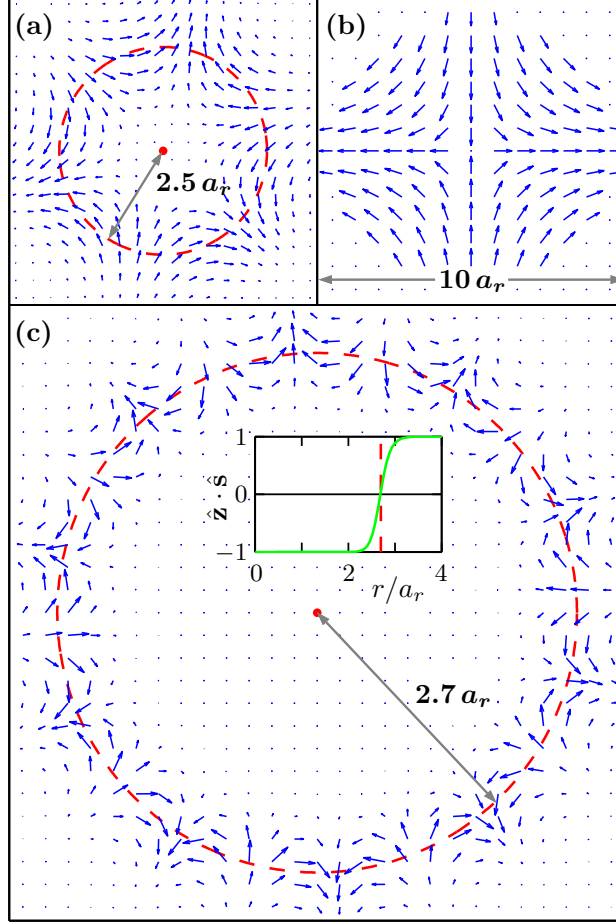


Figure 5.5: Pseudospin textures of a (a) two-quantum skyrmion [for the state in Fig. 5.1(d)], (b) single-quantum spin vortex [Fig. 5.3(d)], and (c) nine-quantum giant skyrmion [Fig. 5.4(a)]. The arrows represent the projection of the local pseudospin $\hat{\mathbf{s}} = \sum_{jk} \Psi_j^* \boldsymbol{\sigma}_{jk} \Psi_k / n_{\text{tot}}$ onto the xy plane. Here $\boldsymbol{\sigma}$ is a vector of the Pauli matrices and $n_{\text{tot}} = |\Psi_1|^2 + |\Psi_2|^2$. The dashed circle is the species interface, where $|\Psi_1| = |\Psi_2|$. The inset in (c) shows the z projection of $\hat{\mathbf{s}}$ as a function of the radial coordinate r .

Figure 5.5 shows $\hat{\mathbf{s}}$ for some of the ground states in Figs. 5.1, 5.3, and 5.4. The $(2, 0)$ vortex in Fig. 5.1(d) is interpreted as a doubly quantized skyrmion [158, 159] located at the circular interface of the two species, where $|\Psi_1| = |\Psi_2|$. Since $\kappa_s = -2$, $\hat{\mathbf{s}}$ rotates by -4π about $\hat{\mathbf{z}}$ when the interface is traversed azimuthally; additionally, the projection $\hat{\mathbf{z}} \cdot \hat{\mathbf{s}}$ changes from -1 to 1 when the

interface is crossed radially. For the $\langle 2, 1 \rangle$ vortex in Fig. 5.3(d), the $U(1)$ gauge winds by 3π and the spin $\hat{\mathbf{s}}$ by -2π . However, because now $\hat{\mathbf{z}} \cdot \hat{\mathbf{s}}$ vanishes everywhere, this state is not a skyrmion but instead corresponds to a singly quantized *spin vortex*. The defect is structurally similar to the so-called cross disgyration in the fermionic superfluid ${}^3\text{He-A}$ [320, 321]. Finally, the states in Fig. 5.4 feature giant skyrmions with (a) $\kappa_s = -9$ and (b) $\kappa_s = -12$.

5.5 Summary and Conclusions

In this study, we have demonstrated that two-species BECs in rotating harmonic traps are able to host thermodynamically stable multiquantum (or giant) vortices. Such topological entities rarely exist in the ground state and have thus been elusive in BECs, whereas they are observed and useful in, e.g., mesoscopic superconductivity [281, 282, 283, 284, 285]. In the present case, their stability is not induced by elaborate external potentials [310, 311, 312, 313, 314, 315, 316, 317, 318, 322, 323, 324] but is an inherent property of the harmonically confined, mass-imbalanced two-species system: The giant vortex in the heavier species is stabilized by its coupling to the lighter, giant-vortex-free species.

Experimentally, the presence of the MQV could be verified, e.g., by measuring the orbital angular momentum using surface wave spectroscopy [325, 326, 327] or by detecting the κ_j -dependent concentric density ripples that would form in free expansion [328]. Due to its ground-state nature, the MQV is expected to be highly reproducible, long lived, and therefore amenable to extensive measurements.

We also classified the discovered states into spin-skyrmion (coreless) and spin-vortex (cored) variants, both of which can be realized in a mixture ${}^{87}\text{Rb}$ - ${}^{41}\text{K}$ BEC [151, 152, 153, 154, 155, 156]. The similarities of these vortices with fractional [212] and skyrmionic [210] vortex states in multiband superconductors, as well as the rich possibilities for the creation and tuning of multispecies BECs [151, 152, 153, 154, 155, 156, 272, 273, 274], open a wide avenue for exploring emergent physics in multicomponent quantum systems consisting of inherently nonidentical components.

The author contributed significantly to the basic concept, implemented and performed all numerical calculations, participated in analyzing the results.

The results presented in this Chapter were published as: P. Kuopanportti, N. V. Orlova, and M. V. Milošević, Ground-State Multiquantum Vortices in

Two-Species Superfluids, Phys. Rev. A **91**, 043605 (2015).

CHAPTER 6

Summary and outlook

In this thesis, multi-component quantum systems were studied, such as multi-band superconductors, nano and atomically thin films, and multi-component Bose-Einstein condensates. New phenomena, which appear exclusively in these multi-component systems, are inherently connected with the complexity of interacting many-particle system stemming from the multi-component nature and the competing effects arising between constituent components of the system. Due to those exciting properties, multi-component systems provide numerous prospects and challenges for future studies. In this thesis, the solid platform for such studies was provided by deriving the consistent Ginzburg-Landau theory for multiband superconductors and superconducting nanofilms, bearing in mind that the GL theory is to date the most convenient theoretical tool to study superconducting properties and related phenomena in the proximity of the critical temperature T_c . Rotating and harmonically trapped multi-component Bose-Einstein condensates were also studied in this thesis as example of a multicomponent system that exhibits rich and pronounced quantum phenomena, which can then be experimentally realized and further manipulated in a broad range of parameters.

In what follows, the main results of the thesis are summarized in concreto.

In **Chapter 2**, the Ginzburg-Landau theory for the multiband superconductors was derived from the multiband BCS Hamiltonian. The derivation is based on the Gor'kov truncation of the matrix gap equation. The procedure invokes the expansion of the band gaps in powers of τ (where $\tau = 1 - T/T_c$). In the expansion, we removed incomplete contributions into the band gaps which are of orders higher than $\tau^{1/2}$, i. e., higher than the precision of the

solution of the original Gor'kov truncation. After performing this procedure, the accuracy of the gap matches the accuracy of the Gor'kov truncation. Further, we considered two scenarios for the solution for the critical temperature T_c . When the solution for T_c is not degenerate, we found that the Ginzburg-Landau theory of a multiband superconductor maps onto a single-component GL formalism in which only a unique order parameter exists, and, as a consequence, the spatial profiles of all band gaps are equivalent. If the solution for T_c is degenerate, which appears due to a symmetry of the system, the Ginzburg-Landau theory acquires multiple order parameters. The detailed analysis was performed for the three-band system, treated as a prototype of a multiband superconductor. For the simple three-band model of pnictides with dominant interband couplings, it was shown that the solution for T_c is twofold degenerate, resulting in existence of two order parameters in the theory, which in turn leads to appearance of non trivial phase difference between the gaps or, so-called, chiral solutions. It was demonstrated that chiral state can be the ground state of such a three-band superconductor, thus can be experimentally realized. The explicit microscopic expressions for the otherwise phenomenological coefficients of the Ginzburg-Landau theory were found.

In **Chapter 3**, it was demonstrated that due to the size quantization of the electron motion limited in one of the dimensions, single-crystalline metallic nanofilms exhibit multiband structure. The Ginzburg-Landau theory appropriate for single-crystalline metallic nanofilms was derived. In the derivation, the suitable BCS Hamiltonian was constructed for such a 2D system by integrating out the coordinate in which the electron motion is limited. The matrix gap equations were obtained for this multiband system from the newly constructed Hamiltonian. Subsequently, the same procedure of the Gor'kov truncation on removing incomplete contributions in the band gaps, similar to the one used in Chapter 2, was employed. The explicit expressions for the coefficients of the Ginzburg-Landau formalism for the single-crystalline metallic nanofilms were also found. The obtained formalism is computationally convenient and efficient, and will serve as a powerful theoretical tool for further investigations of the effects of the multiple-subband structure on, e.g., vortex configurations, critical phenomena and superconducting fluctuations in nano-thin single-crystalline samples.

In the second half of the thesis, the multicomponent Bose-Einstein condensates were studied. In **Chapter 4**, rotating and harmonically trapped Rabi-coupled three-component Bose-Einstein condensates were studied. This system was shown to host unconventional vortex lattices in the rotating ground state of the system. It was demonstrated that the found states can be topologically characterized as a two-dimensional lattice of skyrmions. To

classify the states with different skyrmionic lattices, the average topological index was calculated as the average of pairwise $\mathbb{C}P^1$ topological indices of each pair of components. Different skyrmionic vortex lattices were then grouped into two phase diagrams in the parameter space of the intercomponent interaction strength σ and Rabi coupling frequency ω_{12} of the two components, for other parameters fixed. In this study, equal contributions of all three components were assumed, and the Rabi couplings were the only varied parameters which is possible to achieve in current experiments. Besides the emerging plethora of possible vortex lattice topologies, it was also shown that at certain combinations of signs and values of the Rabi frequencies ω_{ij} relative phase frustration arises in the system resulting in some of the pairwise Rabi energies to become heavily suppressed. Such Rabi suppression leads to an effective reduction of the three-component BEC to a density-density-coupled two-component BEC. These exciting features are not only of fundamental importance, but their observation in an experiment can be used as a proof of frustration in the system under consideration.

In **Chapter 5**, two-component Bose-Einstein condensates in rotating harmonic traps were investigated in three different regimes. The first regime is miscible with intercomponent attractive interaction, the second represents the miscible regime with intercomponent repulsive interaction, while the third is the immiscible regime with intercomponent repulsive interaction, with the consequently separated phases. Stable multiquantum vortices in all three regimes were found, and it was shown that their stability is an inherent property of the harmonically confined, mass-imbalanced two-component system. The discovered states were classified into spin-skyrmion (coreless) and spin-vortex (cored) variants, both of which can be realized in a ^{87}Rb - ^{41}K BEC with the current experimental techniques, and both of which are novel phases in the field.

In future research, it would be of importance to study fundamental vortex properties in nanofilms by employing the multiband Ginzburg-Landau theory for superconducting nanofilms, and further compare the findings to the broadly known Pearl limit for vortices in thin films. Next the effects of lateral confinement should be studied, following recent experiments on a nano-thin Pb islands [330, 331, 332]. Concerning bulk materials, the chiral regime that was shown to arise in three-band superconductors requires a more detailed investigation, particularly with respect to formation of chiral domains and domain walls, as well as the new topological defects such as skyrmions. Even the behavior of critical fields in the chiral regime of a multi-band superconductor is yet to be calculated and understood. Logically, the extension of the Ginzburg-Landau theory to the next order in τ is also beneficial for the studies deeper in the superconducting state. On the BEC side, the study of

the Rabi-coupled multicomponent BECs should be extended to the broader range of multiple parameters playing a role in the equilibrium phases. Besides the stable configurations of the emergent phases, one should pay special attention to dynamics in this system, particularly the nontrivial transitions between the phases, and the vortical transformations therein.

CHAPTER 7

Samenvatting en vooruitzichten

In deze thesis werden multicomponent kwantumsystemen bestudeerd, waaronder multiband supergeleiders, atomair en nanodunne films en multicomponente Bose-Einstein condensaten. Nieuwe fenomenen, welke uitsluitend in deze multicomponent systemen voorkomen, zijn inherent verbonden met de complexiteit van interagerende veel-deeltjes systemen afkomstig van het multicomponent karakter en de concurrerende effecten die ontstaan tussen de samenstellende componenten van het systeem. Dankzij deze opwindende eigenschappen bieden multicomponent systemen talrijke vooruitzichten en uitdagingen voor toekomstige studies. In deze thesis werd de solide basis voor dergelijk studies geleverd door de consistente Ginzburg-Landau theorie af te leiden voor multiband supergeleiders en supergeleidende nanofilms, aangezien de GL theorie tot op heden het meest geschikte theoretische hulpmiddel is om supergeleidende eigenschappen en gerelateerde fenomenen te bestuderen in de buurt van de kritische temperatuur T_c . Roterende en harmonisch opgesloten multicomponent Bose-Einstein condensaten werden ook bestudeerd in deze thesis als voorbeeld van een multicomponent systeem dat rijke en uitgesproken kwantumfenomenen vertoont, welke dan experimenteel kunnen worden gerealiseerd en verder worden gemanipuleerd in een breed bereik van parameters.

In wat volgt worden de belangrijkste resultaten van de thesis concreet samengevat.

In **Hoofdstuk 2** werd de Ginzburg-Landau theorie voor de multiband supergeleiders afgeleid uit de multiband BCS Hamiltoniaan. De afleiding is gebaseerd op de Gor'kov afkapping van de bandkloof vergelijking. De pro-

cedure doet een beroep op de expansie van de bandkloven in machten van τ (met $\tau = 1 - T/T_c$). In de expansie verwijderden we onvolledige bijdragen aan de bandkloven welke van hogere orde zijn dan $\tau^{1/2}$, oftewel, hoger dan de precisie van de oplossing van de oorspronkelijke Gor'kov afkapping. Na het uitvoeren van deze procedure komt de nauwkeurigheid van de bandkloof overeen met de nauwkeurigheid van de Gor'kov afkapping. Verder hebben we twee scenario's beschouwd voor de oplossing van de kritische temperatuur T_c . Wanneer de oplossing voor T_c niet ontaard is, vonden we dat de Ginzburg-Landau theorie voor een multiband supergeleider afgebeeld wordt op een een-component GL formalisme waarin slechts één unieke orderparameter bestaat en, bijgevolg, de ruimtelijke profielen van alle bandkloven equivalent zijn. Als de oplossing voor T_c ontaard is, wat een gevolg is van een symmetrie van het systeem, bevat de Ginzburg-Landau theorie meerdere orderparameters. De gedetailleerde analyse werd uitgevoerd voor het drieband systeem, wat als een prototype van een multiband supergeleider werd behandeld. Voor het simpele drieband model van pnictiden met dominante interband koppeling werd aangetoond dat de oplossing voor T_c tweevoudig ontaard is, wat resulteert in het bestaan van twee orderparameters in de theorie, wat dan weer leidt tot de aanwezigheid van niet-triviale faseverschillen tussen de bandkloven, ook wel chirale oplossingen genoemd. Er werd aangetoond dat een chirale toestand de grondtoestand van zo'n drieband supergeleider kan zijn en dus experimenteel kan worden gerealiseerd. De expliciete microscopische uitdrukkingen voor de normaal gezien fenomenologische coëfficiënten van de Ginzburg-Landau theorie werden bepaald.

In **Hoofdstuk 3** werd aangetoond dat, als gevolg van de kwantisatie geassocieerd met de opsluiting van de elektronen in een van de dimensies, monokristallijne metallische nanofilms een multiband structuur vertonen. De geschikte Ginzburg-Landau theorie voor monokristallijne metallische nanofilms werd afgeleid. In de afleiding werd de correcte BCS Hamiltoniaan voor zo'n 2D systeem geconstrueerd door over de coördinaat geassocieerd met de opsluitingsrichting te integreren. De matrix bandkloof vergelijkingen voor dit multiband systeem werden uit de nieuwe opgestelde Hamiltoniaan bepaald. Vervolgens werd opnieuw de Gor'kov afkapping voor het verwijderen van onvolledige bijdragen aan de bandkloven, gelijkaardig aan de gehanteerde methode in Hoofdstuk 2, toegepast. De expliciete uitdrukkingen voor de coëfficiënten van het Ginzburg-Landau formalisme voor de monokristallijne metallische nanofilms werden ook bepaald. Het verkregen formalisme is efficiënt en geschikt voor computationele doeleinden, en zal dienen als een krachtig theoretisch hulpmiddel voor verdere studies van de effecten van de multisubband structuur op, bijvoorbeeld, vortex configuraties, kritische fenomenen en supergeleidende fluctuaties in nanodunne monokristallijne ma-

terialen.

In het tweede deel van de thesis werden multicomponent Bose-Einstein condensaten bestudeerd. In **Hoofdstuk 4** werden roterende en harmonisch opgesloten Rabi-gekoppelde driecomponent Bose-Einstein condensaten bestudeerd. Van dit systeem werd bewezen dat het ongebruikelijke vortexroosters vertoont in zijn roterende grondtoestand. Er werd aangetoond dat de gevonden toestanden topologisch gekarakteriseerd kunnen worden als een tweedimensionaal rooster van skyrmionen. Om de toestanden met verschillende skyrmionroosters te classificeren werd de gemiddelde topologische index berekend als het gemiddelde van de paarsgewijze $\mathbb{C}P^1$ topologische indices van elk paar van componenten. Verschillende skyrmionische vortexroosters werden vervolgens gegroepeerd in twee fase-diagrammen in de parameter-ruimte van de intercomponent interactiesterkte σ en de Rabi koppelings-frequentie ω_{12} van de twee componenten, voor vaste waarden van andere parameters. In deze studie werden gelijke bijdragen van alle drie de componenten verondersteld en waren de Rabi koppelingen de enige parameters die werden gevarieerd, wat haalbaar is in huidige experimenten. Naast het verschijnen van een overvloed aan mogelijke vortexrooster topologieën, werd ook aangetoond dat bij specifieke combinaties van de tekens en waarden van de Rabi frequenties ω_{ij} frustratie van de relatieve fase ontstaat in het systeem, wat als gevolg heeft dat sommige paarsgewijze Rabi energieën zwaar worden onderdrukt. Dergelijke Rabi onderdrukking leidt tot een effectieve reductie van het driecomponent BEC tot een dichtheid-dichtheid-gekoppeld tweecomponent BEC. Deze opwindende kenmerken zijn niet alleen van fundamenteel belang, maar hun observatie in een experiment kan worden gebruikt als een bewijs van frustratie in het beschouwde systeem.

In **Hoofdstuk 5** werden tweecomponent Bose-Einstein condensaten in roterende harmonische vallen onderzocht in drie verschillende regimes. Het eerste regime is vermengbaar en heeft attractieve intercomponentinteractie, het tweede is het vermengbaar regime met repulsieve intercomponentinteractie, en het derde is het niet-vermengbare regime met repulsieve intercomponentinteractie en bijgevolg met gescheiden fases. In alle drie de regimes werden multikwantum vortices gevonden en er werd aangetoond dat hun stabiliteit een inherente eigenschap is van het harmonisch opgesloten tweecomponent systeem bestaande uit atomen met verschillende massa's. De gevonden toestanden werden geclassificeerd in spin-skyrmion en spin-vortex varianten, welke beide kunnen worden gerealiseerd in een $^{87}\text{Rb} - ^{41}\text{K}$ BEC met de huidige experimentele technieken en welke beide nieuwe fases zijn in het onderzoeksveld.

In toekomstig onderzoek zou het van belang zijn om fundamentele vortexeigenschappen in nanofilms te bestuderen door de multiband Ginzburg-

Landau theorie voor supergeleidende nanofilms te gebruiken, en om de resultaten verder te vergelijken met de welgekende Pearl limiet voor vortices in dunne films. Verder zouden de effecten van laterale opsluiting kunnen worden bestudeerd, volgend op recente experimenten met nanodunne Pb-eilanden [330, 331, 332]. Betreffende bulk materialen, vereist het chirale regime waarvan werd aangetoond dat het ontstaat in drieband supergeleiders een meer gedetailleerde studie, in het bijzonder betreffende de vorming van chirale domeinen en domeinmuren, evenals de nieuwe topologische defecten zoals skyrmionen. Zelfs het gedrag van kritische velden in het chirale regime van een multiband supergeleider is nog niet berekend en begrepen. Logischerwijze is de uitbreiding van de Ginzburg-Landau theorie naar de volgende orde in τ ook voordelig voor studies dieper in de supergeleidende toestand. Op het BEC vlak zou de studie van de Rabi-gekoppelde multicomponent Bose-Einstein condensaten moeten worden uitgebreid naar een breder bereik van meerdere parameters die een rol spelen in de evenwichtsfases. Naast de stabiele configuraties van de mogelijke fases zou er ook speciale aandacht moeten worden besteed aan de dynamica van het systeem, in het bijzonder de niet-triviale overgangen tussen de fases en de vorticale transformaties die zich daarin voordoen.

Bibliography

- [1] V. Moshchalkov, M. Menghini, T. Nishio, Q. H. Chen, A. V. Silhanek, V. H. Dao, L. F. Chibotaru, N. D. Zhigadlo, and J. Karpinski, *Phys. Rev. Lett.* **102**, 117001 (2009).
 - [2] J. Gutierrez, B. Raes, A. V. Silhanek, L. J. Li, N. D. Zhigadlo, J. Karpinski, J. Tempere, and V. V. Moshchalkov, *Phys. Rev. B* **85**, 094511 (2012).
 - [3] Y. Lubashevsky, E. Lahoud, K. Chashka, D. Podolsky, and A. Kanigel, *Nat. Phys.* **8**, 309 (2012).
 - [4] A. Guidini and A. Perali, *Supercond. Sci. Technol.* **27**, 124002 (2014).
 - [5] D. F. Agterberg, V. Barzykin and L. P. Gor'kov, *Phys. Rev. B* **60**, 14868 (1999).
 - [6] V. Stanev and Z. Tešanović, *Phys. Rev. B* **81**, 134522 (2010).
 - [7] L. Komendová, Y. Chen, A. A. Shanenko, M. V. Milošević, and F. M. Peeters, *Phys. Rev. Lett.* **108**, 207002 (2012).
 - [8] A. Vagov, A. A. Shanenko, M. V. Milošević, V. M. Axt, V. M. Vinokur, and F. M. Peeters, *Critical superconductors* arXiv:1311.5624 (2013).
 - [9] C. J. Myatt, E. A. Burt, R. W. Ghrist, E. A. Cornell, and C. E. Wieman, *Phys. Rev. Lett.* **78**, 586 (1997).
 - [10] M. R. Matthews, B. P. Anderson, P. C. Haljan, D. S. Hall, C. E. Wieman, and E. A. Cornell, *Phys. Rev. Lett.* **83**, 2498 (1999).
-

-
- [11] V. Schweikhard, I. Coddington, P. Engels, S. Tung, and E. A. Cornell, Phys. Rev. Lett. **93**, 210403 (2004).
- [12] D. S. Hall, M. R. Matthews, J. R. Ensher, C. E. Wieman, and E. A. Cornell, Phys. Rev. Lett. **81**, 1539 (1998).
- [13] G. Delannoy, S. G. Murdoch, V. Boyer, V. Josse, P. Bouyer, and A. Aspect, Phys. Rev. A **63**, 051602 (2001).
- [14] R. P. Anderson, C. Ticknor, A. I. Sidorov, and B. V. Hall, Phys. Rev. A **80**, 023603 (2009).
- [15] E. J. Mueller, and T.-L. Ho, Phys. Rev. Lett. **88**, 180403 (2002).
- [16] P. Kuopanportti, J. A. M. Huhtamäki, and M. Möttönen, Phys. Rev. A **85**, 043613 (2012).
- [17] K. Kasamatsu, and M. Tsubota, Phys. Rev. A **79**, 023606 (2009).
- [18] U. A. Khawaja, and H. Stoof, Nature **411**, 918 (2001).
- [19] B. T. Geilikman, R. O. Zaitsev and V. Z. Kresin, Solid State Phys. **9**, 642 (1967) [in Russian, Fizika Tverdogo Tela **9**, 821 (1967)].
- [20] V. G. Kogan and J. Schmalian, Phys. Rev. B **83**, 054515 (2011).
- [21] A. A. Shanenko, J. Albino Aguiar, A. Vagov, M. D. Croitoru, and M. V. Milošević, Supercond. Sci. Technol. **28**, 054001 (2015).
- [22] H. Kamerlingh Onnes, Leiden Comm. **120b**, **122b**, **124c** (1911).
- [23] W. Meissner and R. Ochsenfeld, Naturwissenschaften **21**, 787 (1933).
- [24] F. and H. London, Proc. Roy. Soc. (London) **A149**, 71 (1935).
- [25] A. B. Pippard, Proc. Roy. Soc. (London) **A216**, 547 (1953).
- [26] L. Hoddeson, G. Baym, and M. Eckert, Reviews of Modern Physics **59**, 287 (1987).
- [27] V. L. Ginzburg and L. D. Landau, Sov. Phys.-JETP **20**, 1064 (1950) [Zh. Eksp. Teor. Fiz. **20**, 1064 (1950)].
- [28] M. Tinkham, *Introduction to Superconductivity*, (McGraw-Hill, Inc., New York, 1996).
-

- [29] P. G. de Gennes, *Superconductivity of Metals and Alloys*, (Benjamin, New York, 1966).
- [30] E. Maxwell, Phys. Rev. **78**, 477 (1950).
- [31] C. A. Reynolds, B. Serin, and L. B. Nesbitt, Phys. Rev. **84**, 691 (1951).
- [32] J. Bardeen, L. N. Cooper, and J. R. Schrieffer, Phys. Rev. **108**, 1175 (1957).
- [33] J. G. Daunt and K. Mendelssohn, Proc. Roy. Soc. (London) **A185**, 225 (1946).
- [34] W. S. Corak, B. B. Goodman, C. B. Satterthwaite, and A. Wexler, Phys. Rev. **96**, 1442 (1954).
- [35] W. S. Corak, B. B. Goodman, C. B. Satterthwaite, and A. Wexler, Phys. Rev. **102**, 656 (1956).
- [36] L. P. Gor'kov, Sov. Phys.-JETP **36**, 1364 (1959) [Zh. Eksp. Teor. Fiz. **36**, 1364 (1959)].
- [37] G. Bednorz and K. A. Müller, Z. Phys. B **64**, 189 (1986).
- [38] H. Maeda, Y. Tanaka, M. Fukutomi, and T. Asano, Jpn. J. Appl. Phys. **27**, L209 (1988).
- [39] M. A. Subramanian, C. C. Torardi, J. C. Calabrese, J. Gopalakrishnan, K. J. Morrissey, T. R. Askew, R. B. Flippen, U. Chowdhry, A. W. Sleight, Science **239**, 1015 (1988).
- [40] S. A. Sunshine, T. Siegrist, L. F. Schneemeyer, D. W. Murphy, R. J. Cava, B. Batlogg, R. B. van Dover, R. M. Fleming, S. H. Glarum, S. Nakahara, R. Farrow, J. J. Krajewski, S. M. Zahurak, J. V. Waszczak, J. H. Marshall, P. Marsh, L. W. Rupp, Jr., and W. F. Peck, Phys. Rev. B **38**, 893(R) (1988).
- [41] J. L. Tallon, R. G. Buckley, P. W. Gilberd, M. R. Presland, I. W. M. Brown, M. E. Bowden, L. A. Christian, and R. Goguel, Nature **333**, 153 (1988).
- [42] M. K. Wu, J. R. Ashburn, C. J. Torng, P. H. Hor, R. L. Meng, L. Gao, Z. J. Huang, Y. Q. Wang, and C. W. Chu, Phys. Rev. Lett. **58**, 908 (1987).
-

-
- [43] G. Kotliar, Phys. Rev. B **37**, 3664 (1988).
- [44] M. Sigrist and T. M. Rice, Rev. Mod. Phys. **67**, 503 (1995).
- [45] J. W. Loram, K. A. Mirza, J. R. Cooper, and W. Y. Liang, Phys. Rev. Lett. **71**, 1740 (1993).
- [46] X. G. Zheng, C. N. Xu, Y. Tomokiyo, E. Tanaka, H. Yamada, and Y. Soejima, Phys. Rev. Lett. **85**, 5170 (2000).
- [47] T. Wu, H. Mayaffre, S. Krämer, M. Horvatić, C. Berthier, W. N. Hardy, R. Liang, D. A. Bonn, and M.-H. Julien, Nature **477**, 191 (2011).
- [48] P. Monthoux, A. V. Balatsky, and D. Pines, Phys. Rev. B **46**, 14803 (1992).
- [49] D. J. Van Harlingen, Rev. Mod. Phys. **67**, 515 (1995).
- [50] N. D. Mathur, F. M. Grosche, S. R. Julian, I. R. Walker, D. M. Freye, R. K. W. Haselwimmer, and G. G. Lonzarich, Nature **394**, 39 (1998).
- [51] J. Nagamatsu, N. Nakagawa, T. Muranaka, Y. Zenitani, and J. Akimitsu, Nature (London) **410**, 63 (2001).
- [52] S. L. Bud'ko, G. Lapertot, C. Petrovic, C. E. Cunningham, N. Anderson, and P. C. Canfield, Phys. Rev. Lett. **86**, 1877 (2001).
- [53] D. G. Hinks, H. Claus, J. P. Jorgensen, Nature **411**, 457 (2001).
- [54] A. Y. Liu, I. I. Mazin, and J. Kortus, Phys. Rev. Lett. **87**, 087005 (2001).
- [55] J. Kortus, I. I. Mazin, K. D. Belashchenko, V. P. Antropov, and L. L. Boyer, Phys. Rev. Lett. **86**, 4656 (2001).
- [56] P. C. Canfield and G. W. Crabtree, Phys. Today **56**, 34 (2003).
- [57] P. C. Canfield, S. L. Bud'ko, D. K. Finnemore, Physica C **385**, 1 (2003).
- [58] I. I. Mazin, V. P. Antropov, Physica C **385**, 49 (2003).
- [59] H. J. Choi, M. L. Cohen, S. G. Louie, Physica C **385**, 66 (2003).
- [60] D. G. Hinks, J. P. Jorgensen, Physica C **385**, 98 (2003).
- [61] I. I. Mazin, O. K. Andersen, O. Jepsen, A. A. Golubov, O. V. Dolgov, and J. Kortus, Phys. Rev. B **69**, 056501 (2004).
-

-
- [62] G. Blumberg, A. Mialitsin, M. V. Klein, N. D. Zhigadlo, and J. Karpinski, *Phys. Rev. Lett.* **99**, 227002 (2007).
- [63] Y. Kamihara, H. Hiramatsu, M. Hirano, R. Kawamura, H. Yanagi, T. Kamiya, and H. Hosono, *J. Am. Chem. Soc.* **128**, 10012 (2006).
- [64] Y. Kamihara, T. Watanabe, M. Hirano, H. Hosono, *J. Am. Chem. Soc.* **130**, 3296 (2008).
- [65] X. H. Chen, T. Wu, G. Wu, R. H. Liu, H. Chen, and D. F. Fang, *Nature (London)* **453**, 761 (2008).
- [66] M. Rotter, M. Tegel, D. Johrendt, *Phys. Rev. Lett.* **101**, 107006 (2008).
- [67] Clarina de la Cruz, Q. Huang, J. W. Lynn, J. Li, W. Ratcliff II, J. L. Zarestky, H. A. Mook, G. F. Chen, J. L. Luo, N. L. Wang, and P. Dai, *Nature (London)* **453**, 899 (2008).
- [68] Y. Nakai, K. Ishida, Y. Kamihara, M. Hirano, and H. Hosono, *J. Phys. Soc. Jpn.* **77**, 073701 (2008).
- [69] H.-J. Grafe, D. Paar, G. Lang, N. J. Curro, G. Behr, J. Werner, J. Hamann-Borrero, C. Hess, N. Leps, R. Klingeler, and B. Bchner, *Phys. Rev. Lett.* **101**, 047003 (2008).
- [70] A. V. Chubukov, D. V. Efremov, and I. Eremin, *Phys. Rev. B* **78**, 134512 (2008).
- [71] D. Parker, O. V. Dolgov, M. M. Korshunov, A. A. Golubov, and I. I. Mazin, *Phys. Rev. B* **78**, 134524 (2008).
- [72] C. Liu, G. D. Samolyuk, Y. Lee, N. Ni, T. Kondo, A. F. Santander-Syro, S. L. Budko, J. L. McChesney, E. Rotenberg, T. Valla, A. V. Fedorov, P. C. Canfield, B. N. Harmon, and A. Kaminski, *Phys. Rev. Lett.* **101**, 177005 (2008).
- [73] H. Ding, P. Richard, K. Nakayama, K. Sugawara, T. Arakane, Y. Sekiba, A. Takayama, S. Souma, T. Sato, T. Takahashi, Z. Wang, X. Dai, Z. Fang, G. F. Chen, J. L. Luo and N. L. Wang, *EPL* **83**, 47001 (2008).
- [74] K. Matano, Z. A. Ren, X. L. Dong, L. L. Sun, Z. X. Zhao, and G.-q. Zheng, *EPL* **83**, 57001 (2008).
- [75] M. E. Zhitomirsky and V.-H. Dao, *Phys. Rev. B* **69**, 054508 (2004).
-

-
- [76] J. M. Blatt and C. J. Thompson, Phys. Rev. Lett. **10**, 332 (1963).
- [77] A. Paskin and A. D. Singh, Phys. Rev. **140**, A1965 (1965).
- [78] V. Ya. Demikhovskii, Fiz. Tverd. Tela **7**, 3600 (1965) [Sov. Phys.-Solid State **7**, 2903 (1966)].
- [79] B. A. Tavger and V. Ya. Demikhovskii, Zh. Eksp. Teor. Fiz. **51**, 528 (1965) [Sov. Phys.-JETP **24**, 354 (1966)].
- [80] R. Henning, Z. Naturforsch. **229**, 985 (1967).
- [81] V. Z. Kresin and B. A. Tavger, Zh. Eksp. Teor. Fiz. **50**, 1689 (1966) [Sov. Phys.-JETP **23**, 1124 (1966)].
- [82] V. L. Berezinskii, Sov. Phys.-JETP **34**, 610 (1972).
- [83] J. M. Kosterlitz, and D. J. Thouless, J. Phys. C: Solid State Phys. **6**, 1181 (1973).
- [84] M. R. Beasley, J. E. Mooij, and T. P. Orlando, Phys. Rev. Lett. **42**, 1165 (1979).
- [85] A. A. Abrikosov, Sov. Phys.-JETP **5**, 1174 (1957) [Zh. Eksp. Teor. Fiz. **32**, 1442 (1957)].
- [86] V. V. Schmidt, *The Physics of Superconductors*, (Springer-Verlag Berlin Heidelberg, 1997).
- [87] A. A. Abrikosov, L. P. Gor'kov, and I. E. Dzyaloshinsky, *The methods of quantum field theory in statistical physics*, (Universitet, Moscow, 2006).
- [88] V. A. Moskalenko, Phys. Met. Metallogr. **8**, 25 (1959) [in Russian, Fiz. Met. Metalloved. **8**, 503 (1959)].
- [89] H. Suhl, B. T. Matthias, and L. R. Walker, Phys. Rev. Lett. **3**, 552 (1959).
- [90] A. J. Leggett, Prog. of Theor. Phys. **36**, 901 (1966).
- [91] M. V. Milošević and A. Perali, Supercond. Sci. Technol. **28**, 060201 (2015).
- [92] J. R. Cooper, A. Carrington, P. J. Meeson, E. A. Yelland, N. E. Hussey, L. Balicas, S. Tajima, S. Lee, S. M. Kazakov, J. Karpinski, Physica C **385**, 75 (2003).
-

- [93] P. Szabó, P. Samuely, J. Kačmarčík, T. Klein, J. Marcus, D. Fruchart, S. Miraglia, C. Marcenat, and A. G. M. Jansen, *Phys. Rev. Lett.* **87**, 137005 (2001).
- [94] M. Iavarone, G. Karapetrov, A. E. Koshelev, W. K. Kwok, G. W. Crabtree, D. G. Hinks, W. N. Kang, E.-M. Choi, H. J. Kim, H.-J. Kim, and S. I. Lee, *Phys. Rev. Lett.* **89**, 187002 (2002).
- [95] S. Tsuda, T. Yokoya, T. Kiss, Y. Takano, K. Togano, H. Kito, H. Ihara, and S. Shin, *Phys. Rev. Lett.* **87**, 177006 (2001).
- [96] F. Bouquet, R. A. Fisher, N. E. Phillips, D. G. Hinks, and J. D. Jorgensen, *Phys. Rev. Lett.* **87**, 47001 (2001).
- [97] Y. Wang, T. Plackowski, and A. Junodet, *Physica C* **355**, 179 (2001).
- [98] E. A. Yelland, J. R. Cooper, A. Carrington, N. E. Hussey, P. J. Meeson, S. Lee, A. Yamamoto, and S. Tajimaet, *Phys. Rev. Lett.* **88**, 217002 (2002).
- [99] J. Paglione and R. L. Greene, *Nature Phys.* **6**, 645 (2010).
- [100] J. Dong, H. J. Zhang, G. Xu, Z. Li, G. Li, W. Z. Hu, D. Wu, G. F. Chen, X. Dai, J. L. Luo, Z. Fang, and N. L. Wang, *EPL* **83**, 27006 (2008).
- [101] T. Nomura, S. W. Kim, Y. Kamihara, M. Hirano, P. V. Sushko, K. Kato, M. Takata, A. L. Shluger, and H. Hosono, *Supercond. Sci. Technol.* **21**, 125028 (2008).
- [102] H.-H. Klauss, H. Luetkens, R. Klingeler, C. Hess, F. J. Litterst, M. Kraken, M. M. Korshunov, I. Eremin, S.-L. Drechsler, R. Khasanov, A. Amato, J. Hamann-Borrero, N. Leps, A. Kondrat, G. Behr, J. Werner, and B. Büchner, *Phys. Rev. Lett.* **101**, 077005 (2008).
- [103] G. F. Chen, Z. Li, D. Wu, G. Li, W. Z. Hu, J. Dong, P. Zheng, J. L. Luo, and N. L. Wang, *Phys. Rev. Lett.* **100**, 247002 (2008).
- [104] Z.-A. Ren, J. Yang, W. Lu, W. Yi, G.-C. Che, X.-L. Dong, L.-L. Sun, and Z.-X. Hao, *Mater. Res. Innovations* **12**, 105 (2008).
- [105] R. H. Liu, T. Wu, G. Wu, H. Chen, X. F. Wang, Y. L. Xie, J. J. Ying, Y. J. Yan, Q. J. Li, B. C. Shi, W. S. Chu, Z. Y. Wu, and X. H. Chen, *Nature* **459**, 64 (2009).
-

- [106] T. Kondo, A. F. Santander-Syro, O. Copie, C. Liu, M. E. Tillman, E. D. Mun, J. Schmalian, S. L. Budko, M. A. Tanatar, P. C. Canfield, and A. Kaminski, *Phys. Rev. Lett.* **101**, 147003 (2008).
- [107] T. Y. Chen, Z. Tesanovic, R. H. Liu, X. H. Chen, and C. L. Chien, *Nature (London)* **453**, 1224 (2008).
- [108] B. A. Tavger and V. Ya. Demikhovskii, *Usp. Fiz. Nauk* **96**, 61 (1968) [*Sov. Phys.-Usp.* **11**, 644 (1969)].
- [109] D. Eom, S. Qin, M. Y. Chou, and C. K. Shih, *Phys. Rev. Lett.* **96**, 027005 (2006).
- [110] Yu. F. Komnik, E. I. Bukhshtab, and K. K. Man'kovskii, *Zh. Eksp. Teor. Fiz.* **57**, 1495 (1969).
- [111] Yu. F. Komnik, E. I. Bukhshtab, Yu. V. Nikitin, F. I. Chuprinin, and C. Sulkowskii, *Thin Solid Films* **11**, 43 (1972).
- [112] Y. Guo, Y.-F. Zhang, X.-Y. Bao, T.-Z. Han, Z. Tang, L.-X. Zhang, W.-G. Zhu, E. G. Wang, Q. Niu, Z. Q. Qiu, J.-F. Jia, Z.-X. Zhao, Q.-K. Xue, *Science* **306**, 1915 (2004).
- [113] X.-Y. Bao, Y.-F. Zhang, Y. Wang, J.-F. Jia, Q.-K. Xue, X. C. Xie, and Z.-X. Zhao, *Phys. Rev. Lett.* **95**, 247005 (2005).
- [114] T. Zhang, P. Cheng, W.-J. Li, Y.-J. Sun, G. Wang, X.-G. Zhu, K. He, L. Wang, X. Ma, X. Chen, Y. Wang, Y. Liu, H.-Q. Lin, J.-F. Jia, and Q.-K. Xue, *Nat. Phys.* **6**, 104 (2010).
- [115] Y. X. Ning, C. L. Song, Y. L. Wang, X. Chen, J. F. Jia, Q. K. Xue, and X. C. Ma, *J. Phys.: Condens. Matter* **22**, 065701 (2010).
- [116] W. Zhao, Q. Wang, M. Liu, W. Zhang, Y. Wang, M. Chen, Y. Guo, K. He, X. Chen, Y. Wang, J. Wang, X. Xie, Q. Niu, L. Wang, X. Ma, J. K. Jain, M. H. W. Chan, Q.-K. Xue, *Solid State Commun.* **165**, 59 (2013).
- [117] Y.-S. Fu, S.-H. Ji, T. Zhang, X. Chen, J.-F. Jia, Q.-K. Xue, and X.-C. Ma, *Chin. Phys. Lett.* **27**, 066804 (2010).
- [118] Y. Wang, M. Chen, Z. Li, L. Wang, K. He, Q.-K. Xue, and X. Ma, *Appl. Phys. Lett.* **103**, 242603 (2013).
- [119] S. Y. Qin, J. Kim, Q. Niu, and C. K. Shih, *Science* **324**, 1314 (2009).
-

- [120] J. Kim, V. Chua, G. A. Fiete, H. Nam, A. H. MacDonald, and C.-K. Shih, *Nat. Phys.* **8**, 464 (2012).
- [121] S. N. Bose, *Z. Phys.* **26**, 178 (1924).
- [122] A. Einstein, *Sitzungber. Kgl. Preuss. Akad. Wiss.* **1924**, 261 (1924).
- [123] A. Einstein, *Sitzungber. Kgl. Preuss. Akad. Wiss.* **1925**, 3 (1925).
- [124] P. Kapitza, *Nature* **141**, 74 (1938).
- [125] J. F. Allen and A. D. Misener, *Nature* **141**, 75 (1938).
- [126] F. London, *Phys. Rev.* **54**, 947 (1938).
- [127] F. London, *Nature* **141**, 643 (1938).
- [128] C. H. Hecht, *Physica* **25**, 1159 (1959).
- [129] W. C. Stwalley and L. H. Nosanow, *Phys. Rev. Lett.* **36**, 910 (1976).
- [130] D. G. Fried, T. C. Killian, L. Willmann, D. Landhuis, S. C. Moss, D. Kleppner, and T. J. Greytak, *Phys. Rev. Lett.* **81**, 3811 (1998).
- [131] W. Ketterle, *Rev. Mod. Phys.* **74**, 1131 (2002).
- [132] M. H. Anderson, J. R. Ensher, M. R. Matthews, C. E. Wieman, and E. A. Cornell, *Science* **269**, 198, (1995).
- [133] K. B. Davis, M.-O. Mewes, M. R. Andrews, N. J. van Druten, D. S. Durfee, D. M. Kurn, and W. Ketterle, *Phys. Rev. Lett.* **75**, 3969 (1995).
- [134] C. C. Bradley, C. A. Sackett, J. J. Tollet, and R. G. Hulet, *Phys. Rev. Lett.* **75**, 1687 (1995).
- [135] C. J. Pethick and H. Smith, *Bose-Einstein Condensation in dilute gases*, (Cambridge University Press, Cambridge, second edition, 2008).
- [136] L. P. Pitaevskii, *Zh. Eksp. Teor. Fiz.* **40**, 646 (1961) [*Sov. Phys.-JETP* **13**, 451 (1961)].
- [137] E. P. Gross, *Nuova Cimento* **20**, 454 (1961).
- [138] E. P. Gross, *J. Math. Phys.* **4**, 195 (1961).
- [139] N. N. Bogoliubov, *J. Phys. (USSR)* **11**, 23 (1947).
-

-
- [140] A. L. Fetter and A. A. Svidzinsky, *J. Phys.: Condens. Matter* **13**, 135 (2001).
- [141] E. Tiesinga, C. W. Williams, P. S. Julienne, K. M. Jones, P. D. Lett, and W. D. Phillips, *J. Res. Natl Inst. Stand. Technol.* **101**, 505 (1996).
- [142] H. M. J. M. Boesten, C. C. Tsai, J. R. Gardner, D. N. Heinzen, and B. J. Verhaar, *Phys. Rev. A* **55**, 636 (1997).
- [143] E. R. I. Abraham, W. I. McAlexander, C. A. Sackett, and R. G. Hulet, *Phys. Rev. Lett.* **74**, 1315 (1995).
- [144] J. Stenger, S. Inouye, D. M. Stamper-Kurn, H.-J. Miesner, A. P. Chikkatur, and W. Ketterle, *Nature* **396**, 345 (1998).
- [145] M. R. Matthews, B. P. Anderson, P. C. Haljan, D. S. Hall, M. J. Holland, J. E. Williams, C. E. Wieman, and E. A. Cornell, *Phys. Rev. Lett.* **83**, 3358 (1999).
- [146] J. Williams, R. Walser, J. Cooper, E. Cornell, and M. Holland, *Phys. Rev. A* **59**, 31(R) (1999).
- [147] P. Maddaloni, M. Modugno, C. Fort, F. Minardi, and M. Inguscio, *Phys. Rev. Lett.* **85**, 2413 (2000).
- [148] S. Inouye, S. Gupta, T. Rosenband, A. P. Chikkatur, A. Görlitz, T. L. Gustavson, A. E. Leanhardt, D. E. Pritchard, and W. Ketterle, *Phys. Rev. Lett.* **87**, 080402 (2001).
- [149] C. Hamner, J. J. Chang, P. Engels, and M. A. Hofer, *Phys. Rev. Lett.* **106**, 065302 (2011).
- [150] C. Hamner, Y. Zhang, J. J. Chang, C. Zhang, and P. Engels, *Phys. Rev. Lett.* **111**, 264101 (2013).
- [151] G. Ferrari, M. Inguscio, W. Jastrzebski, G. Modugno, G. Roati, and A. Simoni, *Phys. Rev. Lett.* **89**, 053202 (2002).
- [152] G. Modugno, M. Modugno, F. Riboli, G. Roati, and M. Inguscio, *Phys. Rev. Lett.* **89**, 190404 (2002).
- [153] J. Catani, L. De Sarlo, G. Barontini, F. Minardi, and M. Inguscio, *Phys. Rev. A* **77**, 011603 (2008).
- [154] G. Thalhammer, G. Barontini, L. De Sarlo, J. Catani, F. Minardi, and M. Inguscio, *Phys. Rev. Lett.* **100**, 210402 (2008).
-

-
- [155] K. Aikawa, D. Akamatsu, J. Kobayashi, M. Ueda, T. Kishimoto, and S. Inouye, *New J. Phys.* **11**, 055035 (2009).
- [156] J. Catani, G. Barontini, G. Lamporesi, F. Rabatti, G. Thalhammer, F. Minardi, S. Stringari, and M. Inguscio, *Phys. Rev. Lett.* **103**, 140401 (2009).
- [157] K. Kasamatsu, M. Tsubota, and M. Ueda, *Phys. Rev. Lett.* **91**, 150406 (2003).
- [158] S.-J. Yang, Q.-S. Wu, S.-N. Zhang, and S. Feng, *Phys. Rev. A* **77**, 033621 (2008).
- [159] P. Mason, and A. Aftalion, *Phys. Rev. A* **84**, 033611 (2011).
- [160] C. Chin, R. Grimm, P. Julienne, and E. Tiesinga, *Rev. Mod. Phys.* **82**, 1225 (2010).
- [161] A. L. Fetter, *Rev. of Mod. Phys.* **81**, 647 (2009).
- [162] E. A. Cornell, D. S. Hall, M. R. Matthews, and C. E. Weiman, *J. Low Temp. Phys.* **113**, 151 (1998).
- [163] W. Bao, D. Jaksch, and P. A. Markowich, *J. Comp. Phys.* **187**, 318 (2003).
- [164] A. Klein, D. Jaksch, Y. Zhang, and W. Bao, *Phys. Rev. A* **76**, 043602 (2007).
- [165] R. Kato, Y. Enomoto, and S. Maekawa, *Phys. Rev. B* **44**, 6916 (1991).
- [166] R. Kato, Y. Enomoto, and S. Maekawa, *Phys. Rev. B* **47**, 8016 (1992).
- [167] M. V. Milošević, R. Geurts, *Physica C* **470**, 791 (2010).
- [168] E. M. Lifshitz and L. P. Pitaevskii, *Statistical Physics, part 2*, (Pergamon, Oxford, 3rd edition, 1980).
- [169] D. R. Tilley and J. Tilley, *Superfluidity and Superconductivity*, (Hilger, Bristol, 2nd edition, 1986).
- [170] E. J. Yarmchuk, M. J. V. Gordon, and R. E. Packard, *Phys. Rev. Lett.* **43**, 214 (1979).
- [171] W. F. Vinen, *Superconductivity*, (Dekker, New York, 1969).
-

-
- [172] B. P. Anderson, *J. Low Temp. Phys.* **161**, 574 (2010).
- [173] L. Onsager, *Nuovo Cimento Suppl.* 2 **6**, 249 (1949).
- [174] L. Onsager, *Nuovo Cimento Suppl.* 2 **6**, 281 (1949).
- [175] R. P. Feynman, *Prog. Low Temp. Phys.* **1**, 17 (1955).
- [176] U. Essmann and H. Trauble, *Phys. Lett.* **24A**, 526 (1967).
- [177] N. V. Sarma, *Philos. Ma.* **17**, 1233 (1968).
- [178] J. Garaud, J. Carlström, E. Babaev, and M. Speight, *Phys. Rev. B* **87**, 014507 (2013).
- [179] U. Al Khawaja, and H. Stoof, *Nature* **411**, 918 (2001).
- [180] T. H. R. Skyrme, *Proc. Roy. Soc. Ser. A.* **226**, 521 (1954).
- [181] T. H. R. Skyrme, *Ibidem.* **230**, 277 (1955).
- [182] T. H. R. Skyrme, *Proc. Roy. Soc. Ser. A.* **247**, 260 (1958).
- [183] T. H. R. Skyrme, *Ibidem.* **252**, 236 (1959).
- [184] H. F. Hess, R. B. Robinson, R. C. Dynes, J. M. Valles, Jr., and J. V. Waszczak, *Phys. Rev. Lett.* **62**, 214 (1989).
- [185] P. L. Gammel, D. J. Bishop, G. J. Dolan, J. R. Kwo, C. A. Murray, L. F. Schneemeyer, and J. V. Waszczak, *Phys. Rev. Lett.* **59**, 2592 (1987).
- [186] C. A. Bolle, P. L. Gammel, D. G. Grier, C. A. Murray, D. J. Bishop, D. B. Mitzi, and A. Kapitulnik, *Phys. Rev. Lett.* **66**, 112 (1991).
- [187] K. Harada, T. Matsuda, J. Bonevich, M. Igarashi, S. Kondo, G. Pozzi, U. Kawabe and A. Tonomura, *Nature* **360**, 51 (1992.)
- [188] A. Bezryadin, Yu. N. Ovchinnikov, and B. Pannetier, *Phys. Rev. B* **53**, 8553 (1996).
- [189] L. Ya. Vinnikov, J. Karpinski, S. M. Kazakov, J. Jun, J. Anderegg, S. L. Budko, and P. C. Canfield, *Phys. Rev. B* **67**, 092512 (2003).
- [190] T. H. R. Skyrme, *Ibidem.* **262**, 237 (1961).
- [191] T. H. R. Skyrme, *Proc. R. Soc. Lond. A* **260**, 127 (1961).
-

- [192] T. H. R. Skyrme, Nucl. Phys. **31**, 556 (1962).
- [193] V. G. Makhan'kov, Yu. P. Rybakov, and V. I. Sanyuk, Usp. Fiz. Nauk **162**, 1 (1992).
- [194] A. P. Balachandran, *The skyrme soliton*, (Opening talk at the Soliton Workshop at the Lewes Center for Physics, University of Delaware, Delaware, June 1984).
- [195] N. S. Kiselev, A. N. Bogdanov, R. Schäfer, and U. K. Rößler, Journal of Physics D: Applied Physics **44**, 392001 (2011).
- [196] J.-I. Fukuda, S. Žumer, Nature Communications **2**, 246 (2011).
- [197] D. F. Agterberg, E. Babaev, and J. Garaud, Phys. Rev. B **90**, 064509 (2014).
- [198] L. D. Landau, E. M. Lifshitz, *Statistical Physics, part1*, (Nauka, Moscow, 1976) [English translation: Pergamon Press, Oxford, 1980].
- [199] V. Z. Kresin, Journal of Low Temp. Phys. **11**, 519 (1973).
- [200] M. L. Teague, G. K. Drayna, G. P. Lockhart, P. Cheng, B. Chen, H. H. Wen, and N. C. Yeh, Phys. Rev. Lett. **106**, 087004 (2011).
- [201] C. Brun, I. Po Hong, F. Patthey, I. Y. Sklyadnev, R. Heid, P. M. Echenique, K. P. Bohnen, E. V. Chulkov, and W. D. Schneider, *ibid.* **102**, 207002 (2009).
- [202] A. Gurevich, Phys. Rev. B **67**, 184515 (2003).
- [203] A. A. Golubov and A. E. Koshelev, Phys. Rev. B **68**, 104503 (2003).
- [204] E. Babaev and M. Speight, Phys. Rev. B **72**, 180502 (2005).
- [205] E. Babaev, J. Jäykkä, and M. Speight, Phys. Rev. Lett. **103**, 237002 (2009).
- [206] E. Babaev, J. Carlström, and M. Speight, Phys. Rev. Lett. **105**, 067003 (2010).
- [207] T. K. Ng and N. Nagaosa, EPL **87**, 17003 (2009).
- [208] X. Hu and Z. Wang, Phys. Rev. B **85**, 064516 (2012).
- [209] T. Yanagisawa, Y. Tanaka, I. Hase, K. Yamaji, Physica C **471**, 675 (2011).
-

-
- [210] J. Garaud, J. Carlström, and E. Babaev, Phys. Rev. Lett. **107**, 197001 (2011).
- [211] J. Carlström, J. Garaud, and E. Babaev, Phys. Rev. B **84**, 134518 (2011).
- [212] R. Geurts, M. V. Milošević, and F. M. Peeters, Phys. Rev. B **81**, 214514 (2010).
- [213] T. Yanagisawa, Y. Tanaka, I. Hase and K. Yamaji, J. Phys. Soc. Jpn. **81**, 024712 (2012).
- [214] G. E. Volovik and L. P. Gor'kov, Sov. Phys.-JETP **61**, 843 (1985) [Zh. Eksp. Teor. Fiz. **88**, 1412 (1985)].
- [215] M. Sigrist and K. Ueda, Rev. Mod. Phys. **63**, 239 (1991).
- [216] A. A. Shanenko, M. V. Milošević, F. M. Peeters, and A. V. Vagov, Phys. Rev. Lett. **106**, 047005 (2011).
- [217] A. Vagov, A. A. Shanenko, M. V. Milošević, V. M. Axt, and F. M. Peeters, Phys. Rev. B **86**, 144514 (2012).
- [218] A. V. Vagov, A. A. Shanenko, M. V. Milošević, V. M. Axt, and F. M. Peeters, Phys. Rev. B **85**, 014502 (2012).
- [219] C. J. Thomson and J. M. Blatt, Phys. Lett. **5**, 6 (1963).
- [220] D. A. Kirzhnits and Y. G. Maksimov, Phys. Met. Metallogr. **22**, 45 (1966) [Fiz. Met. Metalloved. **22**, 520 (1966)].
- [221] E. H. Hwang, S. Das Sarma, and M. A. Stroscio, Phys. Rev. B **61**, 8659 (2000).
- [222] A. L. Fetter and J. D. Walecka, *Quantum Theory of Many-Particle Systems*, (Dover, New York, 2003).
- [223] V. H. Dao, L. F. Chibotaru, T. Nishio, and V. V. Moshchalkov, Phys. Rev. B **83**, 020503 (2011).
- [224] A. Chaves, L. Komendová, M. V. Milošević, J. S. Andrade Jr., G. A. Farias, and F. M. Peeters, Phys. Rev. B **83**, 214523 (2011).
- [225] S.-Z. Lin and X. Hu, Phys. Rev. B **84**, 214505 (2011).
- [226] M. A. Silaev, Phys. Rev. B **83**, 144519 (2011).
-

-
- [227] H. H. Weitering, Chem. Phys. Chem. **10**, 3183 (2010).
- [228] G. R. Stewart, Rev. Mod. Phys. **83**, 1589 (2011).
- [229] R. Khasanov, M. Bendele, A. Amato, K. Conder, H. Keller, H.-H. Klauss, H. Luetkens, and E. Pomjakushina, Phys. Rev. Lett. **104**, 087004 (2010).
- [230] J.-P. Wang, Phys. Rev. B **82**, 132505 (2010).
- [231] Y. Tanaka, Phys. Rev. Lett. **88**, 017002 (2002).
- [232] A. A. Shanenkov, M. D. Croitoru, and F. M. Peeters, Phys. Rev. B **75**, 014519 (2007).
- [233] W. Zhao, Q. Wang, M. Liu, W. Zhang, Y. Wang, M. Chen, Y. Guo, K. He, X. Chen, Y. Wang, J. Wang, X. Xie, Q. Niu, L. Wang, X. Ma, J. Jain, M. H. W. Chan, Q.-K. Xue, Solid State Comm. **165**, 59 (2013).
- [234] Y. Chen, A. A. Shanenkov, and F. M. Peeters, Phys. Rev. B **81**, 134523 (2010).
- [235] A. Perali, A. Bianconi, A. Lanzara, N. L. Saini, Solid State Comm. **41**, 181 (1996).
- [236] A. A. Shanenkov and M. D. Croitoru, Phys. Rev. B **73**, 012510 (2006).
- [237] A. Larkin and A. Varlamov, *Theory of Fluctuations in Superconductors*, (Oxford University Press, Oxford, 2004).
- [238] Y. Chen, A. A. Shanenkov, A. Perali, and F. M. Peeters, J. Phys.: Condens. Matt. **24**, 185701 (2012).
- [239] A. A. Shanenkov, M. D. Croitoru, A. V. Vagov, V. M. Axt, A. Perali, and F. M. Peeters, Phys. Rev. A **86**, 033612 (2012).
- [240] E. Rotenberg, H. Koh, K. Rossnagel, H. W. Yeom, J. Schäfer, B. Krenzer, M. P. Rocha, and S. D. Kevan, Phys. Rev. Lett. **91**, 246404 (2003).
- [241] I.-P. Hong, C. Brun, F. Patthey, I. Yu. Sklyadneva, X. Zubizarreta, R. Heid, V. M. Silkin, P. M. Echenique, K. P. Bohnen, E. V. Chulkov, and W.-D. Schneider, Phys. Rev. B **80**, 081409(R) (2009).
- [242] J. Pearl, Appl. Phys. Lett. **5**, 65 (1964).
-

-
- [243] L. Komendová, M. V. Milošević, A. A. Shanenko, and F. M. Peeters, *Phys. Rev. B* **84**, 064522 (2011).
- [244] A. E. Koshelev and A. A. Golubov, *Phys. Rev. Lett.* **92**, 107008 (2004).
- [245] A. E. Koshelev, A. A. Varlamov, and V. M. Vinokur, *Phys. Rev. B* **72**, 064523 (2005).
- [246] K. Ueno, S. Nakamura, H. Shimotani, A. Ohtomo, N. Kimura, T. Nojima, H. Aoki, Y. Iwasa, and M. Kawasaki, *Nature Mat.* **7**, 855 (2008).
- [247] J. T. Ye, S. Inoue, K. Kobayashi, Y. Kasahara, H. T. Yuan, H. Shimotani, and Y. Iwasa, *Nature Mat.* **9**, 125 (2010).
- [248] K. Ueno, S. Nakamura, H. Shimotani, H. T. Yuan, N. Kimura, T. Nojima, H. Aoki, Y. Iwasa, and M. Kawasaki, *Nature Nanotech.* **6**, 408 (2011).
- [249] J. R. Abo-Shaeer, C. Raman, J. M. Vogels, and W. Ketterle, *Science* **292**, 476 (2001).
- [250] P. Engels, I. Coddington, P. C. Haljan, and E. A. Cornell, *Phys. Rev. Lett.* **89**, 100403 (2002).
- [251] M. W. Zwierlein, J. R. Abo-Shaeer, A. Schirotzek, C. H. Schunck, and W. Ketterle, *Nature (London)* **435**, 1047 (2005).
- [252] K. Kasamatsu, M. Tsubota, and M. Ueda, *Int. J. Mod. Phys. B* **19**, 1835 (2005).
- [253] P. Kuopanportti, N. V. Orlova, and M. V. Milošević, *Phys. Rev. A* **91**, 043605 (2015).
- [254] K. Kasamatsu, M. Tsubota, and M. Ueda, *Phys. Rev. Lett.* **93**, 250406 (2004).
- [255] K. Kasamatsu, M. Tsubota, and M. Ueda, *Phys. Rev. A* **71**, 043611 (2005).
- [256] M. Cipriani and M. Nitta, *Phys. Rev. Lett.* **111**, 170401 (2013).
- [257] D. T. Son and M. A. Stephanov, *Phys. Rev. A* **65**, 063621 (2002).
- [258] D. S. Dantas, A. R. P. Lima, A. Chaves, C. A. S. Almeida, G. A. Farias, and M. V. Milošević, *Phys. Rev. A* **91**, 023630 (2015).
-

-
- [259] M. Eto and M. Nitta, Phys. Rev. A **85**, 053645 (2012).
- [260] N. V. Orlova, A. A. Shanenko, M. V. Milošević, F. M. Peeters, A. V. Vagov, and V. M. Axt, Phys. Rev. B **87**, 134510 (2013).
- [261] M. Sigrist and D. F. Agterberg, Prog. Theor. Phys. **102**, 965 (1999).
- [262] S. Gillis, J. Jäykkä, and M. V. Milošević, Phys. Rev. B **89**, 024512 (2014).
- [263] Y. Matsunaga, M. Ichioka, and K. Machida, Phys. Rev. Lett. **92**, 157001 (2004).
- [264] L. Allen and J. H. Eberly, *Optical Resonance and Two-Level Atoms* (A Wiley-Interscience publication, 1975).
- [265] H. Zeng, W. Zhang, and F. Lin, Phys. Rev. A **52**, 2155 (1995).
- [266] M. Cipriani and M. Nitta, Phys. Rev. A **88**, 013634 (2013).
- [267] N. Lo Gullo, T. Busch, and M. Paternostro, Phys. Rev. A **83**, 053612 (2011).
- [268] D. S. Hall, M. R. Matthews, C. E. Wieman, and E. A. Cornell, Phys. Rev. Lett. **81**, 1543 (1998).
- [269] K. W. Madison, F. Chevy, W. Wohlleben, and J. Dalibard, Phys. Rev. Lett. **84**, 806 (2000).
- [270] S. B. Papp, J. M. Pino, and C. E. Wieman, Phys. Rev. Lett. **101**, 040402 (2008).
- [271] S. Sugawa, R. Yamazaki, S. Taie, and Y. Takahashi, Phys. Rev. A **84**, 011610 (2011).
- [272] D. J. McCarron, H. W. Cho, D. L. Jenkin, M. P. Köppinger, and S. L. Cornish, Phys. Rev. A **84**, 011603 (2011).
- [273] A. Lercher, T. Takekoshi, M. Debatin, B. Schuster, R. Rameshan, F. Ferlaino, R. Grimm, and H.-C. Nägerl, Eur. Phys. J. D **65**, 3 (2011).
- [274] B. Pasquiou, A. Bayerle, S. M. Tzanova, S. Stellmer, J. Szczepkowski, M. Parigger, R. Grimm, and F. Schreck, Phys. Rev. A **88**, 023601 (2013).
- [275] M. P. Mink, C. M. Smith, and R. A. Duine, Phys. Rev. A **79**, 013605 (2009).
-

-
- [276] E. K. Dahl, E. Babaev, and A. Sudbø, *Phys. Rev. B* **78**, 144510 (2008).
- [277] M. Roncaglia, M. Rizzi, and J. Dalibard, *Sci. Rep.* **1**, 43 (2011).
- [278] M. Abraham, I. Aranson, and B. Galanti, *Phys. Rev. B* **52**, 7018(R) (1995).
- [279] I. Aranson and V. Steinberg, *Phys. Rev. B* **53**, 75 (1996).
- [280] A. C. Santos, V. S. Bagnato, and F. E. A. dos Santos, e-print arXiv:1405.0992.
- [281] A. S. Melnikov and V. M. Vinokur, *Nature (London)* **415**, 60 (2002).
- [282] V. A. Schweigert, F. M. Peeters, and P. S. Deo, *Phys. Rev. Lett.* **81**, 2783 (1998).
- [283] A. Kanda, B. J. Baelus, F. M. Peeters, K. Kadowaki, and Y. Ootuka, *Phys. Rev. Lett.* **93**, 257002 (2004).
- [284] I. V. Grigorieva, W. Escoffier, V. R. Misko, B. J. Baelus, F. M. Peeters, L. Y. Vinnikov, and S. V. Dubonos, *Phys. Rev. Lett.* **99**, 147003 (2007).
- [285] T. Cren, L. Serrier-Garcia, F. Debontridder, and D. Roditchev, *Phys. Rev. Lett.* **107**, 097202 (2009).
- [286] T.-L. Ho, *Phys. Rev. B* **18**, 1144 (1978).
- [287] T. Mizushima, K. Machida, and T. Kita, *Phys. Rev. Lett.* **89**, 030401 (2002).
- [288] T. Mizushima, K. Machida, and T. Kita, *Phys. Rev. A* **66**, 053610 (2002).
- [289] T. Mizushima, N. Kobayashi, and K. Machida, *Phys. Rev. A* **70**, 043613 (2004).
- [290] R. J. Dodd, K. Burnett, M. Edwards, and C. W. Clark, *Phys. Rev. A* **56**, 587 (1997).
- [291] D. S. Rokhsar, *Phys. Rev. Lett.* **79**, 2164 (1997).
- [292] H. Pu, C. K. Law, J. H. Eberly, and N. P. Bigelow, *Phys. Rev. A* **59**, 1533 (1999).
- [293] T. Isoshima and K. Machida, *Phys. Rev. A* **60**, 3313 (1999).
-

-
- [294] A. A. Svidzinsky and A. L. Fetter, *Phys. Rev. Lett.* **84**, 5919 (2000).
- [295] S. M. M. Virtanen, T. P. Simula, and M. M. Salomaa, *Phys. Rev. Lett.* **86**, 2704 (2001).
- [296] Y. Kawaguchi and T. Ohmi, *Phys. Rev. A* **70**, 043610 (2004).
- [297] A. D. Jackson, G. M. Kavoulakis, and E. Lundh, *Phys. Rev. A* **72**, 053617 (2005).
- [298] J. A. M. Huhtamäki, M. Möttönen, and S. M. M. Virtanen, *Phys. Rev. A* **74**, 063619 (2006).
- [299] E. Lundh and H. M. Nilsen, *Phys. Rev. A* **74**, 063620 (2006).
- [300] P. Capuzzi and D. M. Jezek, *J. Phys. B: At. Mol. Opt. Phys.* **42**, 145301 (2009).
- [301] P. Kuopanportti, E. Lundh, J. A. M. Huhtamäki, V. Pietilä, and M. Möttönen, *Phys. Rev. A* **81**, 023603 (2010).
- [302] P. Kuopanportti and M. Möttönen, *Phys. Rev. A* **81**, 033627 (2010).
- [303] A. Marte, T. Volz, J. Schuster, S. Dürr, G. Rempe, E. G. M. van Kempen, and B. J. Verhaar, *Phys. Rev. Lett.* **89**, 283202 (2002).
- [304] M. Erhard, H. Schmaljohann, J. Kronjäger, K. Bongs, and K. Sengstock, *Phys. Rev. A* **69**, 032705 (2004).
- [305] A. Widera, O. Mandel, M. Greiner, S. Kreim, T. W. Hänsch, and I. Bloch, *Phys. Rev. Lett.* **92**, 160406 (2004).
- [306] C. D’Errico, M. Zaccanti, M. Fattori, G. Roati, M. Inguscio, G. Modugno, and A. Simoni, *New J. Phys.* **9**, 223 (2007).
- [307] T. Kishimoto, J. Kobayashi, K. Noda, K. Aikawa, M. Ueda, and S. Inouye, *Phys. Rev. A* **79**, 031602 (2009).
- [308] E. G. M. van Kempen, S. J. J. M. F. Kokkelmans, D. J. Heinzen, and B. J. Verhaar, *Phys. Rev. Lett.* **88**, 093201 (2002).
- [309] H. Wang, A. N. Nikolov, J. R. Ensher, P. L. Gould, E. E. Eyler, W. C. Stwalley, J. P. Burke, J. L. Bohn, C. H. Greene, E. Tiesinga, C. J. Williams, and P. S. Julienne, *Phys. Rev. A* **62**, 052704 (2000).
- [310] U. R. Fischer and G. Baym, *Phys. Rev. Lett.* **90**, 140402 (2003).
-

-
- [311] C. Josserand, *Chaos* **14**, 875 (2004).
- [312] A. Aftalion and I. Danaïla, *Phys. Rev. A* **69**, 033608 (2004).
- [313] A. D. Jackson, G. M. Kavoulakis, and E. Lundh, *Phys. Rev. A* **69**, 053619 (2004).
- [314] A. L. Fetter, B. Jackson, and S. Stringari, *Phys. Rev. A* **71**, 013605 (2005).
- [315] J.-k. Kim and A. L. Fetter, *Phys. Rev. A* **72**, 023619 (2005).
- [316] H. Fu and E. Zaremba, *Phys. Rev. A* **73**, 013614 (2006).
- [317] M. Correggi, T. Rindler-Daller, and J. Yngvason, *J. Math. Phys.* **48**, 042104 (2007).
- [318] M. Correggi, F. Pinsker, N. Rougerie, and J. Yngvason, *Phys. Rev. A* **84**, 053614 (2011).
- [319] E. J. Mueller, *Phys. Rev. A* **69**, 033606 (2004).
- [320] K. Maki and T. Tsuneto, *J. Low Temp. Phys.* **27**, 635 (1977).
- [321] N. D. Mermin, *Rev. Mod. Phys.* **51**, 591 (1979).
- [322] T. P. Simula, S. M. M. Virtanen, and M. M. Salomaa, *Phys. Rev. A* **65**, 033614 (2002).
- [323] P. Kuopanportti and M. Möttönen, *J. Low Temp. Phys.* **161**, 561 (2010).
- [324] E. O. Karabulut, F. Malet, G. M. Kavoulakis, and S. M. Reimann, *Phys. Rev. A* **87**, 043609 (2013).
- [325] F. Chevy, K. W. Madison, and J. Dalibard, *Phys. Rev. Lett.* **85**, 2223 (2000).
- [326] P. C. Haljan, B. P. Anderson, I. Coddington, and E. A. Cornell, *Phys. Rev. Lett.* **86**, 2922 (2001).
- [327] A. E. Leanhardt, A. Görlitz, A. P. Chikkatur, D. Kielpinski, Y.-i. Shin, D. E. Pritchard, and W. Ketterle, *Phys. Rev. Lett.* **89**, 190403 (2002).
- [328] S. Seo, J.-y. Choi, and Y.-i. Shin, *J. Korean Phys. Soc.* **64**, 53 (2014).
-

-
- [329] V. Cherkez, J. C. Cuevas, C. Brun, T. Cren, G. Ménard, F. Debontridder, V. S. Stolyarov, and D. Roditchev, *Phys. Rev. X* **4**, 011033 (2014).
- [330] T. Cren, D. Fokin, F. Debontridder, V. Dubost, and D. Roditchev, *Phys. Rev. Lett.* **102**, 127005 (2009).
- [331] T. Cren, L. Serrier-Garcia, F. Debontridder, and D. Roditchev, *Phys. Rev. Lett.* **107**, 097202 (2011).
- [332] T. Nishio, S. Lin, T. An, T. Eguchi, and Y. Hasegawa, *Nanotechnology* **21**, 465704 (2010).
-